

# **Integration of Biomimetic Pressure Mapping and Actuation in Soft Electroactive Elastomer Composites**

by

Richard James Morrin Ellingham

A thesis submitted for the degree of  
Doctor of Philosophy

in

Mechanical Engineering

at the

**UNIVERSITY OF CANTERBURY**

October 2024

# **Declaration of Authorship**

I, AUTHOR NAME, declare that this thesis titled, 'Integration of Biomimetic Pressure Mapping and Actuation in Soft Electroactive Elastomer Composites' and the work presented in it are my own. I confirm that:

- This work was done wholly or mainly while in candidature for a research degree at this University.
- Where any part of this thesis has previously been submitted for a degree or any other qualification at this University or any other institution, this has been clearly stated.
- Where I have consulted the published work of others, this is always clearly attributed.
- Where I have quoted from the work of others, the source is always given. With the exception of such quotations, this thesis is entirely my own work.
- I have acknowledged all main sources of help.
- Where the thesis is based on work done by myself jointly with others, I have made clear exactly what was done by others and what I have contributed myself.

Signed:

---

Date:

*“We’ve made good progress with the brains of robots but their bodies are still primitive. We need a new kind of robot body that is inspired by elegance, efficiency, and by the soft materials found in nature. Indeed, this has become the key idea of a new field of research called soft robotics.”*

C. Keplinger, 2019

UNIVERSITY OF CANTERBURY

## *Abstract*

College of Engineering  
Mechanical Engineering

Doctor of Philosophy

by Richard James Morrin Ellingham

Some of the world's most advanced technology is rigid due to various factors such as; manufacturability, miniaturisability, physical linearity, and more ideal linear physical mechanics. Since before the industrial revolution rigid sensors and actuators have been evolving and have been refined to a high level, but now these rigid devices are encountering limitations, leading to demand for soft robotic solutions that mimic biological evolution. This thesis develops and integrates an artificial skin and artificial muscle technology by combining of Electrical Impedance Tomography (EIT), carbon black silicone rubber (CBSR) elastomer composites, and Dielectric Elastomer Actuators (DEAs) to enhance pressure mapping, strain sensing, and actuation capabilities. CBSR elastomer composites, noted for their high stretchability, piezoresistivity, and biocompatibility, were investigated to understand their non-linear time dependent phenomena in particular, resistance relaxation behavior. This research contributes to optimising the design of flexible dynamic strain sensors by modelling the response of resistance to transient strain inputs. The next part of the thesis describes development of an EIT-based pressure mapping system using a CBSR sensing domain that mimics pressure mapping qualities of human skin. This system was evaluated for its spatial and temporal resolution, showing potential for creating artificial pressure-sensitive skin with practical applications. At the core of this thesis, the integration of EIT-based sensing with DEAs was tested and analysed to improve the mapping of compressive forces across the actuator electrode surfaces. Despite trade-offs in accuracy due to electrode compliance, this approach offers promising advancements for applications requiring precise actuation and pressure mapping. This work has contributed towards filing a patent for an DEA-EIT actuator-sensor device. Additionally, the research has uncovered unintentional power generation in DEA-EIT systems through FEA studies and analytical validation, which could function as Dielectric Elastomer Generators (DEGs) with mapped compressive load inputs. This finding highlights the multi-functionality of DEAs and suggests opportunities for energy harvesting applications. To aid the portability of EIT-based pressure mapping sensor developed, a low-cost circuit and evaluation tools were developed. This system enables comprehensive characterisation of various sensing domains and supports advancements in EIT-based soft sensor technology, with implications for biomedical devices, robotics, and energy harvesting. Overall, this thesis advances the field of soft sensors by investigating an electroactive material and using the material to integrate EIT-based pressure mapping with dielectric elastomer actuator technologies, providing new insights and applications in dynamic sensing and actuation.

## *Acknowledgements*

I would like to thank many people who have implicitly and explicitly helped me get through my doctorate. First, the UC Bioengineering office including the Lung Ladies, Lung lads, IPC, Hamish for infinite Friday beers, and Nic's abstract art. Also included in the office, Geoff Chase, for a constant stream of stories and advice always within earshot. The Mechanical Engineering post-grad office for baking, fruit, and comic relief. The UC Mechanical and Electrical department technicians for yarns and practical advice. All of the students and project groups I tutored and mentored, keeping me on my toes throughout the doctorate. Thanks for the motivation from all of my friends with the never-ending question 'so... when do you finish', a very motivating and difficult question answer. Something that prolonged the journey but kept me sane, were the technical the side jobs and fun adventures with colleagues and friends maintaining my sanity. A special thanks to my supervision and collaborations abroad, including my materials science work in IMDEA with Juan Jose and Anastasia and my time with with the MEiTNER soft robotics research group led by Markus Vorrath. Thanks to my internal supervision from Tim teaching me what PHD stands for and my co-supervisors Chris and Lui who have been a good source of advice, yarns, and general guidance. A thank you to my family for being supportive in times of strife. Finally, I would like to thank my partner Tess for her ongoing support and distractions from my PhD work.

# Contents

<b>Declaration of Authorship</b>	<b>i</b>
<b>Abstract</b>	<b>iii</b>
<b>Acknowledgements</b>	<b>iv</b>
<b>List of Figures</b>	<b>xi</b>
<b>List of Tables</b>	<b>xvii</b>
<b>Abbreviations</b>	<b>xix</b>
<b>Symbols</b>	<b>xxi</b>
<b>1 Introduction and Motivation</b>	<b>1</b>
1.1 Why Go Soft and Not Rigid? . . . . .	1
1.2 Research Objectives . . . . .	3
1.3 Chapter Contributions . . . . .	4
1.4 Publications . . . . .	5
<b>2 Literature Review</b>	<b>7</b>
2.1 Bio-Sensing - Skin form and function . . . . .	7
2.1.1 Skin Construction and Types . . . . .	9
2.1.2 Characterising skin . . . . .	10
2.1.3 Skin Modelling . . . . .	12
2.2 Artificial Sensing - Pressure Mapping Technology . . . . .	13
2.2.1 Capacitive . . . . .	14
2.2.2 Magnetic . . . . .	15
2.2.3 Optical . . . . .	16
2.2.4 Acoustic . . . . .	16
2.2.5 Resistive . . . . .	17
2.2.6 Soft Pressure mapping technology comparison . . . . .	18
2.3 Bio-Actuation - Muscle Form and Function . . . . .	20
2.3.1 Characterising a muscle . . . . .	21
2.3.2 Muscle Mechanics . . . . .	22
2.4 Artificial Actuation - Electromagnetic Actuator Technology . . . . .	24
2.4.1 Current Driven - Ionic polymer–metal composite actuator . . . . .	24

2.4.2	Magnetically Driven - Magnetorheological Elastomer . . . . .	26
2.4.3	Electrostatically Driven - HASEL actuator . . . . .	27
2.4.4	Electrostatically Driven - Dielectric Elastomer Actuators . . . . .	29
2.5	Electroactive Material - Soft Conductive Particle Piezoresistive Composites . . . . .	31
2.5.1	Conductive Particle Elastomer Conduction Mechanisms . . . . .	31
2.5.2	Fabricating Conductive Particle Elastomer Composites . . . . .	34
2.5.3	Viscoelasticity in Composite Elastomers . . . . .	35
2.6	Soft Sensor and Actuator Technology Integration . . . . .	36
2.6.1	Electrical Impedance Tomography and Pressure Mapping . . . . .	37
2.7	Literature Review Conclusions . . . . .	40
<b>3</b>	<b>Characterising Non-Linear Behaviour in Carbon-Black Elastomer Nano-Composites</b>	<b>43</b>
3.1	Introduction . . . . .	44
3.1.1	Background . . . . .	44
3.2	Methods . . . . .	47
3.2.1	Composite Fabrication . . . . .	47
3.2.2	Material Imaging . . . . .	48
3.2.3	Stress-Strain-Resistance Measurement . . . . .	52
3.3	Results and Analysis . . . . .	54
3.3.1	Stress-Strain and Viscoelasticity . . . . .	54
3.3.2	Quasi-Static Tensile Resistance-Strain . . . . .	55
3.3.3	Dynamic Resistance-Strain-Rate Response . . . . .	56
3.3.4	Falling Edge Strain-Rate-Resistance . . . . .	58
3.3.5	Resistive Relaxation Fitting . . . . .	60
3.3.6	Resistance-Stress Relationship . . . . .	63
3.4	Discussion . . . . .	65
3.4.1	Fabrication . . . . .	65
3.4.2	Quasi-static Tensile Resistance-Strain . . . . .	65
3.4.3	Dynamic Resistance-Strain-Rate Response . . . . .	65
3.4.4	Falling Edge Strain-Rate-Resistance . . . . .	66
3.4.5	Resistive Relaxation Fitting . . . . .	66
3.4.6	Resistance-Stress Relationship . . . . .	67
3.4.7	Viscoelasticity . . . . .	67
3.4.8	Repeatability . . . . .	67
3.4.9	Further Discussion and Future Work . . . . .	68
3.5	Conclusions . . . . .	70
<b>4</b>	<b>An Electrical Impedance Tomography Based Soft Pressure Mapping Sensor</b>	<b>73</b>
4.1	Introduction . . . . .	74
4.1.1	Related Work . . . . .	75
4.2	Methodology . . . . .	76
4.2.1	Fabrication . . . . .	76
4.2.1.1	Localised Stress Testing . . . . .	77
4.2.1.2	EIT Measurement . . . . .	78
4.2.2	1D Material Characterisation . . . . .	79
4.2.2.1	Quasi-static Piezoresistivity . . . . .	80
4.2.2.2	Transient Piezoresistivity . . . . .	80
4.2.3	Sensor Performance Metrics . . . . .	81

4.2.3.1	Pre-processing . . . . .	81
4.2.3.2	Spatial Performance . . . . .	82
4.2.3.3	Temporal Performance . . . . .	83
4.2.3.4	Localised Force Sensing Performance . . . . .	84
4.3	Results . . . . .	85
4.3.1	1D Material Characterisation . . . . .	85
4.3.1.1	Quasi-static Piezoresistivity . . . . .	85
4.3.1.2	Transient Piezoresistivity . . . . .	86
4.3.2	Sensor Performance Metrics . . . . .	88
4.3.2.1	Pre-processing . . . . .	89
4.3.2.2	Spatial Performance . . . . .	89
4.3.3	Randomised Location and Strain Testing . . . . .	91
4.3.3.1	Temporal Performance . . . . .	93
4.3.3.2	Localise Force Sensing Performance . . . . .	93
4.4	Discussion . . . . .	95
4.4.1	Quasi-static Piezoresistivity . . . . .	95
4.4.2	Pre-processing . . . . .	96
4.4.3	Performance Metrics . . . . .	96
4.4.3.1	Spatial Performance . . . . .	96
4.4.3.2	Temporal Performance . . . . .	98
4.4.3.3	Localised Force Sensing Performance . . . . .	99
4.4.4	Real World Applications, Manufacturability, and Scalability . . . . .	99
4.5	Conclusions . . . . .	100
<b>5</b>	<b>A Portable EIT-Based Pressure Mapping Sensor and Validation System</b>	<b>103</b>
5.1	Introduction . . . . .	104
5.2	Design Methodology and Analysis . . . . .	106
5.2.1	EIT cycle and load sequence . . . . .	107
5.2.2	Small signal measurement . . . . .	108
5.2.3	Signal generation . . . . .	110
5.2.4	Signal conditioning . . . . .	110
5.2.5	Switching circuit . . . . .	112
5.2.6	Position control and measurement . . . . .	112
5.2.7	Force measurement . . . . .	113
5.2.8	Sensing domain . . . . .	114
5.3	Validation and Characterisation . . . . .	115
5.3.1	Sensor capabilities . . . . .	116
5.4	Discussion . . . . .	117
5.5	Conclusions . . . . .	118
<b>6</b>	<b>Integration of EIT-based Pressure Mapping with Dielectric Elastomer Actuators</b>	<b>121</b>
6.1	Introduction . . . . .	122
6.1.1	Background . . . . .	123
6.1.1.1	Dielectric Elastomer Actuators . . . . .	123
6.1.1.2	Soft EIT-based Pressure Mapping . . . . .	125
6.1.2	Simultaneous Pressure Mapping and Actuation . . . . .	126
6.2	Methodology . . . . .	126

6.2.1	Dielectric Elastomer Preparation . . . . .	127
6.2.2	Compliant Electrode Fabrication . . . . .	128
6.2.3	DEA Hardware . . . . .	129
6.2.4	EIT Hardware . . . . .	130
6.2.5	Experimental Method . . . . .	131
6.2.5.1	DEA Validation . . . . .	131
6.2.5.2	EIT-based Pressure Mapping on DEA . . . . .	132
6.2.6	Simultaneous Actuation and Pressure Mapping . . . . .	134
6.3	Results . . . . .	136
6.3.1	Fabrication . . . . .	136
6.3.2	DEA Validation . . . . .	137
6.3.3	EIT Validation . . . . .	138
6.3.4	Simultaneous Actuation and Pressure Mapping . . . . .	142
6.4	Discussion . . . . .	143
6.4.1	Fabrication . . . . .	143
6.4.2	DEA Validation . . . . .	144
6.4.3	EIT Validation . . . . .	145
6.4.4	Simultaneous Actuation and Mapping . . . . .	146
6.4.5	Altered Actuation Performance . . . . .	146
6.4.6	Dielectric Breakdown . . . . .	147
6.5	Conclusions . . . . .	147
6.6	Future Work . . . . .	148
<b>7</b>	<b>Unintentional Power Generation in a DEA-EIT Sensor-Actuator Device</b>	<b>149</b>
7.1	Introduction . . . . .	150
7.1.1	Background . . . . .	150
7.2	Methodology . . . . .	153
7.2.1	DEA Load Study . . . . .	154
7.2.2	Deformed DEA Electrostatics Study . . . . .	155
7.2.3	Voltage and Energy Generation . . . . .	155
7.3	Results . . . . .	155
7.3.1	DEA Load Study . . . . .	156
7.3.2	Deformed DEA Electrostatics Study . . . . .	156
7.3.3	Voltage and Energy Generation . . . . .	157
7.4	Discussion . . . . .	159
7.5	Conclusions . . . . .	161
<b>8</b>	<b>Beyond Rigid - A Softer Future</b>	<b>163</b>
8.1	Future Work . . . . .	164
8.2	Concluding Statements . . . . .	166
<b>A</b>	<b>Strain-Stress-Resistance Experiments</b>	<b>167</b>
<b>B</b>	<b>EIT-based Pressure Sensor Review</b>	<b>171</b>
<b>C</b>	<b>EIT-based Pressure Sensor Performance Metrics</b>	<b>175</b>
C.1	Noise Removal . . . . .	175
C.2	More Threshold Percentage Masks . . . . .	177

C.3	Quasi-static Conductance Strain Fitted Data . . . . .	178
C.4	1D and 2D Strain Settling Times . . . . .	179
C.5	Performance Metrics Example . . . . .	181
C.6	Randomised test <i>SD</i> metrics data . . . . .	182
<b>D</b>	<b>Portable EIT-based Pressure Sensor Build and Operation</b> . . . . .	<b>183</b>
D.1	Build Methodology . . . . .	183
D.1.1	ERT Sensor . . . . .	183
D.1.2	Sensing Domain . . . . .	185
D.1.3	Cartesian force applicator . . . . .	186
D.2	Operation instructions . . . . .	188
D.2.1	ERT sensor power modes . . . . .	189
D.2.2	ERT sensor programming . . . . .	189
D.2.3	ERT sensing domain preparation . . . . .	190
D.2.4	Load application point and strain configuration . . . . .	190
D.2.5	Load experiment execution . . . . .	191
D.2.6	Touch-based mesh bed levelling . . . . .	191
D.2.7	Data capture . . . . .	192
D.2.8	Data processing . . . . .	193
D.3	Construction and Operational Safety . . . . .	193
D.3.1	Construction . . . . .	193
D.3.2	Operation . . . . .	194
<b>E</b>	<b>Dielectric Elastomer Generator Validation</b> . . . . .	<b>195</b>
E.1	$\Delta V$ Calculation . . . . .	195
	<b>Bibliography</b> . . . . .	<b>199</b>



# List of Figures

2.1 Examples of the locations of proprioceptors and cutaneous mechanoreceptors in the human body. . . . .	8
2.2 Clockwise from top left: IMU pose estimation [1] (© 2022 MDPI), stretch sensor knee joint pose estimation [2] (© 2020 IEEE), encoder elbow pose joint estimation [3], stretch sensor hand joint pose estimations [4]. . . . .	9
2.3 Various pressure mapping devices. From top-left then clockwise: Xsensor wheelchair pressure mapping sheet (© 2024 XSENSOR® Technology) [5], Pressure Profile Systems pressure sensors on a robotic hand (© 2023 PPS UK limited) [6], Soft pressure mapping gripper(© 2023 PowerON) [7], Tekscan thin pressure mapping platform [8](© 2024 Tekscan Inc.), Tactilus seat pressure mapping system [9](© 2024 Sensor Products Inc.) . . . . .	14
2.4 A sensel with grey electrodes across a blue dielectric medium. Left: Uncompressed state. Right: Compressed state . . . . .	15
2.5 Example of a magnetically-based pressure mapping system designed by Yan et al. [10] (© 2022 IEEE). . . . .	15
2.6 Example optical pressure mapping sensor using a planar PDMS waveguides. a) Schematic of the two-directional stretchable optical pressure sensor. The active pressure area is comprised of PDMS. b) A cross section view of the optical pressure sensor (© 2012 Wiley) [11]. . . . .	16
2.7 Components of a biological muscle contractile unit and meta-structure. . . . .	20
2.8 Stress and strain of active and passive muscles (© J. Teran   ACM 2003) [12] . .	23
2.9 Diagram of the typical architecture of an IPMC actuator [13] (© 2018 Yanjie Wang and Takushi Sugino) . . . . .	24
2.10 Diagram showing MRE contraction forces when a magnetic field is applied [14] . .	26
2.11 Diagram of the typical architecture and the contraction stages of a HASEL actuator [15] . . . . .	28
2.12 Diagram of the simplified stages of HASEL actuator production [15] . . . . .	28
2.13 DEA with two compliant light-grey electrodes and a transparent light blue dielectric elastomer. Showing deformation without and with a voltage applied across the electrodes. . . . .	29
2.14 Two grey highly conductive electrodes across a CPEC cuboid showing enlarged black conductive particles within a blue polymer matrix. Left: An uncompressed CPEC. Right: A compressed CPEC. . . . .	32
2.15 Example percolation threshold plot for a conductive particle composite with the plot settling at the conductive particle resistivity. . . . .	32
2.16 Example of a randomised cube percolation with a volume percentage of 8% of $1\mu\text{m}$ particles . . . . .	33
2.17 Electrical conduction and tunnelling representation diagram. . . . .	33
2.18 AC conduction RC network representation diagram. . . . .	34

2.19	Linear viscoelastic models (a) Maxwell (b) Kelvin-Voight (c) A solid linear model variant (d) A Burgers model variant. . . . .	36
2.20	EIT adjacent drive pattern sequence for a circular domain with 16 boundary electrodes. . . . .	38
3.1	Mechanical spring dashpot diagram of the generalised Kelvin body model adapted from Fung et al. [16] . . . . .	46
3.2	The steps involved in creating the CBSR composite material . . . . .	48
3.3	Microscope images at x20 magnification of a CBSR specimens with cross-sections made by; Left: Cutting with a scalpel. Right: Inducing an embrittlement fracture. . . . .	49
3.4	SEM images of; (A): CB agglomerated particles $\times 40,000$ . (B): CBSR cross-section top surface edge site 1 $\times 250$ . (C): CBSR cross-section site 1 $\times 2000$ . . . . .	50
3.5	(A): Typical screenshot from the focused Raman microscope. Normalised Raman spectrum of (B) the plain SR. (C) the top surface of CBSR specimen. (D) the cross-sectional surface of CBSR specimen. . . . .	51
3.6	The composite dog-bone test specimen pierced by 4 metal pin electrodes. The outer and inner electrodes connected to an SMU current source and voltmeter respectively . . . . .	52
3.7	Photo of test measurement setup . . . . .	53
3.8	System architecture for the electromechanical tensile test rig showing data/physical connections . . . . .	54
3.9	The loading and unloading of 30% strain on a composite test specimens with CB weight percentages from top to bottom of 10%, 7.5%, and 0% with data collected over five loading and unloading cycles . . . . .	55
3.10	Linear quasi-static resistance-strain fit for 7.5 w.t.% CBSR specimen . . . . .	56
3.11	Strain input waveform for investigating strain-rate dependent resistance . . . . .	56
3.12	Resistance response from saw-tooth strain input Figure 3.11. . . . .	57
3.13	Resistance vs strain hysteresis loops from from a saw-tooth strain input. . . . .	57
3.14	Left: Singular tensile strain pulse with resulting stress and resistance response. Right: Zoomed to highlight falling edge shoulder phenomena. . . . .	58
3.15	Strain-rate resistance relationship showing the specimen returning to a 0% tensile strain state from 20% at a strain-rate of $3.33\%\cdot s^{-1}$ from four tests for a 7.5% CBSR specimen . . . . .	59
3.16	Fitting curves to a range of different tensile falling edge strain strain-rates. . . . .	60
3.17	Comparing the relaxation decay time constants of stress and resistance for a 7.5 w.t.% CBSR composite after a 10% strain step input and fitting generalised Kelvin body models to each. . . . .	61
3.18	Comparing resistance and stress relaxation data against each other occurring during 30 pulses of a 10% strain step input for a 7.5 w.t.% CBSR composite . . . . .	64
3.19	A typical test sequence of a 30 pulse strain train recording the calculated resistance and stress of a 7.5 w.t.% CBSR composite . . . . .	68
3.20	Model architecture for translating between CPEC resistance and the material stress and strain responses. . . . .	69
3.21	Three identical 15% strain pulses at three different current values ,in order, $10\mu A$ , $15\mu A$ , and $20\mu A$ . . . . .	69
4.1	Left: Example of a CBSR sensing domain with gold pin electrodes penetrating material surface around the boundary on top of the rigid sensor holder (orange/black). Right: CBSR sensing domain on an acrylic square. . . . .	77

4.2	Load application areas used for compressive stress testing shown numerically in order of application. . . . .	78
4.3	Architecture of the Cartesian force applicator setup with red arrows being analogue power lines and black arrows being digital data lines . . . . .	79
4.4	Wiring diagram for sensor connection to 4:16 multiplexer and SMU . . . . .	79
4.5	Compressive loading force applicator. Left: Load applicator on sample CBSR material. Right: Pin electrode jig for sample CBSR material compressive loading test. . . . .	80
4.6	Conductance change vs. stress (top) and strain (bottom) data and fitted curves for 8 wt% CBSR. . . . .	86
4.7	Compressive loading applied to the CBSR 8 wt% DUT for 10 loading events of 25% strain. . . . .	87
4.8	Compressive loading and unloading transients for CBSR 8 wt% material undergoing a 20% strain pulse from the first pulse given in Figure 4.7. . . . .	87
4.9	The fourth 1D load event, $L_3$ on the CBSR 8 wt% sample using 5% strain showing a stress, $\sigma$ and resistance, R, relaxation event and their corresponding fitted curves. . . . .	88
4.10	A series of threshold percentage masks (A) 25%, (B) 50%, (C) 75, and (D) 85% for the same reconstruction given in Figure C.2. (E) is the resistance change scale bar. . . . .	89
4.11	Spatial performance metrics comparing threshold percentages of 25, 50, 75, and 85% for a 8 wt% CBSR sample being loaded with 20% compressive strain in nine areas, $L_{0-8}$ , shown in Figure 6.8. . . . .	90
4.12	The ten random load point locations, $L_{rand}$ , and random strain values proportional to red circle size as shown on a polar plot. . . . .	92
4.13	EIT load event $L_0$ on the CBSR 9 wt% sample using 30% strain showing a stress, $\sigma$ and conductance, $\rho$ , relaxation event and their corresponding fitted curves. . . . .	93
4.14	Comparing force estimates, $F_{est}$ , and actual force measurements, $F_{meas}$ , for 5 - 30% strain centre loading events at $L_0$ for the EIT sensor system for 8 wt% CBSR	94
4.15	Comparing force estimates, $F_{est}$ , and actual force measurements, $F_{meas}$ , for 5 - 30% strain centre loading events at $L_0$ for the EIT sensor system for 9 wt% CBSR	95
5.1	System architecture of ERT sensor and CFA setup. The large red arrow shows the direction of the force applicator compression onto the sensing domain (DUT) and analogue/power signals are shown with red arrows and digital signals with black arrows. . . . .	105
5.2	A soft sensor domain connected to the ERT sensor electronics. . . . .	106
5.3	Cartesian force applicator setup with an ERT circuit and EIT reconstruction computer . . . . .	107
5.4	System architecture of ERT sensor and CFA setup (left) and the key internal electrical signals of the ERT circuit (right). With analogue/power signals shown with red arrows and digital signals with black arrows. . . . .	107
5.5	EIT adjacent drive pattern sequence. . . . .	108
5.6	Left: A resistor mesh network for validating the ERT circuit, with the anomalous resistors highlighted in green. Right: The difference between EIT raw voltage data from a homogeneous square 2.2 k $\Omega$ resistor mesh domain and the same domain with a 3.3 k $\Omega$ resistor mesh anomaly. . . . .	109
5.7	Measurement attenuation circuit . . . . .	111
5.8	Passive low-pass filter circuit . . . . .	111
5.9	$R_{DS(on)}$ characteristic diagram for a typical multiplexer analogue channel for a dual and single-ended power supply. . . . .	112

5.10 Static load analysis of the loadcell bracket part [PR9] of maximum allowable load of 100 N showing the magnitude of displacement. . . . .	113
5.11 Reconstruction frames from a random push test sequence on a 1mm thick 100mm diameter sample. Strain and applied locations (x, y) [mm] - Left: 24% (-14.8, -3.4). Right: 36% (-1.9, -21.3) . . . . .	115
5.12 Reconstruction frames from a random push test sequence on a CBSR 100mm diameter sample. The white circle representing the force applicator location and the red dot on the force plot showing the captured frame in time. . . . .	116
5.13 An EIT reconstruction image of a sensing domain with two loads applied simultaneously. Left: Without threshold filtering. Right: With a 75% threshold amplitude filter applied. . . . .	116
5.14 Left: Example sequence a resistive relaxation after a loading event at times $t_1$ to $t_4$ . Right: Example stress, $\sigma$ , and resistive, $\rho$ , relaxation plot generated from an ERT CFA experiment given a 30% strain step input [17]. . . . .	117
6.1 Potential future application of the DEA-EIT device topology. Left: EIT sensor input DEA controlled optical lens. Right: Pressure mapping sensitive skin for a DEA propelled jellyfish soft robot. . . . .	123
6.2 A circular DEA exemplifying its actuation principle. . . . .	124
6.3 A 16 electrode circular EIT domain setup exemplifying its electrical function. Where the dashed lines are representative of an applied electric field [18]. . . . .	125
6.4 Mechanical fabrication of the circular DEA-EIT platforms . . . . .	128
6.5 DEA excitation and measurement setup . . . . .	130
6.6 Architecture of the force applicator and EIT measurement system [17] . . . . .	131
6.7 The two DEA compliant electrode material types used in this work. . . . .	132
6.8 Load application areas used for compressive stress testing in order of application [17]. . . . .	133
6.9 The two spatial performance metrics used for determining accuracy of blob as a load area estimate, where the transparent white circle is the actual load area and the dark purple elements are the load estimate area. . . . .	134
6.10 System architecture for simultaneous DEA actuation and EIT mapping. . . . .	135
6.11 Illustrative experiment timing diagrams. Left: Steady state $V_{DEA}$ where the purple dotted lines represent the time a load event begins. Right: Transient EIT measurements where the red dotted line represents the time an EIT frame capture begins. . . . .	136
6.12 Comparing the measured CB reference DEA strain, the theoretical strain average and range, and the data fitted to Equation 6.3 by fitting either parameter $K$ or $\epsilon_r$ . . . . .	137
6.13 Comparison of the voltage strain relationships between the 100 mm diameter compliant electrodes of various thicknesses, $z_{ce}$ , used for the DEA. . . . .	138
6.14 A 15% strain compression at point $L_1$ applied to 100mm diameter compliant DEA electrodes of 3 compliant electrode thicknesses. . . . .	139
6.15 Vectorised $E_{CoM}$ for the nine load experiment at 20% compressive strain for each $z_{ce}$ value tested on individual DEA-EIT compliant electrode samples. . . . .	140
6.16 Vectorised $E_{CoM}$ for the nine load experiment using the same indentation depth as Figure 6.15 for each $z_{ce}$ value tested on the DEA-EIT integrated samples. . . . .	141
6.17 Loads applied to the compliant ground electrode of a DEA during different steady state voltage excitations, $V_{DEA}$ . . . . .	142
6.18 An unloaded DEA with a captured during various voltage, $V_{DEA}$ , step input artefacts. . . . .	143
6.19 Render of a concept DEA daughter board mounted on the portable ERT board. . . . .	148

---

7.1	Architecture of a DEA-EIT pressure mapping and actuator device with an exploded view of the DEA stack. . . . .	151
7.2	Dielectric elastomer generator scenario sequence with a localised compressive load. . . . .	151
7.3	Loading cases for analysis of capacitance change. Left: 13 mm diameter load. Right: 50 mm diameter load. . . . .	154
7.4	Deformed mesh plot of 13 mm diameter 20 N load case FEM model (x10 scale displacement). Top: 3D view. Bottom: Cross-section zoomed view. . . . .	156
7.5	Electric field simulation of 50 mm diameter 240 N load case. With a zoomed section to show the electric field ‘fringe’ effects at the shoulder of the load cross-section. Volumetric arrows proportional to electric field strength. . . . .	157
7.6	FEM vs analytical solution for voltage generation, $\Delta V$ , for an initial voltage input of 5 kV for the range of loads applied. . . . .	159
7.7	FEM vs analytical solution error for voltage generation, $\Delta V$ , for an initial voltage input of 5 kV for the range of loads applied. . . . .	160
A.1	Strain test sequence showing the shoulder phenomena correlation for varying magnitudes of strain for a 7.5 wt% CBSR specimen dogbone sample. This experiment had an unintentional offset of 1 mm, however this showed a drastic decrease shoulder phenomena when the falling edge is crossing the x-axis. . . . .	167
A.2	Strain test sequence showing the shoulder phenomena correlation for varying magnitudes of strain for a 7.5 wt% CBSR specimen dogbone sample. This experiment used DC measurements, so the macro downward trend in resistance is more obvious than other experimental data given in this work with used a switched AC signal. . . . .	168
A.3	AC vs DC downward trend in resistance for an unstrained 7.5 wt% CBSR composite dogbone specimen. . . . .	168
A.4	The loading and unloading of 30% strain on a composite test specimens over five loading and unloading cycles with fitted second-order polynomial curves for determining hysteresis loop area. Top: 10 wt% CB. Bottom: 7.5 wt% CB. . . . .	169
C.1	An experimental snapshot. Left: Before executing the performance metrics calculations, the noise floor mask was applied to the 9% CBSR material. Right: Time series force data . . . . .	175
C.2	Before executing the performance metrics calculations, the noise floor mask was applied to the 8% CBSR material shown in Figure 4.1 . . . . .	176
C.3	A series of threshold percentage masks (a) 25%, (b) 50%, (c) 75, and (d) 85% for the same reconstruction given in Figure C.1. (e) is the resistance change scale bar. . . . .	177
C.4	Conductance change vs. stress (top) and strain (bottom) data and fitted curves for 9 wt% CBSR. The 5% strain values ignored as the std were larger than the conductance change values. . . . .	178
C.5	Mean settling times for 5 - 30% compressive strain applied to CBSR 8 wt% with the error bars showing the standard deviation from 1D compressive test data. . . . .	179
C.6	Mean settling times for 5 - 30% compressive strain applied to CBSR 9 wt% with the error bars showing the standard deviation from 1D compressive test data. . . . .	179
C.7	Mean settling times for various strains applied to CBSR 8 wt% with the error bars showing the standard deviation of each settling time from the 2D EIT experimental data. . . . .	180
C.8	Mean settling times for various strains applied to CBSR 9 wt% with the error bars showing the standard deviation of each settling time from the 2D EIT experimental data. . . . .	180

C.9	Spatial performance metrics comparing threshold percentages of 25, 50, 75, and 85% for 9 wt% CBSR sample being loaded with 20% compressive strain in nine areas, $L_{0-8}$ , shown in Fig 6.8. . . . .	181
D.1	ERT PCB [PCB1] before and after electrical component population. . . . .	184
D.2	ERT sensor PCBA mounted in enclosure and attached electrode harness showing buttons and the main electrical connections. . . . .	184
D.3	Left: An example of a CBSR sample with copper tape electrodes integrated with a dielectric elastomer actuator setup [19]. Right: Example of a CBSR sensing domain with gold pin electrodes penetrating material surface around the sensing region boundary. . . . .	186
D.4	MK3s print head. Left: Original print head assembly. Right: Dismantled print head assembly [20]. . . . .	186
D.5	Force applicator head assembly. . . . .	187
D.6	MK3s with original print bed tray removed and the ERT sensor trays added. . . . .	188
D.7	ERT PCB pin-out and power mode options. Blue jumpers are for the bipolar supply mode (i.e. $\pm V_s$ attached). Red jumpers are for the +5 V USB supply mode. . . . .	189
D.8	An example plot of the $R_{int}$ values generated on completion of an experiment for a stable experiment. Where the Electrode # 'i' represents the resistance between electrode 'i' and 'i+1'. . . . .	192

# List of Tables

2.1	Comparison of typical mammalian mechanoreceptor characteristics [21]. . . . .	10
2.2	Comparison of different potential piezoresistive sensor materials. Rated 1 to 5, where 1 is low and 5 is high. . . . .	17
2.3	Comparison of soft pressure mapping sensor technologies. Dashes represent data not present in the related paper. . . . .	19
3.1	Strain-rate dynamic resistance offset comparison. Using S1 as the reference resistance loop. . . . .	57
3.2	The fitted parameters for relationship between the specimen tensile strain-rate and the resulting resistance peak for a strain signal falling edge. . . . .	60
3.3	Fitted constants and their mean, $\mu$ , standard deviation values for 0%, 7.5%, and 10% CBSR composite specimens using Equation 3.7. . . . .	62
3.4	Fitted constants and their mean, $\mu$ , and standard deviation values for 0%, 7.5%, and 10% CBSR composite specimens using Equation 3.8. . . . .	63
3.5	Fitted constants and their mean, $\mu$ , standard deviation, $\sigma$ , and coefficient of variation, $CV$ , values for 7.5%, and 10% CBSR composite specimens using Equation 3.9 . . . . .	64
4.1	DUT mechanical characteristics and electrical characteristics . . . . .	77
4.2	DUT noise figure, NF, and noise, $\sigma_n$ , at steady-state . . . . .	85
4.3	CBSR 8 wt% mean and standard deviation for spatial performance metrics across of a nine loads, $L_0-L_8$ and strain value 20%. . . . .	91
4.4	CBSR 8 wt% mean and standard deviation for spatial performance metrics of nine loads, $L_0-L_8$ , a 85% percentage threshold mask, and strain value 20%. . . . .	91
4.5	CBSR 8 and 9 wt% mean and standard deviation for $E_{CoM}$ spatial performance metrics of ten random locations, $L_{rand}$ and random strains $\varepsilon$ . . . . .	92
5.1	An example of the extreme parameter limits of two loading experiments showing the minimum and maximum strains limits for 5 mm and 20 mm diameter force applicators and their required forces respectively. . . . .	114
6.1	Effective bulk modulus, $K_{eff}$ , and coefficient of determination, $R^2$ , for each fit of voltage-strain data for the CBSR compliant electrodes. . . . .	138
6.2	Noise factor and mean inter-electrode resistance, $\bar{R}_{int}$ , for each thickness of compliant DEA electrode used for EIT . . . . .	139
6.3	Mean $E_{CoM}$ and $SF$ values ( $\pm$ std) obtained for each DEA compliant electrode thickness at 20% strains loads . . . . .	141
6.4	Mean $E_{CoM}$ and $SF$ values ( $\pm$ std) obtained for each DEA stack at the same indent depth as 20% strain in Table 6.3 loads. *Where the compliant electrode is part of a DE compliant electrode DEA stack. . . . .	142

7.1	Voltage and energy generation results calculated from FEM values for the 13 mm diameter load cases. . . . .	158
7.2	Voltage and energy generation results calculated from FEM values for the 50 mm diameter load cases. . . . .	158
B.1	Comparison of EIT-based soft pressure mapping sensor technologies. Dashes represent data not present in the related paper. . . . .	173
B.2	Continuation of the comparison of EIT-based soft pressure mapping sensor technologies from Table B.1. Dashes represent data not present in the related paper. . . . .	174
C.1	CBSR 8 and 9 wt% mean and standard deviation for <i>SD</i> spatial performance metrics of ten random locations, $L_{rand}$ and random strains $\varepsilon$ . . . . .	182
D.1	CFA experimental parameter variables. . . . .	190

# Abbreviations

<b>ADC</b>	Analog-to-Digital Converter
<b>CAD</b>	Computer Aided Design
<b>CB</b>	Carbon Black
<b>CE</b>	Compliant Electrode
<b>CFA</b>	Cartesian Force Applicator
<b>CoM</b>	Center of Mass
<b>CPEC</b>	Conductive Particle Elastomer Composite
<b>DE</b>	Dielectric Elastomer
<b>DEA</b>	Dielectric Elastomer Actuator
<b>DEG</b>	Dielectric Elastomer Generator
<b>DUT</b>	Domain Under Test
<b>EIT</b>	Electrical Impedance Tomography
<b>ERT</b>	Electrical Resistance Tomography
<b>FEA</b>	Finite Element Analysis
<b>FEM</b>	Finite Element Modelling
<b>FPC</b>	Flexible Printed Circuit
<b>MUX</b>	Multiplexer
<b>PCB</b>	Printed Circuit Board
<b>PCBA</b>	Printed Circuit Board Assembly
<b>PDMS</b>	Polydimethylsiloxane (AKA silicone)
<b>PNEC</b>	Piezoresistive Nanoparticle Elastomer Composite
<b>SMU</b>	Source Measure Unit
<b>SMD</b>	Surface-Mount Device
<b>SR</b>	Silicone Rubber
<b>EAP</b>	Electro-Active Polymer



# Symbols

$A$	Area	[m <sup>2</sup> ]
$C$	Capacitance	[F]
$\epsilon_0$	Vacuum Permittivity	[Fm <sup>-1</sup> ]
$\epsilon_r$	Relative Permittivity	[a.u.]
$K$	Bulk Modulus	[Pa]
$\nu$	Poisson's Ratio	[a.u.]
$Q$	Electrical Charge	[C]
$U_E$	Electrical Potential Energy	[J]
$U_\epsilon$	Elastic Potential Energy	[J]
$R$	Resistance	[\Omega]
$\sigma$	Stress	[Pa]
$S/\varepsilon$	Strain	[a.u. or %]
$\dot{\varepsilon}$	Strain Rate	[%s <sup>-1</sup> ]
$V$	Voltage	[V]
$Y/E$	Young's Modulus	[Pa]
$z/d$	Thickness	[m]



# Chapter 1

## Introduction and Motivation

The reliance on rigid robotic systems, dominated by rotary motors and conventional sensors, has long constrained the potential for innovation in robotics, limiting the adaptability and creativity needed for future technological breakthroughs. In biology, animals have many actuator units in the form of soft muscles and a multitude of various receptors within soft tissue for sensing their environment and allowing a different range of delicate control and manipulation of the natural world. The rigidity of rotational motors is stifling creativity in the creation and development of devices among other unforeseen future technology. Engineers are often constrained to solving problems and designing solutions using typical rigid sensors and actuators due to their current ubiquity and their evolved increased efficiency. With the rise of research into soft sensor and actuator devices, these soft devices will follow suit of the traditional rigid sensors and actuators and become ubiquitous, reliable, and viable options for engineering design solutions.

This thesis has developed methods and tools for creating and characterising artificial pressure sensitive skin technology. The thesis then continues to explore the integration of this artificial skin technology into an artificial muscle technology. The work in this thesis has ultimately contributed towards filing a provisional patent for DEA-EIT actuator-sensor technology in a quest to bring this work out of the academic realms into real-world applications.

### 1.1 Why Go Soft and Not Rigid?

The requirement for soft robotics in general has been driven by the limitations of current rigid robotic solutions to interact with natural organic material. Manipulation of natural plant and animal tissue have traditionally been handled by humans by hand due to our ability to use

our dexterity and intelligent control systems to ensure minimal undesirable damage. With the advances in technology of various soft robotic actuators[22–26], sensors[27], and soft robotics control[28, 29]. The use of soft robotics in place of rigid alternatives, amongst other benefits, has the opportunity to be more sustainable by decreasing waste products during fabrication, using biodegradable or recyclable materials, shelf life, and use of renewable resources[24]. The use of soft robotics brings the opportunity to create devices with a reduced bill of materials size and less moving parts for maintenance. The use of soft robotics in biomedical and aerospace applications is especially desirable due to current technology in these environments often experiencing difficulties in certain areas where soft robotics thrives. The engineering difficulties in these aerospace and biomedical environments including heat dissipation, lubrication, and mass[30–33].

Soft sensor and actuator technology may replace many traditional rigid equivalents and be adopted by emerging technologically advanced companies requiring advanced automation and robotic handling. The most common rigid actuator market, the global electric motor market, was valued at USD 142.2 billion in 2020[34]. Adjacently, the pressure mapping sensor global market value, focused mainly on the health sector, was valued at USD 480 million in 2023[35]. These market values indicate that there could be a high value in soft robotics when a percentage of the companies in these markets were to move to using soft sensor and actuator alternatives.

Soft robotic actuation can be achieved through various mechanisms including thermal, electrochemical, fluidic, magnetic, and electrostatic. Similarly, soft stress-strain sensing can be achieved through various physical principles such as resistive, capacitive, magnetic, and optical sensing methods. The function of many soft actuators can be inverted such that the deformation of the actuator can produce a signal used for self sensing, in electroactive polymer (EAP) technologies such as dielectric elastomer actuators (DEAs) [36–39] and ionic polymer-metal composites (IPMCs) [40]. EAPs have the benefit of electronic control over other soft actuator and sensor technologies controlled by fluids, heat, or light which often contain the complexity and bulk of an additional energy transduction process.

To make current soft sensor and actuator technology become more biomimetic, we must physically integrate both sensor and actuator technology as well see in biological tissue. Proprioception in artificial muscle technology has been made a reality. This is seen in the self-sensing of one dimensional strain of DEAs usually through capacitive measurement between the compliant electrodes during operations to obtain the magnitude of a contraction. However, the pressure

mapping done similar to the mechanosensation performed by cutaneous mechanoreceptors on an artificial muscle device, in particular a DEA, has not been explored as of writing this thesis.

This thesis has converged on the use of conductive particle based elastomer composites and their use in sensors and actuators, in particular an electrical impedance tomography (EIT) based artificial skin and it's integration into the artificial muscle technology, dielectric elastomer actuators. The composite type used throughout the thesis is simple to fabricate but not well understood in terms of its electromechanical transient and dynamic characteristics. This composite has been characterised in one-dimension several times in literature already however, since a two dimensional sensing application of this composite is desired the characterisation of the sensor in two dimensions was completed. A method to do such 2D sensing is using EIT. EIT has been used in the past for a huge range of applications, with few exploring the use of EIT as a pressure mapping sensor.

## 1.2 Research Objectives

The research objectives and questions for this thesis are given below:

1. Characterise static, dynamic, and transient phenomena seen in conductive particle elastomer composites.
2. From the characterisation above, mitigate the effects of the transient phenomena for further use in electroactive sensor and actuator technology.
3. Develop an electrical impedance tomography based pressure sensor and validate its performance
4. Design the hardware for sensing and characterisation of the above pressure sensor.
5. Investigate the effects of integrating electrical impedance tomography based pressure mapping onto a dielectric elastomer actuator.
6. Investigate unintentional energy generation impacts in the above electrical impedance tomography dielectric elastomer actuator device.

### 1.3 Chapter Contributions

Chapters 3 - 7 contain the core novel research contributions. Chapters 2 and 8 provide essential background knowledge, and conclusions for the thesis respectively.

**Chapter 2 - Literature Review:** explores the nature of biological skin and muscle from an engineering perspective, quantifying necessary functions and properties desired to replicate or supersede for their artificial equivalents. Then the state-of-the-art soft sensors and actuators and their function are described.

**Chapter 3 - Characterising Non-Linear Behaviour in Carbon-Black Elastomer Nano-Composites:** uncovers the dynamic and time-dependent electromechanical properties of carbon black silicone composites, in order to understand the composite capabilities before using it in soft sensors and actuators.

**Chapter 4 - An Electrical Impedance Tomography Based Soft Pressure Mapping Sensor:** discusses the use of electrical impedance tomography to create a pressure mapping sensor and provides tools for analysing the suitability to various applications and choosing a suitable sensing domain.

**Chapter 5 - A Portable EIT-Based Pressure Mapping Sensor and Validation System:** gives the small form factor, low-cost hardware design for a EIT-based pressure mapping device and a Cartesian force applicator system for the pressure mapping sensor's characterisation.

**Chapter 6 - Integration of EIT-based Pressure Mapping with Dielectric Elastomer Actuators:** describes the integration of the EIT-based pressure mapping technology discussed in the previous chapters and its integration with dielectric elastomer actuators, and the novel device's capabilities.

**Chapter 7 - Unintentional Power Generation in a DEA-EIT Sensor-Actuator Device:** simulates and analyses the unintended power generation of the simultaneous sensor-actuator device discussed in the previous chapter.

**Chapter 8 - Beyond Rigid - A Softer Future:** summarises the key research findings of the thesis and discusses the future direction of the technology discussed in the thesis and acknowledges the future of soft robotics.

## 1.4 Publications

Publications towards this thesis include three conference papers [18, 19, 41], one journal paper [17], one journal paper under review, and one provisional patent filed.

- “Stress and Resistance Relaxation for Carbon Nanoparticle Silicone Rubber Composite Large-Strain Sensors” - Proceedings 17th IEEE/ASME International Conference on Mechatronic and Embedded Systems and Applications (MESA) - R Ellingham, T Giffney
- “Carbon black silicone piezoresistive electrical impedance tomography stress sensor device” - Proceedings Electroactive Polymer Actuators and Devices (EAPAD) XXIV - R Ellingham, T Giffney
- “An electrical impedance tomography based artificial soft skin pressure sensor: Characterisation and force modelling” - Sensors and Actuators A: Physical - R Ellingham, C Pretty, L Holder-Pearson, K Aw, T Giffney
- “Deformation mapping in dielectric elastomer actuators using electrical impedance tomography” - Proceedings Electroactive Polymer Actuators and Devices (EAPAD) XXVI - R Ellingham, Y Choi, T Giffney



# Chapter 2

## Literature Review

Humans can complete complex tasks due to their intelligence, dexterity, and physical make up. Such complex tasks include agricultural picking, culinary preparation, factory goods processing, and biomedical practice. To complete these tasks with machines it is important to quantify these human qualities that the technology must match or supersede. To set quantifiable constraints for the design of bio-mimetic sensors and actuators the first part of this chapter is focused on understanding and quantifying human skin and muscle tissue often required for these complex human tasks. Subsequently, artificial skin and artificial muscle state-of-the-art technology is reviewed. The integration of soft sensing and actuation technology is reviewed and the sensor-actuator integration explored in this thesis is justified. Finally, background theory on piezoresistive elastomer composites which will be utilised with specific sensor and actuator technology is given to provide a foundational materials knowledge base of the thesis.

### 2.1 Bio-Sensing - Skin form and function

Skin is the largest organ in the human body with many functions, however this thesis only aims to replicate some pressure-sensitive functions of skin. Two pressure-sensitive categories of skin and muscle tissue transducers which allow for dexterous manipulation of objects are:

1. Proprioceptors: respond to internal mechanical stimuli in a joint capsule, tendon, or muscle to give the sense of motion.
2. Cutaneous mechanoreceptors: respond to mechanical stimuli usually external to the body, including pressure and vibration, for the localisation of sensations.

Locations of both proprioceptors and cutaneous mechanoreceptors are illustrated in Figure 2.1. Proprioceptors aid in determining pose estimates of body parts in space, acting as sensors providing feedback closed-loop control for the neurological motion control of body parts. Whereas cutaneous mechanoreceptors have various roles including object recognition, manipulation control, as well as motion control.

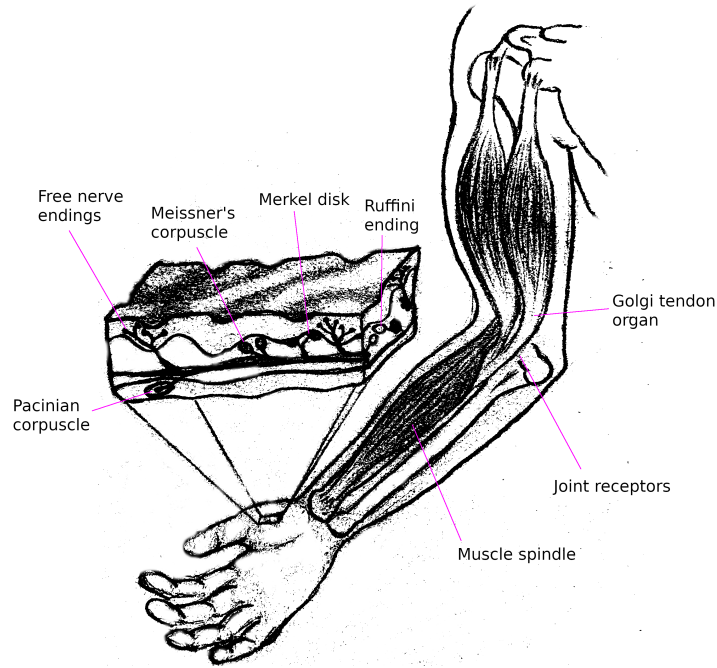


FIGURE 2.1: Examples of the locations of proprioceptors and cutaneous mechanoreceptors in the human body.

The function of both kinds of receptor have been mimicked by certain device technologies. For example, proprioceptors have been mimicked in wearables and human assistive devices where joint motion has been estimated by rigid sensors such as rotary/linear encoders, inertial measurement units (IMUs), and soft stretch sensors; both rigid and stretchable sensors have been fixed adjacent to joints to calculate pose estimates of limbs [1–4]. The rigid sensors can be higher resolution but are often bulky and don't accurately represent the deformation undergone by the human limbs. Soft flexible sensing alternatives are scarce but do not constrain the natural limb motion. However, optical motion capture systems can accurately map un-occluded limbs with high accuracy without encumbering the subject. Examples of such devices are displayed in Figure 2.2.

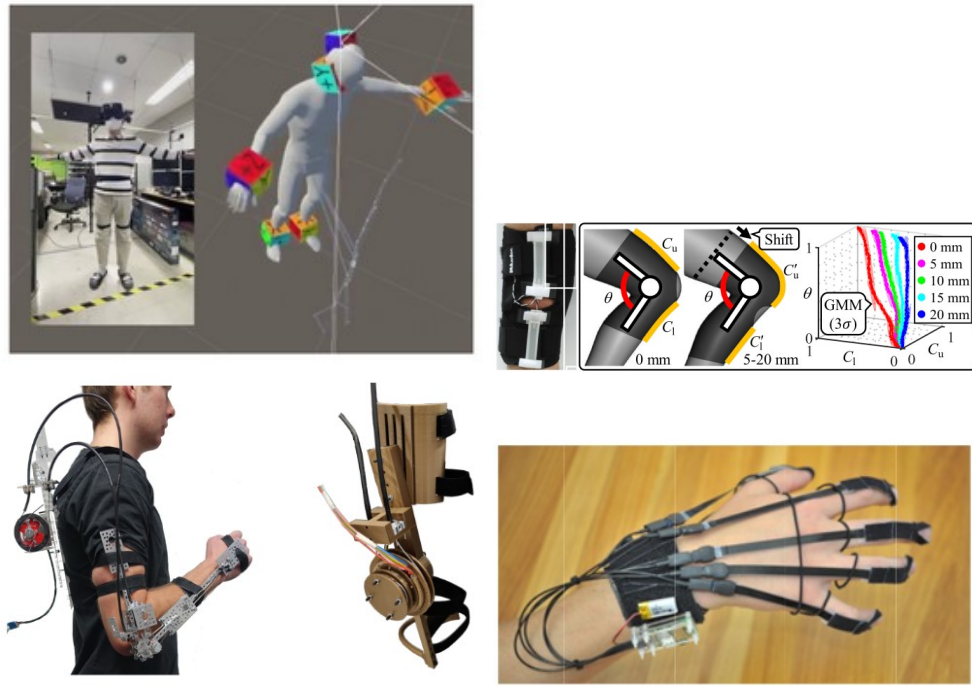


FIGURE 2.2: Clockwise from top left: IMU pose estimation [1] (© 2022 MDPI), stretch sensor knee joint pose estimation [2] (© 2020 IEEE), encoder elbow pose joint estimation [3], stretch sensor hand joint pose estimations [4].

### 2.1.1 Skin Construction and Types

Skin is a laminate structure consisting of three main layers, the epidermis, dermis, and hypodermis. The top two layers the epidermis and dermis are a subset of the cutaneous layer which contain the majority of the pressure-sensitive mechanoreceptors [42].

The skin can be categorised as glabrous/hairless or non-glabrous/hairy. Glabrous skin contains many of the mechanoreceptors given in Figure 2.1 whereas non-glabrous skin will also contain C-tactile afferent receptors for obtaining sensations through hair follicles. However this work is exploring simple monolithic/homogeneous-composite bodies so will not be replicating the sensor function of non-glabrous skin.

Depending on the region of skin different force resolution and spatial resolution will incur. Relevant cutaneous mechanoreceptors and their functions are given in Table 2.1. The tensile properties of skin is governed by skin tension lines, also called Lager's lines, which show the direction in which the maximal stretch can occur.

TABLE 2.1: Comparison of typical mammalian mechanoreceptor characteristics [21].

Mechanoreceptor	Meissner corpuscle A1	Ruffini Corpuscle A2	Pancian Corpuscle B1
<b>Perceptual sensory functions</b>	Skin movement, handling objects	Skin stretch, movement direction, hand shape, and finger position	Fine tactile discrimination, form and texture perception
<b>Skin stimulus</b>	Dynamic deformation	Skin stretch	Indentation depth
<b>Localisation</b>	Dermal papillae	Dermis	Basal layer of epidermis / around guard hair
<b>Conduction velocity</b>	35 - 70 m/s	35 - 70 m/s	35 - 70 m/s
<b>Receptive field</b>	22 mm <sup>2</sup>	60 mm <sup>2</sup>	9 mm <sup>2</sup>
<b>Receptor density</b>	150 / cm <sup>2</sup>	10 / cm <sup>2</sup>	100 / cm <sup>2</sup>

### 2.1.2 Characterising skin

The sensing qualities of skin is crucial for the sensory feedback in complex manipulation tasks. To aid the creation of technology that mimics qualities of biological pressure sensitive skin, the mechanical properties must be characterised. Similar to soft/flexible sensor technology, biological human skin is highly variable in terms of its mechanical and sensing properties depending on the region of skin, giving large variation in skin characteristics. To match or supersede the function of human skin soft sensing technology must be configurable in terms of their mechanical characteristics. Skin can be characterised in terms of the following mechanical characteristics:

- Elastic modulus - The static elastic properties determined by a linear region of stress and strain of the material. [Pa]
- Storage and loss modulus - The dynamic elastic and viscoelastic properties determining the relationship between stress and strain. [Pa]
- Ultimate tensile stress (UTS) - The maximum tensile stress that a material can tolerate before breaking [Pa]

- Life cycle - The time or number of actuation cycles in which it takes for the actuator to degrade such that it cannot perform its intended purpose to specified standards.
- Viscoelastic creep and relaxation - All viscoelastic materials will experience strain creep and stress relaxation to varying degrees depending on the viscoelastic properties of the material. [mm.s<sup>-1</sup> and s]
- Skin thicknesses - the thickness of all layers of skin the cutaneous epidermis and dermis and thickness of the hypodermis. [mm]
- Skin surface area - Biological skin has a large surface area and can also be regionalised to map skin function and sensitivity. [m<sup>2</sup>]
- Isotropy/Anisotropy - The directionality of skin properties, also known as skin tension lines, give a topological map of the maximal stretch (i.e. minimal elastic modulus) direction of regions of skin.

Some of the functional properties in terms of pressure mapping include:

- Spatial resolution and touch acuity - The spatial resolution of biological skin, which is mainly dependent on the innervation, mechanoreceptors density, and thickness of the cutaneous layers of skin [43–45].
- Static force resolution - This is the detection resolution of static or slow-acting forces acting upon the skin [45].
- Temporal resolution - This is the detection resolution of fast-acting forces acting upon the skin often required for texture recognition [43, 45].

A quantitative characterisation of mechanical and pressure sensing functional skin properties include:

- Elastic modulus - varies largely depending on test method, test skin type, and subject. Values found in literature include  $83.3 \pm 34.9$  MPa [46], 0.1 - 2.4 MPa [47], and 10.4 - 89.4 kPa [48].
- Storage and loss modulus - varies largely depending on test method, test skin type, and subject. Values found in literature range include  $141.9 \pm 34.8$  Pa and  $473.9 \pm 42.5$  Pa at 0.8 Hz [49],  $473.9 \pm 42.5$  Pa and  $32.3 \pm 10.0$  Pa at 205 Hz [50].

- Ultimate tensile stress - Two studies showed comparable results of  $21.6 \pm 8.4$  MPa [46] and  $28.0 \pm 5.7$  MPa [51].
- Life cycle - Skin cells are constantly growing, dying, and shedding. Skin is always actively remodelling based on external stimuli [42].
- Strain creep - The strain creep was found to be 2.7 kPa.s for a 10 Pa step input on a dermis skin sample [49].
- Skin thicknesses - The thickness of human cutaneous skin ranges from 0.6 to 2.6 mm with an average skin thickness of 2 mm [43].
- Skin surface area - The average surface area of skin in adult humans is  $1.7 \pm 0.1$  m<sup>2</sup> [43].
- Isotropy/Anisotropy - The tension lines in skin are determined by collagen fibre orientation and dynamic stretch events [52]. The elastic modulus of human skin was reported to be  $160.8 \pm 53.2$  MPa parallel to the skin tension lines and  $70.6 \pm 59.5$  MPa perpendicular to the tension lines [51]. The UTS of human skin was reported to be  $28.0 \pm 5.7$  MPa parallel to the tension lines and  $15.6 \pm 5.2$  MPa perpendicular to the tension lines [51].

Some common metrics used in the biomedical field include:

- Spatial resolution and touch acuity - The tactile field area increases with indentation depth for certain mechanoreceptors with a range of 5 - 12.6 mm<sup>2</sup> [53]. Two point discrimination is another metric for determining spatial resolution and has been determined as  $3.7 \pm 0.7$  mm [54]. The receptive field varies depending on the mechanoreceptors used so has been reported to be between 1 and 60 mm<sup>2</sup> as another methods of inferring spatial resolution [21].
- Force resolution - Minimum force detection on various regions of human skin was found to be between 67 - 1007 mg [55], and fast and slow acting mechanoreceptors 0.73 - 122.6 mN [56].
- Temporal resolution - Depending on the mechanoreceptors utilised, a frequency range of 0 to 800 Hz can be perceived by human skin [53]

### 2.1.3 Skin Modelling

Developing robust mechanical models for human skin is non-trivial for three main reasons:

1. High degree of viscoelasticity
2. Self-regeneration and healing
3. Constructed from various types of cells in a laminate structure

To solve the complexity of modelling such a material a review by Landry et al. [43] shows that many researchers have applied various non-linear mechanical models including Ogden, Mooney–Rivlin, Neo-Hookean, Yeoh, Humphrey, and Veronda–Westmann. When recreating an artificial muscle it is desirable to minimise the mechanical material model complexity so that the material can be more easily integrated into a control system with known behaviour. Similar modelling techniques can be used to model conductive particle elastomer composites due to the similar hyper-elastic and viscoelastic behaviours observed.

## 2.2 Artificial Sensing - Pressure Mapping Technology

This section outlines some of the main technologies which are flexible and/or soft a comparable softness to human skin tissue and can map force events throughout a surface. Through comparison of various materials EAPs have shown many similarities in mechanical properties to biological skin, identifying EAPs as a promising material for further use in sensor and actuator devices. A particular focus on electroactive polymer (EAP) based sensing is present due to the potential of miniaturising the technology and the range of miniaturised electronics currently available. EAPs are polymer materials which can be used as transducers that change electrical properties based on a mechanical input, and vice-versa.

Pressure mapping devices can be categorised into their various sensing technology, such as resistive, capacitive, inductive, magnetic, optical, and acoustic. Transduction methods have been compared by Tiwana et al. [57], with recommendations to pursue ‘capacitive, resistive, piezoelectric, piezoresistive or a combination’ of methods to replicate mechanoreceptors in the human skin. However, additional optical and magnetic/inductive methods will also be considered in the following sections.

Pressure mapping is widely used for many applications including sports equipment grip analysis, foot pressure in gait analysis, in production line part alignment, hospital patient bed and chair pressure injury mitigation, headphone pressure analysis, among many others. These applications are useful for increasing quality of life, optimising sporting performance, object detection, and production efficiency optimisation.

Cutaneous mechanoreceptors have been mimicked by the development of pressure mapping of flexible surfaces. Examples of such technologies include, foot pressure based gait analysis, wheelchair seat pressure mapping. Commercially available examples of these sensors are shown in Figure 2.3.



FIGURE 2.3: Various pressure mapping devices. From top-left then clockwise: Xsensor wheelchair pressure mapping sheet (© 2024 XSENSOR® Technology) [5], Pressure Profile Systems pressure sensors on a robotic hand (© 2023 PPS UK limited) [6], Soft pressure mapping gripper(© 2023 PowerON) [7], Tekscan thin pressure mapping platform [8](© 2024 Tekscan Inc.), Tactilus seat pressure mapping system [9](© 2024 Sensor Products Inc.)

Many of these pressure mapping technologies don't accurately mimic desirable qualities of regular biological skin and are specialised for their specific use cases.

### 2.2.1 Capacitive

Similar to resistive pressure mapping, capacitive pressure mapping has more commonly been done using arrays of capacitive elements. The operating principle of capacitive-based strain

sensors rely on the deformation of sensel capacitors comprising of a dielectric elastomer and electrodes [58–60].

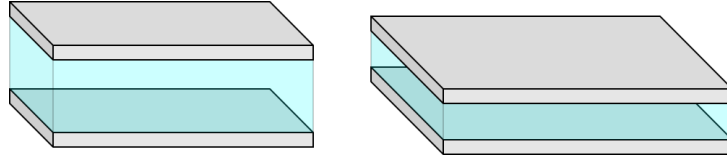


FIGURE 2.4: A sensel with grey electrodes across a blue dielectric medium. Left: Uncompressed state. Right: Compressed state

A pressure mapping sensor can be formed by making an array of the sensel shown in Figure 2.4 an attaching capacitive sensing electronics. To sense a change in capacitance electronics often will use an AC source to determine the phase change due to the change in capacitance and/or using the time constant formed by the changing sensing capacitance.

### 2.2.2 Magnetic

Magnetic strain mapping devices can be achieved using several methods. One method is to have a three layer stack with Hall effect sensors [10, 61]. The stack is made up of a the bottom layer full of rigidly connected three dimensional Hall effect sensors, the second layer is made from an elastomer, and the top layer has a magnetic particle unit placed at a set distance above each of the Hall effect sensors. The movement of the magnets alters the magnitude and direction of magnetic field sensed and data can be interpolated to create a map of strain deformation, as shown in Figure 2.5.

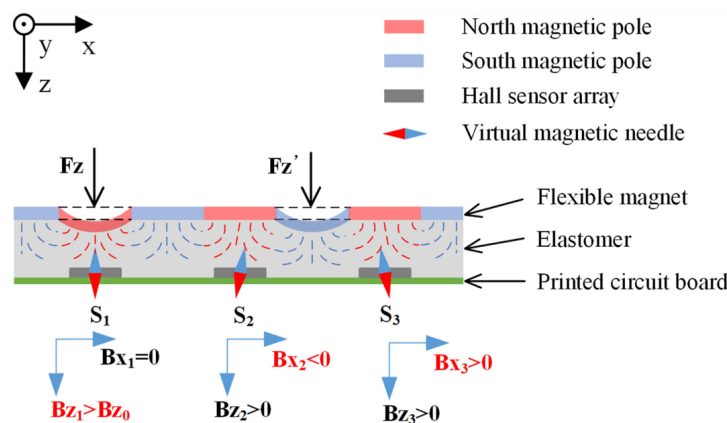


FIGURE 2.5: Example of a magnetically-based pressure mapping system designed by Yan et al. [10] (© 2022 IEEE).

The main advantages of this method is that each hall sensor can detect in three dimensions, hence normal and shear forces can be detected, and using magnetism for sensing means less electrical noise in the system. The main disadvantages of this method of sensing is the added complexity in scaling the system and the electronics required and the rigid surface required.

### 2.2.3 Optical

There are various methods for making a optically driven artificial skins. A recent review has been curated by Lee et al. [62] all of the different methods of using optics for creating tactile sensors. The main advantages of optical sensors include the high speed sensor response, immunity to electrical noise, and their non-invasive nature. The main disadvantages include, the bulky hardware required for driving the optics and signal processing, the potential interference of external light sources, and the materials that can carry optical signals. An example application of an optically-based soft pressure mapping sensor is provided in Figure 2.6.

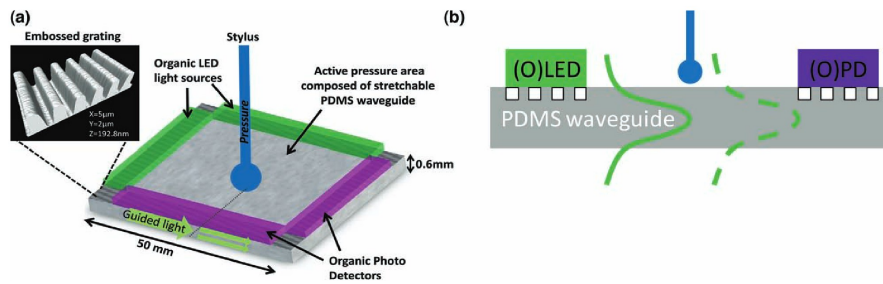


FIGURE 2.6: Example optical pressure mapping sensor using a planar PDMS waveguides. a) Schematic of the two-directional stretchable optical pressure sensor. The active pressure area is comprised of PDMS. b) A cross section view of the optical pressure sensor (© 2012 Wiley) [11].

### 2.2.4 Acoustic

Acoustic soft tactile sensing has not been explored much compared to the other forms of sensing given. Park et al., Hughes and Correll [63, 64] have created a system which uses passive acoustic tomography (PAT) to localise and classify different types of touch. This form of tactile sensing is the most similar to the biological system of mechanoreceptors which are specialised to detect certain frequencies of vibration.

### 2.2.5 Resistive

Soft resistive pressure mapping has been commonly achieved in the past by using arrays of piezoresistive sensor elements, some of which are shown in Table 2.3. The resistive elements can be made using several different flexible piezoresistive materials, such as conductive particle polymer composites [65–67], intrinsically conductive polymers [66, 68, 69], microfluidic metals [70–72], hydrogel structures [63, 73, 74], and flexible piezoresistive semiconductors [75, 76].

TABLE 2.2: Comparison of different potential piezoresistive sensor materials. Rated 1 to 5, where 1 is low and 5 is high.

Material:		Conductivity	Piezoresistivity	Softness	Manufacturability	Durability	Toxicity
Conducting polymer [68, 69, 77, 78]	2	2	1	2	3	3	
Electrolytic hydrogel [13, 66, 77, 79–81]	3	4	5	3	2	3	
Conductive particle paste / liquid metal [70, 71, 82]	5	2	4	2	2	2	
Conductive textile / fabric [83–85]	4	4	4	2	5	4	
Conductive particle polymer [67, 86–88]	3	5	4	4	4	4	

Conducting polymers, also known as intrinsically conducting polymers (ICPs), were discovered and developed by Shirakawa et al. [89] in 1977. ICPs are doped to change their electron band structure to allow for electrical conduction, however are very difficult to fabricate and not durable due to their water solubility. Electrolytic hydrogels are a hydrogel which have absorbed a electrolytic fluid. The electrolytic fluid provides a conductive through the material, however it can be temperature sensitive, due to electrolyte solution evaporation and the changing mechanical properties. Conductive particle paste and liquid metals, often have high conductivity, but can be difficult to fabricate with due to their fluid state. Conductive fabrics and textiles are often used to block EMI and have often comprise a 2D weave of conductive fibres

requiring several steps to manufacture. Conductive particle polymers are similar to conductive particle paste, however can be made of varying polymers drastically altering the mechanical storage and loss moduli. This allows for a range of elasticity and stiffness in the material and increased piezoresistivity, making conductive particle polymers a promising material for further development of artificial skin and muscle technology.

### **2.2.6 Soft Pressure mapping technology comparison**

To improve upon existing pressure mapping technology and ensure novelty, the state-of-the-art technologies are compared. There have been a range of works investigating sensors with a range of softness' and performance. A comparison of these start-of-the-art soft pressure mapping sensor works is given in Table 2.3. The range of softnesses seen in this comparison is comparable to that mentioned in Section 2.1.2. However other characteristics such as durability, reliability, biocompatibility, topology, and resolution of each sensor technology cannot match that of biological human skin.

The main advantage for using EAP based composite materials for pressure mapping sensors over magnetic and optical sensors include the lack of bulky external drive components such as electromagnetics, lasers, and optical detectors. Although capacitive sensors have similarly small bulk for their external drive components compared to resistive sensors, capacitive sensors require more complex layering, which increases the fabrication complexity when scaling into a 2D array of capacitive sensels.

TABLE 2.3: Comparison of soft pressure mapping sensor technologies. Dashes represent data not present in the related paper.

1st Author	Sensing principle	Sensing region material	Sensing region elastic modulus or shore hardness	Electrodes per sensing position	Repeatability	Time series data given	Spatial resolution	Temporal resolution
Gilanizadehdizaj [90]	Piezoresistive	Ecoflex30-00 rGO sponge	40 kPa	2 sensels / electrode	10 cycles for each stress	-	10 × 10 mm	-
Fu [91]	Piezoresistive	Carbon black silicone composite	1.5 MPa	0.625 sensels / electrode	50000 cycles	Yes.	12 × 12 mm	60 ms
Yang [92]	Piezoresistive	Ecoflex graphene sponge	-	2 sensels / electrode	800 cycles	Yes.	10 × 10 mm	150 ms
Liang [60]	Capacitive	PDMS, PET, Si, SiO <sub>2</sub> , Cu laminate	4000 MPa	1 sensel / electrode	-	Implicitly.	4 × 4 mm	-
Yan [10, 61]	Magnetic	Ecoflex 00-50	83 kPa	11 IC pins / sensel	30,000 cycles	Yes.	0.2 mm	15 ms
Rossiter [93]	Optical	Polymer foam	-	2 sensels / electrode	-	-	10 × 10 mm	-
Shimdera [94]	Optical	Super clear silicone	40 A	N/A. One fibre optic LASER and one camera.	Error rose 1.7% in 30 days	Yes.	approx. 20 × 20 mm / 0 - 1100 um	Sample rate 1.6s.
Ramuz [11]	Optical	PDMS	-	N/A. Two arrays of OLEDs and Detectors used.	900 cycles	Yes.	Not localised.	300 ms

## 2.3 Bio-Actuation - Muscle Form and Function

Biological muscles are a product of millions of years of evolution and the motion and other mechanical characteristics of biological structures is yet to be outperformed by artificial muscle technology. To determine how to quantify the performance of a biological muscle this section gives foundational knowledge about muscle function, structure, and how it can be characterised from an engineering perspective rather than the typical biological perspective, so that similar actuator devices with similar attributes can then be investigated.

Biological muscle is a naturally occurring tissue comprised of muscle fibres bundled together to apply a contractile force on connecting tissue or, in the case of smooth muscle, applying a force on itself. The base actuator units of muscle are proteins myosin and actin filaments, which effectively slide against each other to produce a contractile motion. The root cause of a muscle contraction is an electrochemical signal sent from the central nervous system to a motor neuron/s which travel to the muscle where electrochemical reactions take place for the contraction to occur [95].

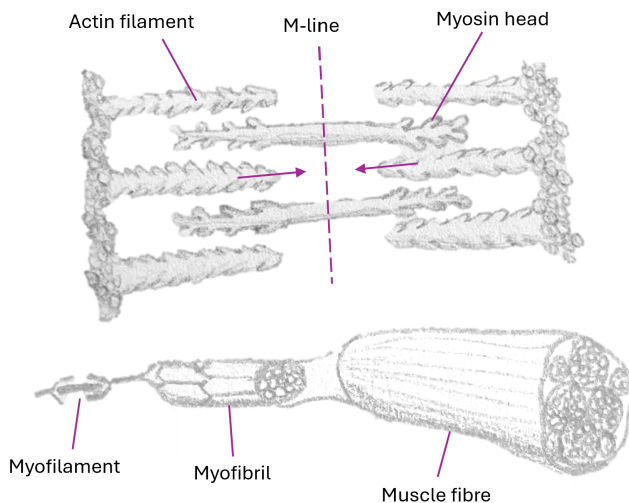


FIGURE 2.7: Components of a biological muscle contractile unit and meta-structure.

The sliding motion of the myosin and actin filaments is due myosin heads binding to the actin and pulling the actin towards a middle line (M-line) in multiple stroke actions. These filament actuators are stacked in three dimensions within a muscle fibre to amplify contractile stress and strain as shown in Figure 2.7.

On a macro scale, muscle is made up of bundles of fasicles connected together with a tissue called perimysium. Within the fasicles are many muscle fibres (i.e. muscle cells) which are

surrounded by a connective tissue called endomysium. Within the muscle fibres there are many sacromeres stacked within a cylindrical-like structure called a myofibril. Each sacromere contains a contractile unit of myofilaments.

### 2.3.1 Characterising a muscle

To quantify the performance of a biological muscle, certain metrics are compared. An artificial and biological muscle can be characterised using typical mechanical material parameters such as:

1. Stress - Force that is applied to the normal of the cross section of the muscle through various states of muscle excitation. [ $Pa$ ]
2. Strain - The muscle change of length due to the stress applied through various states of muscle excitation. [%]
3. Elastic modulus - The elasticity determining the relationship between stress and strain for the linear region of the stress strain characteristic curve. [ $Pa$ ]
4. Actuation voltage - The voltage required to trigger saltatory conduction in a neuron [V]
5. Energy density - The work done by the muscle per unit volume or mass. [ $J.kg^{-1}$ ]
6. Power density - The work done by the muscle per unit volume or mass per unit time. [ $W.kg^{-1}$ ]
7. Ultimate tensile strength - The maximum tensile stress that a material can tolerate before breaking. [ $Pa$ ]
8. Efficiency - The work done by the muscle compared to the energy put into the system, known as metabolic cost in biological muscles. [%]
9. Actuation frequency - The frequency range of actuation cycles using the system's method of excitation. [Hz]
10. Stroke - The maximum displacement an actuator can achieve [m]
11. Life cycle - The time or number of actuation cycles in which it takes for the actuator to degrade such that it cannot perform its intended purpose to specified standards.

Only the main characteristics of muscle have been described above. If wanting to mimic other qualities of a biological muscle they should be quantified on a case by case basis depending on the artificial muscle technology being investigated. Some of the above biological muscle metrics have been quantified by previous research as seen below:

- Actuation voltage - action potential voltage threshold for a muscle resting at -70 mV is -55 mV. With a peak voltage of +30 mV [96, 97].
- Actuation frequency - action potentials are commonly between 4 - 12Hz [98]
- Energy density - energy densities ranging from 0.4 - 40  $J.kg^{-1}$  [99].
- Power density - power densities ranging from 9 - 284  $W.kg^{-1}$  [100]
- Actuation frequency - natural actuation frequencies ranges 1 to 180 Hz [100].
- Strain - ranging from 5 - 30% [101].
- Efficiency - Thermodynamic efficiency of human muscle is typically between 20-35% [102]. However other biological muscle has been seen to reach efficiencies of up to 77% [102].

### 2.3.2 Muscle Mechanics

A variety of simplified electromechanical muscle models have been developed. Understanding these models is essential for exploring how biomimetic actuators can be applied in assistive soft robotic devices. First, some fundamental biomechanical muscle models will be discussed.

The stress and strain involved in muscle contraction is more complex than uniform materials and is non-linear. The stress and strain of a passive muscle (i.e. contractile units are not producing internal muscle tension) can be modelled with the following equation;

$$\frac{d\sigma}{d\varepsilon} = \alpha(\sigma + \beta) \quad (2.1)$$

Where  $\varepsilon$  &  $\sigma$  are strain and stress respectively. A solution for this is first order ODE is;

$$\sigma = \mu e^{\alpha\varepsilon} - \beta \quad (2.2)$$

Where  $\mu$  is a free parameter determined empirically. The stress-strain of a passive muscle can be likened to tension being applied yarn. As more strands of the yarn are pulled into tension

the stress increases, then as the last strands are brought into tension a maximum stress is reached, until the yield stress is reached. Linear approximations can still be made over regions of elongation depending on accuracy required for application. The stress-strain of an active muscle (i.e. when it is tetanised) is approximated to a piece-wise quadratic function or bell curve. It is important to note that the stress for both active and passive muscle is near zero when the strain is less than 0.4, demonstrating the yarn-like nature of the muscle stress-strain as shown in Figure 2.8.

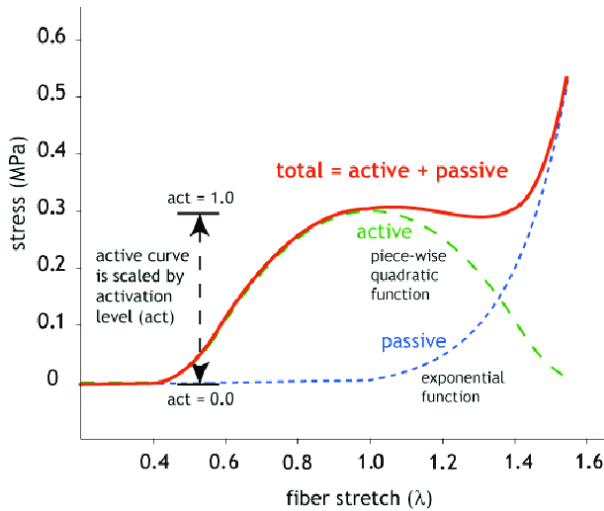


FIGURE 2.8: Stress and strain of active and passive muscles (© J. Teran | ACM 2003) [12]

Hill's muscle models commonly refer to a mechanical three element model [103] composed from, one parallel non-linear spring element, one series non-linear spring element, and a contractile unit.

Similar to EAP-based artificial skin and artificial muscles, biological muscles also require electrical stimulation in the form of neuronal action potentials to function. These models often require many input parameters to determine the out contraction force and strain of a muscle such as action potential frequency, nerve conduction velocity, calcium ion absorption dynamics, and concentrations of many other molecules required in the process [104]. In contrast, when designing artificial muscle technology there is opportunity to control the parameters for their electromechanical models.

## 2.4 Artificial Actuation - Electromagnetic Actuator Technology

Artificial muscle actuator technology has been refined over the course of the 21st century to more closely match biological muscle and supersede them in certain performance metrics. The most prominent soft actuator technologies researched in recent years include, ionic polymer-metal composite (IPMC) actuators, hydraulically amplified self-healing electrostatic (HASL) actuators, magnetorheological elastomer (MRE) actuators, and dielectric elastomer actuators (DEAs). Each of these having qualities similar to that of biological muscle usually with a trade-off in actuation response time, actuation force, and actuation strain for their various possible topologies. This section gives a brief overview of four state-of-art soft EAP actuator technologies.

### 2.4.1 Current Driven - Ionic polymer–metal composite actuator

Ionic polymer-metal composite actuators (IPMCs) are soft actuators that can be actuated at a much lower excitation voltage than DEAs, commonly less than 10V. IPMCs are also desirable as artificial muscles they have shown large bending deformations, simple to fabricate, light weight and thin in design, and can have a fast actuation response time ( $> 15$  Hz) at small displacements [105]. IPMCs also have a high work density and maintain a constant volume during actuation like biological muscles [106].

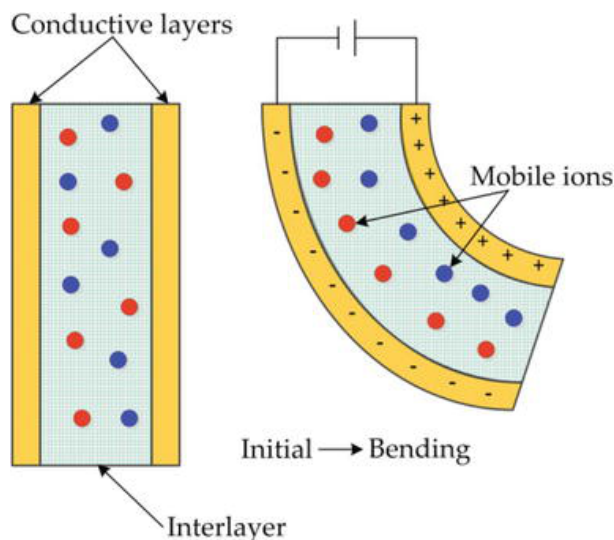


FIGURE 2.9: Diagram of the typical architecture of an IPMC actuator [13] (© 2018 Yanjie Wang and Takushi Sugino)

An IPMC is made up of an ionic polymer inter-layer, two electrode conductive layers, and a voltage source. The ionic polymer inter-layer allows for ionic transport and is typically made of treated Nafion or Flemion. These materials are typically used as ion exchange membranes so have the characteristics desired for the transporting ions during the actuation of the IPMC actuator. The two electrodes are made of a suitably conductive and flexible material. The inter-layer is treated such that it is filled with water molecules and cations, with the chemical backbone of the inter-layer being slightly negatively charged. When a voltage is applied across the electrodes the cations are repelled from the cathode and travel towards the anode while the water molecules are displaced in the opposite direction towards the cathode. The ionic polymer then swells as the cations repel each other along the anode side of the inter-layer, while the polymer elements on the cathode side effectively shrink [107]. This swelling adjacent to the cathode provides the device's bending actuation.

There are many variations of the design and manufacturing of IPMCs to optimise the actuator for an application as shown by [108].

Although the process of manufacturing IPMCs is simple, the typical duration for the ionic polymer to absorb the necessary ions and undergo necessary reaction during fabrication can exceed 48 hours [109]. There has been much research into the optimal manufacturing of an IPMC [108, 110, 111]. The use of additive manufacturing has been used successfully to generate more complex geometries using fused filament deposition [112].

IPMCs can also be used as sensors. When an IPMC undergoes bending due to an external force there is a potential generated across the electrodes, which indicates bending direction and magnitude [113].

Two key deficiencies of current IPMC actuator technology are the maximum force output achievable and the life cycle of the actuator in a dry (non-aqueous) environment. The force output optimisation of IPMCs has been investigated by several researchers, all of which having a maximum actuation force in the milli-newton scale [113–115]. Because the IPMC actuators rely on hydrated ionic transport to actuate this means if the IPMCs are in a dry environment then over time they will decrease their maximum actuation force.

The applications of this actuator is limited to applications requiring a small actuation force and a wet environment. Some current applications include flexible catheters [116], small biomimetic robotics [117, 118], and aquatic robotics [119, 120].

### 2.4.2 Magnetically Driven - Magnetorheological Elastomer

Magnetorheological elastomer (MRE) actuators, also known as magnetoactive soft materials (MSMs), are a relatively new form of actuator however the theory reinforcing operating principle has been known since at least the 1980s [121]. The structure of an MRE actuator generally consists of a ferromagnetic elastic composite and a driving magnetic field. An example of this is a composite of iron-carbonyl powder and PDMS. The operating principle of MREs is magnetostriiction, where magnetic flux travelling through the MRE will change mechanical characteristics within the elastomer (i.e. stiffness and/or deformation of the body). The operation of a MRE actuator is similar to a DEA however instead of having an electric field cause a contraction it is a magnetic field causing a deformation. An MRE is typically made of silicone rubber containing magnetic ferrite based particles uniformly distributing throughout its volume. This kind of actuator is current controlled and can hence operate at a low voltage. This helps mitigate the risk of electric shock of a device in close proximity to humans, unlike HASEL and DE actuators discussed in the following Sections 2.4.3 and 2.4.4.

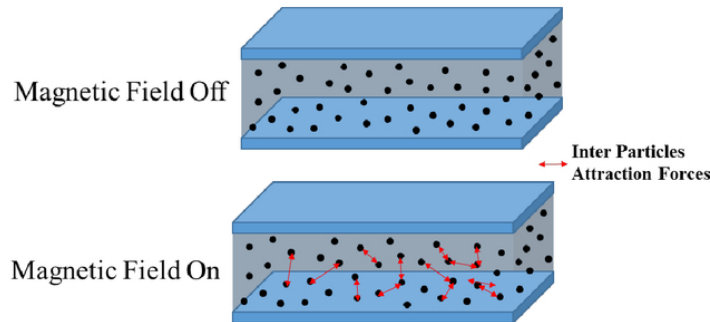


FIGURE 2.10: Diagram showing MRE contraction forces when a magnetic field is applied [14]

A key issue with using magnetorheological elastomers as soft actuators is that they require heavy gauge conductors for the high current they require for generating a magnetic field. The high current requirement means that actuators have only been created that have a rigid electromagnet driving a soft MRE [122].

When manufacturing MREs, uncured liquid silicone rubber is mixed with magnetic (commonly carbonyl iron) particles to form a 3D matrix of cross-linked elastomer with homogeneously dispersed magnetic particles. A core issue when creating an MRE is the agglomeration and corrosion of magnetic particles due to residual water within the mixing operation. The magnetic particles can be processed to have a hydrophobic quality to mitigate this issue [123, 124]. During

the curing process a magnetic field can be applied to align the particles within the elastomer to control the particle isotropy [124, 125].

There have been attempts to use additive manufacturing to make MREs [124, 126], however the method described has not optimised the structure of MRE for any application and the particle dispersion throughout the MRE has not been proven uniform throughout the print volume.

To sense the contraction and deformation of an MRE a hybrid iron-carbon particle elastomer composite can be made. Where the carbon particles' contribute to the material piezoresistivity to determine the material loading [127, 128].

The current applications of MRE actuators are limited, however magnetorheological fluid (MRF), is a fluid which becomes more viscous with an applied magnetic field as currently has many modern applications. This fluid substance is largely used in applications where damping control is desired such as vehicle suspension [129], medical assistive devices [130] and helicopter seat damping [131]. Potential MRE actuator applications include fluid valve control [122] and active vibration control similar to that mentioned for MRFs [129].

#### 2.4.3 Electrostatically Driven - HASEL actuator

A hydraulically amplified self-healing electrostatic (HASEL) actuator is a recent soft actuator technology developed in 2018 by Kellaris et al.[15] which displays many qualities that are superior than current artificial muscle technology. HASEL actuators are made up of three main components: electrodes, dielectric fluid, and an elastomeric shell. The electrodes need to be highly conductive, able to handle high electric potential, and can be solid or flexible. Hydrogel electrodes have been proven to be a good material for the electrodes because of their elasticity while still maintaining a high conductivity [132]. In one application the hydrogel material is bonded to a polydimethylsiloxane (PDMS) substrate for mechanical strength and for ease of bonding to the actuator bi-axially-oriented polypropylene (BOPP) shell [15, 73]. HASEL actuators use high electric potential across two electrodes to create an electrostatic force. This force induces a zipping effect which pulls the electrode together from one end to the other as the electric field strength increases. The zipping of the two electrodes pushes the dielectric fluid into the reservoir increasing the pressure which alters the shape of the reservoir bounds providing an actuation motion. When the electrodes have displaced all of the fluid between them the actuation displacement is at a maximum. The electrostatic zipping action allows a large force to be generated due to snap-through transition. Snap-through transition is an actuation instability

which has been discussed in previous research as a means of amplifying DEA actuation strain [133].

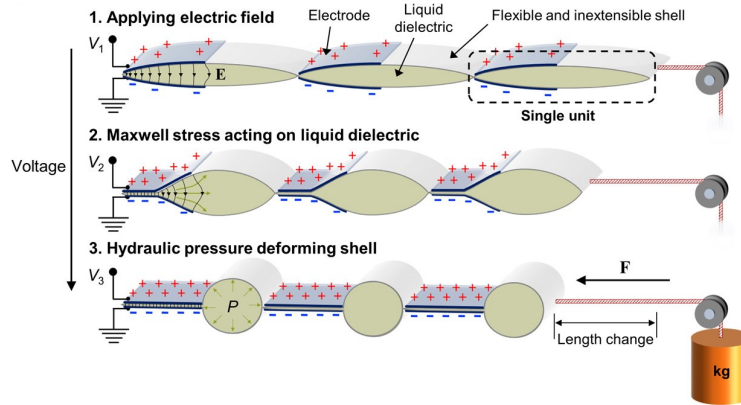


FIGURE 2.11: Diagram of the typical architecture and the contraction stages of a HASEL actuator [15]

Recorded efficiency values of HASEL actuators of 21% are comparable to that of human muscles of 20 - 35% [102]. The actuators have had a frequency response of up to 20Hz. Large strains of 124% have been recorded, but can only be achieved when actuating at a resonant frequency. Strains of up to 79% have been recorded using a linear planar HASEL actuator configuration and DC voltage stepping. Else, strains of only 10% have been recorded for static steady strain [15]. Because there is a relationship between the motion of the actuation and capacitance between the electrodes, this means self sensing can be achieved through the electrodes. Although due to the flexible and fluid nature of the device, modelling of the HASEL is difficult and limited in accuracy.

The simple and commonly used manufacturing process for HASEL actuators is completed in six steps as shown by the diagram below:

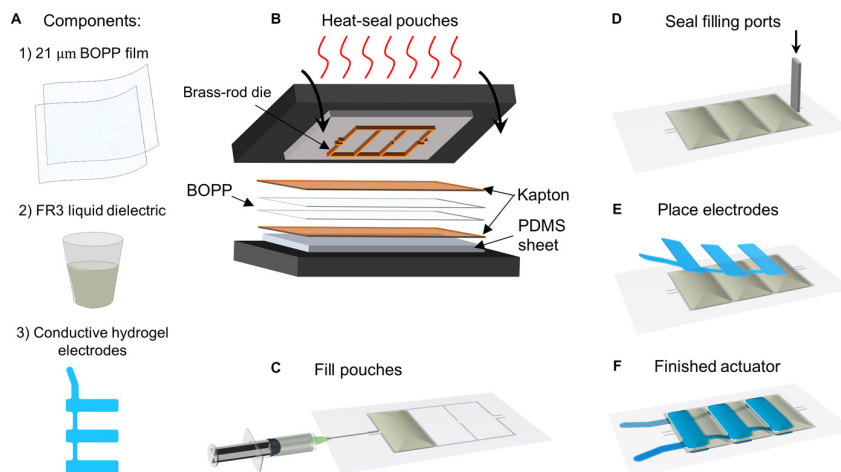


FIGURE 2.12: Diagram of the simplified stages of HASEL actuator production [15]

Other attempts have been made to use polyjet inkjet based additive manufacturing to make the whole HASEL actuator and have been successful with proof of concept, but are yet to be developed from prototype stage [134].

The cyclic life of HASEL actuators are high, because of their self-healing properties. When there is a dielectric breakdown through the liquid dielectric the damage caused is not permanent like when a DE breaks down. The liquid may form some small air bubbles, however these may not effect the operation of the actuator, instead this can increase the likelihood of another dielectric breakdown. The cycle life of the HASEL actuator was seen to be larger than one million with a given torus shaped HASEL actuator [132]. The HASEL technology is promising with a number topologies possible, including toroidal, planar linear [132], and scorpion metasoma(tail) [135].

#### 2.4.4 Electrostatically Driven - Dielectric Elastomer Actuators

DEAs share many similar characteristics to biological muscle such as, the large strains achievable, the high elastic energy density, many topologies/configurations achievable, and constant volume during its contraction. Compared to the previous soft actuator technologies discussed, the dielectric elastomer actuator (DEA) better fits the term ‘artificial muscle’.

A DEA consists of a dielectric elastomer (DE) film sandwiched between two compliant electrodes. To excite the actuation, a high electric potential is applied to across the electrodes creating an electrostatic force between the two compliant electrodes. This force pulls the two electrodes together applying stress (known as Maxwell’s stress) to the elastomer and hence strain parallel and perpendicular to direction of the electrostatic force. When the DEA is contracted the surface area of the electrodes increases and the thickness of the DE decreases causing a change in capacitance and Maxwell’s stress.

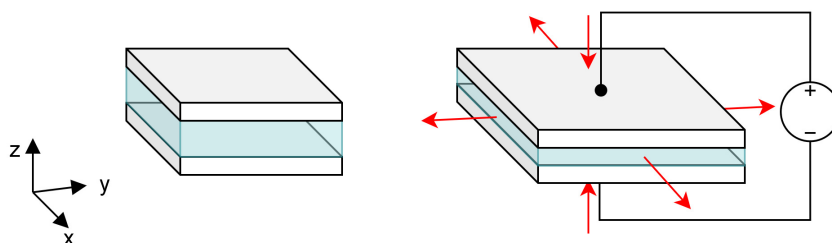


FIGURE 2.13: DEA with two compliant light-grey electrodes and a transparent light blue dielectric elastomer. Showing deformation without and with a voltage applied across the electrodes.

A dielectric elastomer actuator can be modelled as a flexible parallel plate capacitor in its simplest form. Using this we can determine the electrostatic pressure to be:

$$\sigma_{es} = \epsilon_0 \epsilon_r \frac{V^2}{z^2} \quad (2.3)$$

Where  $\sigma_{es}$  is the electrostatic pressure,  $\epsilon_0$  and  $\epsilon_r$  are the vacuum and relative permittivity constants,  $V$  is the voltage potential applied across the electrodes and  $z$  is the thickness of the DE. The electrodes used for a DEA need to be made of a conductive material, but require similar elasticity to the dielectric material. An ideal material for these electrodes would have high conductivity. This conductivity would change minimally and predictively under large strains. Many composites have been used in practice for these electrodes, with the most common in early development being a silicone rubber and carbon powder composite or a carbon grease. However, the unpredictable nature of carbon powder elastomer composites has lead to research into many other materials/silicone additives such as hydrogels, graphene sheets, metallic nanostructures, carbon nanotubes, liquid metal [136–139]. The ideal material for the dielectric elastomer should have a high elastic modulus and a high electric breakdown voltage. The elastic modulus needs to be sufficiently low so that less electrostatic pressure can create a larger strain. The actuation force is also a function of the dielectric constant, with increased dielectric constant resulting in increased actuator force.

While the breakdown voltage of the material needs to be sufficiently high such that the material will not break down at the maximum desired strain. If a material can be found with a high enough electric breakdown strength at a smaller thickness than current research prototypes then a higher stress can be achieved giving a larger or equivalent actuation force at a lower voltage.

While disc shaped DEAs are the most commonly used actuator topology many other topologies exist to generate different actuation motions using the same electrostatic pressure generation principle. These include actuator topologies such as stack [140, 141], helical [142], bending [143], lens [144], cylindrical, and rolled shaped actuators [145]. Each of which having a range of applications.

DEAs are often fabricated in a laboratory environment using a pre-strained elastomer. The pre-straining accomplishes four key qualities; stores elastic strain energy, ensures DE is planar within the bounds of the jig, controls the initial thickness of the DE, and puts the DE in an optimal stress-strain region, often taking advantage of elastomer hyper-elasticity. There is no standard practice for the fabrication of DEAs, other methods such as additive manufacturing

have also been explored to generate more complex geometries and to increase production speed [146, 147].

As well as actuating, DEAs can also be used for sensing. DEAs can be used as sensitive capacitive sensors, where any strain applied to the DE will relate to the effective capacitance between the two electrodes [36, 148, 149].

Currently DEAs often require voltages within the kilo-volt range to generate an adequate stress and strain for a range of applications. A key problem encountered by researchers designing DEAs is the trade-off between actuation force and strain magnitude [140]. This high voltage requirement may deem the technology dangerous for use where there is a possibility that a human may come into physical contact with the high voltage electrodes.

## 2.5 Electroactive Material - Soft Conductive Particle Piezoresistive Composites

Most soft sensors and actuators require low-stiffness materials for their active sensing/actuation domains. The requirement of softness is governed by the mechanical modulus values depend on the application requirements. The use of conductive particle elastomer composites is explored in this work due to the customisability of the electromechanical characteristics. Although HASEL actuators have been defined soft actuators they commonly BOPP or BOPP-like plastic polymers which are flexible, however do not have the desired stretchability of elastomers. When comparing the limited amount of relatively soft piezoresistive materials in comparison Table 2.2, conductive particle polymers were determined to have the best fit for the sensor and actuator technology developed in this work. A core part of this thesis is understanding the behaviour of conductive particle elastomer composites for their use as a range of EAP-based sensing and actuating devices. The characteristics that make conductive particle elastomer composites (CPECs) ideal for soft sensor and actuator devices often include, its customisable low stiffness, conductivity, piezoresistivity, elasticity, mouldability, as well as its 3D printability, low toxicity, durability, cost, simple fabrication process, and sustainability [124, 150–152].

### 2.5.1 Conductive Particle Elastomer Conduction Mechanisms

Depending on the fabrication process stages stated in Section 2.5.2 for fabricating CPECs, the dispersion of conductive particles will always vary.

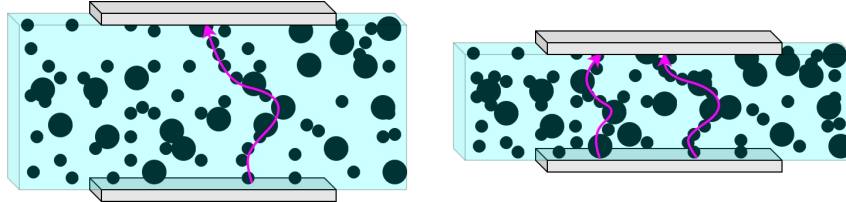


FIGURE 2.14: Two grey highly conductive electrodes across a CPEC cuboid showing enlarged black conductive particles within a blue polymer matrix. Left: An uncompressed CPEC. Right: A compressed CPEC.

Derived from percolation theory [67], there is a percolation threshold volume percentage of CB required for there to be a high likelihood that there is a conductive link of CB particles between two sides of a volume. Some of the physical features of these conductive percolation networks can be quantified and directly relate to the macro-level electromechanical properties of the material. Such characteristics of a conductive percolation network include, the type of conductive particle(s) used, particle dispersion, the elastomeric matrix, and any impurities or voids. The aspect ratio of a conductive particle filler can drastically change the conductivity and piezoresistivity of a CPEC. For example the aspect ratio of carbon nanotube particles (CNTs) is very large compared to that of regular carbon black (CB) particles, this has been shown to give improved conductivity for smaller weight/volume percentages [153, 154], among other electromechanical property changes. Also the inherent particle conductivity a core parameter to consider when choosing a conductive particle composite. An example percolation threshold plot is shown in Figure 2.15.

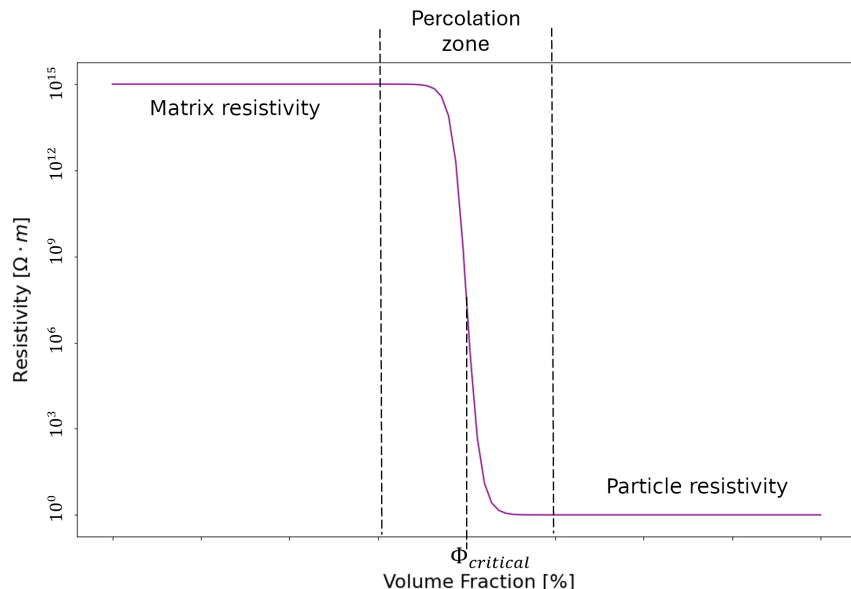


FIGURE 2.15: Example percolation threshold plot for a conductive particle composite with the plot settling at the conductive particle resistivity.

Conductive particle dispersion is an important characteristic of CPECs when optimising the electrical properties of a CPEC. Particle dispersion includes the inter-particle distance distribution [152], particle agglomeration distribution [155], particle isotropy/anisotropy [156], and sedimentation [157]. The filler elastomer matrix also contributes to the piezoresistive effect, through its viscoelasticity, elastic modulus, and dielectric permittivity within the CPEC.

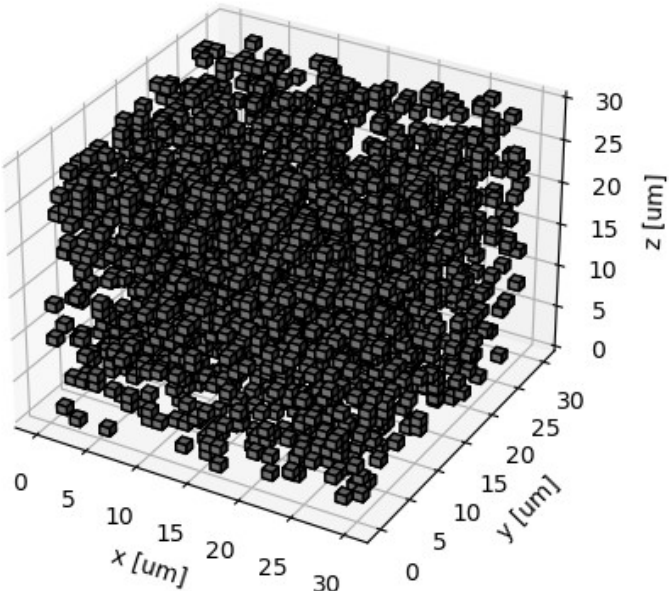


FIGURE 2.16: Example of a randomised cube percolation with a volume percentage of 8% of  $1\mu\text{m}$  particles

Micromodels for CPECs and the relationship between particle and electric charge motion are often computationally heavy, overly idealised, and non-invertible [158]. A micromodel example can be seen in Figure 2.16. However, micromodeling of CPECs may give insight into understanding complex physical phenomena that may relate to the macroscale models made for CPECs. An alternate method for modelling CPECs is the formation of macroscale models [159].

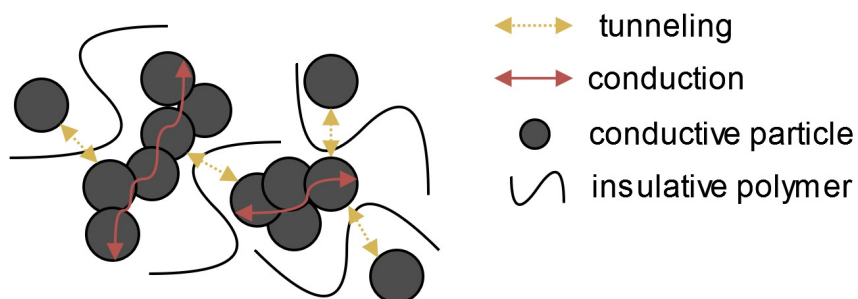


FIGURE 2.17: Electrical conduction and tunnelling representation diagram.

Electrical DC conduction through a CPEC occurs via two main mechanisms, electrical conduction and quantum tunnelling [87, 160–162]. Electrical conduction uses the conduction band electrons shared by adjacent atoms to allow movement of electrons throughout chains of cascading these conductive atoms. The second mechanism of conduction is through quantum tunnelling which is stochastic in nature and allows for conduction through insulative boundaries between the percolative network of conductive particles [163, 164].

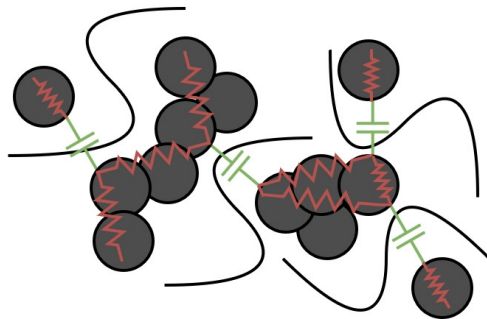


FIGURE 2.18: AC conduction RC network representation diagram.

The a CPEC can be modelled with an RC network as shown in Figure 2.18. Electrical AC conduction can occur through a CPEC through capacitive means depending of particle spacing with a decrease in reactance becoming more prominent for composites near the percolation threshold [88, 151, 165].

### 2.5.2 Fabricating Conductive Particle Elastomer Composites

Before exploring the known conduction and piezoresistive mechanisms and models for CPECs, it is important to understand how the fabrication process of a CPEC may affect its physical structure.

CPECs are made by dispersing conductive particles through a curable liquid elastomer matrix. To change the electromechanical properties of the material, the dispersion of the conductive particles throughout the matrix can be optimised through various methods such as mixture sonication, and mix speed and timing. Sonication serves to minimise the agglomerations of primary conductive particles as a preliminary step. This involves a mixture of the conductive particles and a liquid, usually in the form of a solvent, to be placed in a ultra-sonication bath.

The sonication bath performs a frequency sweep and it has been shown that sudden implosion cavitation near the agglomerates help cause the separation of the agglomerates into their primary particles [166, 167]. The degree of deagglomeration and dispersion is affected by various factors

including sonication time, frequency of oscillations, oscillation intensity, particle wettability, and liquid matrix viscosity [82, 167].

This sonication usually occurs before the particles and solvent are added to the elastomeric matrix due to the large viscous damping effects of liquid elastomers. The next step involves mixing the dispersed conductive particles throughout the liquid elastomer, this can be done using a variety of mixing methods, including a planetary mixer, magnetic mixer, screw mixer, static mixers, amongst others [152, 155, 168, 169]. During the mixing process often the liquid solvent used in the dispersion stage is evaporated, leaving only the curable elastomer and the conductive particles. Although often impurities and voids are a by-product of the previous processes which can give undesirable qualities.

When sufficient mixing of the liquid elastomer and conductive particles have been completed the material is formed into a desired final shape using advanced additive manufacturing methods [58, 126, 146, 147, 170–172] or traditional moulding [173] or film making techniques [174]. During the moulding process the material undergoes a form of curing, such as UV, catalysed, or moisture curing. If the composite material has not already been integrated into a device containing electrodes and other mechanical support structures these are integrated at the end of the process.

### 2.5.3 Viscoelasticity in Composite Elastomers

A core difference between a pure elastomer and a composite elastomer is the degree of apparent viscoelasticity. Composite elastomers exhibit viscoelastic phenomena [175] similar to regular human biological tissue [16]. These viscoelastic phenomena include strain creep, stress relaxation, hysteresis, and a strain-rate stiffness relationship. The viscous component of viscoelasticity is more prominent in polymer plastics and plastic composites due to the bonding mechanism between polymer chains within the material. Elasticity is often the result of bond stretching within a polymer material, whereas viscous effects are often due to the temporary nature of secondary bonds in polymer which break, slip, and reform.

The Payne and Mullins effects are important to note when analysing mechanical stress-strain testing results for elastomer composites with conductive filler particles. The Payne effect describes the effect where with a deformation in the material changes the modulus of the material, due to breaks in the microstructure of the material [176]. Jalocha [177] and Avila-Torrado et al.

[178] have clearly displayed the Payne effect experimentally where they compared different conductive fillers and determined their complex moduli for a range of strains and strain frequencies using dynamic mechanical analysis (DMA). The Mullins effect is where the stress-strain curve of a particle filled elastomer composite relies on the maximum load input experienced by the material. The effect causes composite softening due to the lack of stiffening in the composite fillers relative to the usual stiffening seen in the elastomer matrix [179].

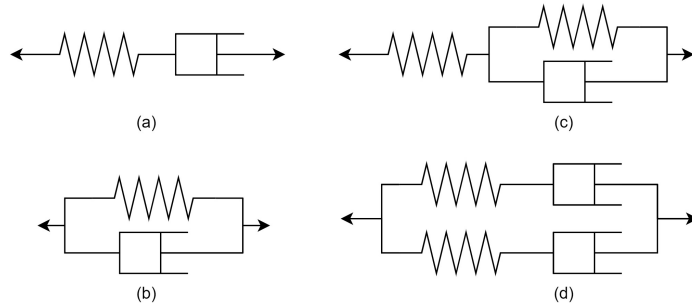


FIGURE 2.19: Linear viscoelastic models (a) Maxwell (b) Kelvin-Voight (c) A solid linear model variant (d) A Burgers model variant.

Several linear mechanical models of viscoelastic material are described by simplifying the material to a combination of discrete spring and dashpot elements such as the Maxwell, Kelvin-Voight, Burger, and standard linear models seen in Figure 2.19. A generalised Maxwell or Prony series linear models can often be used when the other models are underfitting the material data [180, 181].

Non-linear viscoelastic models are similar to the above linear models, however they introduce fractional order elements to model the complex modulus of a material more accurately [182]. Fractional modelling has also proven useful in complex electrical impedance modelling using constant phase elements (CPEs). These CPEs more accurately describe the non-idealness of real-world capacitors, where a current leakage through the dielectric material exists [183, 184].

## 2.6 Soft Sensor and Actuator Technology Integration

As mentioned in Section 2.4 comparing electromagnetically driven actuator technology. Each of these technologies can use their active actuation area as a sensor area. IPMCs can sense bending direction and deformation with output voltage. MREs have been shown to self sense with the additional dispersion of conductive particles. HASEL and DE actuators have been shown to self sense using capacitive means.

In this thesis the integration of a artificial skin and muscle is desired to advance the current state of soft robotic technology. To emulate this integration with current soft pressure mapping and soft actuator technology each of these actuators can be arrange in an array structure to generate pressure maps while maintaining actuation function. However, this array design introduces complications with connecting each sensel/actuation-unit and the bulk involved with wire routing and related circuitry. A more elegant solution is to maintain the active sensing and actuation area free of wires with the addition of only periodic boundary electrodes, which can be achieved using electrical impedance tomography (EIT). An EIT-based pressure mapping solution explores a piezoresistive film that can wrap around many surface topologies including adding soft actuator surfaces.

### 2.6.1 Electrical Impedance Tomography and Pressure Mapping

To approximate changes of resistivity in a planar CPEC sensing domain a technique called electrical impedance tomography (EIT) can be used. EIT generates impedance maps for a domain under test (DUT). Unlike most pressure mapping sensors, EIT uses periodically spaced boundary electrodes to pass known electrical current and measure voltage potentials around the DUT. From these known current injections and voltage measurements, an ill-posed inverse problem can be defined. To obtain an EIT image reconstruction three key steps are required: data acquisition, forward modelling, and inverse problem solving. A constant current can be employed to capture solely the resistance values of the DUT. To capture impedance data an AC signal is implemented to sweep through a range of frequencies.

Various electrode excitation patterns can be utilised for EIT, each with distinct reconstruction performance characteristics [185–187]. The most prevalent excitation pattern is the Adjacent Electrode pattern, where a current source is placed across adjacent electrodes, and the voltages at all other adjacent electrodes are measured [188]. This process repeats for each pair of adjacent electrodes as exemplified in Figure 5.5

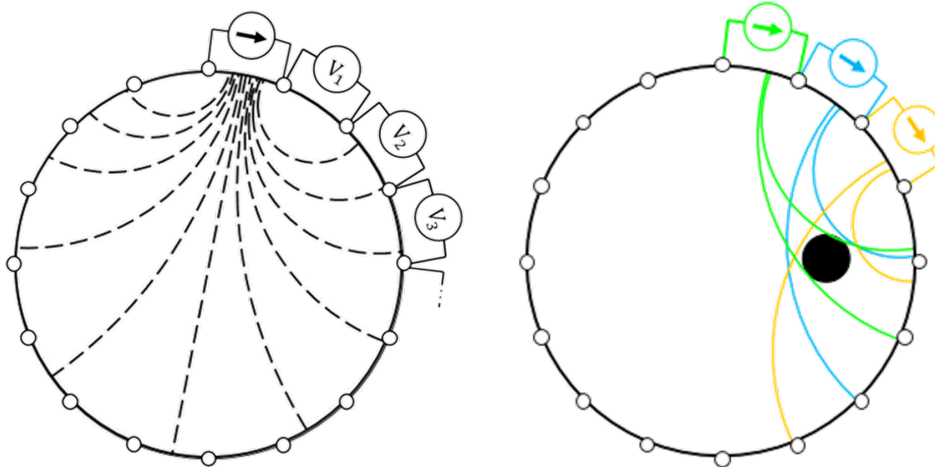


FIGURE 2.20: EIT adjacent drive pattern sequence for a circular domain with 16 boundary electrodes.

The forward problem in EIT is a well-posed mathematical problem, so linear algebra can be employed for obtaining electric field data for a DUT of known conductivity and a known current injection. Utilising a mesh-based coordinate system and FEM, proves to be an efficient solution for the forward model, accommodating diverse shapes. Solving the forward problem entails applying Maxwell's electromagnetic formulae and Ohm's law to determine how an electric field would propagate through the DUT, considering the DUT conductivity. voltage,  $\phi$ , in a domain,  $\Omega$  is governed by the Equation 2.4 derived from Maxwell's equations [189],

$$\nabla \cdot \gamma(x, \omega) \nabla \phi = 0, \quad (2.4)$$

where  $x$  is a point in  $\Omega$  with admittance,  $\gamma$ , and  $\omega$  is the angular frequency of the driving current. Admittivity,  $\gamma$ , comprises of a real and imaginary parts  $\rho(x, \omega) + i\omega\epsilon(x, \omega)$ , where  $\rho$  is the electric conductivity, and  $\epsilon$  is the electric permittivity. Current is applied to the surface of the domain,  $\delta\Omega$ , through electrodes like those given in 5.5 and the current density,  $J$ , can be formulated with the equation

$$\gamma \frac{\delta \phi}{\delta v} = J \quad \text{on} \quad \delta\Omega, \quad (2.5)$$

where  $v$  is a spatial unit restricted to the DUT boundary,  $\delta\Omega$ . A common continuum model used for EIT incorporates Equations 2.4, 2.5, and the Law of Charge Conservation, whereby the sum of the current density and sum of the voltages on the boundary is zero. However to use these equations in practice the electrical current,  $I$ , is known and not current density,  $J$ . This

is found by integrating Equation 2.5 for each  $i$ th electrode as shown in the following equation,

$$\int_{e_i} \gamma \frac{\delta\phi}{\delta v} ds = I_i, \quad i = 1, 2, \dots, n, \quad (2.6)$$

where  $e_i$  is the part of DUT boundary,  $\delta\Omega$  at the  $i$ th electrode and  $I_i$  is the current injected at the  $i$ th electrode. Another assumption is made with the electrode gap model when the current density between the electrodes is on  $\delta\Omega$  is zero, while the current across each electrode is constant.

Unlike typical biomedical EIT imaging where there is often significant and variable electrode impedance, the device in this work uses DC meaning that no complete electrode model is needed on top of the above model constituents.

An initial estimate of the DUT resistivity is necessary for the first step of an EIT algorithm. Once the EIT forward model is solved, EIT inverse problem can be solved iteratively using the forward problem's solution. This inherently unstable problem requires optimisation algorithms and regularisation to create and linearise a solution [188, 190–192]. This work uses an efficient inverse solver algorithm called Newton One-Step Error Reconstructor (NOSER) which uses a regularised form of Newton's method to solve a modified version of the inverse forward problem to generate an impedance or conductivity map based on known current and voltage values[189].

The NOSER EIT reconstruction is done via the formula

$$\rho = \rho^0 C + 2 \sum_{k=1}^K \sum_{j=1}^K v_{k,j} P^{k,j}, \quad (2.7)$$

where  $C$  and  $P^{k,j}$  are predetermined vectors that depend only on the known geometry and regularisation parameters, and  $\rho^0$  and  $v^{k,j}$  are scalars determined from known data.  $k$  and  $j$  are the related to amount of the electrodes used and the electrode drive pattern used.

Once the EIT reconstruction algorithm has been tuned for an application, often post-processing is completed on the reconstructed EIT image for filtering and to capture data specific for the application. A consortium of experts in the field of medicine and biomedical imaging have constructed metrics for quantifying the quality of an EIT reconstruction as shown by Adler et al. [193] and their GREIT (Graz consensus Reconstruction algorithm for EIT) performance metrics. Although GREIT has been optimised for human thorax imaging, researchers who have used EIT pressure sensing purposes have also developed performance metrics, most of which agree with the GREIT metrics [65, 194–198].

## 2.7 Literature Review Conclusions

The purpose of this thesis was to develop novel sensor and actuator technology that mimics the pressure mapping capabilities of human skin and combine this with the actuation properties of human muscle. Through this review of current literature, several key conclusions can be drawn that will lay the foundational knowledge for the rest of this work.

The review of biological skin has revealed quantitative parameters that define its mechanical and sensory capabilities. This review highlighted mechanical characteristics such as the elastic modulus, viscoelastic creep, and surface area, as well as functional properties like spatial and temporal resolution. These factors provide a foundation for designing artificial skin that can replicate or even surpass the sensing functions of soft human skin. The review on pressure mapping technologies was then completed showing a range of different transduction methods for similarly soft sensing domains, showing that replicating human mechanoreceptor sensation is a multifaceted problem. Human skin uses various mechanoreceptors with different qualities and trade-offs and similarly different pressure mapping technologies use different pressure transduction methods each with different performance characteristics and limitations. The parallel review on biological and artificial muscles showed that DEAs and HASEL actuators are promising technologies for mimicking biological muscle quantitatively. Although characteristics common to both technologies such as high actuation voltage and limited device lifetime limit the applications of them. DEAs were shown to be more akin to human muscle and skin tissue than HASEL actuators due to not only their flexibility, but their high degree stretchability, potential biocompatibility, and potential for integration with an EIT-based soft pressure mapping technology. The integration of these DEA and EIT-based pressure mapping technologies has not yet been explored in previous literature.

The thesis has converged on using CPECs to fabricate EAP sensor and actuator devices, hence a brief literature review highlighting CPEC fabrication techniques and electromechanical characterisation has been given. These composites exhibit beneficial properties like flexibility, tunable electromechanical behaviour, and ease of fabrication, which make them suitable for integrating into soft robotic systems. However, challenges such as achieving uniform particle dispersion, minimising agglomeration, and optimising the conductive network for stable long-term operation are still active areas of investigation. Hence, this thesis first characterises some of the dynamic and time dependent properties of the material for repeated discretely categorised strain input scenarios.

The investigation of the dynamic electromechanical characteristics of CPECs and how they are used in EIT-based pressure sensors and their integration into dielectric elastomer actuators is shown in this thesis; generating technology that is more akin human muscle and skin for future integration within ubiquitous rigid robotics.



## **Chapter 3**

# **Characterising Non-Linear Behaviour in Carbon-Black Elastomer Nano-Composites**

### **Overview**

This work has converged on using conductive particle elastomer composites (CPECs) as the electroactive base for creating improved sensor-actuator devices, due to their superior qualities outlined in the Literature Review. CPECs can be strained > 100% and return to their original shape while having repeatable piezoresistive qualities that can be altered through their fabrication process. Understanding the dynamic characteristics of a CPEC is critical for using the material in dynamic sensor and actuator devices. Although the fabrication of a CPEC can be simple, the characterisation and optimisation of such a material for soft robotic applications can require complex models and display non-linear time-dependent behaviour. In this work we uncover several repeatable mathematical relationships seen within the material concerning dynamic time series behaviour between tensile strain, stress, and resistance data.

First a linear quasi-static model is generated to give a simple formula for estimating strain given a resistance input for a steady state system. Then the time-dependent and dynamic phenomena of the CPEC material were explored. Analogously to fitting stress relaxation to a two-unit generalised Kelvin mechanical model, this work has fitted the resistive relaxation seen after a strain step input to a three-unit generalised Kelvin model. A non-linear relationship was found between resistive and stress relaxations, which negates the hypothesis that the stress

relaxation is directly related to the resistive relaxation. For a strain falling edge signal, a positive correlation was found between increased strain-rate and the resistance peak seen in the tensile specimens. Similarly a positive correlation was found between the pre-strain amplitude and the resistance peak generated, for a strain falling edge signal. We have demonstrated a technique to reduce apparent resistance measurement drift in resistance experiments by using a switched AC current source instead of DC.

All of the behaviours determined in this work set a foundation for understanding the viscoelastic electromechanical nature of a CPEC for further development of the material in more complex sensor and actuator systems. Future work aims to generate a non-linear inverse model to more accurately determine the strain of the CPEC material given a resistance input. Analysis will also be extended to not just the composite resistance but the resistivity to give more generalisable relationships. With this inverse model the CPEC material would be suited to a plethora of biomedical and agricultural applications which require delicate and non-toxic sensing systems.

### 3.1 Introduction

As discussed in the Literature Review chapter, conductive particle elastomer composites are desirable for soft sensor and actuator applications for a variety of reasons. However, it is crucial to understand the electromechanical behaviour of these composites to create complex control systems with such materials. Although conductive particle elastomer composites (CPECs) are simple in concept, consisting of dispersed particles through an elastomer matrix, the electromechanical behaviour is not well understood on a macro or micro-scale. This chapter will focus on only tensile stress characterisation and modelling of the specimen. Compressive characterisation and modelling is covered in the subsequent chapters. This work endeavours to understand the material behaviours of carbon black silicone rubber composites on a macro-scale to help create improved inverse models so that the material can be used more accurately for stress/strain sensors and with greater predictability for actuator applications.

#### 3.1.1 Background

Carbon nanoparticle-silicone elastomer composites are stretchable conductive materials with diverse applications such as, highly elastic strain sensors [67, 173, 199], dielectric elastomer actuators [200, 201] and electromyography electrodes [173, 202, 203]. Understanding the dynamic

resistive relaxation characteristics of carbon black (CB) silicone rubber (SR) elastomer composites would improve performance in fields which require high efficiency of space, power and accuracy, such as the devices used in biomedical and aerospace fields. Unlike many common strain gauges, CBSR composites can have strains of over 300% without yielding [204] depending on the type of SR and CB used and the method of fabrication. This strain and the strain used in this work is higher than commonly used constantan alloy strain gauges, which typically have a maximum strain of  $\pm 3\%$  [205], with traditional metal alloy based strain gauges often having significant plastic deformation after less than  $10^4$  cycles [205] at this 3% strain.

Some characteristics of CBSR composites which make it suitable for strain sensors include that, the material is relatively inexpensive, readily available, non-toxic, bio-compatible, and can have a high gauge factor. Other alternative composite conductive particles, such as carbon nanotubes (CNTs) [206, 207] and metallic particles [139, 208], have been seen to be more carcinogenic than CB alternatives [209–211]. The fabrication of CBSR composites requires a degree of optimisation to ensure that the carbon particles are adequately dispersed to ensure high conductivity and high yield strength of the material. More importantly the homogeneous dispersion of CB particles means improved repeatability of experimental results and more accurate models for the eventual applications of CBSR composites. A comprehensive model of how the resistivity changes with strain has not yet been developed.

While previous work from our research group [212, 213] has focused on the response to quasi-static and low-strain-rate behaviour, these materials show dynamic effects where a significant resistance strain-rate relationship is present. The main characterisation investigated in this work for CBSR sensing involves understanding the relationship between the mechanical stress relaxation, electrical resistive relaxation and strain in time. Both stress and resistance relaxation phenomena are discussed in this section and are shown in our experimental work in Figure 3.14. A difference in time constants between the stress and resistive relaxations have been noted before in literature [207, 214, 215], but never accurately modelled with the physical theory explained. Mersch et al. [216] have classified several transient ‘shoulder’ events and their related deformation events, compressive, tensile, and bending. These transient peaks have been observed by several researchers using the similar CBSR materials, however there is no conclusive mathematical model relating these transient peaks to strain in time. An understanding of this resistive relaxation and other transient phenomena would mean an accurate model could be made to predict the relationship between stress, strain and resistance within a CBSR composite.

Determining a stress-strain-resistance model would also allow us to understand the limitations of using this composite in sensing and actuation applications, so that the material can be used simultaneously as an actuation excitation electrode and a strain sensor. Understanding these characteristics may give rise to new applications of the composites material, for example, if the resistive relaxation properties of the material were known, it could be used as a mechanically activated timing device. An oscillatory flexible dynamic circuit has been demonstrated when mimicking the motion of a caterpillar as shown by Henke et al. [200], where the resistive relaxation modelling is useful for more accurate electrical circuit dynamics. The theory behind mechanical stress relaxation is widely known and has been modelled using a variety of mathematical models [16] depending on the material modelled.

It is known that silicone rubber composites are viscoelastic materials and clearly exhibit the three traits of a viscoelastic material [16]: stress relaxation, strain creep, and stress-strain hysteresis. Stress relaxation is an effect observed when a step input of strain is applied to a material and there is a transient stress decay response which converges to a steady state value. A commonly used model for viscoelasticity is the generalised Kelvin body model of order  $n$  shown in Figure 3.1.

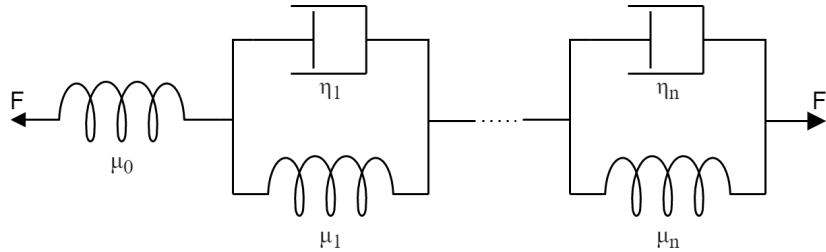


FIGURE 3.1: Mechanical spring dashpot diagram of the generalised Kelvin body model adapted from Fung et al. [16]

Where  $F$  is the force applied to the material, and  $\mu$  and  $\eta$  values represent the spring and damping component constants, respectively. The stress relaxation function for this model is found in Equation 3.1, for,  $n$ , serial repeating units.

$$G(t) = a_0 + \sum_{i=1}^n a_i \cdot e^{-t/\tau_i} \quad (3.1)$$

Where  $a_0$ ,  $a_i$  are the magnitudes of relaxation and  $\tau_i$  are the relaxation decay time constant components. All of the constants  $a_0$ ,  $a_i$ , and  $\tau_i$  are functions of  $\eta$  and  $\mu$ .

Initially the relationship between the stress relaxation and resistive relaxation of the material is investigated. However, the generalised model can easily over-fit the data, if  $n$  is too high. To

mitigate over-fitting, a generalised model with the minimum amount of repeating units while maintaining a high  $R^2$  is used.

Few mathematical models describing the viscoelastic-resistance relationship have been formulated. Laaraibi et al. [217] developed a time-invariant model which uses a relaxation parameter to account for the viscoelastic effect. Mersch et al. [216] developed a model using transverse and longitudinal viscoelastic parameters to model a similar CBSR material. Both models show promise towards creating a more comprehensive physical model. However, the both models aren't tested for a randomised range of input strain signals.

## 3.2 Methods

The core experimental part of this chapter will be described from composite fabrication through to simultaneous strain tensile tests and resistance measurements. This is followed by the analysis data for resistance-strain phenomena, to quantitatively match the phenomena these to black-box and viscoelastic models.

### 3.2.1 Composite Fabrication

The CBSR composite was composed of Vulcan XC-72 CB powder (Fuel Cell Store, Bryan, USA) and two part Pt cured Dragon Skin 10 NV SR (SmoothOn, Macungie, USA). The CB powder has an average particle size of 50 nm and typical bulk density of 96 kg/m<sup>3</sup>. This grade of SR was chosen due to the following characteristics low elastic modulus,  $E$ , of 186 kPa tensile strength,  $\sigma_Y$ , of 2.75 MPa, and a low mixed viscosity,  $\eta$ , of 6,000 cps [218]. This  $E$  value is within the range of human skin tissue and the low  $\eta$  facilitates material processing in potential future applications with additive manufacturing.

The volume resistivity of pure CB powder itself is between  $10^{-1}$  and  $10^2 \Omega \cdot \text{cm}$  depending on how densely the particles are packed and the purity of the CB [67]. The ability of a CB matrix embedded within a highly insulative SR substrate to become conductive is determined mainly by the dispersion of the CB particles, and the tunnelling that occurs between conductive CB and insulative SR bodies within the material volume [67, 207]. The composite being created must be highly conductive without compromising the elastic modulus and yield strength of the material. From percolation theory observed in literature [67] there is a threshold volume percentage of CB required to ensure that conductivity is maintained with certainty throughout

the composite volume within the linear volume resistivity region. The percolation threshold for composite used in this work was difficult to predict due to the unknown configurations of agglomerations and dispersion of CB particles within the composite material. Empirically it was found that a CB volume percentage of 7.5% or greater meant the composite material had a resistivity of less than  $3.5 \text{ k}\Omega \cdot \text{cm}$  consistently with the fabrication method used.

The first fabrication step was to mix the CB nano-powder with part A of the liquid SR using a KK-50S planetary mixer (Kurabo, Osaka, Japan). A mixing function was used with specific rotational velocities and times for each axis, which was well suited towards de-aeration and viscous particle mixing. The composite mixture was then mixed with the cross-linker part B of the liquid SR using the same planetary mixing function to ensure adequate dispersion of the CB particles throughout the SR volume.

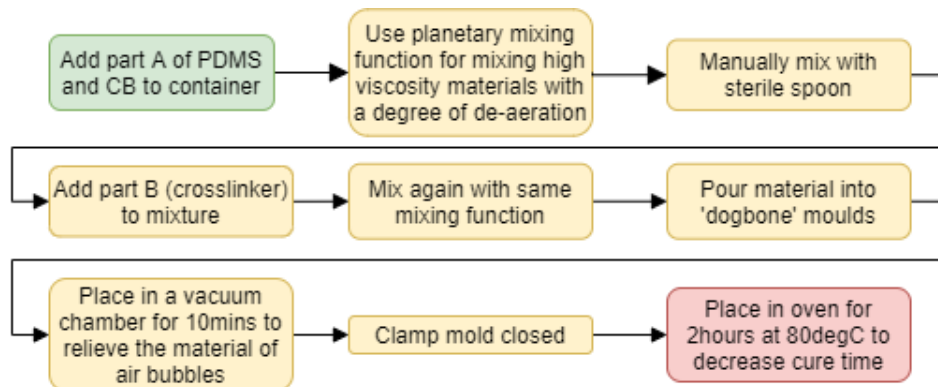


FIGURE 3.2: The steps involved in creating the CBSR composite material

For the fabrication of the CBSR specimens, a standard dog-bone shaped mould was developed for the mixed CBSR to cure in, based on ASTM standard D412 [219]. Before the mould was clamped shut the composite filled mould was immediately placed in a vacuum chamber for ten minutes to de-aerate the still liquid, curing CBSR mixture. The specimen was placed in a lab oven at a temperature of 80 °C for a two hours to accelerate curing. It has been shown that an increase in curing temperature for two part SR increases elastic moduli and decreases yield strength [220, 221].

### 3.2.2 Material Imaging

To determine how the microstructure may effect the macro-behaviour observed in the following electromechanical testing of the material, three optical imaging methods were used, including optical microscopy, scanning electron microscopy (SEM), and Raman spectroscopy.

The initial step was to observe the fabricated CBSR composite specimen using a stereoscopic microscope to view the internal structure of the CBSR composite specimens as shown in Figure 3.3.

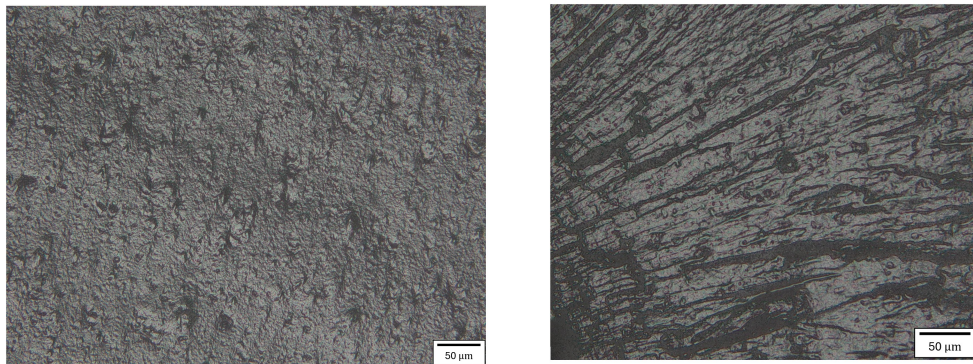


FIGURE 3.3: Microscope images at x20 magnification of a CBSR specimens with cross-sections made by; Left: Cutting with a scalpel. Right: Inducing an embrittlement fracture.

It is known in literature that preparing flat planar surfaces through elastomer composites for micro- and nano-scopic imaging is non-trivial [222]. Due to the silicone material elasticity and a low embrittlement point of -60 to -70°C , traditional polymer composite specimen machining methods cannot be used if a flat surface is desired. Because of the lack of water content in the CBSR composite traditional biological specimen preparations methods are also not feasible.

Two methods were trialled to prepare the cross-sectional surface of the specimen for imaging, a scalpel cut and an induced embrittlement fracture. The scalpel cut was completed at room temperature conditions aligned vertically with the specimen. The induced embrittlement fracture used required extreme cooling by pouring liquid nitrogen over the specimen for 2 minutes, then snapping the specimen in two.

The induced embrittlement fracture shown in Figure 3.3 shows a very rough surface finish due to the many localised stress concentrations formed around voids and CB particles in the composite, and the non-crystallinity of the elastomer. The scalpel incision method showed an improved surface finish with a low amplitude undulating surface finish.

To observe smaller features such as voids and CB particle dispersion within the CBSR specimen the Apreo 2S FEG-SEM (Thermo Fisher Scientific, Waltham, USA) was used. Initially the CB particles were imaged validating their nominal primary particle size and displaying the agglomerated structure as shown in Figure 3.4. The nominal particle size was found to be  $48 \pm 20$  nm randomly sampling and averaging over 30 particles observed via SEM images. The top surface edge of the CBSR specimens were imaged to highlight the difference in surface

roughnesses. Finally the dispersion of the CB particles was attempted, however due to surface charging of the relatively highly insulative silicone matrix the image resolution was limited as shown in 3.4.

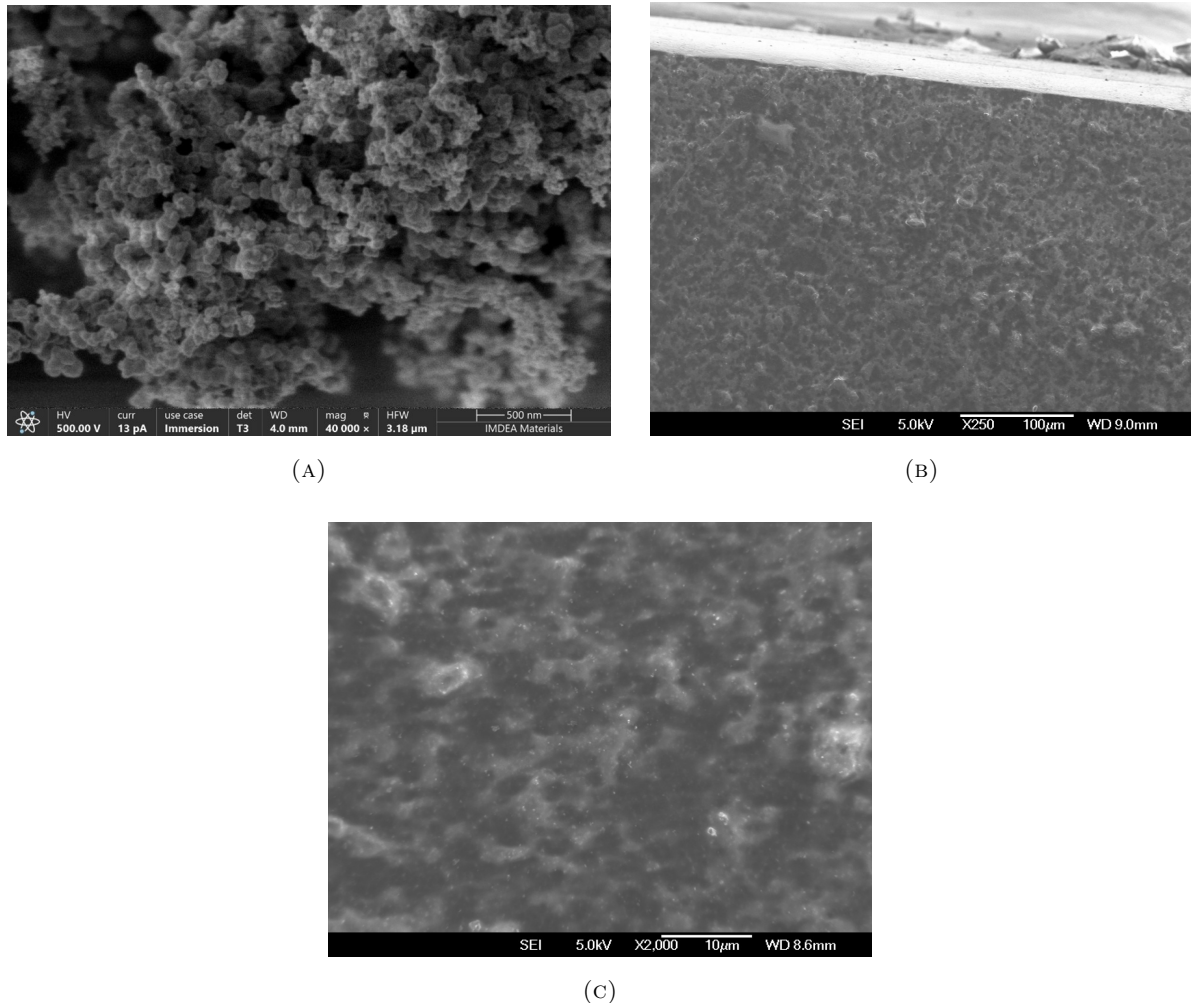


FIGURE 3.4: SEM images of; (A): CB agglomerated particles  $\times 40,000$ . (B): CBSR cross-section top surface edge site 1  $\times 250$ . (C): CBSR cross-section site 1  $\times 2000$ .

When measuring CBSR specimen for bulk electrical properties a reliable electrical connection to the material's conductive matrix is necessary. Obtaining high conductivity connection between the measurement electrodes and the material volume was investigated. The surface of the cured CBSR specimen is smooth and has proven highly insulative upon measurement, indicating that there is a thin insulative silicone film around the edges of the specimen as shown in Figure 3.4b. This surface insulation film existed in each side of the specimen, potentially indicating that the viscosity of the SR matrix is high enough to prevent the CB nanoparticles from settling on the bottom surface of the mould used. The white dots shown in Figure 3.4c represent carbon particles throughout the SR matrix. Resolution was limited due to the insulative SR matrix

charging from the electron beam. This is resolution discrepancy is apparent when comparing to the more conductive CB particles in Figure 3.4a.

To determine the presence and dispersion of CB particles on the surface of the CBSR specimens a inVia confocal Raman microscope (Renishaw, Wotton-under-Edge, United Kingdom) was used. A 532 nm laser with a was used in the Raman microscope. Several surface and cross-sectional images were taken showing a considerable difference in the CB-SR ratio as shown in Figure 3.5. The prominent  $1350\text{ cm}^{-1}$  and  $1600\text{ cm}^{-1}$  intensity peaks indicate the presence of CB and the prominent  $490\text{ cm}^{-1}$ ,  $2906\text{ cm}^{-1}$ , and  $2965\text{ cm}^{-1}$  peaks indicate the presence of SR [223, 224].

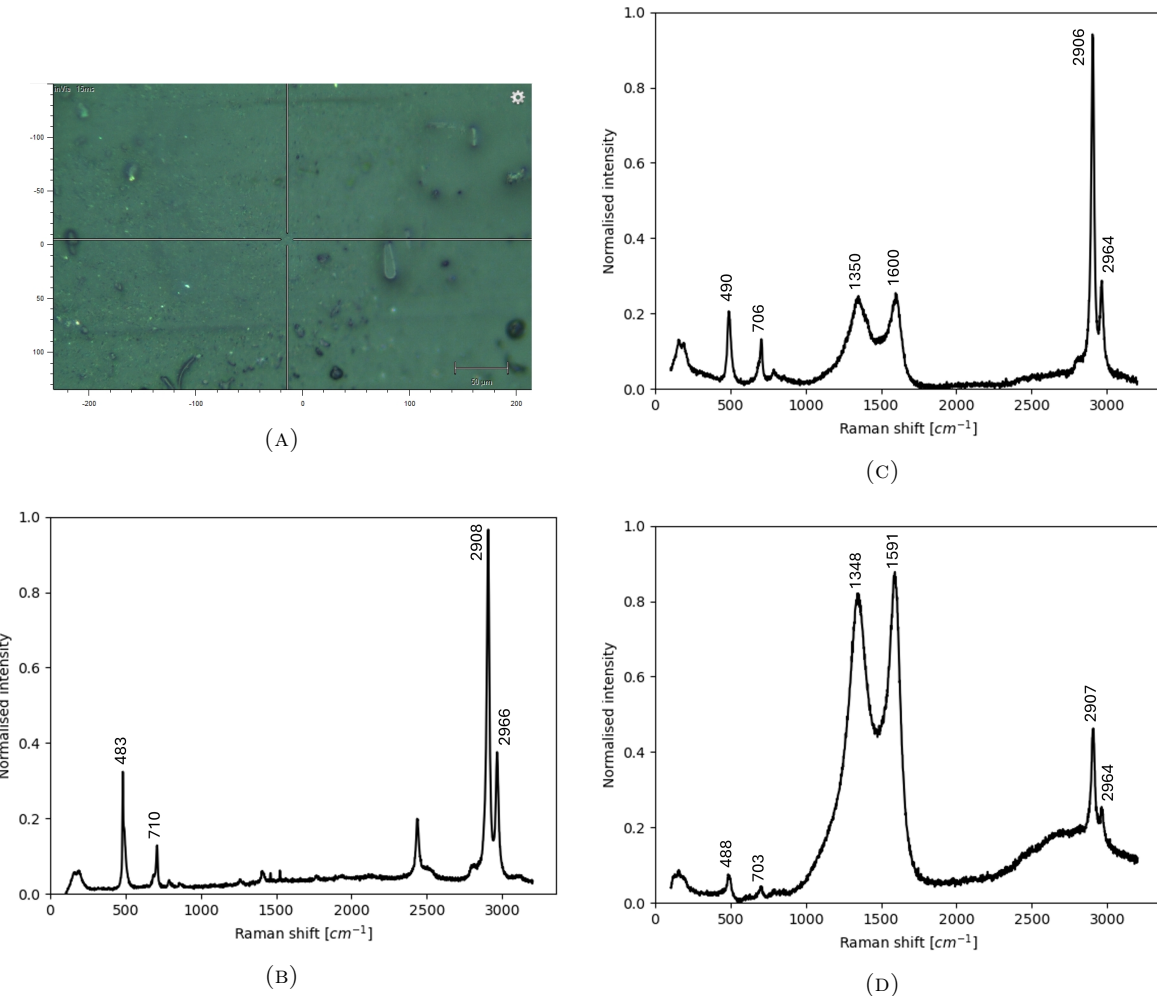


FIGURE 3.5: (A): Typical screenshot from the focused Raman microscope. Normalised Raman spectrum of (B) the plain SR. (C) the top surface of CBSR specimen. (D) the cross-sectional surface of CBSR specimen.

These plots in Figures 3.5b - 3.5d show that surface electrodes will have a smaller chance of obtaining a reliable connection to the conductive network to the internal the CBSR composite, due to the low CB particle content measured at the surfaces on the specimens. Hence to maintain

a reliable electrical contact to the percolative network this layer must be removed or electrodes must penetrate this material surface layer.

### 3.2.3 Stress-Strain-Resistance Measurement

A custom test measurement device was made for measuring the desired characteristics of the CBSR material, so that parameters driving the data collection such as the current source and strain profile could be easily customised to suit the experiment. The strain, stress, and resistivity of the specimen were measured in parallel. The setup included the use of a 500 g TAL221 loadcell (HT Sensor Technology Co. Limited., Xi'an, China) in combination with a linear actuator stage driven by a NEMA23 stepper motor and a 2634B Keithley source measurement unit (SMU) (Tektronix, Beaverton, USA). The loadcell was found to have a resolution of  $\pm 30$  mN and the linear actuator stage used a G201x micro-stepper controller (Geckodrive, Santa Ana, USA) allowing for  $40 \mu\text{m}$  steps.

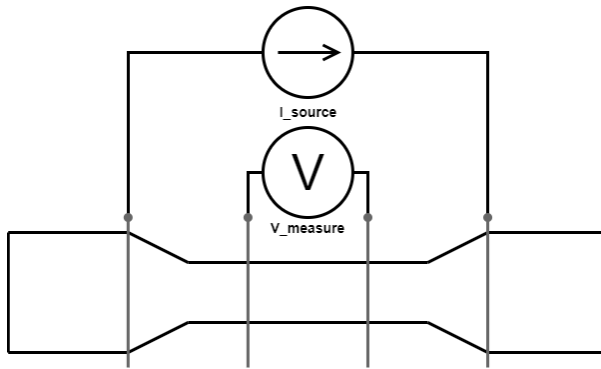


FIGURE 3.6: The composite dog-bone test specimen pierced by 4 metal pin electrodes. The outer and inner electrodes connected to an SMU current source and voltmeter respectively

The SMU current source used was switched between  $\pm I_{src}$  at 10 Hz to mitigate charging effects otherwise observed within the measurements. The four-wire method uses four pin electrodes as seen in Figure 3.6 to avoid the surface insulation observed in Figure 3.5. The four-wire method applies a constant current source through the outer electrodes and uses a voltmeter on the inner two electrode to determine the resistance of the specimen. The four-wire electrode configuration exhibited a larger signal-to-noise-ratio (SNR) compared to the two-wire alternative for resistance measurements. Four-wire pin electrodes were selected because they resulted in minimal specimen deformation, exhibited a high measurement SNR, no slip, and the electrode can pierce through the specimen which ensured a constant electrode impedance. The inner

pin electrodes were symmetric about the centre and placed 20 mm apart with the outer pin electrodes being 40 mm apart as shown in Figure 3.7.

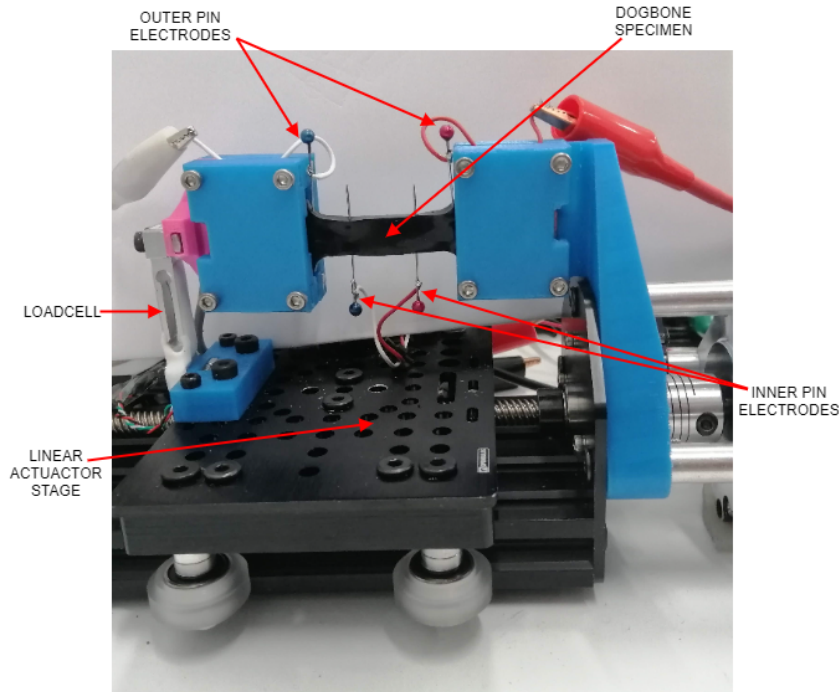


FIGURE 3.7: Photo of test measurement setup

The dogbone specimen was held in place using clamps with an a 3D pyramidal array surface. The specimen clamp strain was calculated using the specimen Poisson's ratio and the maximum expected tensile experiment strain; to ensure the specimen would not slip, and ensure minimal deformation to the specimen.

The measurements were completed using controlled sinusoidal, saw-tooth, and pulse trains of strain to ensure repeatability of the models were consistent across varying experimental parameters. If this material is used as a sensor the model fitted to the stress relaxation must hold over many consecutive tensile strain events. As these materials are intended as large strain sensors, the main strains tested in this work were ranged between 0 and 30%, with a strain-rates ranging from 0 to  $6.67 \% \cdot s^{-1}$ . Two samples of each CBSR weight percentage 7.5 and 10 wt% were used in this work's experiments to ensure repeatability.

All data was captured through serial interfaces and logged on a PC with a python-based program. An open source G-code platform GRBL was used to control the motion of the linear actuator. The PyVISA library was used to obtain all of the measurement data and to send commands to measurement devices. A calibration procedure ensured that the stress and strain

of the specimen was always zero'd before each experiment. The functional architecture of the system is shown in Figure 3.8.

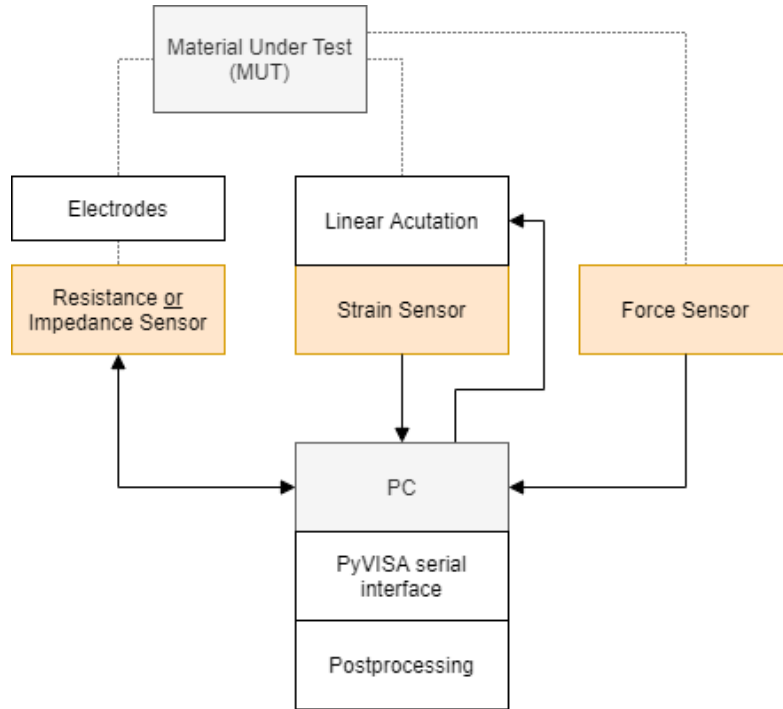


FIGURE 3.8: System architecture for the electromechanical tensile test rig showing data/physical connections

### 3.3 Results and Analysis

The CBSR composite material has shown complex nonlinear behaviour in previous literature as discussed in Section 3.1, hence a piece-wise approach to modelling the CBSR composite has been taken to describe the electromechanical dynamic behaviours of the material. To understand the transient behaviour of CPECs several dynamic repeatable electromechanical characteristics of CBSR have been classified and mathematical representations fitted. This section aims to provide repeatable mathematical relationships for several dynamic phenomena working towards creating an overarching model which combines each of the phenomena.

#### 3.3.1 Stress-Strain and Viscoelasticity

All of the specimens fabricated indicated a degree of viscoelasticity shown by the hysteresis seen when loading and unloading the material with 30% tensile strain in Figure 3.9. The 0, 7.5, and 10 w.t.% CB specimens have average elastic moduli, as measured in the loading phase, of 205.2 kPa, 321.4 kPa, and 342.1 kPa, respectively.

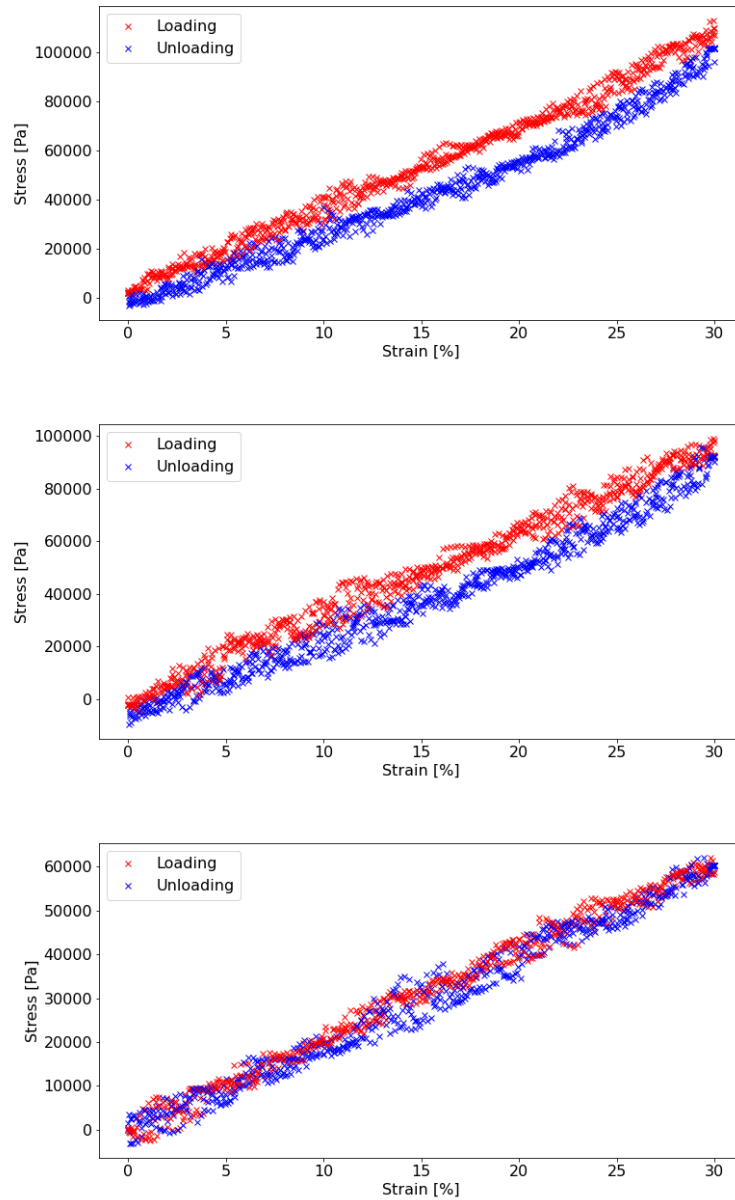


FIGURE 3.9: The loading and unloading of 30% strain on a composite test specimens with CB weight percentages from top to bottom of 10%, 7.5%, and 0% with data collected over five loading and unloading cycles

Using the difference in the modulus of resilience between the loading and unloading curves for each percentage of 10 and 7.5 wt% of CB, the hysteresis loop areas were  $3830 \pm 890$  and  $3680 \pm 900$  respectively.

### 3.3.2 Quasi-Static Tensile Resistance-Strain

To understand how the material could be used for a low-frequency response application the underlying steady-state relationship between resistance and strain was found by producing a

quasi-static linear resistance-strain formula for strains between 0 to 30% strain. Data was gathered using steady-state measurements from four separate tensile strain pulses performed on the same CBSR specimen as shown in Figure 3.10.

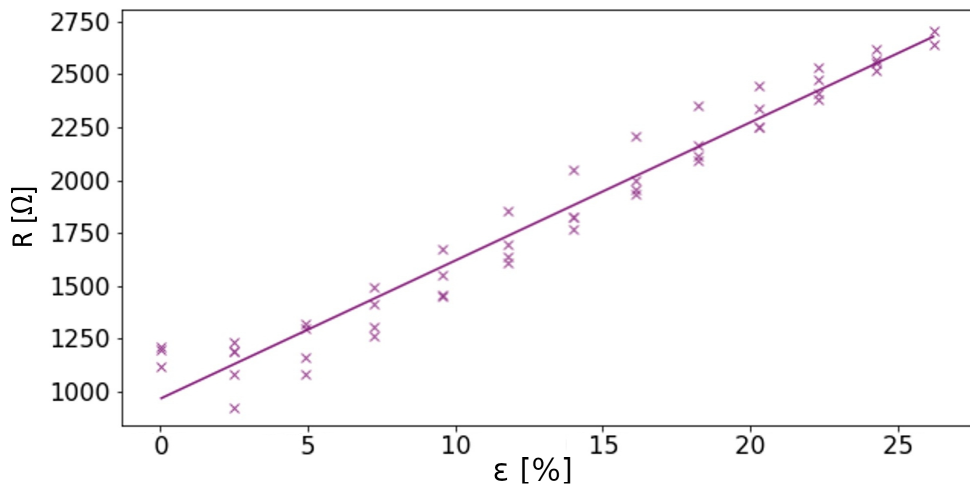


FIGURE 3.10: Linear quasi-static resistance-strain fit for 7.5 w.t.% CBSR specimen

The fitted parameters for the linear quasi-static model are given in Equation 3.2.

$$R = 6530 \cdot \varepsilon + 970 \quad (3.2)$$

### 3.3.3 Dynamic Resistance-Strain-Rate Response

When using this material as a tensile strain sensor many applications will require a strain-rate superseding the capabilities of the quasi-static model given in Section 3.3.2 due to the resistive relaxation in the material characterised in Section 3.3.5. The dynamic characteristics of the CBSR material is investigated to find a relationship between the strain-rate and resistance. Several saw-tooth strain signal experiments were completed using four different strain-rates of 1.67, 3.33, 5, and 6.67  $\text{%}\cdot\text{s}^{-1}$ . To avoid measuring a time-dependent relationship instead of the desired strain-rate dependent relationship, each set of different strain-rates were repeated as shown in Figure 3.11.

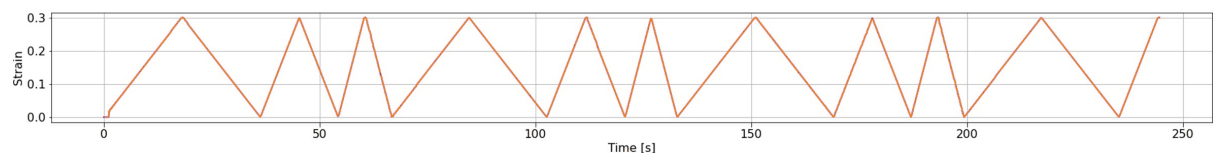


FIGURE 3.11: Strain input waveform for investigating strain-rate dependent resistance

The resulting resistance response exhibits a shoulder peak phenomena where a second peak is developed when suddenly decreasing the strain-rate. Unlike the similarity between the stress and resistance relaxations, this a phenomena not replicated in the stress response only the resistance response. The resistance response is shown in Figure 3.12.

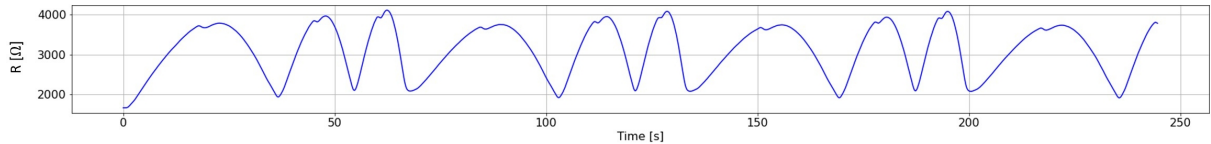


FIGURE 3.12: Resistance response from saw-tooth strain input Figure 3.11.

Hysteresis loops were used in Figure 3.13 to show resistance offset as a function of the strain-speed and simultaneously displaying the resistance hysteresis loops of different strain speeds.

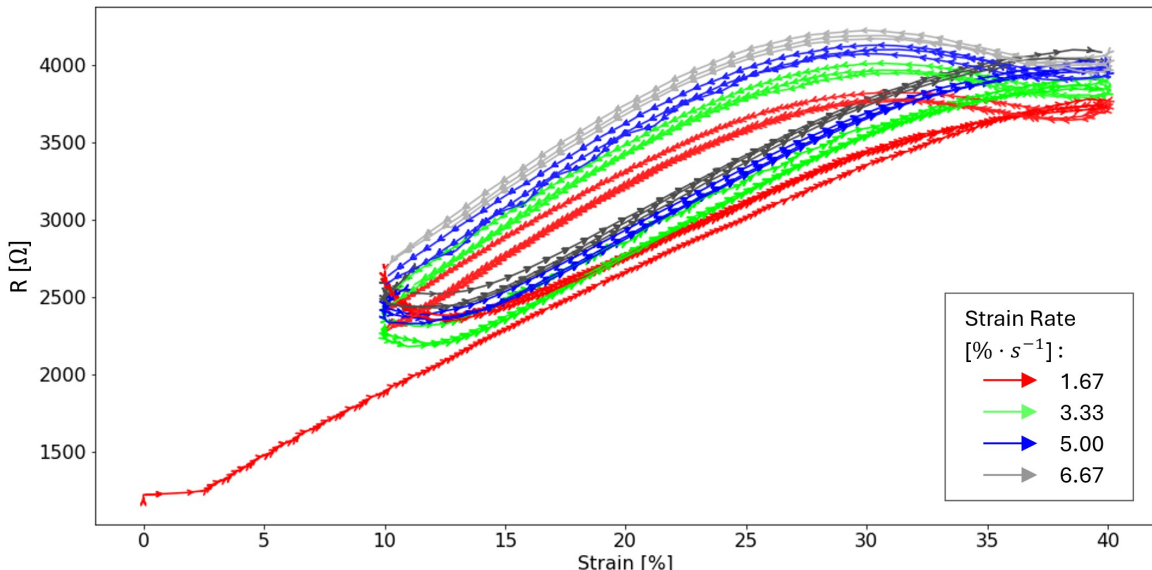


FIGURE 3.13: Resistance vs strain hysteresis loops from from a saw-tooth strain input.

The material was pre-strained to mitigate non-linear effects that may arise near 0% strain. Using the  $1.67 \text{ \%}\cdot\text{s}^{-1}$  strain-rate as a reference the average resistance offset of the other three strain-rates tested were calculated as shown in Table 3.1.

TABLE 3.1: Strain-rate dynamic resistance offset comparison. Using S1 as the reference resistance loop.

Strain-rate #	S1	S2	S3	S4
$\dot{\varepsilon} [\text{\%}\cdot\text{s}^{-1}]$	1.67	3.33	5.00	6.67
$\Delta R_{S1} [\text{\%}]$	0	+5.0	+8.3	+10.7

### 3.3.4 Falling Edge Strain-Rate-Resistance

A narrow peak in the measured resistance has been observed in the collected data during a falling edge. This peak is not present in the stress plot shown in Figure 3.14, hence is a proposed characteristic of electrical behaviour only as a function of strain as the change in resistance is assumed to be primarily due to conductive particle motion.

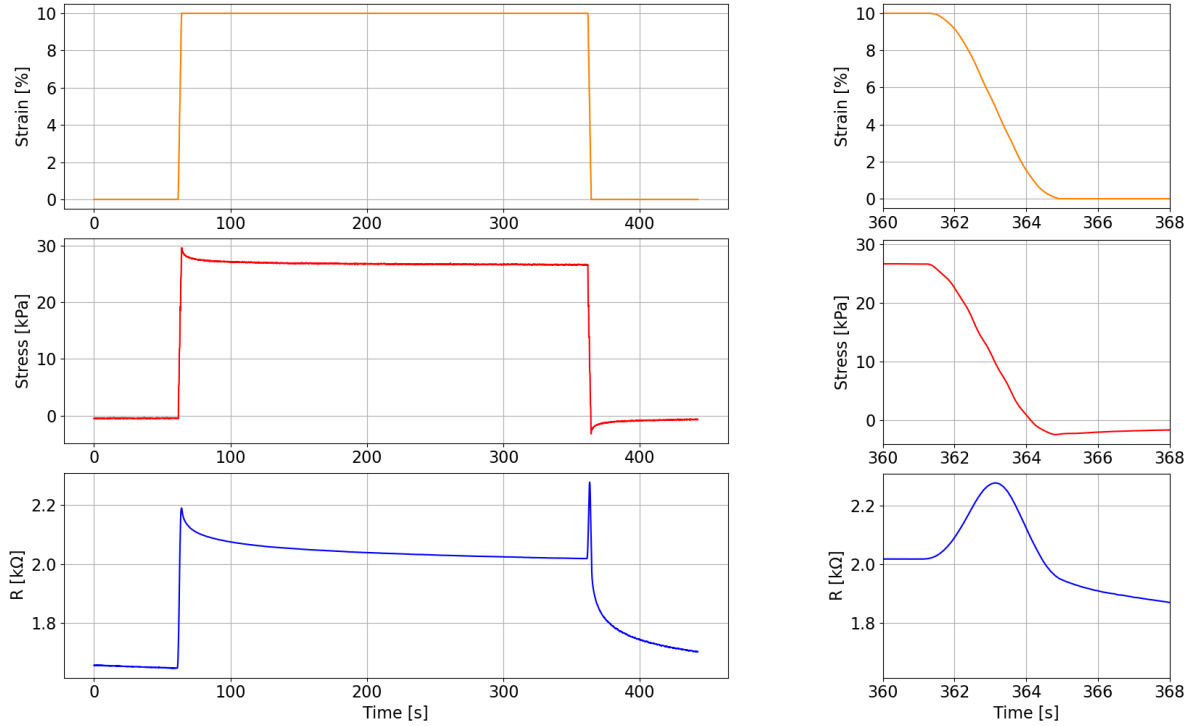


FIGURE 3.14: Left: Singular tensile strain pulse with resulting stress and resistance response.  
Right: Zoomed to highlight falling edge shoulder phenomena.

A parameter fit study has been completed to determine the resistance peak amplitude can be determined with a range of strain-rates. We can see a repeated phenomena in Figure 3.15 whereby the derivative of the resistance signal seems to be equal to the strain curve. The resistance peak curve,  $R_p$ , can be modelled with a second order polynomial. When differentiated, this peak gives a linear function in a similar form of the linear strain curve seen in Figure 3.15. Hence we form Equation 3.3 which relates resistance to strain as a function of time.

$$\frac{dR_p}{dt} = J(\varepsilon) \cdot t + c \quad (3.3)$$

where  $J$  is a function of strain,  $\varepsilon(t)$ , and  $c$  is an offset bias determined by the initial strain condition.

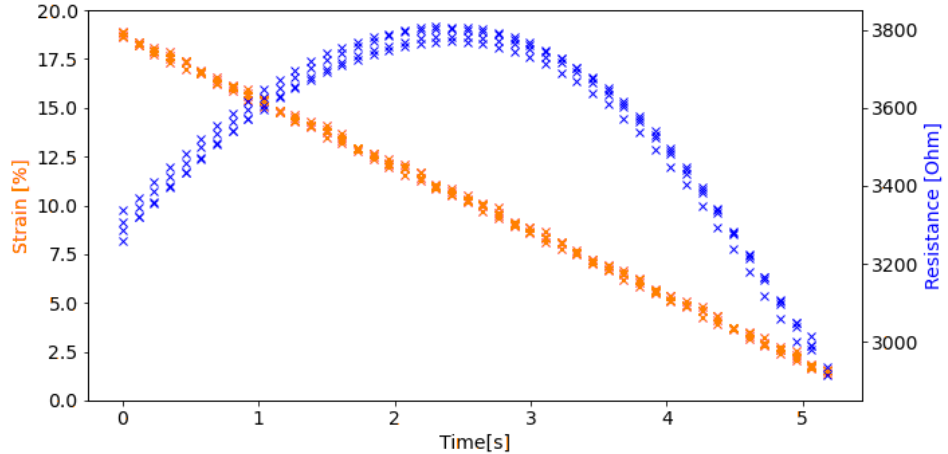


FIGURE 3.15: Strain-rate resistance relationship showing the specimen returning to a 0% tensile strain state from 20% at a strain-rate of  $3.33\%\cdot s^{-1}$  from four tests for a 7.5% CBSR specimen

To show the strain-rate resistance relationship, more strain pulse train tests of 20% strain were completed. Using 20% strain allowed observation of sufficient data points to observe a trend. The pulses had four repetitions with a range of strain-rates,  $\dot{\varepsilon}(t)$ , of 1.67, 3.33, 5.00, and  $6.67\%\cdot s^{-1}$ . Using a 7.5 w.t.% CBSR specimen we obtain a relationship that agrees with the strain resistance component equation 3.3. As  $\dot{\varepsilon}(t)$  increases through strain-rates in parallel with the magnitude of the resistance peak relative to the previous steady state of value resistance. Two formulae are fitting to the linear strain and resistance peak features given by Equations 3.4 and 3.5 respectively.

$$\varepsilon = A \cdot t + B \quad (3.4)$$

$$R_{peak} = C \cdot (t - D)^2 + E \quad (3.5)$$

The resulting plots fitting of the averaged data points for the strain and resistance peak curves are given in Figure 3.16.

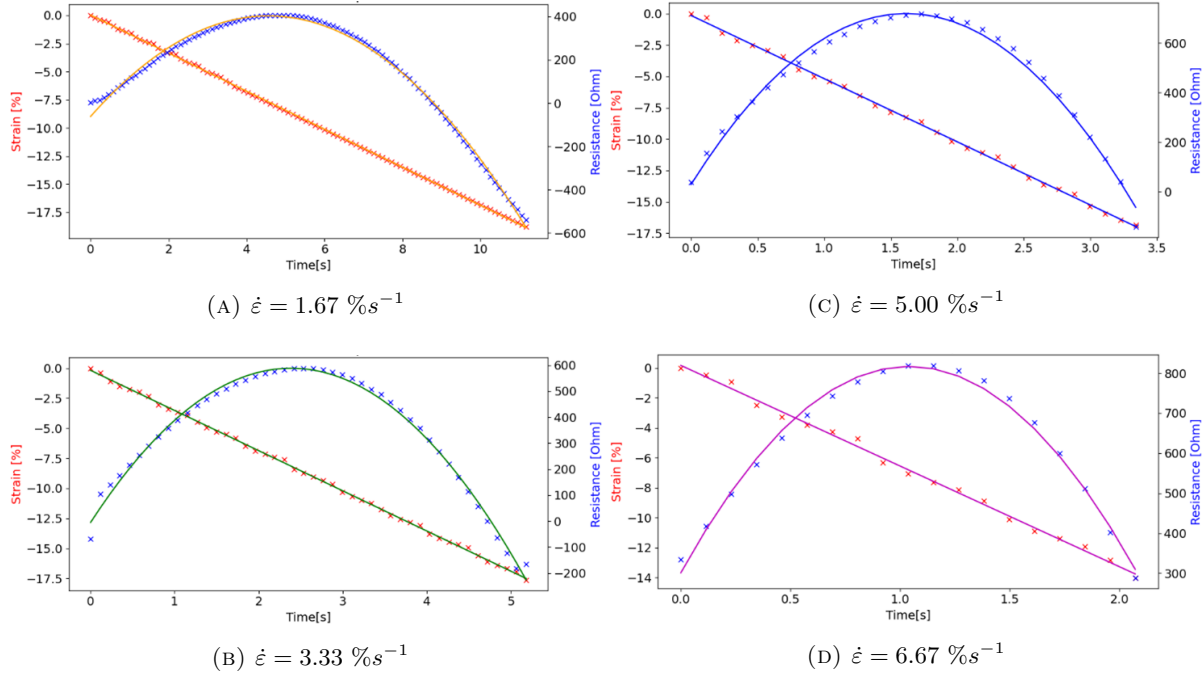


FIGURE 3.16: Fitting curves to a range of different tensile falling edge strain strain-rates.

TABLE 3.2: The fitted parameters for relationship between the specimen tensile strain-rate the resulting resistance peak for a strain signal falling edge.

Strain rate [%/s]	— 1.67	— 3.33	— 5.00	— 6.67
A ( $\times 10^3$ )	$-16.8 \pm 0.1$	$-33.40 \pm 0.02$	$-50.3 \pm 0.4$	$-66.8 \pm 0.4$
B ( $\times 10^3$ )	$-0.45 \pm 0.93$	$-0.69 \pm 1.20$	$-1.77 \pm 1.72$	$-0.13 \pm 2.15$
C	$-22.1 \pm 0.6$	$-103.0 \pm 2.3$	$-250.0 \pm 10.0$	$-479.0 \pm 32.9$
D	$4.58 \pm 0.02$	$2.37 \pm 0.02$	$1.60 \pm 0.06$	$1.12 \pm 0.05$
E	$403.0 \pm 13.5$	$587.0 \pm 23.5$	$712.0 \pm 7.19$	$809.0 \pm 26.5$

### 3.3.5 Resistive Relaxation Fitting

The initial model chosen to fit the stress and resistive relaxation data was the generalised Kelvin body model shown in Figure 3.1 with  $n = 3$  cascading elements using Equation 3.6 to fit the model. Fitting the data using Levenberg–Marquardt non-linear least square algorithm over 30 data sets showed an instability with the algorithm using this model. When feeding the previously fitted stress relaxation model parameters as initial conditions for the fitting of the next stress relaxation data set, the values of the parameters diverged exhibiting signs of overfitting. This divergence of the model parameters gave a large standard deviation showing the model was changing significantly each iteration of fitting. Hence a more simple model using Equation

3.1 with  $n = 2$  was used to fit the stress relaxation data to Equation 3.7 with lower standard deviation of the model constants. Conversely when the resistive relaxation model analogous to stress relaxation model, shown in Equation 3.8, was fitted to the resistive relaxation data there was a stable fit with an improved goodness of fit.

The decay time constants of the two models are different with the resistance having an longer overall decay which can clearly be seen in Figure 3.17. Below in stress relaxation models  $G_{1,2}(t)$ , shown in Equation 3.6 and 3.7, the constants  $a_{0-3}$  and  $\tau_{S1-S3}$  represent the components of magnitude and time decay of the stress relaxation, respectively.

$$G_1(t) = a_0 + a_1 e^{-t/\tau_{S1}} + a_2 \cdot e^{-t/\tau_{S2}} + a_3 \cdot e^{-t/\tau_{S3}} \quad (3.6)$$

$$G_2(t) = a_0 + a_1 \cdot e^{-t/\tau_{S1}} + a_2 \cdot e^{-t/\tau_{S2}} \quad (3.7)$$

Analogously for the resistive relaxation function  $H(t)$ , the constants  $b_{0-3}$  and  $\tau_{R1-R3}$  represent the components of magnitude and time decay of the resistive relaxation, respectively.

$$H(t) = b_0 + b_1 \cdot e^{-t/\tau_{R1}} + b_2 \cdot e^{-t/\tau_{R2}} + b_3 \cdot e^{t/\tau_{R3}} \quad (3.8)$$

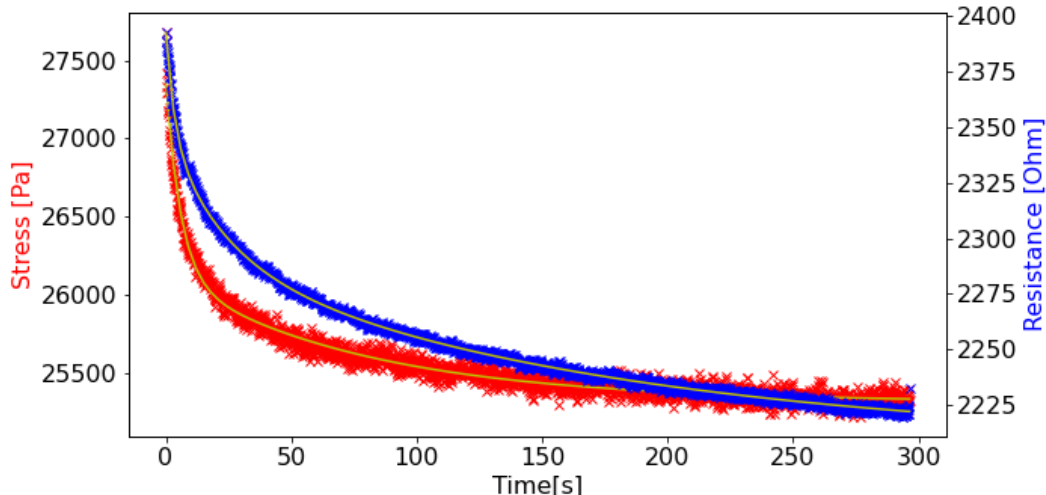


FIGURE 3.17: Comparing the relaxation decay time constants of stress and resistance for a 7.5 w.t.% CBSR composite after a 10% strain step input and fitting generalised Kelvin body models to each.

The mean magnitude and decay time constants for the resistance and stress relaxations using 30 relaxation periods to fit the models to are given in table 3.5.

TABLE 3.3: Fitted constants and their mean,  $\mu$ , standard deviation values for 0%, 7.5%, and 10% CBSR composite specimens using Equation 3.7.

### Stress Model Parameters

0 % CB Specimen	
Parameter	$\mu$
$a_0$	$20344 \pm 42$
$a_1$	$387 \pm 60$
$a_2$	$527 \pm 58$
$\tau_{S1}$	$72.1 \pm 23.5$
$\tau_{S2}$	$5.8 \pm 1.5$
7.5 w.t.% CB Specimen	
Parameter	$\mu$
$a_0$	$25363 \pm 33$
$a_1$	$802 \pm 43$
$a_2$	$1242 \pm 52$
$\tau_{S1}$	$71.0 \pm 9.5$
$\tau_{S2}$	$5.8 \pm 0.7$
10 w.t.% CB Specimen	
Parameter	$\mu$
$a_0$	$32303 \pm 165$
$a_1$	$1071 \pm 54$
$a_2$	$1649 \pm 47$
$\tau_{S1}$	$84.1 \pm 10.6$
$\tau_{S2}$	$6.5 \pm 0.7$

TABLE 3.4: Fitted constants and their mean,  $\mu$ , and standard deviation values for 0%, 7.5%, and 10% CBSR composite specimens using Equation 3.8.

<b>Resistance Model Parameters</b>	
7.5 w.t.% CB Specimen	
Parameter	$\mu$
$b_0$	$2154 \pm 52$
$b_1$	$81.1 \pm 5.4$
$b_2$	$56.4 \pm 3.7$
$b_3$	$42.2 \pm 3.4$
$\tau_{R1}$	$181.1 \pm 33.6$
$\tau_{R2}$	$22.8 \pm 3.8$
$\tau_{R3}$	$3.5 \pm 0.6$
10 w.t.% CB Specimen	
Parameter	$\mu$
$b_0$	$1650 \pm 97$
$b_1$	$55.2 \pm 8.9$
$b_2$	$77.4 \pm 12.2$
$b_3$	$38.4 \pm 9.5$
$\tau_{R1}$	$169.6 \pm 61.7$
$\tau_{R2}$	$21.9 \pm 9.7$
$\tau_{R3}$	$3.0 \pm 1.6$

### 3.3.6 Resistance-Stress Relationship

To display the non-linear relationship between the stress and calculated resistance within the material they are plotted against each other over 30 sequential relaxation periods of 300s similar to the relaxation shown in Figure 3.17. The non-linear relationship between stress and resistance changes over time for each relaxation as shown in Figure 3.18, where the data for the first relaxation is displayed in green and the last relaxation in blue.

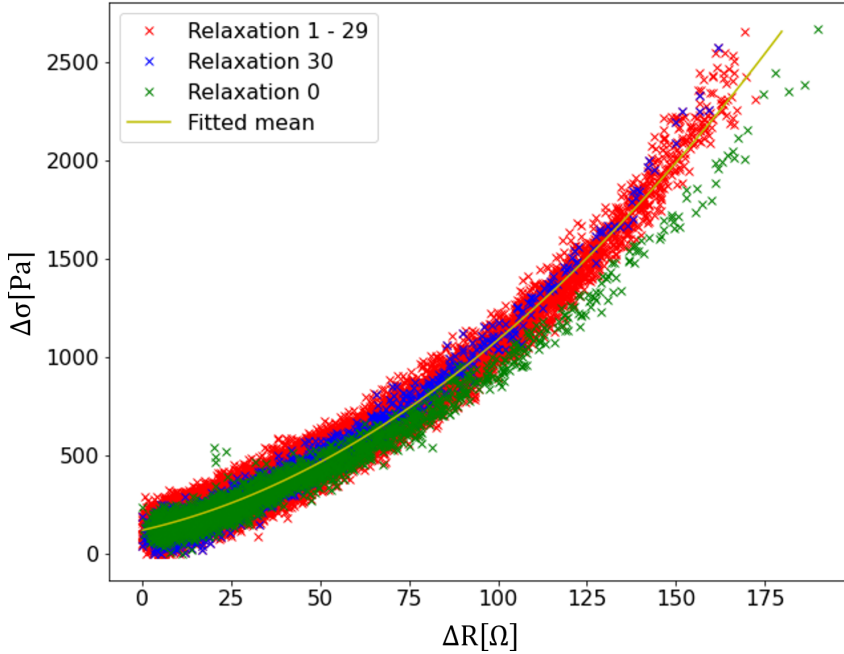


FIGURE 3.18: Comparing resistance and stress relaxation data against each other occurring during 30 pulses of a 10% strain step input for a 7.5 w.t.% CBSR composite

The stress-resistive relaxation data was fitted to a generic second order polynomial of the form,

$$\sigma(R) = aR^2 + bR + c \quad (3.9)$$

where  $\sigma$  is stress,  $R$  is the calculated resistance. When fit to the latter 15 cycles of a 30 cycle 10% strain pulse train of stress relaxation data we get the constant values for  $a$ ,  $b$  and  $c$ .

TABLE 3.5: Fitted constants and their mean,  $\mu$ , standard deviation,  $\sigma$ , and coefficient of variation,  $CV$ , values for 7.5%, and 10% CBSR composite specimens using Equation 3.9

#### 7.5 w.t.% CB Specimen

Parameter	$\mu$	
$a$	0.055	0.006
$b$	4.15	1.06
$c$	121.8	16.3

#### 10 w.t.% CB Specimen

Parameter	$\mu$	
$a$	0.098	0.007
$b$	6.37	0.76
$c$	155.8	38.8

### 3.4 Discussion

This work has successfully uncovered several mathematical relationships between stress, strain, and resistance. The repeatability has also been displayed graphically and calculating the variance of the fitted models given. This section analyses the results given in the previous sections and highlights limitations of the experiments given.

#### 3.4.1 Fabrication

In this work, mixing has been performed using a planetary mixer. It has been shown in other works [67, 225] that other mixing methods, such as using a sonication bath and the addition of solvents, can yield more homogeneous particle dispersion. A higher degree of CB particle dispersion has also been shown to alter the viscoelastic creep properties [225], and is therefore likely to affect the time constant of resistance.

Composite imaging and experimentation showed the existence of a thin insulative film on the composite surface inhibiting the use of surface electrodes to give a good electrical connection to the percolated CB network. The imaging also showed the existence of voids in the micron scale which contribute towards the material viscoelasticity. The optimisation of particle dispersion and investigation into the effects of void dispersion and sizing could give insight into maximising the material gauge factor.

When characterising the reference pure SR material, the elastic modulus was larger than the 186.2 kPa elastic modulus specified by the manufacturer, likely due to the heat assisted curing process used [220].

#### 3.4.2 Quasi-static Tensile Resistance-Strain

The quasi-static linear model given show promise for using the composite CBSR material for applications requiring a low frequency response sensor. This also gives a good steady-state part of a more complex model which includes the non-linear and time-dependent dynamics.

#### 3.4.3 Dynamic Resistance-Strain-Rate Response

Increasing strain-rates were shown to increase the offsets in resistance over a range of strains as shown in Figure 3.13. Showing the existence of a repeatable relationship between strain-rate

and resistance, for constant strain rates. For strain acceleration different phenomena arose, such as the shoulder phenomena.

### 3.4.4 Falling Edge Strain-Rate-Resistance

A 'falling edge' resistance shoulder phenomena was observed and is clearly seen in Figures 3.12 and 3.14. This is a result of a change in strain rate. The amplitude of this peak was shown to increase with an increasing change in strain-rate from a steady state strain. The shoulder phenomena may exist on the rising edge of the strain adding to the resistive relaxation response however this was not easily distinguishable. In previous literature, the effects of the strain-rate and sudden change in strain-rate on apparent resistance of the CBSR material has not been modelled or shown. Another characteristic of the falling edge shoulder phenomena is the apparent positive correlation between the strain magnitude prior to the falling edge and the amplitude of the shoulder phenomena, as shown below in Appendix A. Another characteristic of note is that the shoulder phenomena is almost not present on a falling edge that goes from a tensile (positive) strain to a small compressive (negative) strain which is also shown in Figure A.1.

### 3.4.5 Resistive Relaxation Fitting

The generalised Kelvin model has been applied to predict the stress relaxation of the CBSR composite and analogously the resistive relaxation seen for a positive strain step input. The data gathered show that the stress relaxation time constant values decrease with an increasing CB percentage, indicating that all constants in Equations 3.8 and 3.7 are also functions of CB percentage. The repeatability of this stress relaxation for strain step inputs shows promise to use of this material in controlled environments, such as factory production lines, where there are known periodic strain step inputs. An application for the resistive relaxation decay time characterisation could be for timer with a soft robotic system.

One aim of this work was to prove the hypothesis that the stress relaxation time constant is different to that of the observed resistive relaxation and able to be modelled mathematically. The apparent difference in time constants and the fitting of the data to two different equations show that the stress relaxation is not linearly related to the resistive relaxation shown clearly in Figure 3.17.

### 3.4.6 Resistance-Stress Relationship

A hypothesis for the resistive relaxation phenomena is that it may be correlated to the stress relaxation [207]. This work found that the relationship between the two variables, resistance and stress, during their concurrent relaxation events was non-linear. This non-linearity was found to have a good fit to a second order polynomial as shown in Figure 3.18. The Mullin's effect was evident in the results and a time-dependence where the concavity of the polynomial fitted increased after the first strain pulse. A physical explanation behind the second order relationship between stress and strain relaxation could be due to strain dependence of the elastomer dielectric constant and hence capacitance as shown in literature [226, 227].

### 3.4.7 Viscoelasticity

The hysteresis loop seen in the 10 w.t.% CB sample has a larger hysteresis loop showing that there is increased viscous/damping compared with the other two specimens percentages of CB. The pure SR specimen had no discernible hysteresis from the data as shown in Figure 3.9 and with second order polynomials fitted in Figure A.4. The hysteresis loop area is larger in the higher percentage CB composite indicating a higher degree of particle friction and effective viscosity within the material. The difference in hysteresis and hence viscoelastic properties, across the specimens leads to different stress relaxation properties across the three different percentages of CB composite materials in this work.

### 3.4.8 Repeatability

The resistive relaxation model must be predictable over many strain cycles for use within high-stretch strain sensor applications. If the resistive relaxation changes over time this needs to be modelled. Each test sequence showed that there was a downward trend in the calculated magnitude of resistance for each pulse over time.

The physical phenomena driving this downward trend in resistance magnitude was theorised to have two possible causes. The first cause being; the accumulation of charge within material over time generated by current source, due to the CBSR material having an RC-network-like behaviour. The second potential cause being; the gradual alignment of the CB particle network due to the electrostatic attraction of CB chains. This could be tested by increasing the current used and observing the gradient of the downward trend.

The charging theory was mitigated by using an alternating polarity measurement technique. The reversible current source was switched at 10 Hz dampedened this downward trend, however the downward trend in resistance was still observed as shown in Figure 3.19. An example of an experiment with the previous non-switched DC current is shown in Appendix Figures A.2 and A.3 for comparison.

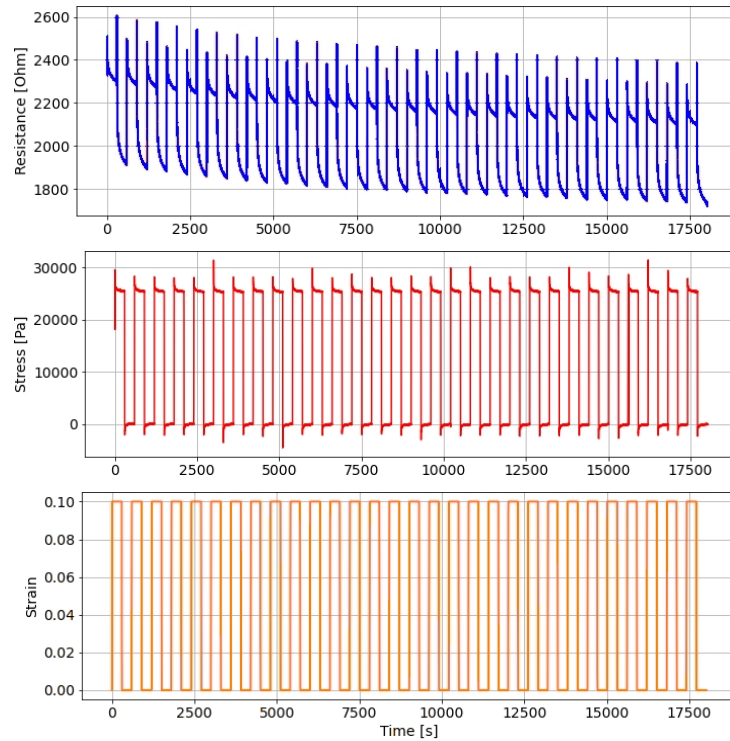


FIGURE 3.19: A typical test sequence of a 30 pulse strain train recording the calculated resistance and stress of a 7.5 w.t.% CBSR composite

### 3.4.9 Further Discussion and Future Work

An encompassing model for translating resistance samples to a stress value can be seen in Figure 3.20. The two main phenomena which have shown to most significantly deviate from the quasi-static model being the resistive relaxation and the shoulder peak phenomena.

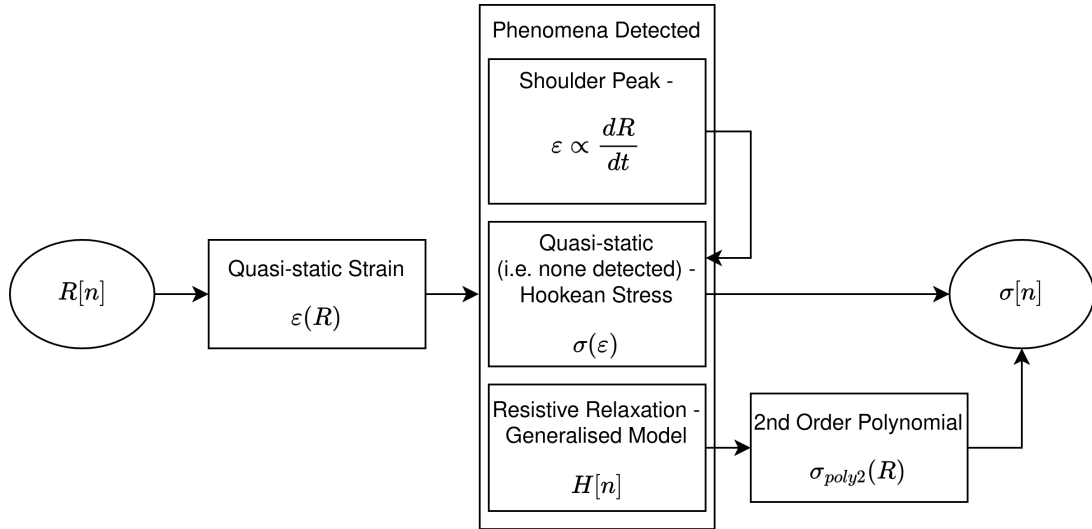


FIGURE 3.20: Model architecture for translating between CPEC resistance and the material stress and strain responses.

It must be noted that for fitting the resistive relaxation, stress-resistive relaxation and the falling edge phenomena the data was zeroed on the x and y axes for ease of the regression algorithm fitting.

A sufficiently high current source value was required to ensure a SNR that would not hinder data analysis. There seemed to be a wetting current threshold where the SNR dropped as shown by the  $20\ \mu\text{A}$  resistance pulse response in Figure 3.21.

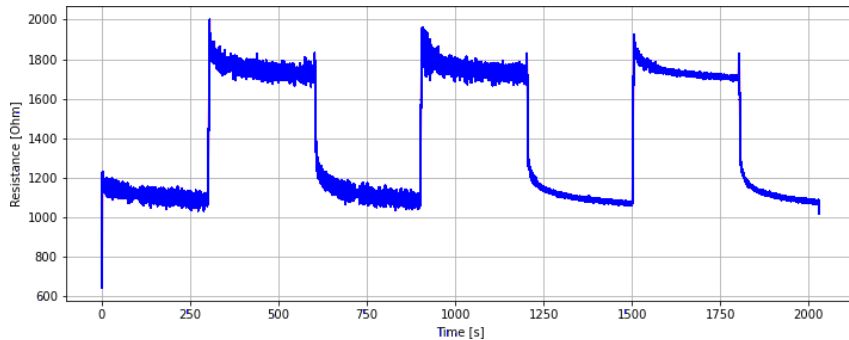


FIGURE 3.21: Three identical 15% strain pulses at three different current values ,in order,  $10\ \mu\text{A}$ ,  $15\ \mu\text{A}$ , and  $20\ \mu\text{A}$ .

A limitation of using this material as a strain sensor is the non-linearity of the material above a certain strain value, at which the composite's resistivity diverges towards a highly insulative value within the giga-ohms range. This non-linear behaviour of CBSR can be used as a mechanically activated switching device [200]. If modelled, this non-linearity could extend the range of strains that can be measured.

The consideration of temperature and strain history [16] could be used in further research to characterise a CBSR-based strain sensor for a range of application environments.

Future work includes creating a model that incorporates all of the behaviours shown in this work so that an accurate inverse model can be created to use the material as a strain sensor. To capture all of these phenomena models that can capture and recreate time-dependent phenomena such as recurrent neural networks (RNNs) could be used.

### 3.5 Conclusions

The CBSR material used in this work provided exaggerated non-linear effects compared to literature where these non-ideal phenomena are often quashed and ignored. The relationships discussed in this work could be used to define a CBSR-based strain sensor models and show the expected behaviours in the composite material for different strain application scenarios.

In order to improve the accuracy of dynamic strain measurements with CBSR composites a stress and analogous resistive relaxation model was formed. The generalised Kelvin model, Equation 3.7 was used to fit to the stress relaxation data for three specimen with CB weight percentages of 0, 7.5% and 10%. The variation in the fitted stress relaxation parameters was higher than the resistive relaxation parameters. All of the stress relaxation model parameters increased with increasing weight percentage of CB, indicating an increase in viscoelasticity. The resistive relaxation time constant and offset parameters both decreased with increasing CB wt%. However the change in these parameters is not large and more experimentation with two CB weight percentages would be required to create a model of how the relaxation changes with CB wt%. The standard deviation of parameters increased with increasing CB wt%.

With the models developed we have shown that the apparent resistive relaxation can be modelled, which will enable more accurate estimation of dynamic strain when these materials are applied as sensors.

Many repeatable behaviours of the CBSR material have been found in this chapter which have not been elucidated in previous literature. Mathematical relationships between parameters stress, strain, and resistance have been developed. These mathematical relationships may be related to physical phenomena occurring within the viscoelastic material, however this work has not found a generalised model that can be inverted to accurately obtain a stress or strain given a resistance input. Future work will look into non-linear time series modelling methods such as,

physics-informed deep neural operator networks (PINNs), recurrent neural networks (RNNs) and autoregressive-based models like ARIMA.

This chapter establishes a foundation for understanding the electromechanical characteristics of the CPEC material, setting the stage for further development of the material in a sensing and actuation devices as displayed subsequent chapters. Through the investigation of this novel sensor and actuator technology, specific behaviours given here will be investigated to further understand the potential of the material.



## **Chapter 4**

# **An Electrical Impedance Tomography Based Soft Pressure Mapping Sensor**

### **Overview**

To accomplish pressure mapping with comparable properties to human skin, a novel conductive particle elastomer based sensor device has been created. Using electrical impedance tomography (EIT) to drive a pressure mapping sensor device shows great potential, due to the customisability of the sensing domain and the non-invasive nature of the boundary electrodes required. To translate this research device into a commercial application the performance of such an EIT-based sensor must be quantifiable and repeatable, to be further optimised. In this work a series of experiments on a carbon black silicone rubber sensing domain were repeated for various load locations, strains, and carbon black percentages. Capturing this data gave insight into the how the sensing domain performs over time and captured the transient events limiting the sensor. Metrics were determined to quantify the sensor's spatial resolution. A quasi-static conductance-force model of the material was developed with an accuracy of  $\pm 0.78$  N. One important metric is temporal resolution, as it is the least quantified performance metric in literature, however can be the most important for some applications. For the sensor domains tested, average settling times of between 19.0 - 44.5 s and 22.5 - 36.0 s were determined for 8 and 9 wt% CBSR samples. A series of randomised test loads gave similar spatial performance results to the structured

experiments. This sensor platform shows promise for future applications, with further materials development and modelling the rise of a biomimetic pressure sensitive skin is imminent.

<sup>1</sup>

## 4.1 Introduction

Approximately 1 billion years after the first animals developed mechanosensation [228], evolution has allowed humans to detect pressure through the use of many mechanoreceptors lying within the skin and other organ tissue. As mentioned in the Literature Review, two mechanoreceptors which are desirable to mimic human touch are Merkel's disks and Meissner's corpuscles [229]. Both of which are ubiquitous in human hands and lips for high spatial resolution, low pressure and low frequency touch/pressure events [230]. These mechanoreceptors in a human hand enable object identification and closed loop fine motor control.

With the creation of pressure mapping technology which has the similar soft mechanical properties and sensing qualities to that of human skin, many applications requiring dexterous human-like touch could be directly fulfilled. This work presents characterisation of a soft mapping pressure sensor which utilises electrical impedance tomography to map resistance changes and subsequently stress changes throughout a soft material surface.

The number of applications that require 2D pressure sensing using a soft surface is extensive. Such applications include: robotic gripper object detection, medical mattresses and cushions, limb prostheses and wearable robotics, sport equipment, smart furniture, and rehabilitation devices. The following characteristics are desirable for each of these applications: force sensitivity, low toxicity, cost-effectiveness, repeatability, and high elasticity. In this work, a system showcasing each of these desirable characteristics has been developed.

The sensor platform utilises a piezoresistive nanoparticle elastomer composite (PNEC) in a thin sheet topology to create an artificial sensitive skin. This artificial skin is composed of a highly elastic piezoresistive material, and its deformation can be identified through electrical impedance tomography (EIT) for the reconstruction of the material resistivity image. Using 16 boundary electrodes, EIT facilitates the mapping of applied forces on this monolithic homogeneous material. Subsequently, an inverse model is applied to estimate compressive force loads on the material.

---

<sup>1</sup>Content from this chapter has been taken from a publication in Sensors and Actuators A: Physical [17]

Understanding the electromechanical properties of the PNEC material used in this work is essential for creating an accurate dynamic sensor. When elastomeric composites with conductive particles, such as the PNEC, exhibit viscoelasticity, the degree of hysteresis varies based on the constituents of the composite material [41]. This viscoelasticity is a major limiting factor when using PNECs for EIT-based pressure sensing due to the poor frequency response introduced by the large transient effects seen in the material. In this work these transient phenomena are captured and characterised for 1D and 2D compressive load cases.

Various methods and topologies of 2D pressure mapping sensors can be employed for a 2D resistivity measurement. However, many of these methods involve intrusive and intricate electrode placement within the material domain [59, 90, 194, 231–233]. Since the materials utilised in this study are soft, the utilisation of relatively rigid metal electrodes distributed throughout the material would significantly alter the material’s electromechanical deformation response. This necessitates use of the non-invasive method imaging method EIT.

#### 4.1.1 Related Work

Various methods and devices have been designed for localising loads in two-dimensions on a soft domain. A limiting factor found with non-EIT based methods of pressure mapping were the size of discretely sensed regions, also known as sensels. Often these sensels are limited by factors in the fabrication process and the bulk of electrode wires required. This bulk is exemplified high electrode-to-sensel ratio. Example load mapping technology include, optical [11, 93, 94], piezoresistive [90–92], capacitive [60], and magnetic [61].

Other attempts at creating artificial sensitive skins using EIT have been shown in a review by Silvera-Tawil et al. [194]. This review provides adequate evidence to display a growing interest in the field; however, there is still no commercial EIT-based pressure sensor that is comparable in terms of spatial and temporal resolution, to commercially available non-EIT-based 2D pressure sensors. One of the earliest applications of EIT to an elastic piezoresistive domain was achieved by Knight and Lipczynski [234] in 1990. Since this application, several other similar systems have been created using EIT and similar pressure sensitive fabrics or elastomeric materials[65, 185, 194, 235–238]. A comparison of similar devices is given in Appendix B.1. None of these researched devices focus on using a material with similar softness, and quantify the stress data captured in real-time like this work. All of the referenced ‘EIT’ soft sensors employ electrical resistivity tomography (ERT), however, the term ERT is most commonly associated

with geological subsurface imaging applications, henceforth, EIT is be used in place of ERT in this work.

## 4.2 Methodology

To ensure the applicability of Electrical Impedance Tomography (EIT) with a soft PNEC sample, we fabricated the material for testing. The material needed to adhere to specific requirements: highly elastic, high yield strength, low resistivity, high piezoresistivity, non-toxic, and be a low Shore hardness of 5A - 25A akin to human soft tissue [43, 194, 239, 240]. Additionally, a system of devices was devised to facilitate EIT measurements which concurrently captured force, strain, and timestamps for each measurement. Lastly, to evaluate the sensor's suitability for diverse applications, spatial, temporal, and localised force sensing performance metrics were quantified.

### 4.2.1 Fabrication

The fabrication of the piezoresistive composite materials, as described and justified in previous chapter and in our previous work [41], involved dispersing 8 and 9 wt% of carbon black (CB) nanoparticles in a silicone rubber (SR) matrix. Because of the difference in fabrication processes seen in literature [241, 242] and degree of dispersion generating variability in the percolation, an iterative trial and error approach using the starting point found in literature was used to get 8 wt % and 9 wt % values for CB in SR. Within this range the material was sufficiently conductive while maintaining mechanical strength through sufficient elastomeric cross-linking. Previous research indicates that there is a weight percentage at which the gauge-factor/piezoresistivity is at a maximum within a similar range used in this work [243, 244]. The composite, designated as the domain under test (DUT), was created using 50 nm average diameter XC 72R CB nanoparticles (Cabot, Alpharetta, USA) in a Dragon Skin 10 NV silicone rubber matrix (SmoothOn, Macungie, USA). Homogeneous dispersion was ensured using an ARV-310 vacuum planetary mixer (Thinky, Tokyo, Japan).

TABLE 4.1: DUT mechanical characteristics and electrical characteristics

Sample	CB wt [%]	$R_{int}$ [kΩ]	E [kPa]
SR	0	$> 1 \times 10^9$	186.16
CBSR	8	$18.1 \pm 9.8$	132.5
CBSR	9	$4.5 \pm 1.4$	98.1

The inter-electrode resistance,  $R_{int}$ , was measured to give an indication of material homogeneity. Elastic modulus,  $E$ , was calculated from several stress-strain cycles between 0 and 30%. The  $R_{int}$  and  $E$  are given in Table 4.1. A CBSR sample developed showing the circular sensitive region with boundary pin electrodes is shown in Figure 4.1.

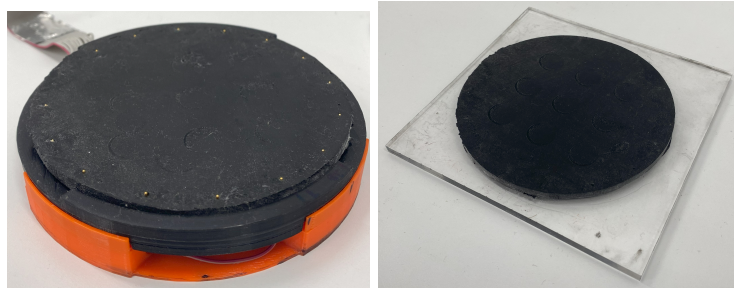


FIGURE 4.1: Left: Example of a CBSR sensing domain with gold pin electrodes penetrating material surface around the boundary on top of the rigid sensor holder (orange/black). Right: CBSR sensing domain on an acrylic square.

#### 4.2.1.1 Localised Stress Testing

Quantitative results are required for spatial quantification of the EIT image reconstructions. A cylindrical force applicator head with a diameter of 13 mm and area of 133 mm<sup>2</sup> was used to apply the nine compressive loads shown in Figure 6.8.

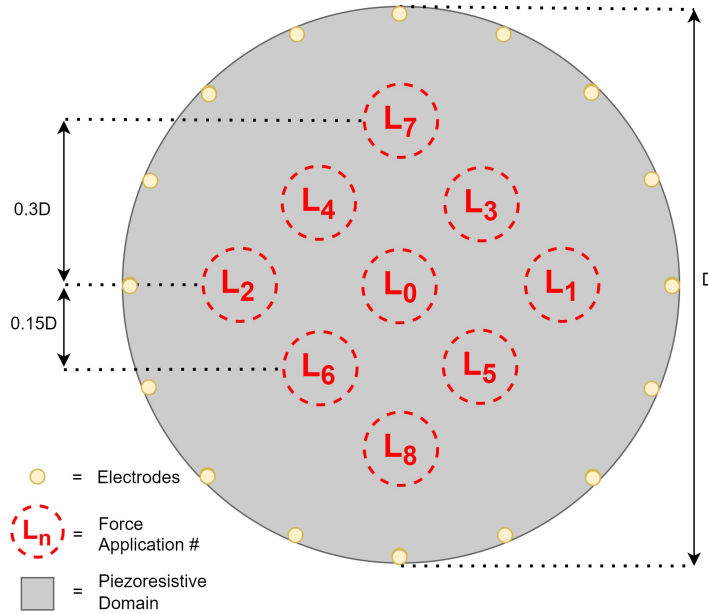


FIGURE 4.2: Load application areas used for compressive stress testing shown numerically in order of application.

#### 4.2.1.2 EIT Measurement

EIT data acquisition usually requires a current or voltage source, one or multiple voltmeters, and a switching device. When integrating a mechanical pressure validation system a Cartesian force applicator (CFA) and is also required to capture data simultaneously. The system architecture and DUT electrical connections are shown in Figure 4.3 and 4.4. This work uses a 2634b source measure unit (SMU) (Keithley, Solon, USA) as a current source and voltage measurement unit for EIT data acquisition. In the following chapter the SMU is miniaturised to a specialised PCB for portable, battery-powered applications.

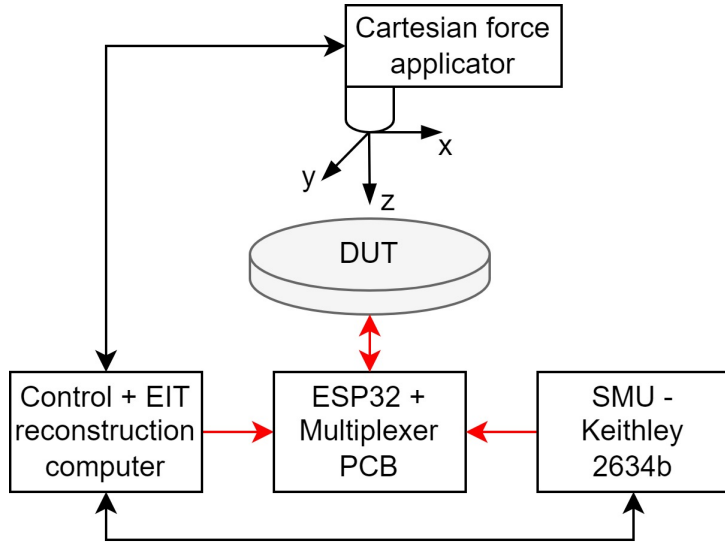


FIGURE 4.3: Architecture of the Cartesian force applicator setup with red arrows being analogue power lines and black arrows being digital data lines

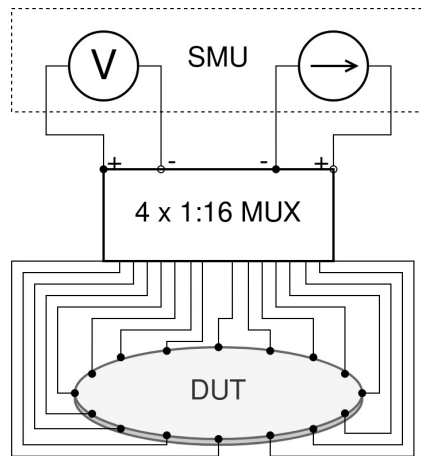


FIGURE 4.4: Wiring diagram for sensor connection to 4:16 multiplexer and SMU

#### 4.2.2 1D Material Characterisation

Prior to utilising CBSR materials as a 2D pressure sensor, the piezoresistive properties were analysed in one dimension to establish resistance-stress/strain relationships for each CBSR sample. This 1D material testing was conducted using the Cartesian force applicator in conjunction with the SMU. The stress-strain relationship of the material was determined in previous work and shown in Table 4.1. The 1D analysis gave quantitative insight into the material resistivity response to strain in different known areas of the Domain Under Test (DUT) and aligned with the phenomena characterised in the previous chapter, Section 3.3.2.

#### 4.2.2.1 Quasi-static Piezoresistivity

To determine the piezoresistivity or gauge factor of the material, pin electrodes were pierced through the CBSR samples so that the pin electrodes were parallel and at a distance of 35 mm from each other. The pins were 2.5 mm from each end of the sample. A 2634b SMU was used to apply a constant current of 1 mA between the two pin electrodes while ten compressive loading cycles were applied. The ten loading cycles were applied at strains of 5, 10, 15, 20, 25, and 30%, with a duty cycle of 50% and period of 120 s. Loads were applied using the Cartesian force applicator with a 20 mm x 20 mm square flat force applicator head. The strain rate was kept at a constant  $16.67\% \cdot s^{-1}$  to dampen the amplitude of transient effects as proven in previous work [41].

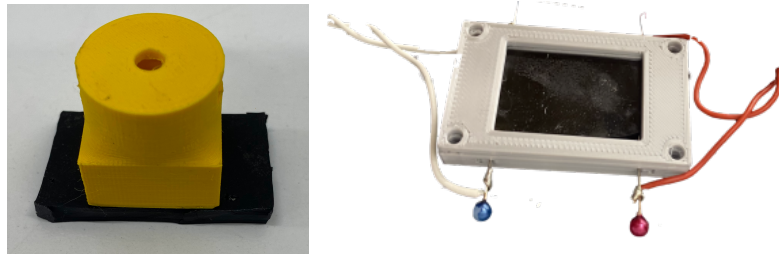


FIGURE 4.5: Compressive loading force applicator. Left: Load applicator on sample CBSR material. Right: Pin electrode jig for sample CBSR material compressive loading test.

When using this material to estimate stress based on resistance, any transient effects that are not correlated between resistance and stress must be accounted for. To obtain a stress reading from this PNEC CBSR material using the quasi-static model given in Equations 4.1 and 4.2, transient events were ignored, so only the steady-state conductance of the material was utilised.

$$\frac{\Delta\rho}{\rho_0} = \alpha_\sigma\sigma + \beta_\sigma \quad (4.1)$$

$$\frac{\Delta\rho}{\rho_0} = \alpha_\varepsilon\varepsilon + \beta_\varepsilon \quad (4.2)$$

Where  $\alpha$  and  $\beta$  are the linear fit parameters,  $\sigma$  is the compressive stress,  $\varepsilon$  is the strain,  $\Delta\rho$  is the change in conductance, and  $\rho_0$  is the original material conductance.

#### 4.2.2.2 Transient Piezoresistivity

There are two main piezoresistive events that occur during these compressive stress pulse response experiments. They are the compressive loading and unloading transients. Both of which

result in stress relaxation and resistance relaxation behaviour until a steady-state resistance is reached. The stress relaxation can be approximated by a generalised Kelvin linear viscoelastic model [245] as shown in the previous chapter Section 3.3.5. A two component model was found to fit all curves without overfitting, the relaxation model from a step input is given in Equation 4.3.

$$G_2(t) = a_0 + a_1 e^{-t/\tau_1} + a_2 e^{-t/\tau_2} \quad (4.3)$$

Where  $G_2(t)$  is the stress relaxation function,  $a_0$  is the relaxation offset,  $a_1$  &  $a_2$  are the magnitude weightings for each time constant  $\tau_1$  &  $\tau_2$ . Equation 4.3 derived from the generalised Kelvin viscoelastic model was used analogously for the resistance relaxation. To ensure repeatability of the experiment the ten loading and unloading events were fitted using equation 4.3 to the each relaxation, then the  $R^2$  goodness of fit was compared for all of the relaxations.

An important temporal characteristic of this system is the settling time,  $t_s$ , given a strain step input. In this system the resistance step response settling time was the time taken to reach and stay within a specified tolerance about final steady-state resistance, given a strain step input. The tolerance chosen is about the steady state was  $\pm 15\%$ .

#### 4.2.3 Sensor Performance Metrics

To ensure that the resistance/conductance image reconstructions which will form stress maps are valid solutions, the quality of the reconstructions needs to be quantified computationally. The purpose of this section is to describe various metrics used for sensor validation. These metrics measure the spatial performance, temporal performance, and localised force sensing performance. Many of the spatial and temporal performance metrics have been taken and adapted from Adler et al. [193] and their GREIT (Graz consensus Reconstruction algorithm for EIT) performance metrics.

##### 4.2.3.1 Pre-processing

To ascertain the occurrence of a piezoresistive event in the material, it is necessary to identify a change in resistivity that surpasses the noise floor level. This precaution is taken to differentiate between a stress compression event and potential noise artefacts. A threshold was established to eliminate the noise floor, thereby isolating the loading signal and any noise or artefacts generated by the loading signal(s).

A second threshold filter was implemented to compensate for the regularisation of the reconstruction using a percentage of the largest peak observed in the sensor image domain. The percentage threshold value used in previous work has been 25, 50, 60, 70, 75% of the maximum domain amplitude [193–195]. In this work percentage threshold masking have been applied for comparison. To validate the best percentage threshold, these thresholds were completed for a CBSR 8 and 9 wt% PNEC under nine successive loading events comparing the mean of the three main performance metrics given in Section 4.2.3.2. After these threshold masks have been applied to the 2D EIT images, blob(s) are observed as the sensed regions-of-interest. In this work the term ‘blob’ refers to an amorphous 2D shape made of several aggregated finite mesh elements. These blobs are usually observed after percentage threshold masking of an EIT image reconstruction.

#### 4.2.3.2 Spatial Performance

The three main metrics of spatial performance are the centroid or centre of ‘mass’ error,  $E_{CoM}$ , the detected area overlap  $A_{OL}$  value, and the fit of the detected blob relative to the force input, the shape distortion,  $SD$ .

The  $E_{CoM}$  was found using:

$$E_{CoM} = \sum_i^{N_b} e_{CoM_i} \times \frac{e_i}{e_{total}} \quad (4.4)$$

Where  $N_b$  is the number of elements in the threshold masked blob,  $e_{CoM_i}$  is each individual element centroid,  $e_i$  is the  $i^{th}$  blob element resistance value and  $e_{total}$  is the sum of all of the blob element resistance values. This equation can be easily be inverted for images containing conductance elements in place of resistance elements. The nearer the  $E_{CoM}$  value is to zero, the better the reconstruction in regards to localising the sensed region.

The  $A_{OL}$  was found using:

$$A_{OL} = 100 \times \left[ \frac{\left( \sum_i^{N_b} A_{e_i} \right)}{A_{FA}} + \frac{\left( \sum_i^{N_b} A_{e_i} \right)}{A_b} \right] / 2 : e_{CoM_i} \in \Omega_{FA} \quad (4.5)$$

Where  $A_{e_i}$  is the area of an element and  $\Omega_{FA}$  is the domain of the force applicator area.  $A_{FA}$  and  $A_b$  are the areas of the force applicator and sensed region respectively. The closer the  $A_{OL}$  is to 100%, the more overlap there is between the estimated and actual load application.

The  $SD$  was found using:

$$SD = \left[ \sum_j^{N_p} (\|F_{CoM} - P_j\|_2 - r_{FA})^2 \right] / N_p : P_j \in L_b \quad (4.6)$$

Where  $N_p$  is the number of mesh nodes on the perimeter of the blob,  $F_{CoM}$  is the force applicator centre of mass (CoM) coordinates,  $P_j$  is a node in the set of blob perimetral nodes,  $L_b$ , and  $r_{FA}$  is the radius of the force applicator head. The  $SD$  is essentially the mean square error of the force applicator perimeter and sensed region perimeter taken radially from the force applicator centroid.

#### 4.2.3.3 Temporal Performance

A core problem with using soft PNECs is the temporal resolution they can provide can be limited by the viscoelasticity in the material and how it interacts with the conductive network in the material. This section provides insight into how to determine the frequency response of the material, by observing the relaxation settling time of the material. The maximum time taken to reach a steady-state resistance after a stress event dictates the frequency at which the material can sense stress events. To determine the time taken to reach a steady-state, a variety of compressive stresses and strains at the loading locations,  $L_0-L_8$ , of each DUT are observed.

To determine whether the resistance relaxation observed in the 1D case matches the relaxation of the reconstruction in 2D, the 1D and 2D relaxation settling times were compared to validate whether similar frequency responses were being observed. The EIT measurement equipment was designed such that the reconstruction frequency of 0.4 Hz can capture these transient events observed triggered in the CBSR samples, which are typically in the order of tens of seconds.

From the blob localisation described in section 4.2.3.2 the resistance relaxation data was extracted by plotting the sum of the blob resistance. Similar to the 1D case, the relaxations for stress loading, resistance loading, and resistance unloading scenarios are captured and compared for each CBSR with CB weight percentages of 8 and 9 wt%. The blob resistance relaxation was compared to relaxation deduced from the total image domain resistance to ensure that the only the transient event from the area being loaded was being observed.

#### 4.2.3.4 Localised Force Sensing Performance

As discussed in Section 4.2.2.1, a quasi-static function, Equation 4.1, has been generated that gives a stress based on 1D steady-state conductance measurements. This quasi-static function was applied to the DUT 2D reconstruction to obtain a stress map of the material. To determine the minimum detectable stress of the sensor the conductance noise floor values were input into the linear quasi-static Equation 4.1.

To obtain the stress estimate,  $\hat{\sigma}_j$  and hence force estimate given a known input stress and force, the following steps were completed for each CBSR sample:

1. Determine the most likely sensed region:
  - (a) An EIT reconstruction image of a loaded DUT of a particular strain,  $\varepsilon_j$ , at a steady-state conductance was found. Each element having a change in conductance value,  $\Delta\rho$ , in units  $mS$ .
  - (b) Complete threshold percentage mask on image to localise the sensed region blob(s).
  - (c) The centre of mass error,  $E_{CoM}$ , between each blob and the actual force application CoM was calculated. The blob domain with the smallest  $E_{CoM}$ ,  $\Omega_s$ , is chosen for the following steps.
2. Equation 4.1 was rearranged to get an original conductance estimate for each element:
 
$$\rho_0 = \frac{\Delta\rho}{\alpha\sigma + \beta} \quad (4.7)$$
3. The mean  $\rho_0$  and standard deviation of all of the elements in  $\Omega_s$  were found.
4. Steps 1 to 3 were repeated for each strain,  $\varepsilon_j$ , applied and the mean,  $\rho_0(\varepsilon_j)$  and standard deviation were calculated.
5. The mean of all  $\rho_0(\varepsilon_j)$  across all strain values (i.e.  $\varepsilon_j = 5, 10, 15, 20, 35, 30\%$ ) was calculated as  $\bar{\rho}_0$ .
6.  $\bar{\rho}_0$  was then substituted into Equation 4.1 as  $\rho_0$ , which was rearranged for stress to obtain the stress estimate as a function of mean change in conductance,  $\hat{\sigma}_j(\Delta\bar{\rho}_j)$ , of the sensed blob domain,  $\Omega_s$ .

## 4.3 Results

In the following sections the EIT image pre-processing, spatial, temporal, and localised force sensing performance metrics are displayed and quantified. First the steady state electrical noise,  $\sigma_n$ , and noise figure, NF, were determined, as given in Table 4.2. The NF value is a common metric showing noise amplification as a consequence of the EIT algorithm as used by Adler et al [193].

TABLE 4.2: DUT noise figure, NF, and noise,  $\sigma_n$ , at steady-state

<b>CB wt%</b>	<b>NF</b>	$\sigma_n$ [mS]
8	$1.20 \pm 0.17$	0.69
9	$1.15 \pm 0.11$	0.48

### 4.3.1 1D Material Characterisation

To generate a 2D pressure map from the EIT reconstructions a 1D material electromechanical characterisation was required. The 1D electromechanical relationship can then be extended to form an electromechanical relationship in 2D.

#### 4.3.1.1 Quasi-static Piezoresistivity

Given known strain input data, and measured stress and conductance change output data, a fit is shown in Figure 4.6. The gradient of the linear fit, i.e. the gauge factor, for the CBSR 8 wt% and 9 wt% was calculated as 0.6 and 0.2 respectively. Note that in the 9 wt% relative conductance data the standard deviation of the 5% strain data was similar to that of the mean, hence the linear range of 10 - 30% strain was considered when fitting the curve.

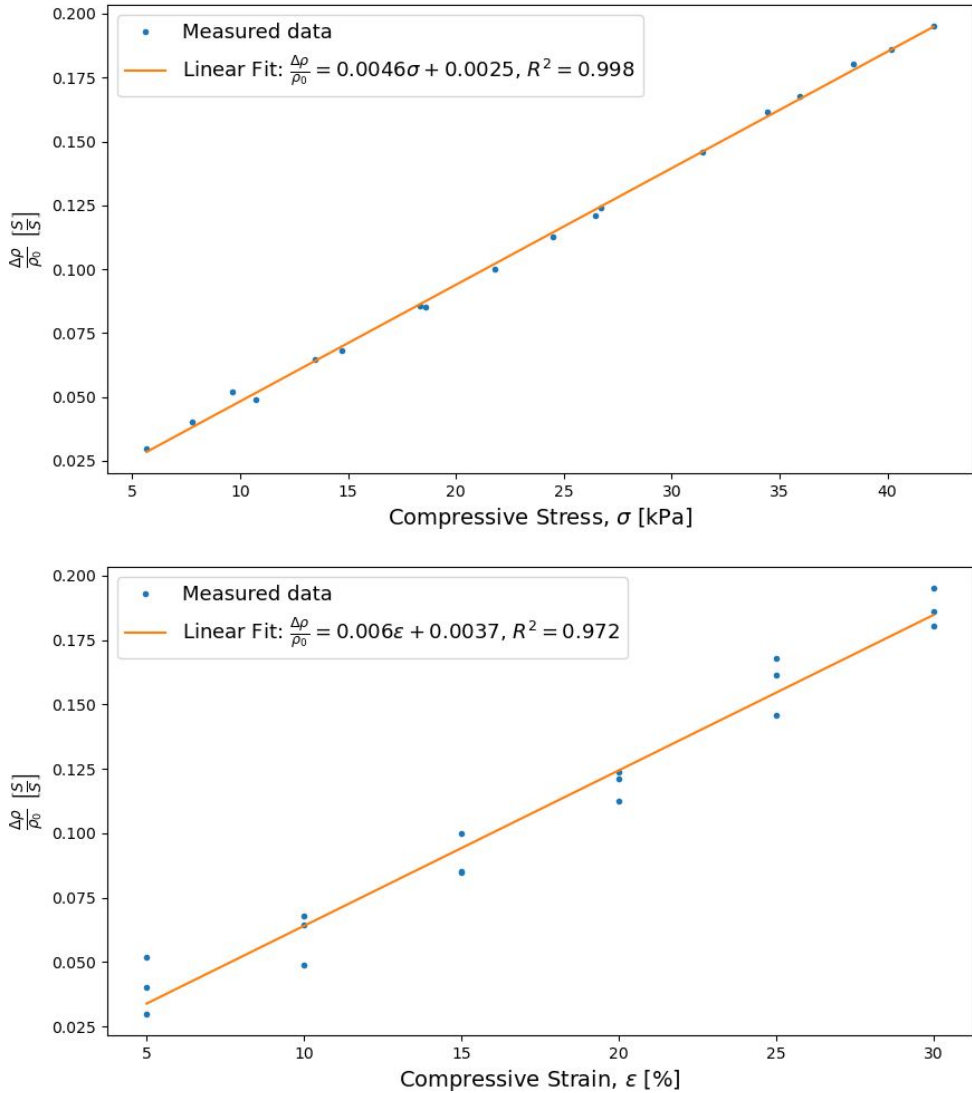


FIGURE 4.6: Conductance change vs. stress (top) and strain (bottom) data and fitted curves for 8 wt% CBSR.

#### 4.3.1.2 Transient Piezoresistivity

The transient piezoresistive effects observed within a PNEC limit the frequency response of the sensor. An example of the transient response of the material to a repeated compressive strain pulse input is displayed in Figure 4.7, clearly showing the stress relaxation of the material due to its viscoelasticity.

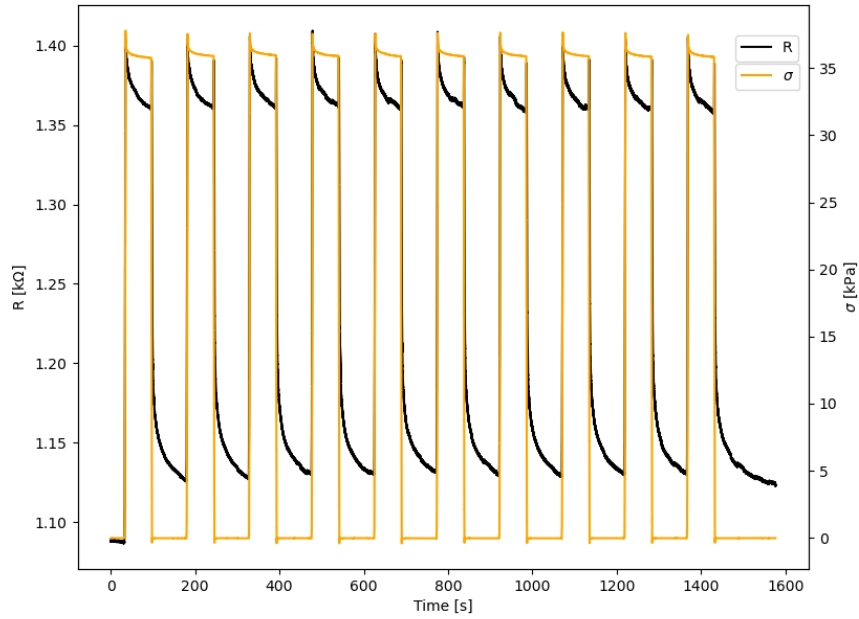


FIGURE 4.7: Compressive loading applied to the CBSR 8 wt% DUT for 10 loading events of 25% strain.

In Figure 4.8 a loading event is shown with the related stress and resistance relaxation curves. The unloading event similarly has a relaxation period for both stress and resistance in the loading case. Unlike the loading stress transient, the resistance transient has a spike during the unloading relaxation event seen in Figure 4.8. This rising edge and peak of this spike are ignored and the resistance relaxation edge is characterised.

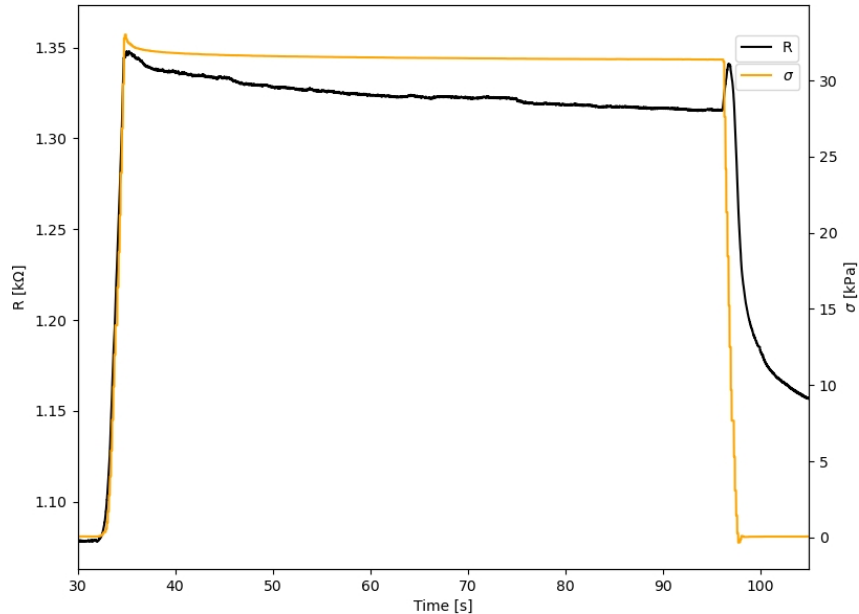


FIGURE 4.8: Compressive loading and unloading transients for CBSR 8 wt% material undergoing a 20% strain pulse from the first pulse given in Figure 4.7.

For each stress relaxation Equation 4.3 was fitted to the data. Due to the similarity of the viscoelastic behaviour seen in the stress-strain relationship, analogously the same generalised linear model was fitted to the resistive relaxation events observed similar to the tensile testing shown in the previous chapter.

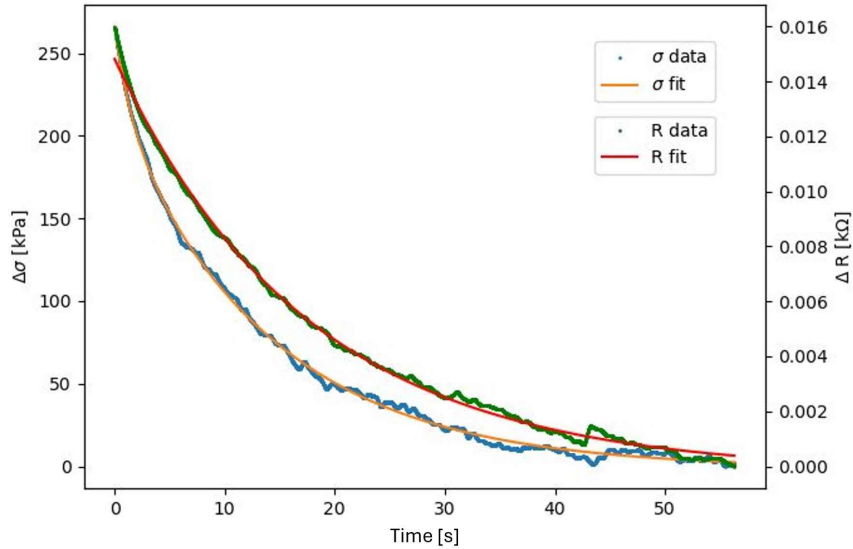


FIGURE 4.9: The fourth 1D load event,  $L_3$  on the CBSR 8 wt% sample using 5% strain showing a stress,  $\sigma$  and resistance,  $R$ , relaxation event and their corresponding fitted curves.

The fitted parameters were found for both 8 and 9 wt% CBSR samples, giving an indication of the differences due to CB weight percentage and the apparent viscoelasticity.

The settling times of the resistance relaxations give an indication of the frequency response of material. Thus, parameters were fitted to a series of relaxations using Equation 4.3, then a series of fit parameters could be used to determine a mean fit. The mean fit was then used to determine the mean settling time over each ten loading events and each of the six strain values. The mean relaxation settling times were compared for each CB weight percentage as shown in Appendices C.5 and C.6.

### 4.3.2 Sensor Performance Metrics

To validate this 2D pressure sensing platform for specific applications the limits of the sensor must be known. Metrics to analyse and quantify the sensor limits such as noise, spatial-, temporal-, and stress- performance metrics are given in this section.

#### 4.3.2.1 Pre-processing

The noise floor limits the detection of small forces. First the noise floor was found from the no load steady-state of material. The maximum noise from the first eight frames was found and this maximum was subtracted from all contiguous images in the time series experiment.

After a noise mask has eliminated the steady state noise floor, different percentage thresholds can be used to compensate for different regularisation and different material push area edge softness as shown in Figure C.3.

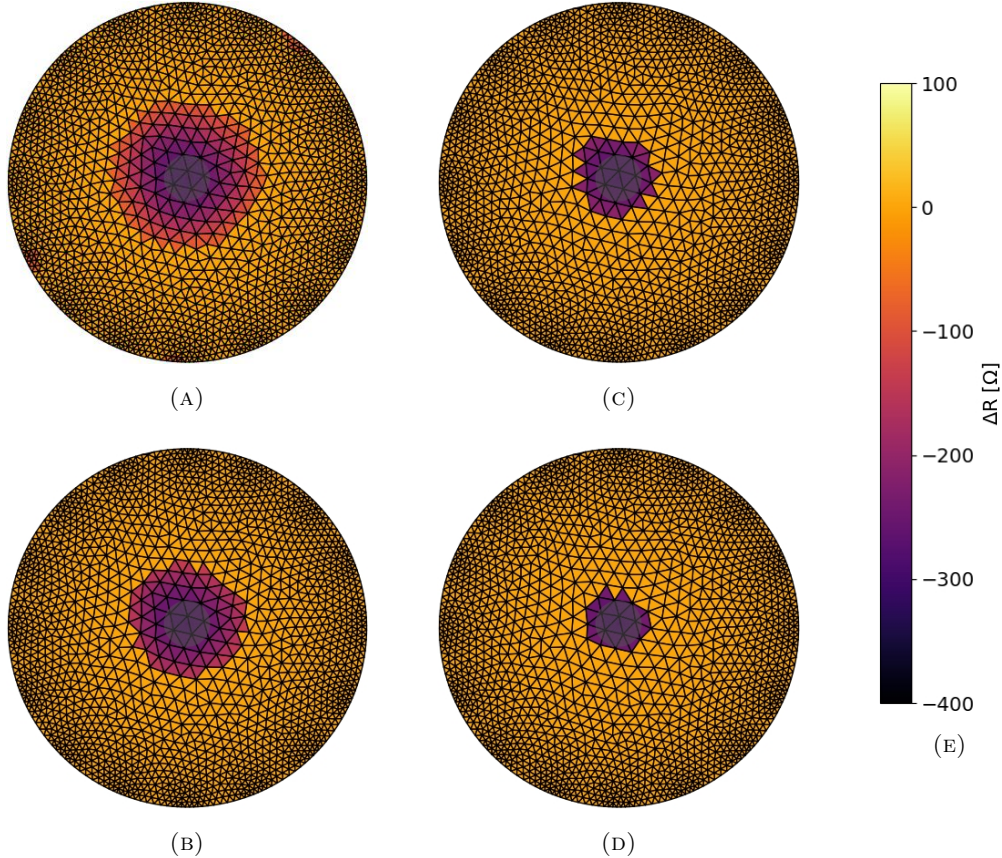


FIGURE 4.10: A series of threshold percentage masks (A) 25%, (B) 50%, (C) 75, and (D) 85% for the same reconstruction given in Figure C.2. (E) is the resistance change scale bar.

The threshold masked image blobs and the force applicator shapes in Figures C.3a - C.3d are compared and quantified in the following section.

#### 4.3.2.2 Spatial Performance

To properly determine where the area and perimeter of a load are, multiple threshold mask filters were applied. To validate the threshold mask percentages the three main performance

characteristics were displayed as separate time series for each material, each applied strain, and each threshold percentage mask. These time series show how each metric changed over the course of a loading test sequence and how the metrics vary across the surface of the DUT. An example comparing this time series data for two instances where a 20% strain pulse train was applied to the nine loading locations with multiple threshold mask percentages is shown in Figures 4.11 and Appendix C.9 for 8 and 9 wt% CBSR samples respectively.

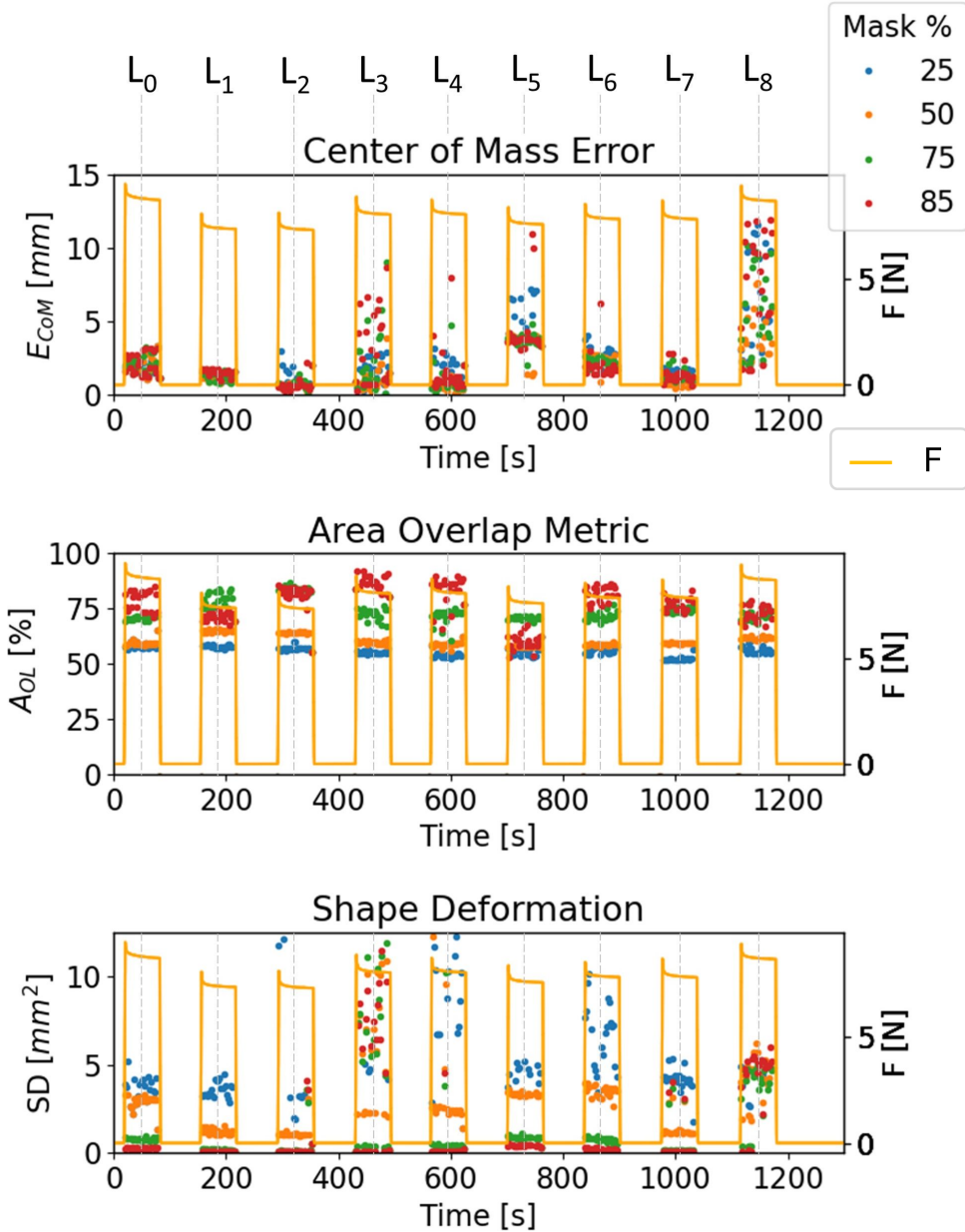


FIGURE 4.11: Spatial performance metrics comparing threshold percentages of 25, 50, 75, and 85% for a 8 wt% CBSR sample being loaded with 20% compressive strain in nine areas,  $L_{0-8}$ , shown in Figure 6.8.

The percentage threshold masks from 25 - 85% were compared by finding the mean of all of the spatial performance metrics for each strain from 5 - 30%. The mean and standard deviation for

each of these metrics from the data shown in Figure 4.11 is given in Tables 4.3 and 4.4.

TABLE 4.3: CBSR 8 wt% mean and standard deviation for spatial performance metrics across of a nine loads,  $L_0-L_8$  and strain value 20%.

%	$E_{CoM}$ [mm]	$A_{OL}$ [%]	$SD$ [mm $^2$ ]
thresh			
0.25	$4.1 \pm 6.3$	$53.3 \pm 15.3$	$10.4 \pm 9.3$
0.5	$3.3 \pm 6.3$	$57.5 \pm 16.3$	$3.6 \pm 4.4$
0.75	$3.8 \pm 6.3$	$69.6 \pm 19.8$	$2.4 \pm 5.8$
0.85	$4.1 \pm 6.4$	$72.5 \pm 21.7$	$2.4 \pm 6.5$

TABLE 4.4: CBSR 8 wt% mean and standard deviation for spatial performance metrics of nine loads,  $L_0-L_8$ , a 85% percentage threshold mask, and strain value 20%.

Load	$E_{CoM}$ [mm]	$A_{OL}$ [%]	$SD$ [mm $^2$ ]
$L_0$	$2.05 \pm 0.70$	$80.39 \pm 4.19$	$0.28 \pm 0.01$
$L_1$	$1.53 \pm 0.23$	$72.32 \pm 1.74$	$0.12 \pm 0.01$
$L_2$	$0.67 \pm 0.41$	$83.00 \pm 2.38$	$0.48 \pm 1.16$
$L_3$	$3.29 \pm 2.17$	$87.93 \pm 2.68$	$5.25 \pm 3.78$
$L_4$	$1.44 \pm 1.61$	$84.81 \pm 5.78$	$2.76 \pm 5.65$
$L_5$	$4.43 \pm 2.09$	$61.08 \pm 3.29$	$7.39 \pm 16.31$
$L_6$	$2.03 \pm 1.05$	$82.19 \pm 3.55$	$3.14 \pm 8.57$
$L_7$	$1.49 \pm 0.56$	$77.68 \pm 2.46$	$0.66 \pm 1.25$
$L_8$	$6.95 \pm 3.67$	$73.69 \pm 3.60$	$3.78 \pm 2.01$

### 4.3.3 Randomised Location and Strain Testing

In a real world application the sensor platform in this work will likely experience a large range of unknown loads in various locations. To ensure that the device operates in a similar fashion to that seen in the structured experimental data, a randomised experiment was completed. The randomised experiment loads were at ten randomised radii,  $r_{rand}$ , angles,  $\theta_{rand}$ , and strain values, all within the ranges, 0 - 40% of the domain radius, 0 - 360°, and 5 - 30% respectively.

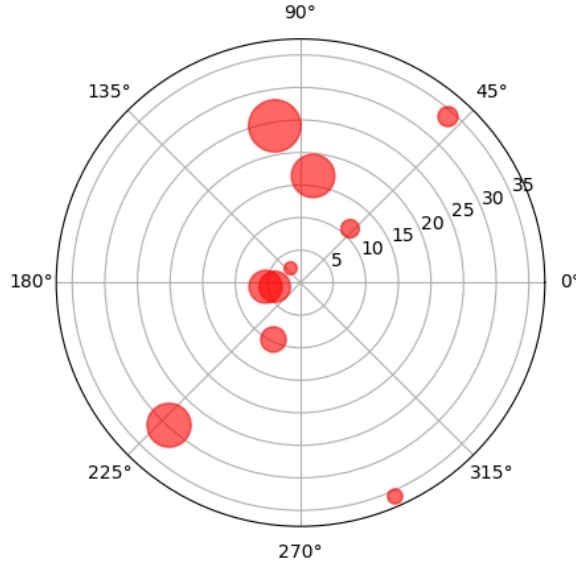


FIGURE 4.12: The ten random load point locations,  $L_{rand}$ , and random strain values proportional to red circle size as shown on a polar plot.

Spatial performance metrics for these tests are given in Tables 4.5 and C.1 with the load points and their magnitudes shown diagrammatically in Figure 4.12. A pseudo-random number generator with a uniform distribution was used for all randomly generated data.

TABLE 4.5: CBSR 8 and 9 wt% mean and standard deviation for  $E_{CoM}$  spatial performance metrics of ten random locations,  $L_{rand}$  and random strains  $\varepsilon$

$L_{rand}(r, \theta)$ [mm, °]	$\varepsilon$ [%]	8wt%	9wt%
		$E_{CoM}$ [mm]	$E_{CoM}$ [mm]
(5.4, 10)	17.9	$3.1 \pm 0.7$	$3.1 \pm 0.5$
(29.8, 337)	24.0	$1.9 \pm 0.4$	$5.0 \pm 0.6$
(4.2, 317)	17.0	$7.9 \pm 2.2$	$9.0 \pm 1.0$
(34.0, 70)	10.9	$6.0 \pm 3.5$	$2.9 \pm 0.5$
(35.8, 137)	8.1	$13.9 \pm 0.6$	$7.7 \pm 4.6$
(9.6, 55)	13.8	$6.0 \pm 1.0$	$10.3 \pm 4.4$
(2.8, 260)	7.0	$12.0 \pm 8.1$	$28.7 \pm 10.9$
(11.2, 114)	10.0	$5.1 \pm 1.2$	$12.0 \pm 1.9$
(24.6, 241)	28.5	$2.3 \pm 0.2$	$2.4 \pm 0.2$
(16.6, 253)	23.6	$3.1 \pm 0.4$	$7.1 \pm 0.5$

#### 4.3.3.1 Temporal Performance

Temporal performance is crucial for time sensitive applications and the settling time of the sensing material domain must be known to apply a quasi-static force model. The fitted stress and resistance relaxation parameters were found for both 8 and 9 wt% CBSR samples, giving an indication of the frequency response of material across all experiments. To ensure a good fit all fits with an  $R^2$  value less than 0.85 were eliminated, as they were a result of poor data or poor fitting algorithm implementation.

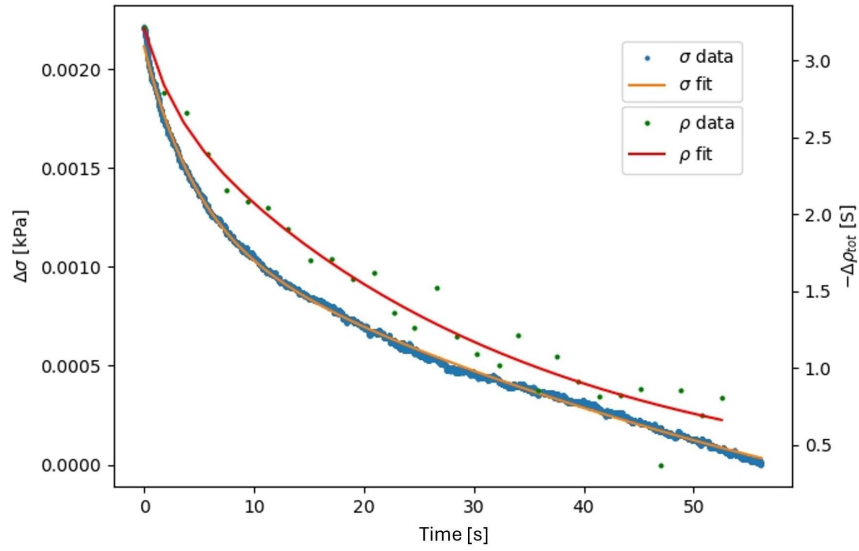


FIGURE 4.13: EIT load event  $L_0$  on the CBSR 9 wt% sample using 30% strain showing a stress,  $\sigma$  and conductance,  $\rho$ , relaxation event and their corresponding fitted curves.

The mean settling time for each strain was calculated across relaxations for all strains, all 9 locations, and all 3 trials. The settling times were compared for each CB weight percentage as shown in Appendices C.7 and C.8.

#### 4.3.3.2 Localise Force Sensing Performance

To determine the localised force sensing performance the linear quasi-static Equation 4.1 was applied to the percentage threshold masked image blobs developed in section 4.2.3.2.

To determine the force sensing limits of the material, the force estimated erroneously due to the EIT reconstruction noise floor was determined. The noise floor is the noise observed over a time series of EIT images when the DUT has zero load applied and there are no resistive transient effects present. The noise floor,  $\Delta\rho_n$ , of unloaded relaxed 8 and 9 wt% CBSR DUT conductance images were calculated as  $\pm 0.33$  and  $\pm 0.34 \mu S$  respectively. An average DUT inter-electrode

conductance,  $\rho_{int}$ , of 55.3 and  $222.2 \mu\text{S}$  was derived from Table 4.1 for CBSR 8 and 9 wt% respectively. A relative change of conductance value,  $\frac{\Delta\rho_n}{\rho_{int}}$ , was then calculated as  $5.97 \times 10^{-3}$  and  $1.53 \times 10^{-3} \mu\text{S}$  for CBSR 8 and 9 wt% respectively. From the quasi-static piezoresistivity Equation 4.1 and the fitted quasi-static piezoresistivity parameters found in Section 4.3.1.1, we calculated the mean force approximation error as 0.17 N for both CBSR 8 and 9 wt%.

The force estimation from the inverse quasi-static Equation 4.1 was compared to the actual force loaded onto the DUT as measured by the force applicator loadcell. Figures 4.14 and 4.15 show data from load applications in the centre ( $L_0$ ) of the respective 8 and 9wt% CBSR DUTs with a force estimation standard deviation of  $\pm 0.78$  and  $\pm 0.81$  N respectively.

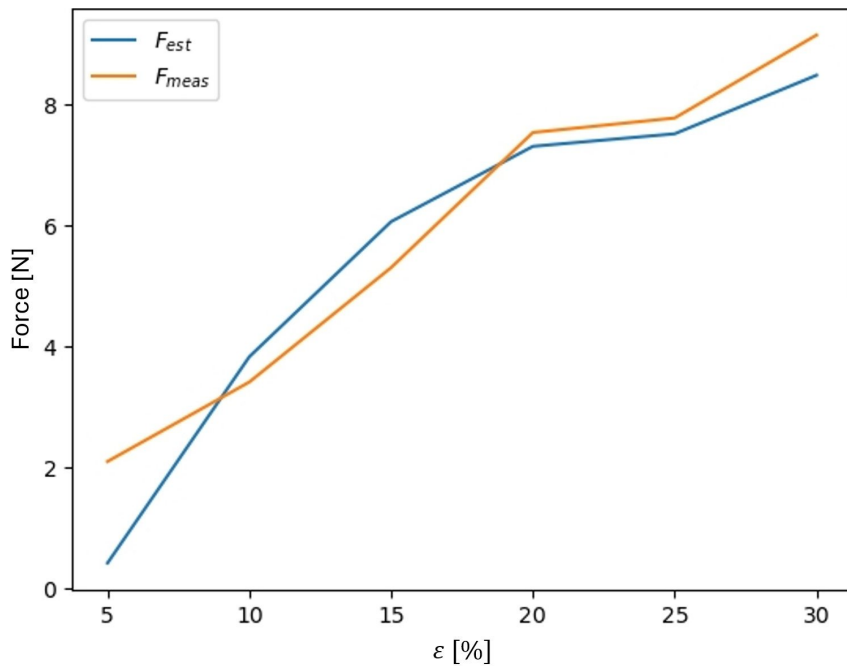


FIGURE 4.14: Comparing force estimates,  $F_{est}$ , and actual force measurements,  $F_{meas}$ , for 5 - 30% strain centre loading events at  $L_0$  for the EIT sensor system for 8 wt% CBSR

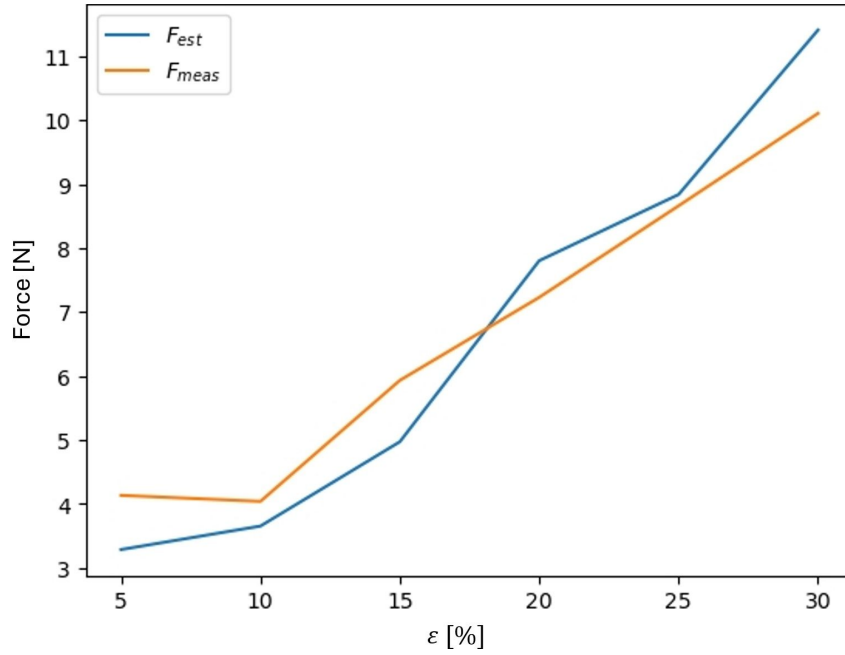


FIGURE 4.15: Comparing force estimates,  $F_{est}$ , and actual force measurements,  $F_{meas}$ , for 5 - 30% strain centre loading events at  $L_0$  for the EIT sensor system for 9 wt% CBSR

## 4.4 Discussion

Potential applications that emulate human-like skin pressure sensing characteristics require a forms of quantification to compare the technology to the specific requirements. This work quantitatively characterises performance metrics to help facilitate that comparison and optimisation process. The sensor developed could be likened to slow acting mechanoreceptors within human skin, such as Meissner's corpuscles and Merkel's discs, which combined can detect static pressure, and high resolution touch. For other EIT-based pressure mapping applications to be realised, the metrics developed in this work are some of the core metrics required to determine which soft sensing domains are suitable and are their limits.

### 4.4.1 Quasi-static Piezoresistivity

To make a low-frequency response load sensor, a quasi-static piezoresistive linear model was created as shown in Section 4.3.1. However, this model is only valid for sufficiently slow pressure applications or after a sufficiently long time period. This time period is determined by the largest expected steady-state relaxation time for the material, using data gathered in the Temporal Performance Section 4.3.3.1.

#### 4.4.2 Pre-processing

The two steps of a noise threshold mask and a percentage threshold mask successfully filtered noise and EIT reconstruction related noise artefacts. The favoured percentage threshold mask chosen for further metrics testing was 85% as this gave the lowest average  $E_{CoM}$  and  $SD$  values from the across all strains applied across all nine loading points.

In the experiments often a blob detection from a previous load will be present in a subsequent load, as expected due to the resistive relaxation. Feature detection could be added in future to ensure that only transients similar to those seen in the initial formation of a blob would signify that the blob is to be analysed. Concurrently, each blob could be tracked individually to determine whether it is a noise artefact or an actual sensed region depending on it's behaviour.

#### 4.4.3 Performance Metrics

To develop sensing domains for future applications, the sensing domains may need take into account certain prior information about the limits of the system.

For example, human hands and feet have some of the highest density of mechanoreceptors in the body. Lower density regions of mechanoreceptors in humans include the back and chest [229]. Higher spatial resolution is require for emulating the pressure mapping of a human hands and feet, compared to the human back and chest. However, the pressure sensing range required by the human hands may be lower than that required by the human feet.

Using this prior information, we can validate the appropriate sensing domain characteristics that give a suitable performance for each different application.

Depending on the application of the sensor the importance of each temporal, spatial, and force sensing performance metrics could all vary.

##### 4.4.3.1 Spatial Performance

All spatial performance metrics,  $E_{CoM}$ ,  $A_{OL}$ , and  $SD$  are key indicators of whether a loading event has been localised correctly.

The  $A_{OL}$  gives a value out of 100 for a certain detected blob. This value is penalised for false positive and true negative elements that overlap (or not) with the force applicator area.

It is important to note, when a force is applied in an small area of a domain, however a blob has been detected over the majority area of the domain, a  $A_{OL}$  value of  $\leq 50\%$  will be given although the blob detection could be completely false. Although the detected blob and force applicator are 100% overlapping the amount of false positive (i.e. blob elements not overlapping with force applicator area) could cover the rest of the DUT, potentially giving a value nearer to 50% than 0%. From this it must be recognised that this metric does not represent a linear relationship between  $A_{OL}$  and the quality of the reconstruction. So the scale of the  $A_{OL}$  value to quality relationship was determined empirically as:

$$0 \leq A_{OL} \leq 50\% = \text{Likely Poor}$$

$$50 \leq A_{OL} \leq 70\% = \text{OK}$$

$$70 \leq A_{OL} \leq 100\% = \text{Good}$$

The  $SD$  is the mean square error between the force applicator perimeter and sensed region perimeter taken radially from the force applicator centroid, so will likely be lower with a low  $E_{CoM}$  and a higher  $A_{OL}$ . The closer the  $SD$  value is to zero the more accurately the shape of the load area applied has been sensed. The  $SD$  metric is also affected significantly by the quantisation error depending on the mesh coarseness.

Comparing the different percentage threshold masks for the experiment shown in Figure 4.11, it was determined that each percentage mask of 50%, 75%, and 85% gave showed the spatial performance for the  $E_{CoM}$ ,  $SD$ , and  $A_{OL}$ . However, the standard deviation of these values is comparable to the mean itself therefore looking at the mean performance metric value in each location was shown in Table 4.4. The lowest  $E_{CoM}$  was found to be  $0.67 \pm 0.41$  mm, at  $L_2$ . The highest  $A_{OL}$  value was found to be  $87.93 \pm 2.68\%$ . The lowest  $SD$  value was found to be  $0.12 \pm 0.01$  mm<sup>2</sup> at  $L_1$ .

The CBSR 8 wt% samples gave superior performance metric results than the 9 wt% samples due to the residual transient effects of previous load events as exemplified in Figure C.9. This will be mitigated in future by using a blob separation algorithm whereby each sensed-region/blob is given a weighting based on its appearance time, size, decay characteristic, and performance metric values.

The spatial performance metrics are useful for quantifying future testing with irregular load application area shapes and multiple loading events in future testing to validate a variety of

irregular and multi-load test cases. Performance metric inconsistencies in the different load locations show that the electromechanical characteristics of the material varies throughout the material. These metrics would all contribute toward a calibration step to compensate for material inhomogeneity, allowing for a range of materials to be used for the sensing domain.

#### 4.4.3.2 Temporal Performance

Many applications require a minimum frequency response hence a temporal study was completed to characterise the transient effects limiting the speed of the sensor. The study focused on the settling time of transient piezoresistive events in the material for varying strain step inputs. With known PNEC material settling times, a filter could be applied to the output of this sensor to get an estimate of the load applied to the material.

To aid future inverse modelling and use of PNECs as pressure sensor it is important to understand each transient states of a load, including the loading phase, steady state, or unloading phase. It was found that on average that unloading events had a higher settling time than loading transients for both CBSR 8 and 9 wt% composites across all strains tested from 5 to 30%. No clear correlation was found between the settling time of the transient strain events and the strain percentage applied to the material. Mean settling times ranging 29 - 36 s and 29 - 41 s have been observed for the CBSR 8 and 9 wt% composites respectively.

A different sensing region material could provide a higher frequency response, such as a carbon nanotube silicone composite which has shown a lower settling time in previous works [246, 247]. Due to the viscoelasticity and elastic rebound in the material the resistance relaxation from previous load applications was often present in subsequent load events, altering the observed resistance relaxation response. Future algorithms developed would aim to eliminate these previous residual relaxations.

Often soft materials are inherently viscoelastic like much soft tissue within the human body [43], so if soft sensor domains are required with a high frequency response this viscoelasticity will need to be compensated for using this work's performance metrics as a foundation.

It is important to note that if the homogeneity in the material is highly irregular, regions of the material will have different degrees of piezoresistivity the frequency response of the material is likely to vary considerably. Further research is required into how the different CB wt % values and their dispersion affect the temporal response of the material.

#### 4.4.3.3 Localised Force Sensing Performance

The sensor platform gave stress estimates that correlated well with the real stress applied to the material, as seen in Figures 4.14 and 4.15. These stress estimates were gathered from the steady-state data gathered from the EIT measurements at approximately 1.5x the settling times found in Section 4.3.3.1 using the algorithm given in Section 4.3.3.2 to ensure the data was at steady state.

Stress relaxation of the composite CBSR material as a whole gives a good indication of macro-mechanical behaviour of the CBSR. It was postulated that the resistance relaxation gives an enhanced insight into the micro(and nano)-structural behaviour of the CBSR composite, because of the different observed behaviours of the CBSR stress and resistive relaxation and also how these relate to different CB weight percentages and their dispersion.

#### 4.4.4 Real World Applications, Manufacturability, and Scalability

Using EIT-based pressure mapping on a larger scale is feasibly as shown by the use of ERT in geophysics [248]. However using the PNEC-based methods given in this work on this scale have not yet been trialled, but potential larger-scale applications include adding a pressure mapping layer under a tennis court to map force exerted by athletes onto a court or a method of measuring foot traffic in buildings and urban areas. The use of the performance metrics discussed in this work would be applicable for both scenarios.

For the tennis court application, the importance of player location and speed may be more important than detecting the footprint shape and exact force applied to the court surface. This means that the  $E_{CoM}$  and decay time values would be more heavily weighted than the  $SD$  and force values, and hence could be tuned for these characteristics. For the urban floor mat application, the importance of footprint shape and force estimation may give useful insight into the physical demographic of people or animals walking across the mat [249]. This may mean that the  $SD$  and force resolution values are more highly weighted in the design and process.

Larger-scale applications of an EIT-based sensor come with challenges such as, scaling the electronics driving the EIT measurement, fabricating such a large homogeneously piezoresistive domain, and ensuring the reliability in a range of outdoor environmental conditions. Conversely, smaller-scale applications are limited by the conductive particle size in the PNEC. A sensing

domain thickness sufficiently larger than the average agglomerate size would be required for reliable EIT mapping and force estimates.

Different forms of tribological wear on the device sensing region would alter the piezoresistive characteristic of the device. Encapsulation of the device could be implemented to minimise wear and increase hermeticity.

The most obvious limitation of this sensor is the frequency response of the material as shown in Appendices C.5 - C.8, which could be algorithmically filtered or inverse-modelled to be corrected. Else, other more responsive, less viscoelastic materials could be used, and/or a capacitive EIT-based pressure mapping device used to improve the frequency response of this device.

Mass production of an EIT-based sensor would use the performance metrics given in this work to calibrate and quality-check the sensing domain and boundary electrode connections. This work also found that using pin boundary electrodes adds to the durability and stability of electrical connection in this device.

## 4.5 Conclusions

An EIT-based piezoresistive sensor using a custom made carbon black silicone rubber composite material has been developed for sensing compressive pressure events and applying performance metrics to obtain the validity of the output EIT images. To be able to apply this EIT-based PNEC pressure sensor to a variety of scenarios, replacing human-like touch, performance metrics has been formed to quantify the sensor's suitability for each application. Sensing domains of 8 and 9 wt% carbon black silicone rubber have been tested using: 6 strain values, 9 load locations, and 3 trials. From this raw data we have calculated data for: spatial resolution, transient settling time, and force sensor resolution.

It was shown that the CBSR 8 wt% sample out performed the CBSR 8wt% sample in terms of spatial and temporal metrics across a range of experiments. The best performance metrics observed in the CBSR 8 wt% sample for  $E_{CoM}$ ,  $A_{OL}$ , and  $SD$ , were  $0.67 \pm 0.41$  mm,  $87.93 \pm 2.68\%$ , and  $0.12 \pm 0.01$  mm<sup>2</sup> respectively for three different load locations. For the sensor domains tested, average settling times of between 19.0 - 44.5 s and 22.5 - 36.0 s were determined for 8 and 9 wt% CBSR samples. A quasi-static conductance-force model of the material was developed with an accuracy of  $\pm 0.78$  and  $\pm 0.81$  N for a range of strains from a centre load test for 8 and 9 wt% CBSR respectively.

Using these performance metric data in future work a piezoresistively inhomogeneous sensor domain could be, calibrated to homogenise the apparent domain piezoresistivity, compensated for transient phenomena, and sense loads with a known degree of accuracy. All of these factors contribute to optimising the EIT-based 2D pressure mapping sensor for different applications. The next chapter includes the development of a low-cost, small circuit to discretely capture the EIT data to open up a larger range of mobile and wearable applications. The work shows promise for future use of an EIT-based sensor in a variety of applications requiring a soft sensing domain and non-invasive rigid electrodes.



## Chapter 5

# A Portable EIT-Based Pressure Mapping Sensor and Validation System

## Overview

This work presents portable, low-cost hardware for pressure mapping using EIT-based soft sensors. An important part of developing these EIT-based pressure sensors is the sensor characterisation as shown in the previous chapter. Therefore, this chapter also provides the design of a system required for characterising and validating the spatial, pressure, and temporal performance of different soft sensor material domains. The system is capable of driving soft EIT-based sensors using a range of sensing materials, shapes, and configurations. The hardware allows for the wireless transmission of EIT data to a remote device. A data capture frame rate of 12.7 Hz allows for the analysis of dynamic events. The maximum current drive voltage is  $\pm 22$  V and a voltage read resolution of  $\pm 0.3 \mu\text{V}$  allowing for a range of sensing domain sizes, thicknesses, and materials. A Cartesian force applicator device has been developed for the automatic characterisation with compression load rates of 0 - 800 mm/min for can sense loads from 0 to 100 N with a resolution of  $\pm 50$  mN. Loads can be applied in the  $xy$  plane with an error of  $\pm 0.01$  mm. A standardised method has been provided for researchers to experiment with a range of different sensing domain materials and shapes. The system described in this work is suitable for both research and practical applications, making it a valuable tool for advancing the field of EIT-based soft sensor technology. All of the hardware and software for the ERT module and

Cartesian force applicator designs developed in this work are open-source and supplied in the supplementary material [250]. To the best of the author's knowledge, no system for characterising soft EIT-based pressure mapping sensors in real-time has been presented in the literature at the time of writing this chapter.

## 5.1 Introduction

To apply the pressure mapping sensor analysis and technology given in the previous chapter to a real world scenario, often portability, development time, and cost become an issue. More importantly there is no commercial product specifically made for pressure mapping sensor devices. To combat this, a novel application specific EIT module has been created in this work for developing EIT-based pressure mapping sensors. In parallel there lacks a commercial system which can simultaneously gather compressive spatio-temporal stress-strain data for characterising the EIT-based pressure sensor technology developed. Hence a Cartesian force applicator has been designed for the purpose of researching and comparing the electromechanical properties of a range of potential sensing domain materials.

Electrical impedance tomography (EIT) is an imaging technique used to map impedance/resistance throughout a material using multiple boundary electrodes. The boundary electrodes inject current through the homogeneous domain instead of a patterned or layered one, allowing the sensor measurements to be non-invasive.

EIT is most commonly used for thorax imaging for clinical respiratory analysis; however, this same method can be used for a multitude of applications with conductive bodies to map changes in impedance/resistance as shown in the previous chapter. Commercial devices that perform EIT, or the DC equivalent electrical resistivity tomography (ERT), exist in large-form factors such as Pulmovista 500 (Draeger, Luebeck, Germany), EIT16/32 (Sciospec Scientific Instruments GmbH, Leipzig, Germany), LuMon (Sentec, Lincoln, USA), Zeta (Zonge International, Tucson, USA), WGMD-4 (WTS Geophysical, Wanchai, Hong Kong). All of these options are application-specific for research, biomedical, and geophysical applications. Several research papers [74, 251–259] have described similar but smaller versions of the commercial products mentioned.

In this work similar physical principles used in bio-medical and geophysical sensing are used to map localised compressive loads on a soft piezoresistive material. A core limiting factor of current pressure mapping technology is the lack of customisability in sensor size, shape, sensing

domain material softness, and sensing material composition [60, 90, 91, 93]. Most often, pressure sensors are given in a rectangular format because of the arrays of wiring and sensing elements required within the sensing domain. EIT-based pressure mapping sensors are not constrained by wires or complex patterning within the sensing domain area. EIT-based pressure sensors can have a homogeneous sensing domain configured in various shapes.

When referring to the circuitry capturing data for an EIT reconstruction the term ERT is used to show the circuit function. However, when referring to the reconstruction computer and resistance images generated the term EIT is used, as these can be generalised for complex impedances. To advance the research of this soft pressure mapping platform technology, we require a system that is low cost, open source, easy to use, portable, and sufficiently flexible to test a range of different sensing domain materials. The system developed in this work is for the research and development of EIT-based pressure mapping sensors.

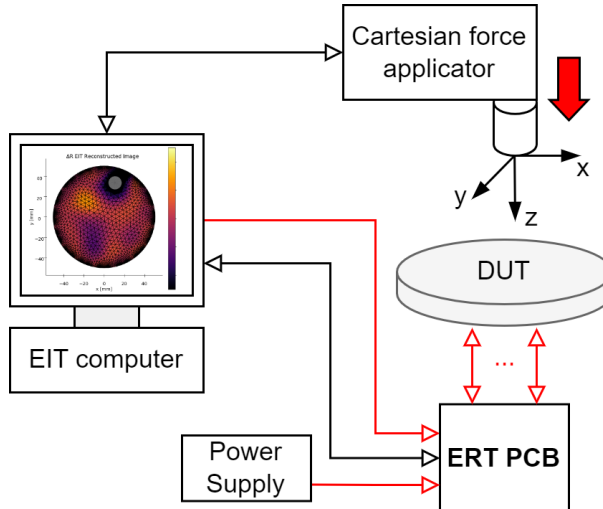


FIGURE 5.1: System architecture of ERT sensor and CFA setup. The large red arrow shows the direction of the force applicator compression onto the sensing domain (DUT) and analogue/power signals are shown with red arrows and digital signals with black arrows.

The hardware of our system has two key components, a circuit for gathering raw ERT data and a Cartesian force applicator (CFA) machine for characterising an EIT-based pressure mapping sensor. The system characterises the sensor and can be used for validating the spatial, pressure, and temporal performance for different piezoresistive sensor material domains. The CFA allows for repeatable experiments and quantifiable data for different sensor configurations.

## 5.2 Design Methodology and Analysis

An EIT-based pressure mapping sensor toolbox has been created that reliably and repetitively collects data for EIT-based pressure mapping and quantification of the sensor performance. The overall system is simple to construct and easy to operate and is split into the subsystems given in Figure 5.1. The build instructions for both subsystems are given in Appendix D.

The ERT sensor consists of an ERT sensor circuit and the sensing domain under test (DUT). The ERT circuit drives the EIT measurements through the sensing domain soft elastomer composite material. The ERT circuit designed is small ( $79 \times 94 \times 12$  mm) for potential use in space-constrained mobile applications. The system has a programmable current source which can drive up to 50 mA of constant current. The voltage measurement circuit has an ADC resolution of  $0.3 \mu\text{V}$ , ensuring that the small signals generated by small localised loads can be detected. The sensing domain in this work is a soft piezoresistive composite made from carbon black (CB) powder and silicone rubber with 16 boundary electrodes made from gold pins and copper tape, as seen in Figure D.3.



FIGURE 5.2: A soft sensor domain connected to the ERT sensor electronics.

To ensure that the sensor can accurately locate pressure points and their magnitude, the CFA device described in this work is used to apply compressive forces at various locations. The CFA test bed allows for loads within a  $220 \times 180$  mm area.

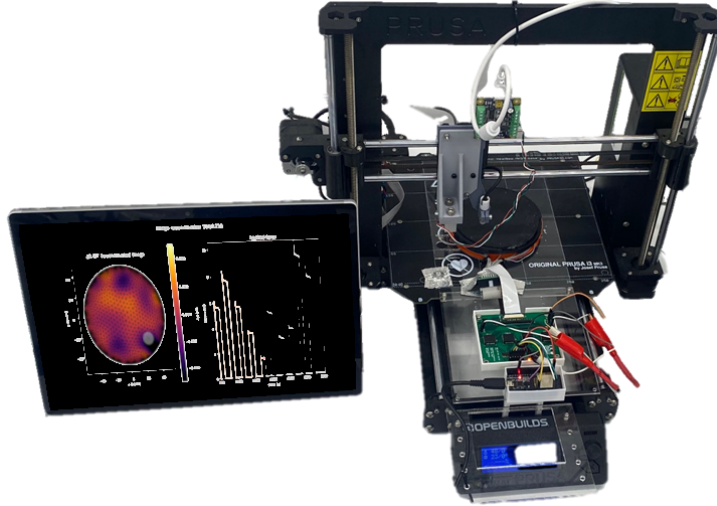


FIGURE 5.3: Cartesian force applicator setup with an ERT circuit and EIT reconstruction computer

Previous research groups have developed EIT hardware for pressure mapping sensors [65, 74, 195, 236, 260]; however, a complete open-source system including validation hardware has not yet been published.

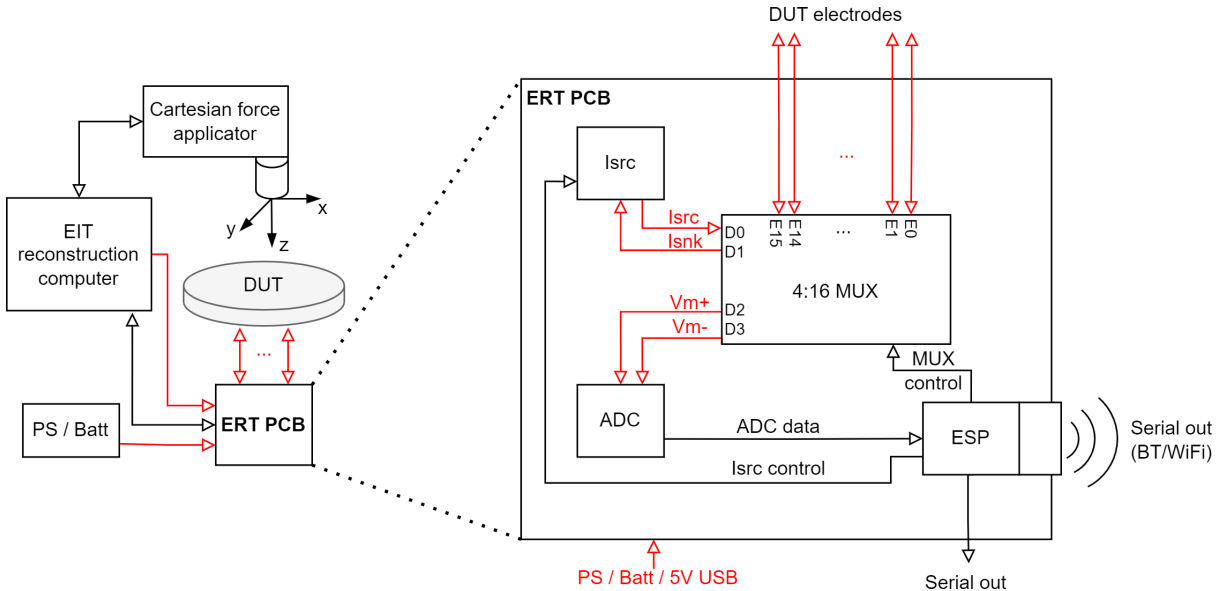


FIGURE 5.4: System architecture of ERT sensor and CFA setup (left) and the key internal electrical signals of the ERT circuit (right). With analogue/power signals shown with red arrows and digital signals with black arrows.

### 5.2.1 EIT cycle and load sequence

While a sequence of compressive loads are applied by the CFA to the sensing domain, concurrently the ERT sensor circuit gathers data for EIT reconstruction. This cyclic EIT data capture

process follows a specific sequence,

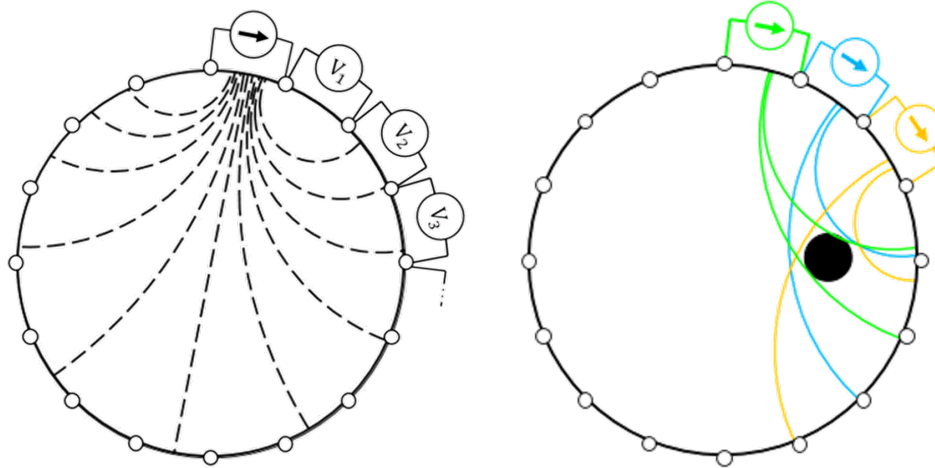


FIGURE 5.5: EIT adjacent drive pattern sequence.

1. A constant current is applied at adjacent electrode positions  $E_i$  and  $E_{i+1}$ , these electrode positions are selected with the ‘MUX control’ line.
2. Sequentially 16 adjacent electrode voltage measurements are completed next, again the electrode positions are selected with the ‘MUX control’ line.
3. Each raw voltage measurement is transmitted through ‘serial out’ to an ‘EIT reconstruction computer’.
4. The next current injection electrode position is selected, i.e.  $i = i + 1$ . Once all 16 current injection positions are completed, 256 voltages are measured giving enough data for one reconstruction frame. This is repeated for the duration of the experiment.

Multiplexing of the voltage measurements was chosen instead of the alternative option of simultaneous voltage measurement, to maintain a low-cost circuit. The simultaneous voltage measurement solution involves 16 separate ADCs, one for each electrode. A DC current source was chosen instead of the AC alternative because the sensing domains do not show significant changes in reactance during loading events. The hardware allows for the loading sequence to be altered and optimised for the sensing domain and application, because of the four independently switchable multiplexers controlling the current source and voltage reading electrodes.

### 5.2.2 Small signal measurement

The range of voltages required for reconstructing minute changes in resistances of a sensing domain spans several orders of magnitudes in EIT systems. Therefore a high dynamic range,

high resolution, low-noise voltage measurement system is required to accurately capture this data.

To evaluate the performance of the system with a standardised testing domain a resistor mesh network was created. The mesh network was created to validate the expected resolution required for generating EIT reconstructions [18] for a variety of different resistances and resistance changes. The resistor mesh network provided a standardised platform with known resistor values and tolerances for the comparison a real and simulated resistor mesh network. The resistor mesh network was chosen to provide a range EIT voltage data comparable to that of the real CBSR composite material.

A script was created to form a square resistor mesh network of various dimensions and various background resistance values. PySpice circuit simulator [261] was used to run a zero noise simulation on the system to show the expected difference in raw ERT voltage data between a homogeneous resistor mesh and a resistor mesh with an anomalous blob as shown in Figure 5.6. The maximum and minimum  $\Delta V_{read}$  values shown in Figure 5.6 and 94.994 mV and 53  $\mu$ V respectively.

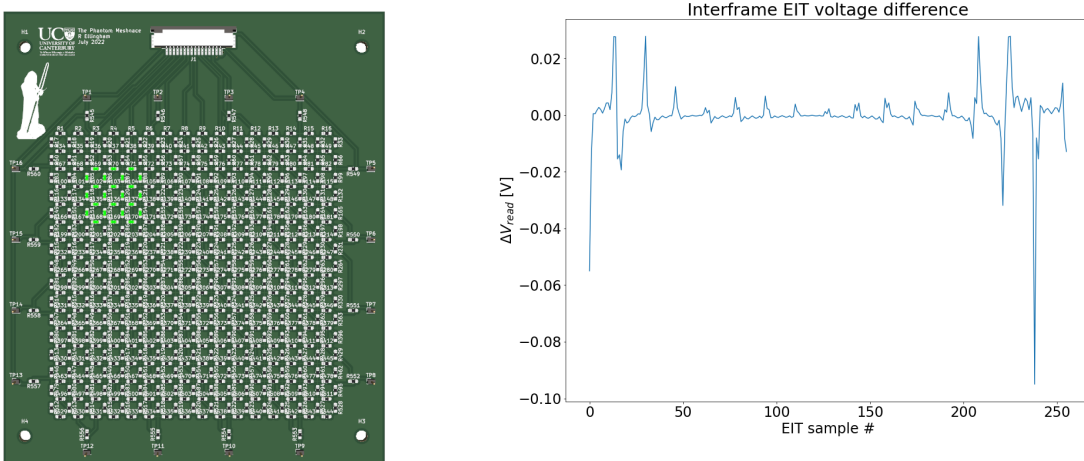


FIGURE 5.6: Left: A resistor mesh network for validating the ERT circuit, with the anomalous resistors highlighted in green. Right: The difference between EIT raw voltage data from a homogeneous square  $2.2\text{ k}\Omega$  resistor mesh domain and the same domain with a  $3.3\text{ k}\Omega$  resistor mesh anomaly.

It is non-trivial to determine the exact resolution required for an EIT based pressure mapping sensor voltage measurements as it depends on the inherent noise of the domain, the force resolution required, the expected external noise, the drive current, the EIT reconstruction algorithm

used, amongst other factors. This work uses a 24 bit ADC so that given an ideal noiseless representative domain the minimum voltage data shown in Figure 5.6 will be an order of magnitude larger than the resolution of the ADC.

### 5.2.3 Signal generation

To ensure a range of soft piezoresistive sensing domains can be tested a range of current source values are required to detect voltage ranges within detectable range of the circuit's ADCs. The current source can drive a current,  $I_{src}$  between 15  $\mu$ A and 50 mA and can be set as a programmable or fixed current source value. The  $I_{src}$  value can be altered by changing the  $R_{Isrc}$  [R7 or R8] value as shown in Equation 5.1.

$$I_{src} = \frac{0.617}{R_{Isrc}} + 15\mu A \quad (5.1)$$

If a fixed current source is desired for the ERT circuit  $R_{Isrc}$  sets the current source value based on Equation 5.1. If the circuit is configured as a programmable current source, the digital potentiometer [U9] controlling the  $R_{Isrc}$  value will a multiple of 39  $\Omega$  up to a maximum of 10 k $\Omega$  or a high impedance state. The possible programmable current source values are given in the `isrc_lookup.xlsx` file in the repository. If the resistivity of the domain is too high the current source supply will saturate to  $V_s$ . Ensure the domain resistivity is sufficiently low for this current source saturation not to occur within its expected range of use. A sufficiently high current value must pass through the domain to ensure low noise readings throughout the boundary electrodes on the domain. This noise predominantly occurs due to electrostatic effects in sensing domains. To ensure this current can be driven for the sensor domain configuration given in this work, a supply voltage,  $\pm V_s$ , of  $\pm 20$  V should be used.

### 5.2.4 Signal conditioning

To ensure that voltage generated by the current injection across a range of piezoresistive sensing domains can be read by the circuit's ADCs, a signal conditioning circuit is required. When using the recommended supply voltage of  $\pm 20$  V, an attenuation stage is required for the input into the ADC. This is done with an operational amplifier (opamp) voltage buffer-divider-buffer circuit as shown in Figure 5.7. When using a single ended 5 V supply to drive the current source this opamp circuit can be bypassed using the jumpers shown in Figure D.8 as the attenuation is not required and the offset and noise due to the opamp circuit can be avoided. However due

to a lack of a negative  $V_{ss}$ , the multiplexer channel resistance will be degraded as exemplified in Figure 5.9.

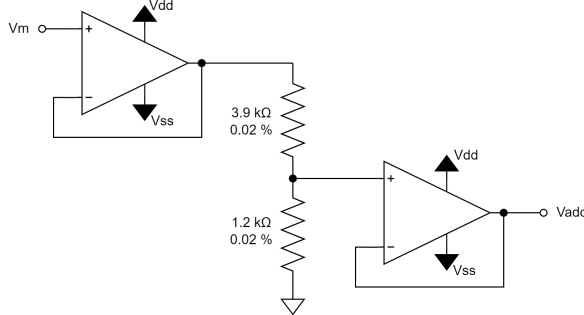


FIGURE 5.7: Measurement attenuation circuit

To allow larger current signals to be driven through the domain a maximum voltage driving the current source of 20 V is used with an attenuation circuit consisting of two voltage buffers and a voltage divider. The attenuation circuit steps down the voltage with a nominal gain of  $0.24 \pm 3\%$ . The attenuation circuit is duplicated for both differential ADC inputs. This circuit is highly sensitive to any noise, DC offset, or component variation. To combat the sensitivity of this circuit the opamps used [U10, U11] have a low input bias current, and low input DC offset voltage, the resistors used have a low tolerance of  $\pm 0.02\%$ .

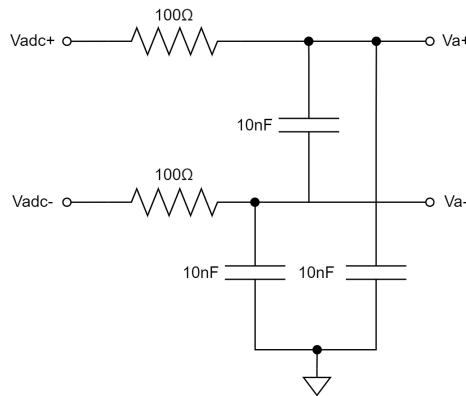


FIGURE 5.8: Passive low-pass filter circuit

A passive low-pass filter has been placed between the opamp circuit and the ADC input to attenuate ADC input noise. The cutoff frequency for this filter has been set to a value of, 1 MHz allowing for sufficient settling time for the maximum potential ADC sample rate of 512 kSPS.

### 5.2.5 Switching circuit

Previous research has shown the trade-offs with different EIT drive patterns [185, 262, 263]. A 4:16 multiplexing circuit allows for a range of EIT switching drive patterns for ERT data acquisition. A multiplexer with a low drain-source on-resistance characteristic for smaller drain voltages has been chosen as the majority of the voltage readings being read through the multiplexer will be nearer to zero than  $\pm V_s$ .

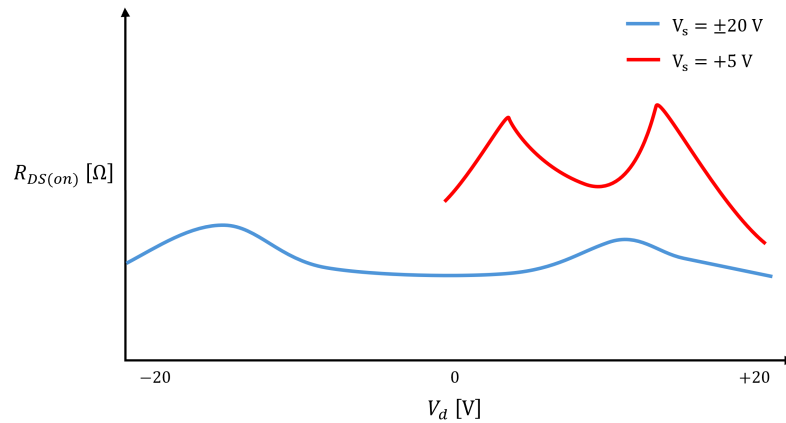


FIGURE 5.9:  $R_{DS(on)}$  characteristic diagram for a typical multiplexer analogue channel for a dual and single-ended power supply.

[264].

Any variation in the  $R_{DS(on)}$  value as a function of  $V_D$  or from channel-to-channel will add to the offset noise read by the ADC lowering the resolution of the ERT pressure sensor. This low  $R_{DS(on)}$  variation can be seen in Figure 5.9. The multiplexer used can switch analogue voltage up to  $\pm 22$  V with a switching time of 200 ns [264].

### 5.2.6 Position control and measurement

To accelerate experiment development a simple and accurate Cartesian force applicator was required. The Prusa MK3s 3D printer was used as the Cartesian force applicator base, because of its proven reliability as a 3D printer to move in x, y, and z axes with high resolution. The printer head was modified to attach the load applicator module described below. The resolution of the force applicator location under without applying a load is 0.01 mm in each axis. Due to the open-loop nature of control of the stepper motors the resolution at high loads may not be reliable.

### 5.2.7 Force measurement

The CFA system is designed to be used with soft piezoresistive sensing domains due to loading limitations of the 3D printer frame and the force applicator head design. The force applicator head must be significantly more rigid than the sensing domain being tested to ensure low strain error.

A static load FEA simulation was completed on the loadcell bracket with the maximum load expected used as 100N. The material of the bracket was PLA with orthotropic material properties. The static simulation used the orthotropic 3D printed PLA properties given by Sosa-Vivas et al. [265] with Caculix FEM solver [266]. As shown in Figure 5.10 the maximum predicted displacement of an FEM element within the loadcell part was 0.13 mm. If using a sufficiently soft domain and small force applicator this maximum displacement has little effect on the data processed, however this may cause significant error within harder domains and/or larger force applicators. Although the device can operate at 100 N, device operation is recommended below 50 N to decrease the strain error due to force applicator deformation.

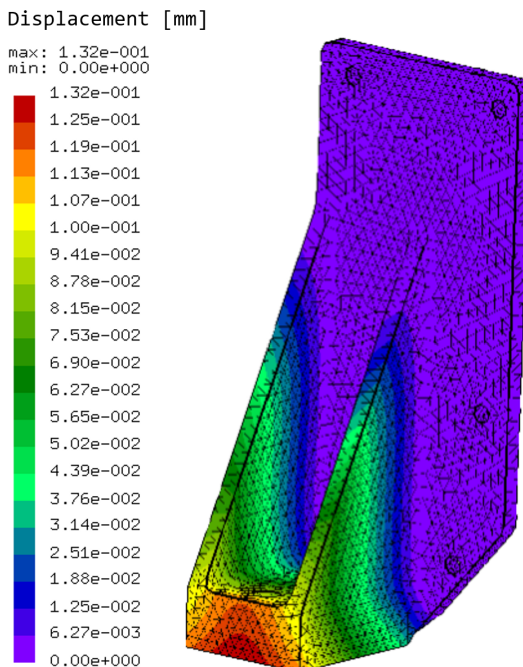


FIGURE 5.10: Static load analysis of the loadcell bracket part [PR9] of maximum allowable load of 100 N showing the magnitude of displacement.

The TAL220 loadcell used was chosen for the sensing domain material. The CBSR material had an elastic modulus of 100 kPa [17] so that range of strain measurements from 0 - 50% could be accurately recorded with the given loadcell. The minimum force is on the limit of what can

be detected as the loadcell is rated for  $\pm 50$  mN resolution [267] across its operating load and temperature range. However the noise of the loadcell was measured to be  $\pm 2.5$  mN during several 15 minute experiments in a  $22 \pm 0.7$  °C regulated room. Examples of experiment loading limits are given in Table 5.1, giving the extreme cases for testing minimum and maximum theoretical strain for 5 and 20 mm diameter force applicator heads on a lower and higher elastic modulus material respectively.

TABLE 5.1: An example of the extreme parameter limits of two loading experiments showing the minimum and maximum strains limits for 5 mm and 20 mm diameter force applicators and their required forces respectively.

Force [N]	Force applicator diameter [mm]	Force applicator area [mm <sup>2</sup> ]	domain elas- tic modulus [kPa]	Theoretical strain [%]	Theoretical stress [kPa]
0.06	5	19.6	60	5.1	3.1
50.00	20	314.2	200	79.6	159.2

### 5.2.8 Sensing domain

A core purpose of this system is to test a range of different sensing materials over a range of shapes and sizes. This platform provides a two degree-of-freedom load application over a  $220 \times 180$  mm area where the load can be applied at heights of 0 to 150 mm.

The example PNEC sensing domain in this work is a carbon black silicone composite. The weight percentage of CB powder in an elastomer matrix to maintain desired mechanical and electrical properties can be tuned as shown in the characterisations completed in literature [241, 242] and in the previous two chapters. The most desirable piezoresistive characteristics found in these works are near the inflection point of the conductivity versus CB weight percentage plot.

Because of the difference in fabrication processes and degree of dispersion generating variability in the percolation, an iterative trial and error approach using the starting point found in literature was used to get 8 wt % and 9 wt % values for CB in SR [241, 242]. Within this range the material was sufficiently conductive while maintaining mechanical strength through sufficient elastomeric cross-linking. Previous research indicates that there is a weight percentage at which the gauge-factor/piezoresistivity is at a maximum within a similar range used in this work [243, 244]. The CB particle dispersion can vary throughout a domain depending on various factors in the fabrication process including mixing technique, solvents used, silicone viscosity, particle size, particle agglomerations, amongst other factors [225, 268–270]. Dispersion

of carbon black particles was ensured by using a relatively low viscosity silicone of 6,000 mPa.s and a centrifugal planetary mixer a method proven to give more homogeneous dispersion than other traditional mixing techniques [271].

### 5.3 Validation and Characterisation

To show that the system is functional, the plots produced from an EIT reconstruction of the voltage data and the force measurements can be compared for a correlation. Examples are given below in Figure 5.11 and 5.12, showing localised blobs at the known locations of the force applicator.

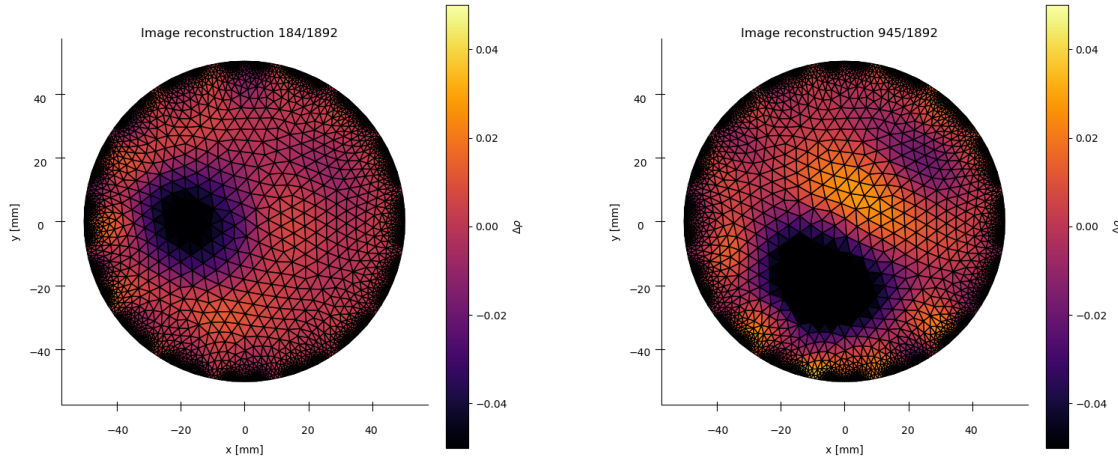


FIGURE 5.11: Reconstruction frames from a random push test sequence on a 1mm thick 100mm diameter sample. Strain and applied locations (x, y) [mm] - Left: 24% (-14.8, -3.4). Right: 36% (-1.9, -21.3)

A raw video of this experiment can be seen in the supplementary material [250]. It may be useful to plot the force profile being applied alongside the EIT reconstruction to verify the data is ready for further processing and modelling.

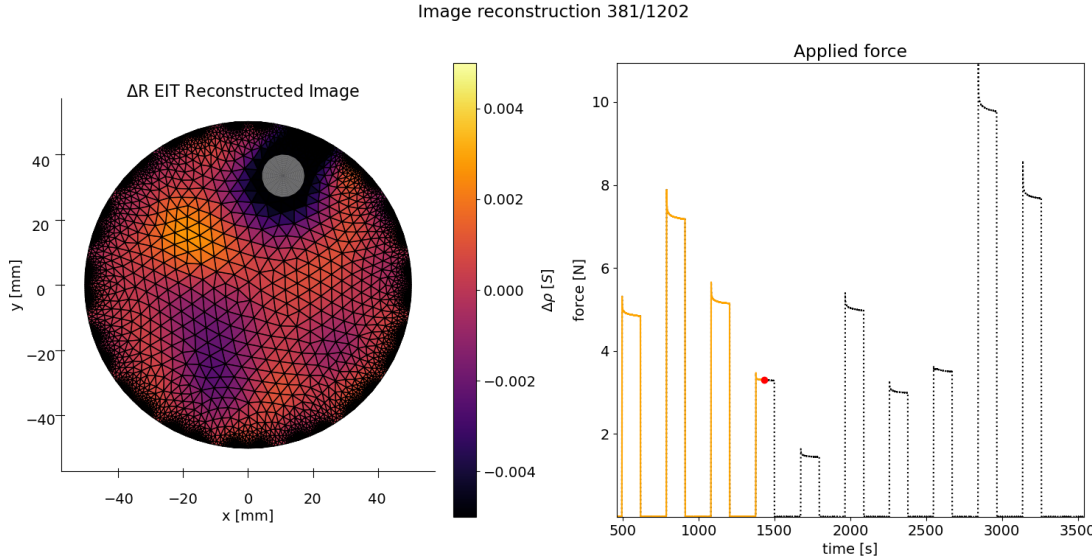


FIGURE 5.12: Reconstruction frames from a random push test sequence on a CBSR 100mm diameter sample. The white circle representing the force applicator location and the red dot on the force plot showing the captured frame in time.

### 5.3.1 Sensor capabilities

Simultaneous application of multiple loads can be achieved with this system using a multi-head force applicator. It has been shown that multiple touch points can be detected as shown in Figure 5.13 the supplementary material and in our previous work [18, 250].

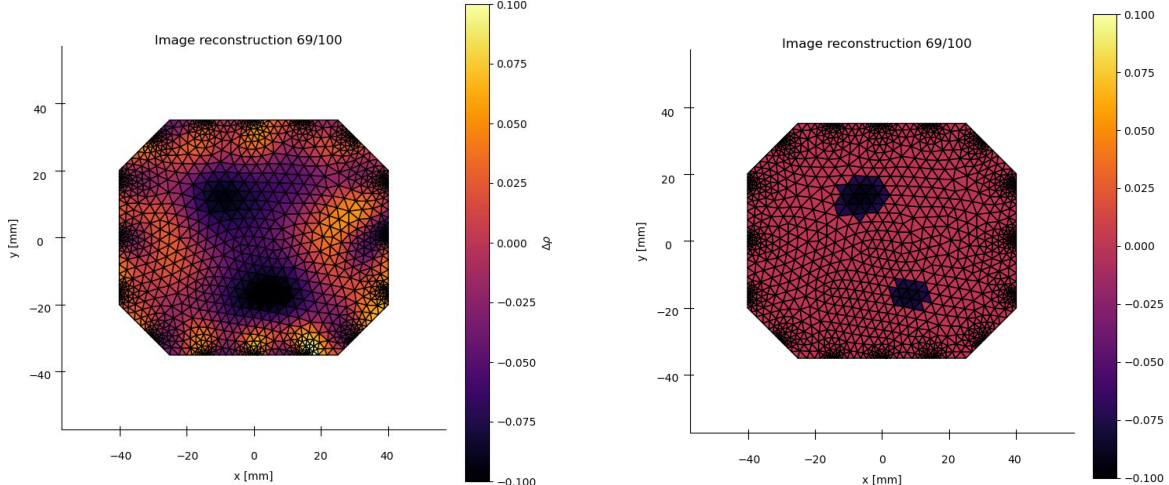


FIGURE 5.13: An EIT reconstruction image of a sensing domain with two loads applied simultaneously. Left: Without threshold filtering. Right: With a 75% threshold amplitude filter applied.

A major factor constraining the application of EIT-based sensors is the poor frequency response of the material, which limits the detection of rapid successive loads. The system given in this

work allows further research into characterising the transient response of a range of sensing domains in 2D. Examples of how transients have been characterised are shown in Figure 5.14

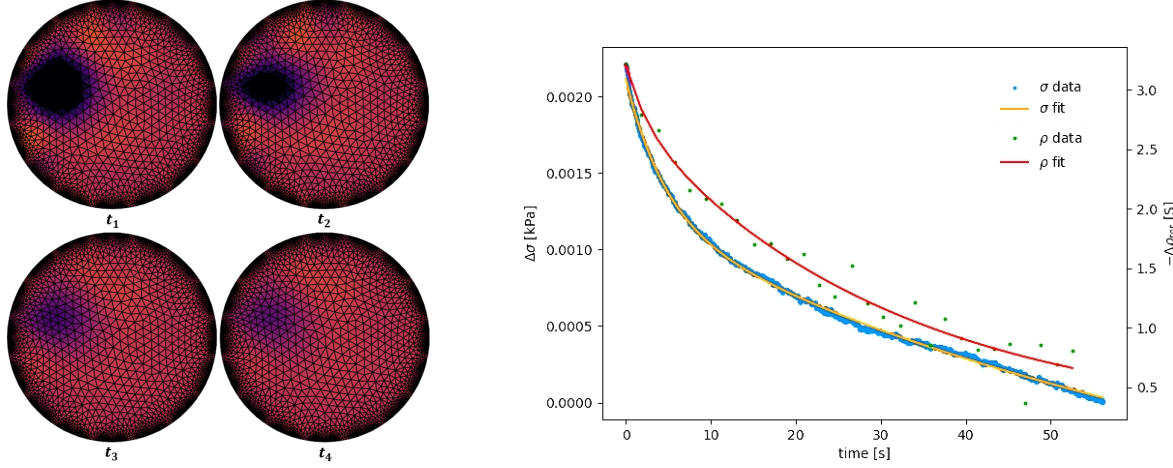


FIGURE 5.14: Left: Example sequence a resistive relaxation after a loading event at times  $t_1$  to  $t_4$ . Right: Example stress,  $\sigma$ , and resistive,  $\rho$ , relaxation plot generated from an ERT CFA experiment given a 30% strain step input [17].

The piezoresistivity of a sensing domain can often vary throughout its volume giving unpredictable results if a homogeneous domain is assumed for the pressure mapping sensor. This system can be used to generate map of the piezoresistivity function of a material surface in 2D dimensions.

## 5.4 Discussion

To move the field of EIT-based soft pressure mapping forward, there is a need to optimise materials for qualities such as pressure sensitivity, homogeneity, electrode connectivity, and dynamic viscoelastic properties. This CFA automates the testing process with easily changeable spatio-temporal parameters, such as strain magnitude, strain rate, and strain profile. This system standardises the analysis of the pressure mapping by allowing for the EIT reconstructed resistance images to be compared with stress and strain data form the sensing domain material.

The hope for the hardware and software given in this paper is that it will provide a standardised platform for future researchers to use to further quantify the utility of other sensing materials, and their compare their performance metrics with standard loading test procedures, as done in our previous work [17]. The ERT sensor and force applicator hardware could be utilised in further research for; 2D piezoresistive material analysis, pressure mapping device characterisation and performance for spatio-temporal performance, dynamic stress sensing performance,

piezoresistivity. These research applications are all working towards development for real-world applications such as robotic skin integration, sports sensing, and prosthetics.

## 5.5 Conclusions

This work has provided the methods and tools to enable further research and development for soft EIT-based pressure sensing systems. The system is low cost, simple to construct, and easy to use. The automation of compression load experiments ensures that experiments are repeatable with quantifiable results and mitigating human error. The automated nature of the CFA device significantly reduces the time to complete a set of experiments and can provide experiment sequences similar to those expected during the real-world application of the sensor. Upon load experiment completion, the system provides clearly formatted raw data files ready for analysis.

A ERT circuit was developed with a data capture frame rate of 12.7 Hz, a drive current of 15  $\mu$ A - 50 mA at  $\pm 22$  V, measurement resolution of  $\pm 0.3$   $\mu$ V. The Cartesian force applicator system developed can apply compressive loads between 0 - 800 mm/min with a xy position resolution of 0.01 mm, and can sense loads from 0 - 100 N with a resolution of  $\pm 50$  mN.

Uses of this system vary from 2D piezoresistive material analysis and pressure mapping sensor characterisation. Extensive research has been conducted into one-dimensional (1D) characterisation of piezoresistive materials. However, the characterisation of these materials in two dimensions (2D) has often been overlooked in past literature [88, 242, 246, 272], often due to the complex and invasive methods required. The device can be used to characterise the electromechanical/piezoresistive properties of a soft thick film material in 2D, quantify EIT reconstruction performance, and generate models predicting localised loads from localised resistance changes.

To push the field of EIT-based pressure mapping forward tools are required to standardise testing and reliably acquire quantifiable data for pressure modelling in different sensing domain materials. A toolbox of hardware and software have been described in this work to make EIT-based pressure mapping realisable for more real-world applications.

Proposed future enhancements of the system include minimising noise and offsets in the signal conditioning ERT circuit, adding an auto-calibration procedure to ensure the ADC and  $I_{src}$  circuits operate at the expected resolution, and reducing the PCB size. Also extending the device to drive and read AC signals may mean the complex electrical properties of some PNECs could

be used to improve the system performance. The ERT sensor and Cartesian force applicator system described in this work will help transition this technology into real-world applications.



# Chapter 6

## Integration of EIT-based Pressure Mapping with Dielectric Elastomer Actuators

### Overview

Dielectric elastomer actuators (DEAs) commonly use flexible conductive electrodes to apply an electric potential to actuate. Depending on the material used, these electrodes often possess predictable piezoresistive properties. Combining electrical impedance tomography (EIT) with a dielectric elastomer actuator (DEA) is investigated in this work to map compressive forces occurring throughout the electrode surfaces. Current self-sensing of a DEA has only been achieved in a one dimension using the overall change in capacitance. The technology in this work could allow for enhanced closed-loop control of electroactive actuators using two-dimensional sensing, broadening the already extensive set of DEA applications. This deformation mapping system also has potential to be used with other piezoresistive materials opening up applications requiring a range of hardnesses and pressure sensitivity. With the material used in this work, the DEA-EIT device has an inherent trade-off between actuation and pressure mapping accuracy driven by the compliant electrode thickness of the DEA. It has been shown experimentally that the simultaneous actuation and EIT mapping can be achieved on the designed hybrid DEA-EIT device. The DEA-EIT device exhibited actuation strains of 2.5 % with a mean centre-of-mass detection error of  $1.66 \pm 0.17$  mm for 2 mm thick DEA electrodes. Future designs will ensure that applications requiring human-like manipulation can be designed, ranging between

biomedical implant devices, agricultural processing equipment, soft optics, and bio-mimicked robotic aquatic life.

## 6.1 Introduction

Fine motor manipulation, pressure sensitivity, and pressure mapping are some core attributes of skin and muscle tissues when innervated to the brain. These functions can be emulated and combined with two core technologies; Dielectric Elastomer Actuators (DEAs), and Electrical Impedance Tomography (EIT) based pressure mapping.

DEAs have been used to mimic biological muscles in many applications, because of the technology's likeness to biological muscle in terms of elasticity, energy density, and various potential shapes/topologies [168, 273, 274]. In previous chapters, it was determined that pressure mapping similar to that of human mechanoreceptors could be emulated using EIT with a piezoresistive nanoparticle elastomer composite (PNEC) in a planar sheet format [18]. The key qualities of the EIT-based sensing platform were that; pressure estimates could be obtained, and the pressure could be mapped and the spatial performance quantified [17]. Like DEAs, this sensing technology has a likeness to human tissue in terms of mechanical characteristics such as elasticity, and the potential of various topologies.

Alongside the visual and other sensory feedback, animals receive when actuating muscle tissue, pressure-sensitive mechanoreceptors are present within the muscle tissue [275] and soft skin tissue to aid control the extent of a muscle contraction. This forms a multi-sensor closed-loop control system with a complex biological control regime. This work is looking towards creating a closed-loop control system which utilises a DEA-based artificial muscle and an EIT-based artificial skin all contained within a stack of two composite electrodes and one dielectric elastomer body. Applications such as the ones conceptualised in Figure 6.1 can be designed with the use of DEA-EIT integrated technology.

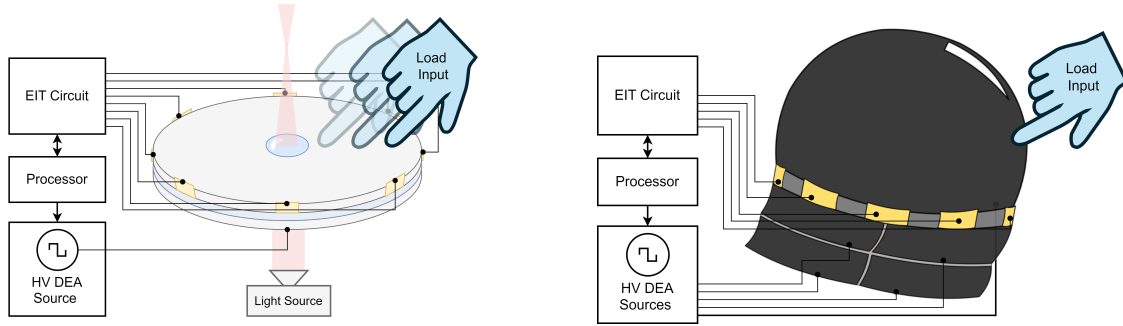


FIGURE 6.1: Potential future application of the DEA-EIT device topology. Left: EIT sensor input DEA controlled optical lens. Right: Pressure mapping sensitive skin for a DEA propelled jellyfish soft robot.

### 6.1.1 Background

The fundamental principles and a brief explanation of the state-of-the-art of each DEA and EIT-based sensor technologies are given in this section. A review of pressure mapping devices with actuation capabilities was then completed. At the time of completing this work, no literature had been found regarding the combination of these two technologies using PNEC electrodes on a DEA for simultaneous execution of sensing and actuation events.

#### 6.1.1.1 Dielectric Elastomer Actuators

DEAs are often referred to as artificial muscles because they share similar characteristics to biological muscle. Although commonly used as an actuator, this technology offers versatile applications as an energy generator [276–278] or sensor and provides attractive features such as high energy density, large displacements, and fast response times. DEAs have been proven to produce strains larger than 1600 % [133] which is significantly larger than that of regular biological muscle. However, large DEA strains can often be at the cost of actuator instability and a low effective force. DEAs have a high work and power density comparable to that of biological muscle and have been found experimentally to have energy densities of around 3.4 J.g<sup>-1</sup> and theoretically an order of magnitude more [201, 278]. A dielectric elastomer actuator (DEA) is a form of soft robotic actuator that induces deformation with an applied electric field. A simple common configuration of DEA is a circular parallel plate capacitor, which consists of a thin elastomer sheet between two compliant conductive electrodes, as shown in Figure 6.2.

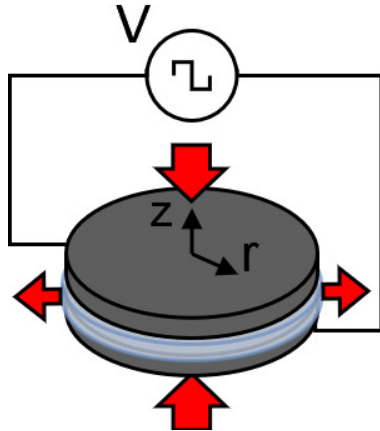


FIGURE 6.2: A circular DEA exemplifying its actuation principle.

When a voltage is applied to the compliant electrodes, an electrostatic force arises between the electrodes causing the dielectric elastomer (DE) membrane to contract by a decrease in thickness and an increase in area. The resulting actuation is controlled by changing the applied voltage. The region encompassing the two compliant electrodes and the DE portion sandwiched between them is called the ‘active region’, i.e. where the electric field is largest. For a simple DEA such as the one shown in Figure 6.2, a simplified formula for the electrostatic force on the compliant capacitor electrodes is given in Equation 6.1.

$$\sigma_{es} = \epsilon_0 \epsilon_r \frac{V^2}{z_{de}^2} \quad (6.1)$$

Where  $\sigma_{es}$  is the electrostatic stress,  $V$  is the applied voltage,  $z_{de}$  is the DE thickness,  $\epsilon_0$  is the permittivity of free space, and  $\epsilon_r$  is the relative permittivity constant of the DE, which is a function of strain [226, 227, 279] and applied voltage [37]. This can be expanded to estimate the DE strain,  $S_{z_{de}}$ , using the bulk modulus,  $K$ , of the DE as shown in Equation 6.2.

$$S_{z_{de}} = \frac{\sigma_{es}}{K} \quad (6.2)$$

Designing a DEA for practical applications is often highly constrained by three key modes of failure as well as the parameters of the constituent components. A common mode of failure is the electromechanical instability of the elastomer. With increasing voltage, the DE compresses until the voltage exceeds the critical point at which dielectric breakdown occurs. At the point of failure, the DE membrane experiences a surge of electrical current, permanently changing the DE insulative properties. The second mode is a loss of tension in the elastomer when an applied voltage is large and the axial force provides an excessively large compression. The stress

in the DE may cause the plane to lose tension such that the elastomer no longer actuates as expected, if at all. Often resulting in visible wrinkles in the DE. The third mode is a physical rupture of the elastomer due to stretching beyond the DE's yield strength [280]. A key benefit of DEA technology is its potential to be fabricated into various topologies depending of the desired application including, parallel plate [133], roll [281], tube [282], helical [173], and conical geometries [283].

### 6.1.1.2 Soft EIT-based Pressure Mapping

To estimate the 2D resistivity of the PNEC a technique called electrical impedance tomography (EIT) was used. A soft EIT-based pressure mapping sensor has the ability to estimate the magnitude and location of deformation events in a planar PNEC material. As discussed in previous chapters the hardware required usually consists of a piezoresistive sensor domain with attached boundary electrodes, EIT driver electronics, and a reconstruction processor. Boundary electrodes allow a non-invasive method of pressure mapping without compromising a monolithic piezoresistive material. Several researchers have created an EIT-based pressure mapping sensor using a range of piezoresistive domains and custom or lab-based hardware [17, 65, 185, 194, 235, 236]. The stages required to generate a pressure image using EIT can be simplified into three core stages, data acquisition, image reconstruction, and inverse force model implementation.

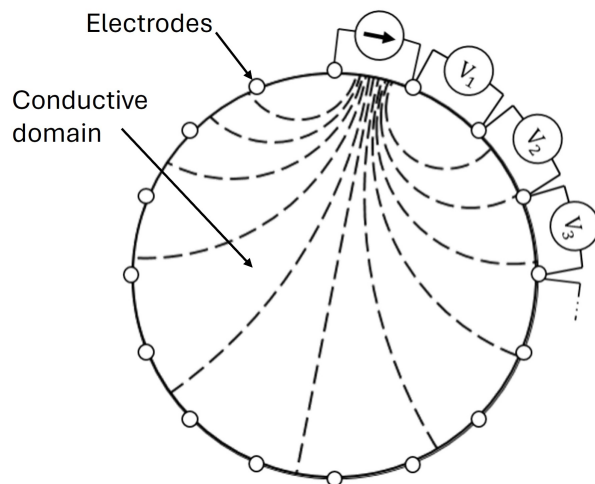


FIGURE 6.3: A 16 electrode circular EIT domain setup exemplifying its electrical function. Where the dashed lines are representative of an applied electric field [18].

### 6.1.2 Simultaneous Pressure Mapping and Actuation

Various researchers have demonstrated and proposed the use of self-sensing DEAs for closed-loop control looking at the one-dimensional deformation of a DEA using their change in capacitance [36, 38, 39, 284]. Multi-degree-of-freedom (multi-DOF) DEA topologies have been created by several researchers [285–288], allowing for a broader range of applications. The complex actuation mechanisms discussed in these papers give rise to the question of having multi-dimensional sensor data for such topologies to aid with the control of such multi-DOF devices.

To sense deformation in multiple dimensions, the current methods used for DEA self-sensing must be altered. To ensure the DEA maintains minimal change to the parallel plate topology, the compliant piezoresistive electrodes can be used and/or altered to be able to determine the deformation of the DEA in more than one dimension. Options for sensing in two dimensions include determining the stretch across the compliant electrode material by measuring the change in resistance of the electrodes diametrically opposed at various angles around the DEA, or adding an extra pressure mapping sensor layer to the DEA stack, or using EIT to map change in resistance of the compliant electrodes. Using diametrically opposed resistance measurements across the compliant electrodes will have limited resolution and is limited in compliant electrode shapes that can be used effectively. Adding another sensing layer to the DEA requires a sensing technology that has a very low elastic modulus, to not hinder the actuation force of the DEA. The limitations given above are why EIT was chosen to sense 2D deformation of a DEA, as it has a relatively high spatial resolution that can be quantified and requires no extra hardware on the DEA body apart from non-invasive electrodes on the boundary of the DEA’s compliant electrode(s).

## 6.2 Methodology

The DEA-EIT actuator-sensor-hybrid system required the two technologies to be verified and fabricated individually before being integrated to observe the effects of combining the two technologies relative to their independent forms. The following sections discuss the fabrication process for the DEA and EIT systems and then the integration of them both into a DEA-EIT device.

To optimise the actuation and sensing capabilities of the DEA-EIT system different parameters of the design were altered, such as the compliant electrode composite used, DE material used,

circumferential electrodes, and magnitude of DE pre-stretch and sizing. The methodology explores the reasoning to certain design choices for the fabrication of the DEA design seen in Figure 6.4.

### 6.2.1 Dielectric Elastomer Preparation

The fabrication of the DEA used a rigid acrylic frame to attach the pre-stretched elastomer. For simplicity, a circular frame was chosen with the DE at a radial pre-stretch of +10%, i.e.  $\lambda_r = 1.1$ , as this is well within the DE's more predictable linear elastic region. The circular acrylic frame of 178 mm inner diameter was fabricated from laser cut acrylic of 4 mm thickness to ensure rigidity.

To achieve uniform stretch of the elastomer sheet, a toroidal shower hose mechanism was placed on the relaxed sheet of 4910 VHB tape (3M, Saint Paul, USA), which would act as a pre-stretcher annulus. The toroidal mechanism has an axis of rotation along its circumference as shown in, giving the ability to roll and stretch the elastomer equiaxially to the desired pre-stretch.

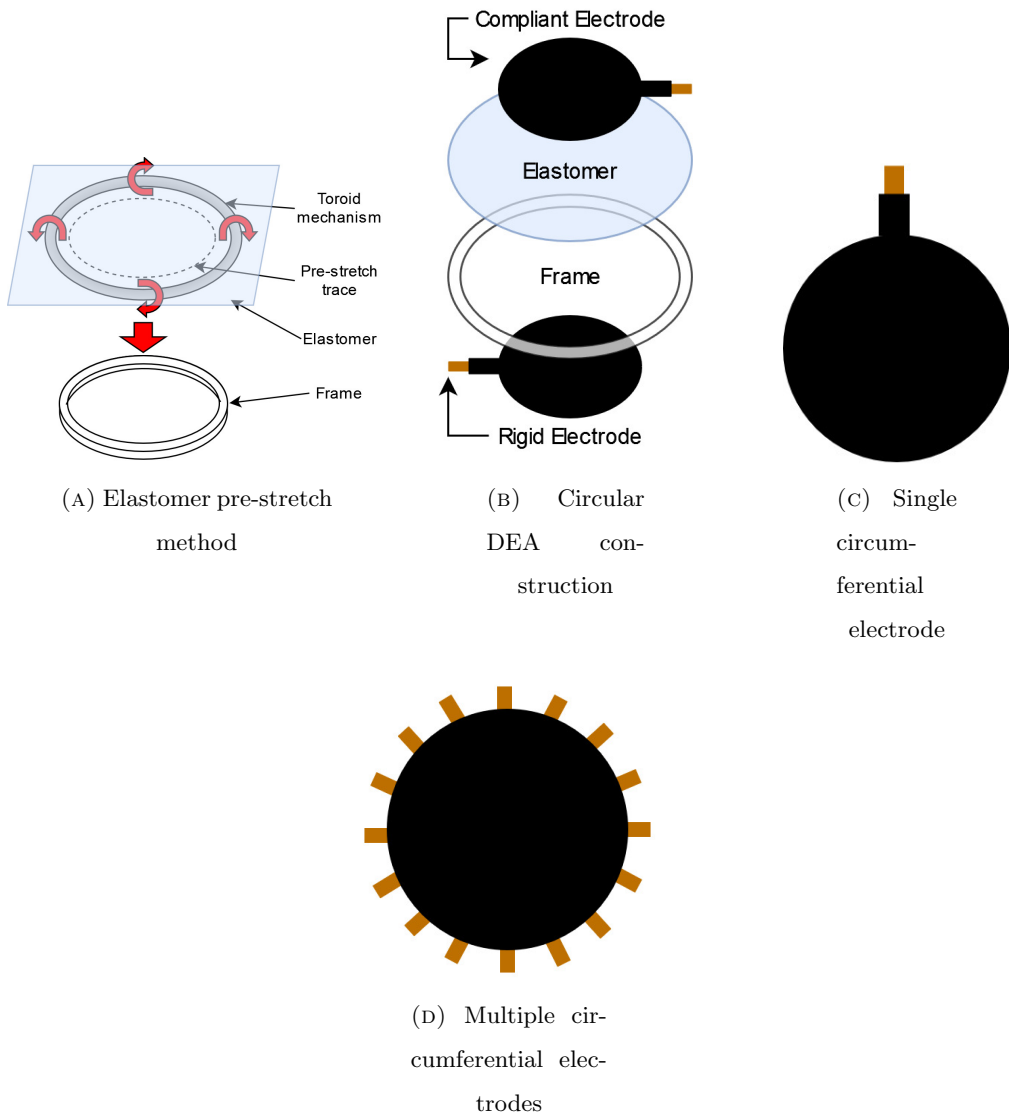


FIGURE 6.4: Mechanical fabrication of the circular DEA-EIT platforms

### 6.2.2 Compliant Electrode Fabrication

Compliant electrodes (or active area) were fabricated using acrylic moulds of varying dimensions. Three thicknesses,  $z_{ce}$ , of the compliant electrode were fabricated, 0.5 mm, 1 mm and 2 mm, with two circular compliant electrodes of 100 mm diameter. Different thicknesses were explored as this would vary the actuation and sensing performance of the electrodes.

Two compliant electrode mediums were used in this work, carbon black (CB) powder and a carbon black silicone rubber (CBSR) composite. Compliant electrodes solely made of CB powder have been used for DEAs in previous literature [289–291], hence this work uses the same compliant electrode type to generate reference data for actuation performance. The CB

powder was used to make a single circumferential electrode configuration DEA as a reference to compare to the following DEA-EIT experiments. The CBSR composite was used to make both single (Figure 6.4b) and multiple (Figure 6.4d) circumferential electrode configurations of DEAs. The CB powder used in all of the compliant electrode samples was Vulcan XC-72 CB powder (Fuel Cell Store, Bryan, USA). The CBSR composite had 8% CB by weight mixed with DragonSkin 10NV silicone rubber (Smooth-On, Macungie, USA). This composite is a piezoresistive medium that has proven useful for EIT pressure mapping and sensing in previous work [17], and DEA actuation [289, 290].

Using the liquid silicone rubber, the CBSR composite mixture was formed by combining part A of the silicone solution and 8 wt% CB and mixing by hand for 10 s. The mixture was then placed in the ARV-310PCE planetary vacuum mixer (Thinky Inc., Tokyo, Japan) to complete a mixing cycle with 500 RPM for 45 s followed by a cycle with 800 RPM for 45 s. In the same mixing container, part B of the silicone solution was added to the mixture and stirred by hand for 10 s and immediately the same mixing cycle in the planetary mixer was completed again. After the cycle was completed, the composite was poured into the mould with attached circumferential copper tape electrodes. The CBSR mixture was then placed in an oven at 80 °C for 4.5 h to ensure the composite was sufficiently cross-linked.

Two types of compliant electrode configuration have been fabricated in this work, single circumferential electrode and multiple circumferential electrodes. The single circumferential electrode configuration was purely for testing DEA actuation. The multiple circumferential electrode configuration consisted of 16 evenly spaced circumferential electrodes. The multiple circumferential electrode configuration was for testing both EIT-based pressure mapping and actuation functionality of the DEA. Prior to curing the compliant electrode in a circular mould, the conductive copper tape circumferential electrodes were placed into the mould. The width of the circumferential electrodes were 8 mm. The circumferential electrodes were placed with a 3 x 8 mm area embedded in the compliant electrode circumference edge with the rest of the circumferential electrode protruding for easy access to external electrical connections.

### 6.2.3 DEA Hardware

The excitation voltage for the DEA was provided by a Trek 610E high voltage supply (Advanced Energy Industries, Fort Collins, USA) providing a maximum voltage output of 10 kV DC. The DEA was placed in a clear insulated box with the high voltage supply leads attached to the rigid copper electrodes of the DEA. The current limit of the high voltage supply was set to its

maximum of 2 mA to maximise the DEA actuation response due to the compliant electrodes charging. The  $RC$  time constant varies depending on the CB percentage in the compliant electrode composite and the DE thickness and dielectric constant used. However, for these experiments the actuation strain were left to reach a steady-state before they were imaged, to mitigate time-dependent phenomena.

For the DEA actuation strain measurement an iPhone 11 camera (Apple Inc., Cupertino, USA) with a resolution was used to obtain images of the radial compliant electrode strain as shown in Figure 6.5. The camera could capture  $2160 \times 3840$  px (i.e. 8.29 MP) 110 mm frames of the 100 mm DEA subject. Hence, the images captured have a resolution of  $50.9 \mu\text{m}/\text{px}$ . Due to compounding physical non-idealities in the system such as incorrect focal, exposure time, and other internal camera parameters the blur seen within these images can be up to the order of 0.5 mm. However, this is minimised by using relative measurements of the DEA diameter in the captured image frames.

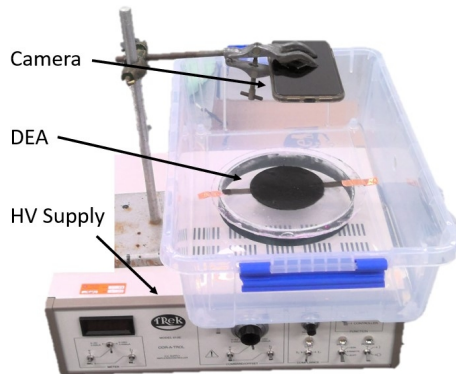


FIGURE 6.5: DEA excitation and measurement setup

#### 6.2.4 EIT Hardware

The EIT hardware allows for data collection to reconstruct a conductance map of the piezoresistive composite used as compliant electrodes in the DEA samples. The hardware required for this function, shown diagrammatically in Figure 6.6, includes a 2634b source measure unit (SMU) (Keithley, Solon, USA), a custom 4:16 multiplexer (MUX) PCB, an ESP32 development board, a Cartesian force applicator, and a reconstruction and control computer.

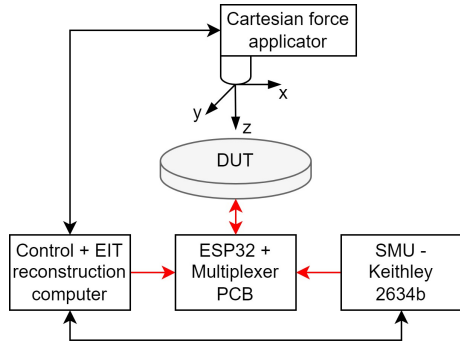


FIGURE 6.6: Architecture of the force applicator and EIT measurement system [17]

The SMU provides a constant current value of 1 mA and reads a series of voltages through the MUX PCB required for the EIT drive pattern. An adjacent electrode EIT drive pattern was used for EIT through the circumferential electrodes of the compliant electrode. The MUX PCB and SMU and controlled by the control computer. Once the data for each image reconstruction has been gathered the control computer was also used for the reconstruction of the conductivity maps of the compliant electrodes. The Cartesian force applicator is made up of a MK3s 3D printer (Prusa, Prague, Czechia) integrated with a loadcell and fabricated applicator tip to apply loads and hence generate data for pressure magnitude and localisation quantification.

### 6.2.5 Experimental Method

Before attempting to have simultaneous DEA actuation and EIT sensing occur in the same device, each system had to be tested independently. First DEA strain voltage relationships were explored followed by EIT-based pressure mapping of the DEA electrodes. Finally the same samples used for EIT testing were subsequently integrated into a DEA device for simultaneous functional testing.

#### 6.2.5.1 DEA Validation

DEA actuation strain measurements were taken from voltages 5 kV to 10 kV in 1 kV increments. The SNR of strain measurements of the DEA excited with voltages  $< 5$  kV were deemed to be too low to generate meaningful data. The excitation voltage was toggled between on and off states waiting for the strain deflection to reach a steady state for the strain measurements. Five radial strain images were captured and measured. The measurements were then averaged to minimise error and determine the radial strain uniformity. The radial strain was found by measuring the

radial change of the circular compliant electrodes between relaxed and electrically contracted states. From the radial compliant electrode strain the planar and thickness deformation of the DE was estimated. The DE is assumed to be incompressible and have a Poisson's ratio,  $\nu$ , of 0.5. The adhesion between the compliant electrode and the DE is assumed to be perfect to simplify the model used here. The thickness strain,  $S_{z_{de}}$ , is calculated using Equation 6.3 [289] and 6.1.

$$S_{z_{de}} = \frac{1}{(S_{r_{ce}} + 1)^2} - 1 \quad (6.3)$$

Where  $S_r$  is the radial strain measured from the equiaxial actuation. The elastic modulus of a hyperelastic material such as VHB is often defined as a non-linear function of strain and strain rate [292]. In this work a linear bulk modulus value,  $K$ , of 142 kPa was used. The bulk modulus was determined by doing a meta-analysis and averaging of the elastic moduli determined at steady state 10% strain for VHB 4905 material in previous literature [39, 292, 293]. The relative permittivity,  $\epsilon_r$ , used in Equation 6.1 was approximated to be  $4.5 \pm 0.2$  due to pre-strain effects seen in literature [226, 227, 279, 294].

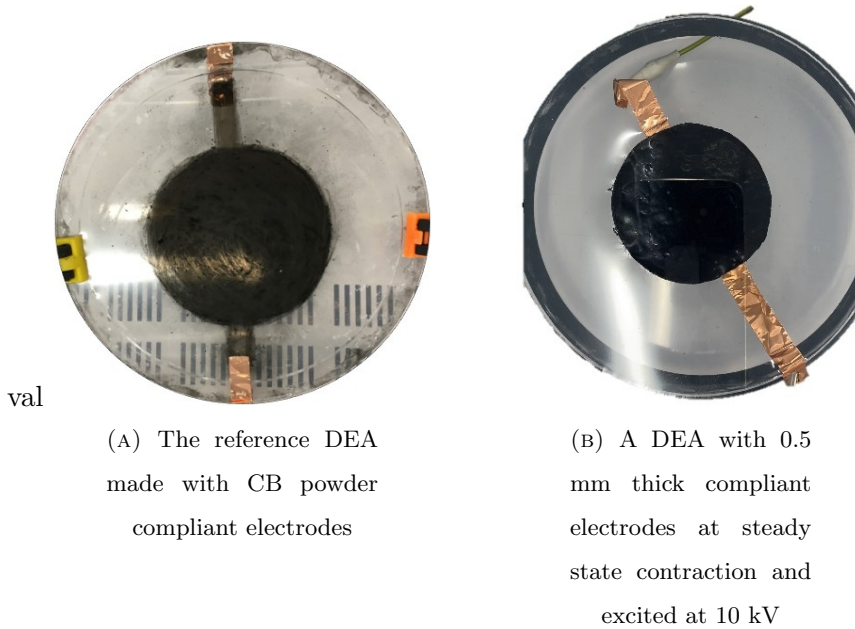


FIGURE 6.7: The two DEA compliant electrode material types used in this work.

### 6.2.5.2 EIT-based Pressure Mapping on DEA

A load sequence on various locations of the compliant DEA electrode was used to show the range of load areas that could be localised using EIT. A similar test procedure used in previous work [17] was applied to the three individual compliant electrodes thicknesses,  $z_{ce}$ , of 0.5, 1,

and 2 mm. Nine load application points were determined on the material at three distinct radii as shown in Figure 6.8.

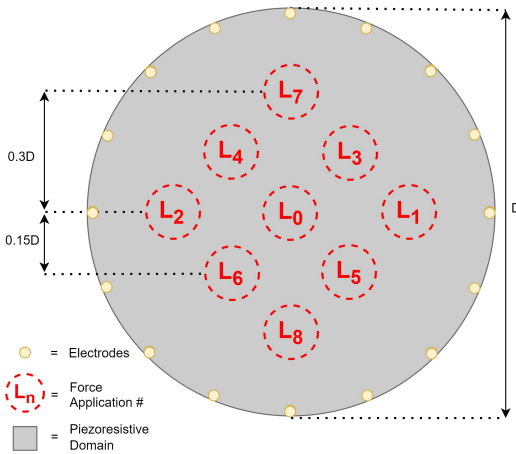


FIGURE 6.8: Load application areas used for compressive stress testing in order of application [17].

A Cartesian force applicator applied the loads with varying strains in the nine locations. Once the compliant electrodes had undergone the first load application tests, they were applied to each side of a DEA and tested again using the same sequence of nine loads. Compressive strains from 0 to 30% of the electrode thickness in 5% increments were applied when to each of the load points using a flat circular 13 mm diameter force applicator. When applying the compressive strain to the compliant electrodes, a slow strain rate of  $16.67\%.s^{-1}$  was used to minimise piezoresistive transient phenomena. After completing the load tests on individual compliant electrodes the compliant electrodes were attached to the DE surface. Next the load test was completed again to the DEA placed on a flat surface.

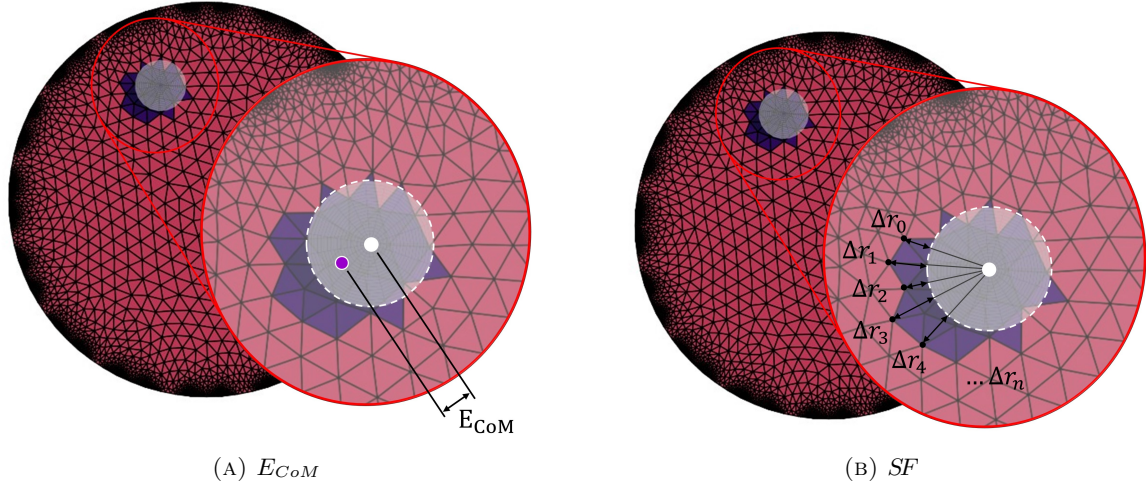


FIGURE 6.9: The two spatial performance metrics used for determining accuracy of blob as a load area estimate, where the transparent white circle is the actual load area and the dark purple elements are the load estimate area.

$$SF = \left( \sum_n^i \Delta r_i^2 \right) / n \quad (6.4)$$

Similar to Chapter 4 experimental EIT data and load data is gathered and EIT conductance images are reconstructed. To form blobs as estimates of the applied loads, post-processing was completed by applying an 85 % threshold mask to the EIT image. These blob images were subsequently analysed using two spatial performance metrics, the centre-of-mass error,  $E_{CoM}$ , and the shape fit,  $SF$ , as exemplified in Figure 6.9. The  $E_{CoM}$  values were determined by calculating the difference between the CoM of the actual load and the blob representing the load estimate. The  $SF$  was determined by calculating the radial mean square error between all of the,  $n$ , perimetral nodes of the blob load estimate and the actual load circumference, as taken from the CoM of the actual load area.

### 6.2.6 Simultaneous Actuation and Pressure Mapping

The DEA-EIT device was tested for simultaneous actuation and pressure mapping to highlight the functional limitations that arise with such a device. Simultaneous actuation and pressure mapping involves an excitation voltage is applied to the DEA whilst completing EIT to the grounded DEA electrode.

To ensure that the EIT electronics are able to operate during transients or dielectric breakdown events, an intermediary 20 V Zener diode array and a current limiting resistor,  $R_{lim}$ , were added to the system as shown in Figure 6.10.

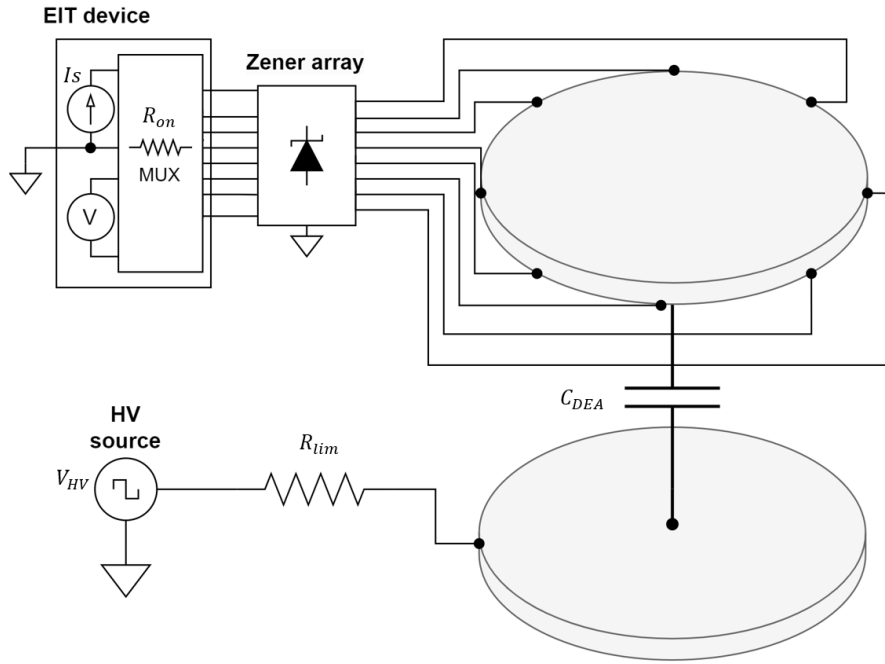


FIGURE 6.10: System architecture for simultaneous DEA actuation and EIT mapping.

When the DEA is switched on, the compliant electrodes charge. During this charging period a voltage will be developed on the HV and low-voltage EIT electrode characterised by the charging capacitance,  $C_{DEA}$ , the HV source resistance,  $R_{lim}$ , and the multiplexer on resistance,  $R_{on}$ . The resistance of the DEA is lumped in with  $R_{lim}$  for the Equations 6.5 and 6.6 below. The charging of the DEA capacitance is governed by Equation 6.5.

$$V_{DEA_{HV}}(t) = V_{HV}(1 - e^{-t/(R_{on} + R_{lim})C_{DEA}}) \quad (6.5)$$

In the configuration shown in Figure 6.10, a voltage divider is created between the  $R_{lim}$  resistor and the multiplexer,  $R_{on}$ , on-resistance to ensure the voltage seen at the multiplexer input pin is sufficiently low. The voltage seen on the multiplexer pin is given by Equation 6.6.

$$V_{MUX}(t) = V_{HV} \frac{R_{on}}{R_{on} + R_{lim}} e^{-t/(R_{on} + R_{lim})C_{DEA}} \quad (6.6)$$

To mitigate the effects of the DEA switching transients during loading experiments, the loads were applied when the DEA voltages were at steady state, as exemplified in Figure 6.11, to observe the effects of the high voltage electrode on the EIT electrode mapping.

To investigate the effects the DEA voltage switching transient has on EIT data capture, EIT frames were captured during switching events as shown in Figure 6.11.

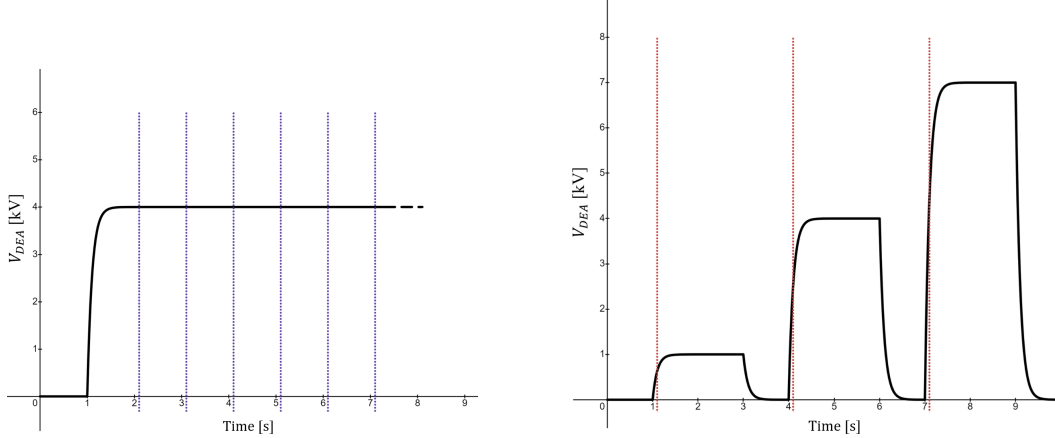


FIGURE 6.11: Illustrative experiment timing diagrams. Left: Steady state  $V_{DEA}$  where the purple dotted lines represent the time a load event begins. Right: Transient EIT measurements where the red dotted line represents the time an EIT frame capture begins.

## 6.3 Results

First the measurements taken during fabrication are explored, followed by the results from the independent DEA actuation validation and EIT pressure mapping validation. Finally, results are presented on the phenomena of concern when integrating HV DEAs with EIT-based pressure mapping.

### 6.3.1 Fabrication

Prior to constructing the DEA, the compliant CBSR inter-electrode resistances,  $R_{int}$ , were measured in a similar fashion to voltage shown in Figure 6.3 to ensure the sufficient conductivity and hence CB particle dispersion for DEA actuation and EIT-based sensing.  $R_{int}$  between the adjacent circumferential electrodes for all samples was consistently  $< 20 \text{ k}\Omega$ , as shown in Table 6.2. Therefore, the  $R_{int}$  values indicated a sufficiently low resistance for the EIT circuitry and indicates sufficiently homogeneous CB particle dispersion.

### 6.3.2 DEA Validation

Before testing the piezoresistive compliant electrodes for both actuation and pressure mapping capability, the reference DEA was tested for its voltage actuation strain relationship. The theoretical actuation strain versus voltage was compared to the measured strain for the reference DEA shown in Figure 6.7a. The actuation strain data gathered is shown in Figure 6.12. The range given was derived from substituting the range of  $K$  and  $\epsilon_r$  parameter values found in previous similar works [39, 292, 293] into Equations 6.1 - 6.3.

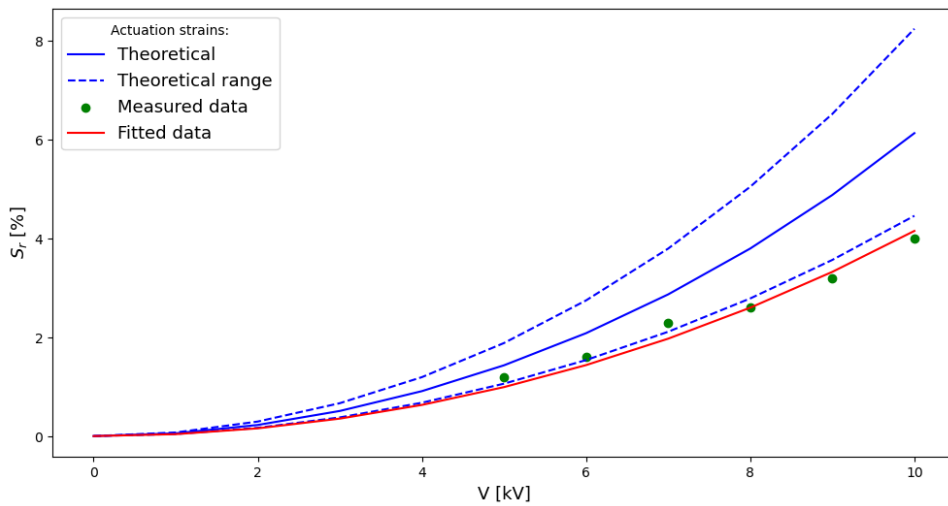


FIGURE 6.12: Comparing the measured CB reference DEA strain, the theoretical strain average and range, and the data fitted to Equation 6.3 by fitting either parameter  $K$  or  $\epsilon_r$ .

The curve fit shown in Figure 6.12 was found to have a linear set of solutions for  $K$  and  $\epsilon_r$  with values similar to those limits of the material given characterisation determined in previous literature [295].

The CBSR compliant electrode experiments showed significantly smaller strains relative to the DEA with the CB powder compliant electrode as displayed in Figure 6.13. The effective mechanical impedance for the DEA with the CBSR compliant electrodes was significantly increased due to the relative thickness of the CBSR electrode and similar bulk modulus relative to the DE VHB material. Hence an effective bulk modulus,  $K_{eff}$ , was calculated from fitting to the measured data, as a sum of the existing DE bulk modulus,  $K$ , and the effect of the compliant electrode's bulk modulus.  $K_{eff}$  is the a key characteristic of using thick compliant electrodes on a DEA that limits the actuation performance. When calculating  $K_{eff}$ ,  $\epsilon_r$  is assumed constant, as the effects of this different compliant electrode thickness on  $\epsilon_r$  is assumed relatively negligible.

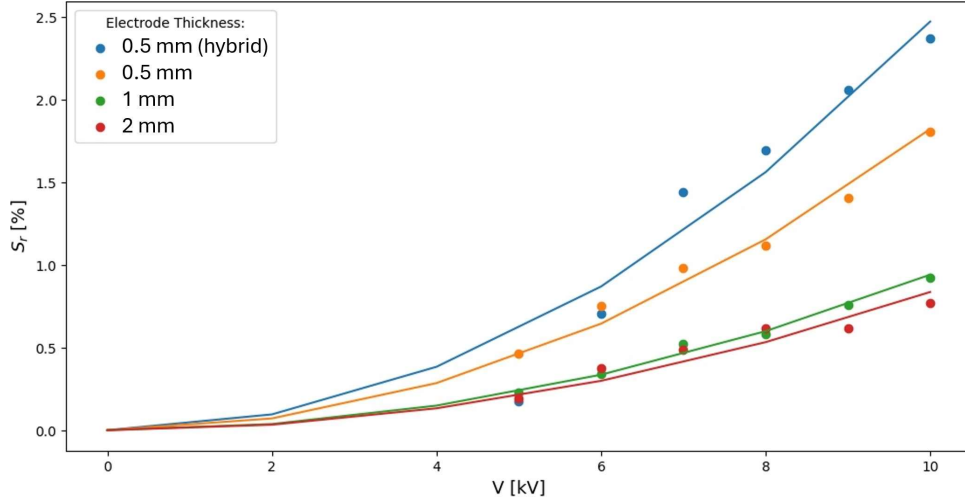


FIGURE 6.13: Comparison of the voltage strain relationships between the 100 mm diameter compliant electrodes of various thicknesses,  $z_{ce}$ , used for the DEA.

The effective bulk modulus impeding the actuation of the DE was calculated for each CBSR compliant electrode thickness by fitting to Equation 6.3 with the results displayed in Table 6.1. To further enhance the actuation strain,  $S_{z_{de}}$  of the DEA-EIT device, the compliant electrodes

TABLE 6.1: Effective bulk modulus,  $K_{eff}$ , and coefficient of determination,  $R^2$ , for each fit of voltage-strain data for the CBSR compliant electrodes.

$z_{ce}$ [mm]	$K_{eff}$ [kPa]	$R^2$
2	966	0.86
1	860	0.99
0.5	450	0.98
0.5 (hybrid)	334	0.91

were hybridised such that one of the compliant electrodes was made from CB powder and the other from the CBSR composite. The hybridised results for the  $K_{eff}$  value are also given in Table 6.1.

### 6.3.3 EIT Validation

Validation of the EIT sensing method on the compliant electrodes was carried out for the three different electrode thickness,  $z_{ce}$ , values to see the differences the thickness may have on the pressure mapping characteristics' spatial performance. Figure 6.14 exemplifies the difference in the conductance reconstructions for a load.

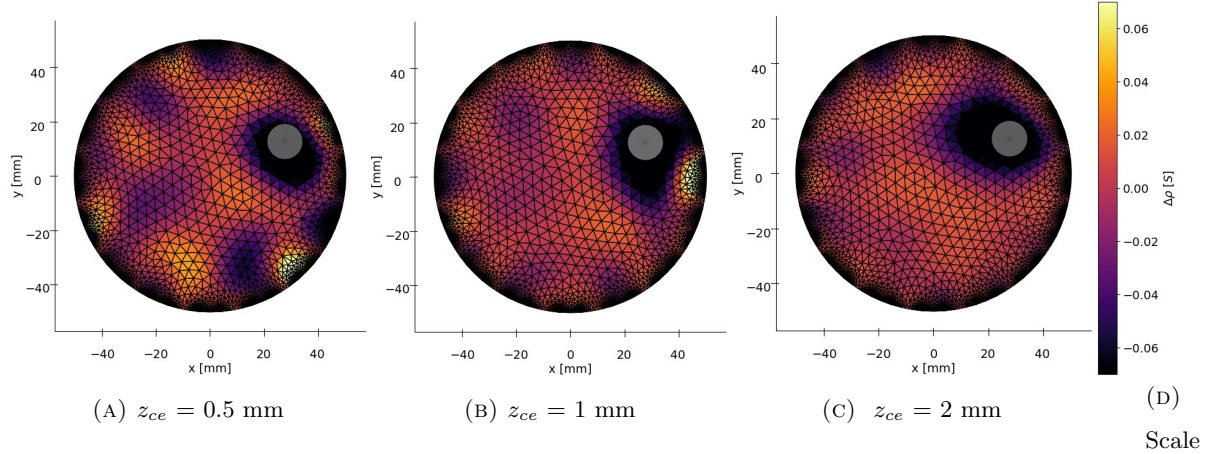


FIGURE 6.14: A 15% strain compression at point  $L_1$  applied to 100mm diameter compliant DEA electrodes of 3 compliant electrode thicknesses.

A significant factor for determining the minimum pressure able to be detected is governed by the noise floor experienced when the domain is in a steady relaxed state. A metric used to quantify the noise floor is the noise figure,  $NF$ , which is commonly used in other applications of EIT [17, 193]. To quantify the domain homogeneity the inter-electrode resistance (i.e. between adjacent electrodes) and respective standard deviation data for each sample was gathered alongside the NF, as shown in Table 6.2.

TABLE 6.2: Noise factor and mean inter-electrode resistance,  $\bar{R}_{int}$ , for each thickness of compliant DEA electrode used for EIT

$z_{ce}$ [mm]	$NF$	$\bar{R}_{int}$ [kΩ]
2	0.99	$4.40 \pm 0.69$
1	0.98	$7.72 \pm 1.14$
0.5	0.96	$9.91 \pm 2.16$

To quantify the localisation performance of the loads applied to the DEA compliant electrode the centre-of-mass error,  $E_{CoM}$ , and shape fit,  $SF$ , of the sensing system were calculated. A polar histogram plot of the  $E_{CoM}$  values from each frame from an experiment are displayed in Figures 6.15a - 6.15b. From this same experiment a mean  $E_{CoM}$  is given in Table 6.3.

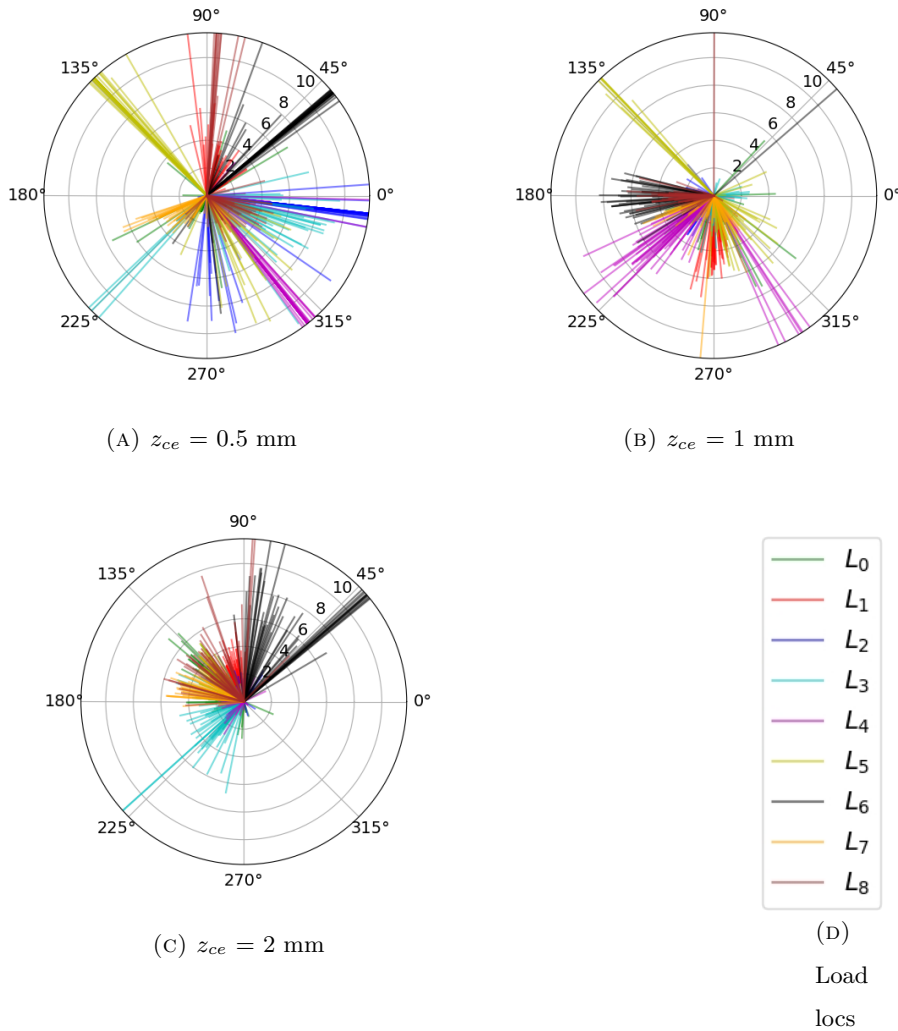


FIGURE 6.15: Vectorised  $E_{CoM}$  for the nine load experiment at 20% compressive strain for each  $z_{ce}$  value tested on individual DEA-EIT compliant electrode samples.

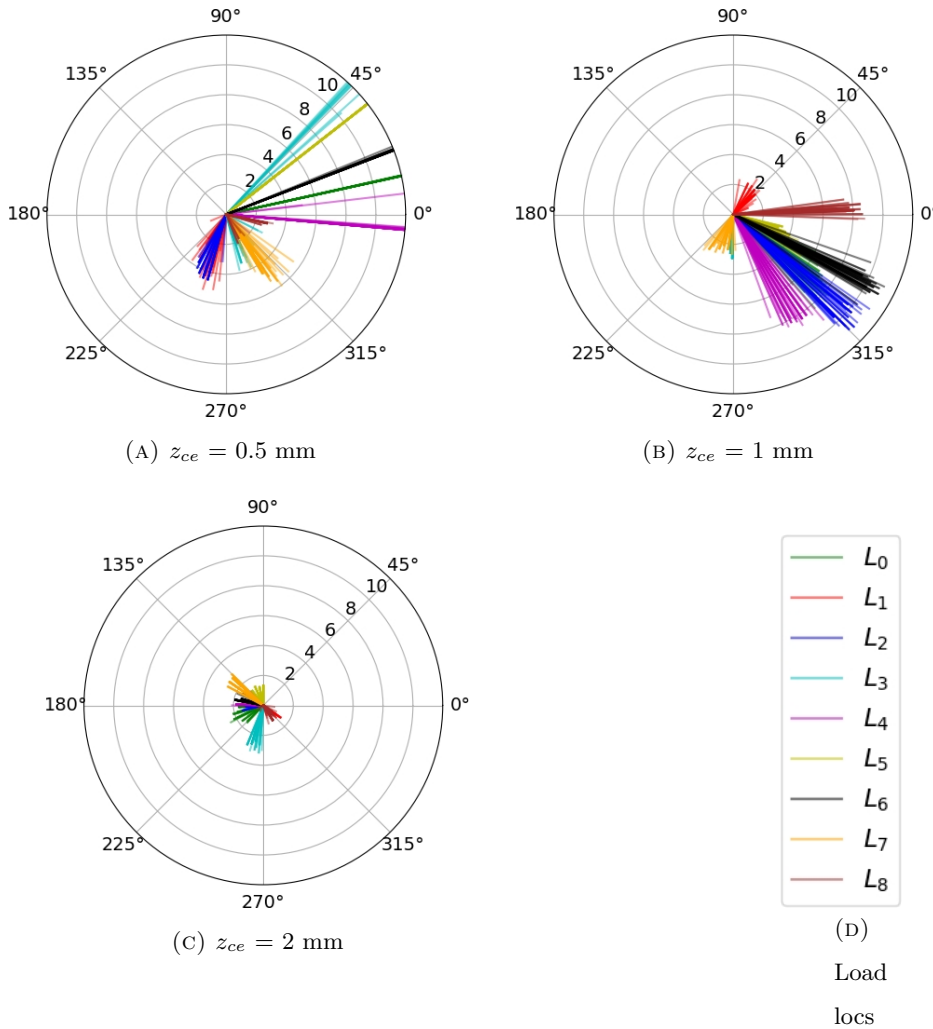


FIGURE 6.16: Vectorised  $E_{CoM}$  for the nine load experiment using the same indentation depth as Figure 6.15 for each  $z_{ce}$  value tested on the DEA-EIT integrated samples.

Mean values for the spatial performance metrics,  $E_{CoM}$  and  $SF$ , were gathered for each strain, each thickness, and at each load point. Spatial performance metric means from two nine load experiment are given in Tables 6.3 and 6.4. The  $SF$  values are found using Equation 6.4.

TABLE 6.3: Mean  $E_{CoM}$  and  $SF$  values ( $\pm$  std) obtained for each DEA compliant electrode thickness at 20% strains loads

$z_{ce}$ [mm]	$\bar{E}_{CoM}$ [mm]	$\bar{SF}$ [ $\text{mm}^2$ ]
2	$4.10 \pm 1.9$	$46.03 \pm 0.51$
1	$4.25 \pm 2.4$	$36.93 \pm 0.92$
0.5	$10.43 \pm 6.1$	$81.92 \pm 8.4$

TABLE 6.4: Mean  $E_{CoM}$  and  $SF$  values ( $\pm$  std) obtained for each DEA stack at the same indent depth as 20% strain in Table 6.3 loads. \*Where the compliant electrode is part of a DE compliant electrode DEA stack.

$z_{ce}^*$ [mm]	$\bar{E}_{CoM}$ [mm]	$\bar{SF}$ [mm $^2$ ]
2	$1.66 \pm 0.17$	$46.03 \pm 0.56$
1	$6.01 \pm 0.44$	$37.03 \pm 1.1$
0.5	$8.83 \pm 1.5$	$81.64 \pm 8.0$

### 6.3.4 Simultaneous Actuation and Pressure Mapping

Simultaneous actuation and pressure mapping has been performed when at a range of actuation strains using excitation voltages ranging from 1 kV to 10 kV. Each DEA voltage excitation yielded similar noise in their reconstruction results as shown in Figure 6.17.

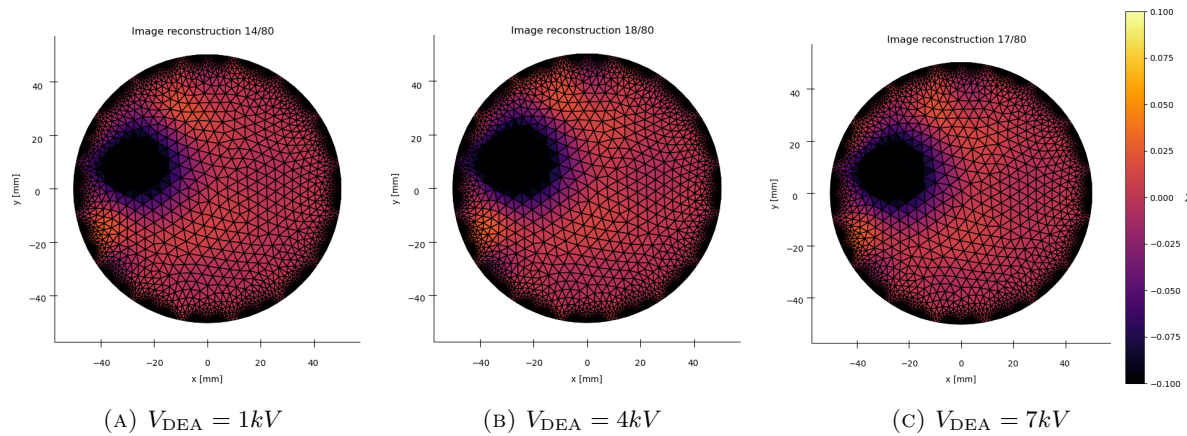


FIGURE 6.17: Loads applied to the compliant ground electrode of a DEA during different steady state voltage excitations,  $V_{DEA}$ .

The next set of experiments observed the transient effects of a high voltage step input the DEA during an EIT cycle. Artefacts such as the ones given in Figure 6.18 occur due the inrush/outrush currents across the DEA's capacitance.

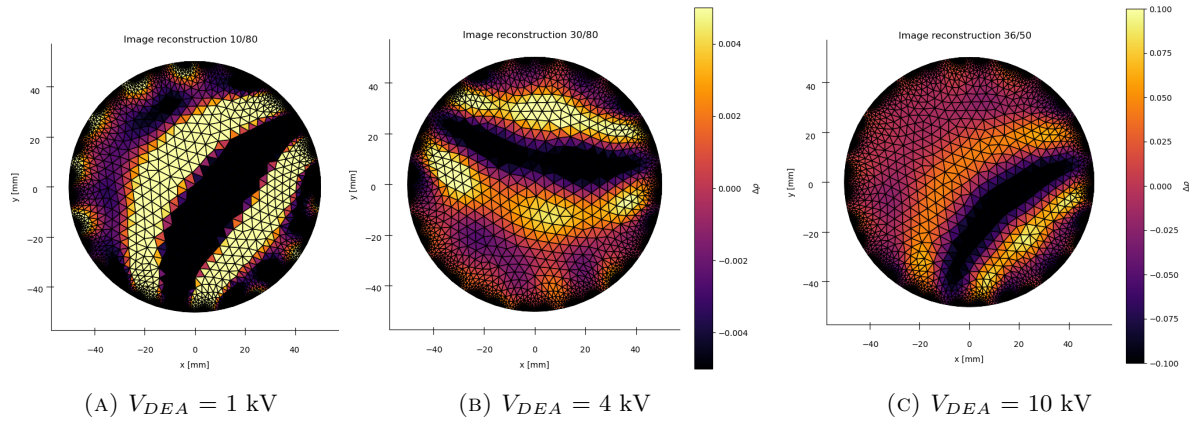


FIGURE 6.18: An unloaded DEA with a captured during various voltage,  $V_{DEA}$ , step input artefacts.

Note that the scale on Figure 6.18 contains two scales and one is an order of magnitude smaller than that seen in Figure 6.17 to highlight and investigate the transient artefact pattern observed.

## 6.4 Discussion

A system was created that could both generate strain and map strain events using common DEA componentry with a circular DEA topology. The major limitations of integrating the two technologies were explored and quantified as a starting point for the further optimisation of such a device.

### 6.4.1 Fabrication

Fabrication methods were successfully developed to create a range compliant electrode composites for successful DEA actuation and EIT-based pressure mapping. The fabrication process had limited quantification of the dispersion of CB particles within the CBSR composite material used for the DEA compliant electrodes. A basic check for homogeneity was done using the device hardware measuring the inter-electrode resistance between adjacent electrodes as shown in Table 6.2. Further validation to check the homogeneity of the whole domain could be done using other invasive or non-invasive methods such as a nail-bed resistance test and/or spectroscopic imaging. Inhomogeneity quantification on a resolution similar to that of the thickness of the material sample is important to obtain a higher SNR and hence  $NF$  value. Dispersion of the CB particles and minimisation of air voids was ensured by using a vacuum planetary

mixer, however a change to a less viscous liquid silicone rubber in future could ensure improved mixing, less air voids, and increased homogeneity.

A key limitation to decreasing the thickness of the compliant electrode occurs at a point where the tear strength of the material is significantly lower than the elastic modulus of the circumferential electrodes, hence increasing the likelihood of mechanical failure through tearing resulting in unstable conductivity or an open-circuit of the electrical connection.

Moulds were used successfully to generate a series of samples, in future work other techniques for film fabrication could be used to improve sample quality such as, screen printing, spin coating, and conductive coating deposition and spray methods [289, 296, 297].

Stress-strain characterisation of DEs in literature clearly shows a hyperelastic softening effect between 50 to 400 % strain for VHB film material whereby the elastic modulus decreases to 40 - 70 kPa [292]. This is significantly less than the assumed  $\sim 142$  kPa elastic modulus resulting from a 10 % pre-stretch in this work. This hyperelastic region should be determined using both the DE and compliant electrode materials' hyperelastic regions to ensure the  $K_{eff}$  is minimised for maximal actuation strain,  $S_{z_{de}}$ .

#### 6.4.2 DEA Validation

Through actuation testing of different compliant electrodes applied to a DEA, models were fitted to the voltage-strain data gathered with  $R^2$  values between 0.86 and 0.99. The model fitting resulted in the formation of effective bulk modulus,  $K_{eff}$ , values of the DEA active region ranging from 334 to 966 kPa for increasing  $z_c e$  values. The use of an effective bulk modulus constant only holds for a small linear range of strains. The CBSR compliant electrodes should be modelled to predict expected behaviours, for use to optimise for a improved performance of sensing and actuation. DEA actuation can also be optimised by tuning the pre-stretch of the DEA.

Mullins effect was expected to be observed in our experiments with CBSR compliant due to the nature of testing conductive particle filled elastomer composites [298]. Mullins effect is the change in the stress-strain relationship when stress testing a sample at a stress value at a stress value higher than the sample has experienced in previous testing. Therefore, often before characterising conductive particle elastomer composites, the composite sample should be subjected to a stress larger than that of the intended future experimentation stresses.

It is well known in literature and is intuitive that mechanical characteristics of a DEA's compliant electrodes have a significant effect on the actuation performance [295, 299]. However, there has been a lack of empirical evidence and subsequent modelling on quantifying how much the thickness of a piezoresistive composite electrode effects actuation performance. This work provides empirical data for creating and validating thick electrode DEA models, as a step towards optimising for both maximal actuation strain and maximal resolution for pressure mapping sensing in future work.

#### 6.4.3 EIT Validation

A metric used to determine the minimum resistance change measured and hence pressure sensed is the noise factor,  $NF$ .  $NF$  is analogous to SNR, but instead using EIT reconstruction noise vs EIT voltage data noise. It was found that for increasing values of  $z_{ce}$  the  $NF$  values also increased. This noise correlation is exemplified in Figure 6.14.

EIT was used to map nine compressive loads applied throughout the material successfully. To compare the performance of each thickness of the compliant electrode the spatial resolution was quantified using two main performance metrics,  $E_{CoM}$  and  $SF$ . For increasing thickness of compliant electrode the  $E_{CoM}$  and its standard deviation decreased by almost an order of magnitude. However, the  $SF$  values were all within the same order of magnitude and had decreasing standard deviations for increasing  $z_{ce}$ .

The vectorised format of the  $E_{CoM}$  gave a good indication of consistent biases that were present in the sample domains when compared across several repetitions of the same experiment. The vectorised  $E_{CoM}$  values do not appear random and may instead be due to inhomogeneity. This data could be used in future in a calibration stage to determine how pressure sensed in particular regions may be spatially biased and preemptively corrected.

To ensure the EIT domain reconstruction was geometrically accurate the circumferential electrodes were modelled in the meshing software to the same width as the real circumferential electrodes. However, the embedded depth of the circumferential electrode was not modelled. Due to the manual nature of the fabrication, significant error of up to 3 mm in the circumferential spacing of the rigid EIT electrodes was present, a factor which would be improved in future iterations especially if automated fabrication were to be implemented.

#### 6.4.4 Simultaneous Actuation and Mapping

The DEA-EIT device constructed in this work has been shown to complete simultaneous actuation and pressure mapping using the method shown in Figure 6.11.

There was no significant noise generated due to an active DEA electrode at a steady state voltage, however this may vary with rapid large loads which change the DEA capacitance and cause a large transient on the grounded EIT compliant electrode. The pressure mapping for 1 - 7 kV scenarios is shown in Figure 6.17.

The transients induced by the large sudden voltage changes are shown as crescent shaped artefact in Figure 6.18. The artefact seen in the image is due to an increase in the grounded DEA electrode voltage at a certain point during the data collection sequence of the EIT voltages.

Not all transient events were captured, which was due to aliasing. A lower EIT sample frequency and higher resolution ‘DEA transient’-‘EIT data capture’ synchronisation would aid in capturing these events more accurately.

This technology show promise and can be further optimised for improved actuation and pressure mapping capability. A system architecture integrating both DEA and EIT-based pressure mapping functionality into a single device is done using the components in Figure 6.10.

#### 6.4.5 Altered Actuation Performance

During a compressive load event to an actuated DEA-EIT device, the DE thickness is decreased which increases the electrostatic stress, Equation 6.2, induced by the same voltage. Therefore during a compressive loading event the stress applied to the material is a combination of the external compressive load and the increased electrostatic load.

Often a DEA is pre-stretched to take advantage of the hyper-elastic region of DE material so for a smaller change in electrostatic stress,  $\Delta\sigma_{es}$ , a larger strain,  $\Delta S_{z_{de}}$ , can be achieved. An externally applied load may mean that the stress-strain region the material may be in is changed (i.e. from a linear to a hyper/hypo-elastic region) and the same  $\Delta\sigma_{es}$  would have a different  $\Delta S_{z_{de}}$ .

#### 6.4.6 Dielectric Breakdown

During a compressive load event to an actuated DEA-EIT device, the DE thickness is decreased which increases the concentration of charge in the strain area. Both factors increasing the likelihood of dielectric breakdown within the material.

Feedback from the EIT pressure sensor could be used to decrease the actuation voltage if the device receives a strain that is likely to cause a dielectric breakdown.

An un-explored research avenue is the structural health monitoring of DEAs using EIT. It may also be possible to alter the system given in this work to map the location and size of any dielectric breakdown using EIT concurrently on each compliant electrode. This would allow for more technology to be developed around the self-healing of DEAs.

### 6.5 Conclusions

This work demonstrates the effective integration of Electrical Impedance Tomography (EIT) with Dielectric Elastomer Actuators (DEAs) for simultaneous pressure mapping and actuation. The findings indicate that the use of piezoresistive nanoparticle elastomer composites (PNEC) allows for the emulation of pressure sensing akin to human mechanoreceptors, enhancing the sensitivity and responsiveness of DEAs in various applications. Effective bulk moduli values were found to quantify the mechanical actuation impedance of each compliant electrode thickness used, ranging from 334 to 966 kPa. Force mapping was successful with decreasing degrees of mapping error with increasing compliant DEA electrode thickness. The best mean centre-of-mass error of  $1.66 \pm 0.17$  mm was found for the thickest, 2 mm, compliant DEA electrode used.

The work highlights the importance of electrode thickness on the performance of pressure mapping, revealing that thicker electrodes may improve the detection of pressure changes due to their lower noise factors. The results suggest that the EIT method can provide valuable feedback for controlling actuation, potentially preventing issues such as dielectric breakdown by adjusting voltage levels in response to detected strain.

Moreover, the research opens avenues for structural health monitoring of DEAs, enabling the mapping of dielectric breakdown locations and sizes, which could lead to advancements in self-healing technologies. Overall, the integration of EIT with DEAs not only enhances their

functionality but also broadens their applicability in fields such as robotics, soft actuators, and wearable technology, paving the way for future innovations in smart materials and systems.

## 6.6 Future Work

The integration of DEA and EIT in a portable package would open a range of applications. To integrate this portable EIT system into the DEA-EIT device mentioned, a DEA driver expansion board would be required for the hardware developed in the previous chapter. This would give an DEA-EIT device could have the capability of contracting and acquiring EIT voltage data for pressure mapping while maintaining a small form factor. A conceptual design of the DEA PCBA mounted on the portable EIT PCBA can be seen in Figure 6.19.

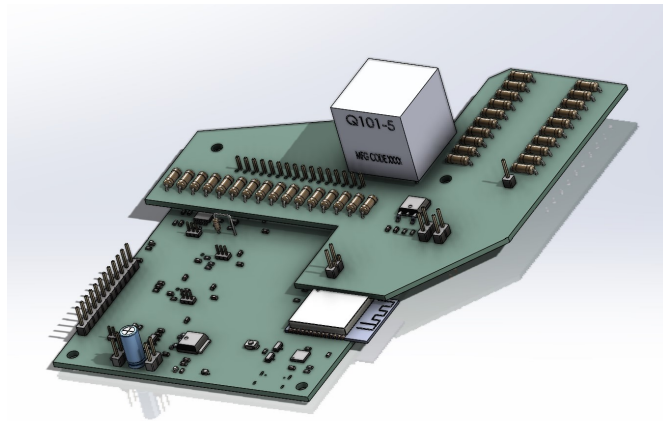


FIGURE 6.19: Render of a concept DEA daughter board mounted on the portable EIT board.

Future work also includes exploring the feasibility of using the DEA-EIT system as a dielectric generator which can power the EIT sensing system. However, more research is required into determining how to minimise the EIT circuit power consumption and maximise accuracy.

## Chapter 7

# Unintentional Power Generation in a DEA-EIT Sensor-Actuator Device

### Overview

This chapter investigates the phenomenon of unintentional power generation in Dielectric Elastomer Actuator (DEA) devices integrated with Electrical Impedance Tomography (EIT) for pressure mapping applications. While DEAs are primarily designed for actuation, they can inadvertently function as Dielectric Elastomer Generators (DEGs) due to localised mechanical strain during operation. The research explores the mechanisms behind this unintended energy generation, focusing on the changes in capacitance that occur when the DEA is subjected to varying loads. Through experimental simulations, the study quantifies the energy produced, revealing that energy generation can range from  $0.2 \mu\text{J}$  to  $4 \text{ mJ}$  depending on the load conditions. The findings highlight the multi-functionality of DEAs; actuation, sensing, and energy generation, emphasising the need for careful management of energy generation to prevent potential damage to connected circuitry. This work contributes to the understanding of DEA-EIT devices and their applications in soft robotics and simultaneous energy harvesting, suggesting that the energy generated could be harnessed for practical use in various scenarios, including vehicular and foot traffic loads. Future work aims towards harnessing the DEG energy shown in this work and using it to power the portable ERT-circuit in Chapter 5 expanding the range of potential applications.

## 7.1 Introduction

Dielectric Elastomer Actuators (DEAs) and Dielectric Elastomer Generators (DEGs) share a similar form whereby they both have compliant conductive electrodes either side of a dielectric elastomer (DE) membrane. However, DEGs represent a class of electromechanical devices that harness mechanical strain to generate electrical energy. DEAs and DEGs can often utilise the same soft electroactive area for actuation and power generation, but differ in the connected electronics. These devices exploit the properties of dielectric elastomers, which are soft, flexible materials capable of undergoing significant deformation. This deformation can be utilised to generate electrical power, making DEGs a promising technology for energy harvesting applications. However, DEGs can also arise as an unintended consequence of loading a DEA device.

In typical DEG configurations, the focus has been on uniform, global strain changes within the dielectric elastomer domain. Previous research has concentrated on scenarios where the entire thickness of the DE is reduced as a result of applied strain, leading to energy generation due to global DE deformations [278, 289, 300].

In contrast, this work explores unintentional DEG scenarios that have arisen from the invention of a hybrid actuation and pressure mapping DEA-EIT device. By investigating the effects of localised thickness reduction within the DE caused during a load event during DEA switching, unintended power generation due to the change in the device capacitance is observed.

This localised approach introduces a new dimension to DEG functionality, where strain is not uniformly applied but concentrated in specific areas. This DEA-EIT integration, as discussed in Chapter 7, allows for precise monitoring and analysis of localised deformations, thereby enhancing understanding potential scenarios where DEG behaviour may occur. In the existing literature, neither the intentional nor unintentional use of a DEA-EIT-like device as a DEG, when subjected to localised loads, has been investigated at the time of writing this work.

### 7.1.1 Background

Before describing how a dielectric generator arises in DEA-EIT device, it is important to understand the function of a DEA-EIT device first as described in detail in the previous chapter. A DEA-EIT device can use the same compliant electrodes and dielectric elastomer to function both as an electroactive actuator and pressure mapping sensor. The DEA function consists of applying a high voltage to a bottom electrode leaving the top electrode as the low voltage

electrode which performs as the pressure mapping surface. The pressure mapping surface is piezoresistive and uses electrical impedance tomography to map any changes in resistance and hence any loads throughout the electrode surface.

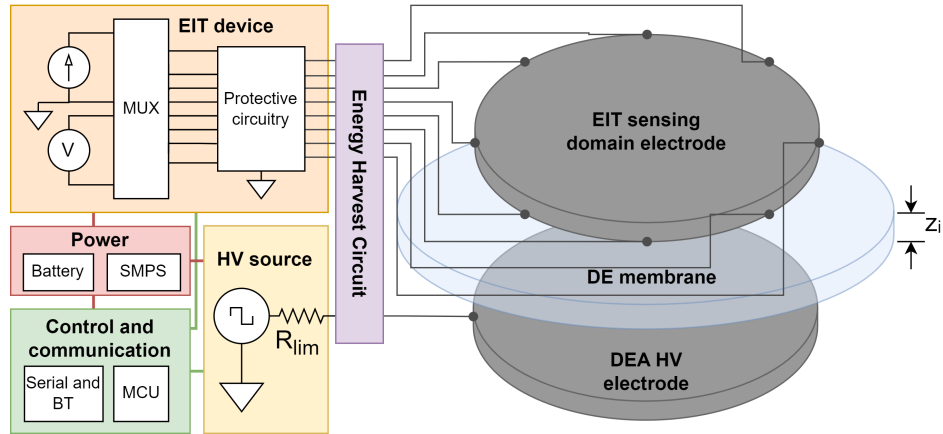


FIGURE 7.1: Architecture of a DEA-EIT pressure mapping and actuator device with an exploded view of the DEA stack.

A DEG may be incidentally be created during simultaneous DEA-EIT operation. This effect will take place when the DEA experiences sufficiently large external strains and DEA voltage switching at specific times. This DEG sequence is shown in Figure 7.2 and is explained as five distinct stages.

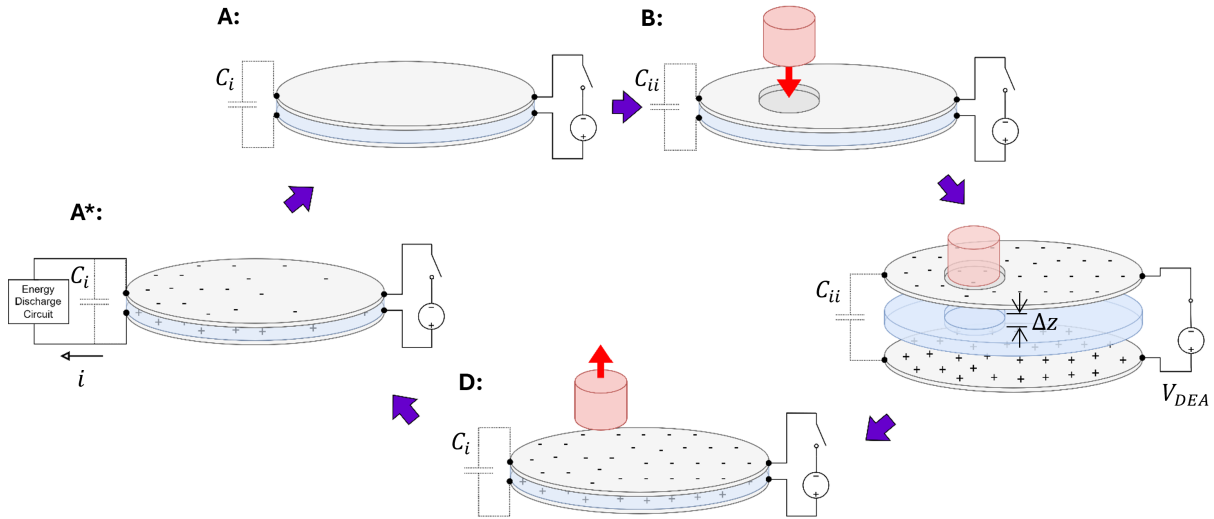


FIGURE 7.2: Dielectric elastomer generator scenario sequence with a localised compressive load.

Where  $C_i$  is the initial capacitance of the DEA,  $C_{ii}$  is the ‘primed’ capacitance of the DEA, the positive and negative signs, + and −, on the compliant electrode represent electrical charge,

and the red cylinder represents the load applicator. The typical operation of a DEG consists of the five main stages described below and exemplified in Figure 7.2. Note that the changes in electrostatic force due to loads are ignored.

**State A:** the DEA has an initial capacitance of  $C_i$ , is deformation free, and has zero voltage applied across the compliant electrodes.

**State B:** the DEA is compressed and deformed with a localised change(s) in thickness of the DE,  $\Delta z$ , increasing the DEA capacitance to  $C_{ii}$ . Work is done on the DEA by the compressive load storing elastic potential energy in the strained DE. As derived from Hooke's law the elastic potential energy,  $U_\varepsilon$  for a material of Young's modulus,  $Y$ , cross-sectional area,  $A_i$ , original thickness,  $z_i$ , and change in thickness,  $\Delta z$  is given in Equation 7.1. This equation is for a singular body with an even change in thickness across the area,  $A_i$ , showing the core parameters governing the elastic potential energy.

$$U_\varepsilon = \frac{YA_i\Delta z^2}{2z_i} \quad (7.1)$$

**State C:** An applied voltage,  $V_i$ , across the compliant electrodes generates electrical charge. The total charge developed,  $Q$ , is given by Equation 7.2.

$$Q = C_{ii}V_i \quad (7.2)$$

Charging the electrodes gives electrical potential energy to the DEA as it is now a charged capacitor. The electrical potential energy of the DEA is given by Equation 7.3.

$$U_{E(C)} = \frac{1}{2}C_{ii}V_i^2 \quad (7.3)$$

**State D:** The DEA is unloaded and returns to its original state with capacitance,  $C_i$ , while maintaining the same charge  $Q$  causing the voltage to increase to  $V_{ii}$  as shown by Equation 7.4.

$$V_{ii} = \frac{Q}{C_i} \quad (7.4)$$

When the load is released the elastic potential energy,  $U_\varepsilon$ , is used as the DEA returns to a relaxed state. In parallel, the increase in voltage on the DEA increases the electrical potential

energy,  $U_{E(D)}$  as shown by Equation 7.5.

$$U_{E(D)} = \frac{1}{2} C_i V_i i^2 \quad (7.5)$$

Resulting in a gain of electrical potential energy  $\Delta U_E$  comprising the difference of  $U_{E(C)}$  and  $U_{E(D)}$ .

**State A\***: The DEA is discharged into the energy harvesting circuit returning the charge and voltage values across the DEA to zero, returning to State A.

The unintended power generation discussed may cause issues with the pressure measurement system if switching significantly high DEA voltage source is done during a significant DEA-EIT surface loading event. A significant loading event is one which changes the capacitance of the DEA such that a voltage is generated by the unintended DEG which is high enough to cause potential harm to the EIT driving circuitry.

## 7.2 Methodology

To confirm the existence of this DEG phenomena in the DEA-EIT device design has undergone a sequence of FEM studies. To determine which compressive loads may give significant capacitance changes that could lead to significant voltage amplification and potentially significant energy generation across DEA electrodes, FEA of a DEA undergoing compressive pressure loading events have been completed. Experimental cases using two different loading areas, as shown in Figure 7.4, with a range of forces were completed. All FEA studies were three dimensional to account for any potential non-symmetric results and variations in fringe effects.

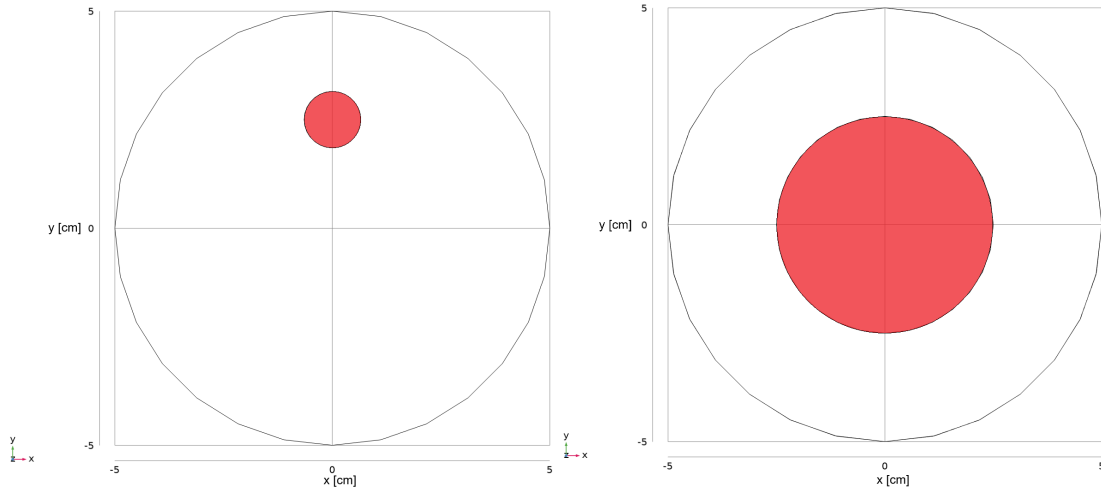


FIGURE 7.3: Loading cases for analysis of capacitance change. Left: 13 mm diameter load.  
Right: 50 mm diameter load.

### 7.2.1 DEA Load Study

To obtain a representation of how the DEA structure will deform during a different loading events, a static load FEA study was performed using COMSOL Multiphysics [301] to determine the expected deformation of the DEA and create mesh models. The deformed mesh models were then used for further electrostatic FEM studies to determine the change in capacitance of the DEA structure. A physics controlled mesh was used with a maximum element size of 10 mm and a minimum element size of 0.2 mm to ensure deformation features within the 0.5 mm thick DE membrane were captured.

The materials used for the FEA load study were closely matched to the characteristics of the material used in previous work [17]. For the compliant electrode a Young's modulus of 100 kPa was used with a Poisson's ratio,  $\nu_{ce}$  of 0.4, an electrode thickness,  $z_{CE}$ , of 0.5 mm, and the diameter of 100 mm. The DE material Young's modulus was set to 90kPa with a Poisson's ratio,  $\nu_{DE}$ , of 0.49, a membrane thickness,  $z_{DE}$ , of 0.5 mm, and the diameter of 100 mm.

The Poisson's ratio of the DE and the compliant CBSR electrodes differs due to viscoelasticity and micro-porosity seen in this material as shown by the SEM images in Figure 3.4 in Chapter 3. To determine the Poisson's ratio more accurately for the composite material, empirical data should be gathered as there is limited data for similar composite material with microporosity.

A static load analysis of the circular areas shown in Figure 7.3, for a range of force values. The loads ranged from 2.5 to 240 N, to obtain comparable strain values to those seen within our previous research [17, 41]. The bottom electrode surface was assumed fixed in place and rigid

to simulate a typical application case where the compliant DEA-EIT material is adhered to a rigid body.

A mesh of the deformed DEA models from each of different load case was saved for use in the next study.

### 7.2.2 Deformed DEA Electrostatics Study

The same mesh parameters from the deformed meshes from the previous load study were used to generate new meshes for an electrostatics study. To determine the change in capacitance from the undeformed DEA model and the deformed DEA cases, an electrostatic study was performed. The same dimensions as the load study were used the compliant electrode was assumed to have an ideal conductivity and the DE membrane relative dielectric permittivity was set to 4.2 as seen in the other studies done on similar DE material [294]. The a positive voltage was set on the upper electrode and the lower electrode was grounded. After the electric field model was generated using COMSOL Multiphysics [301] for each case the compliant electrode capacitance was calculated using Maxwell capacitance matrices [302] .

### 7.2.3 Voltage and Energy Generation

The voltage increase and energy generated for each DEA load case was calculated from the capacitance values determined in the electrostatics studies using Equations 7.2 - 7.5. Analysis of which types of loads can be handled by the DEA-EIT device when undergoing high voltage switching is a critical step for determining the limitations of future applications of the DEA-EIT device. The capacitance results generated from the FEA studies are then validated using parallel plate capacitor Equation 7.6.

$$C = \epsilon_0 \epsilon_r \frac{A}{z} \quad (7.6)$$

Where  $\epsilon_0$  is vacuum permittivity,  $\epsilon_r$  is the relative permittivity of the dielectric,  $A$  is the area of the ‘infinitely’ large parallel plate electrode, and  $z$  is the dielectric thickness.

## 7.3 Results

The a series of models were generated from a sequence of FEM studies to obtain the voltage and energy generated from a DEA acting as a DEG. First results from a static mechanical

load analysis are shown followed by an electrostatic analysis and finally capacitance and energy results were derived from the electrostatic FEA results.

### 7.3.1 DEA Load Study

To determine how various localised loads deform the DEA-EIT device structure FEM was performed. Examples of the deformations caused are given in Figure 7.4. The equivalent strain, ESTRN, was calculated giving an summation of the plastic and elastic strain experienced.

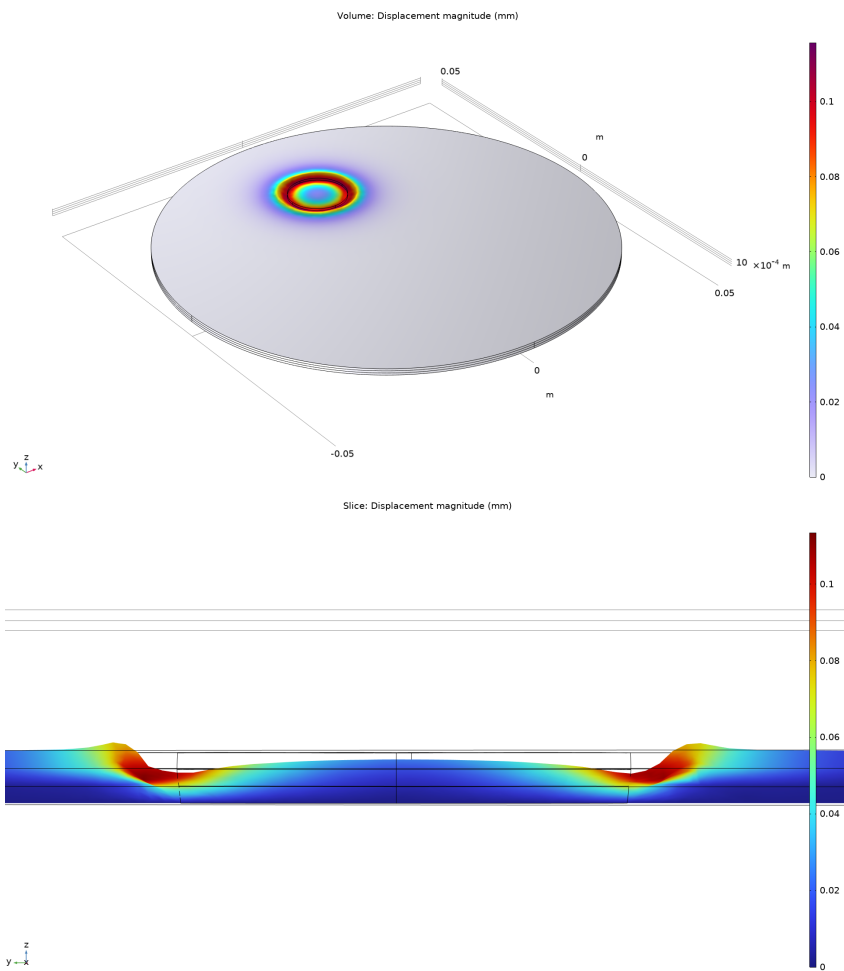


FIGURE 7.4: Deformed mesh plot of 13 mm diameter 20 N load case FEM model ( $\times 10$  scale displacement). Top: 3D view. Bottom: Cross-section zoomed view.

### 7.3.2 Deformed DEA Electrostatics Study

The deformed DEA-EIT structure causes the overall capacitance across the device electrodes to increase. The first step was running an electrostatic FEM study to generate an electric field, as shown in Figure 7.5.

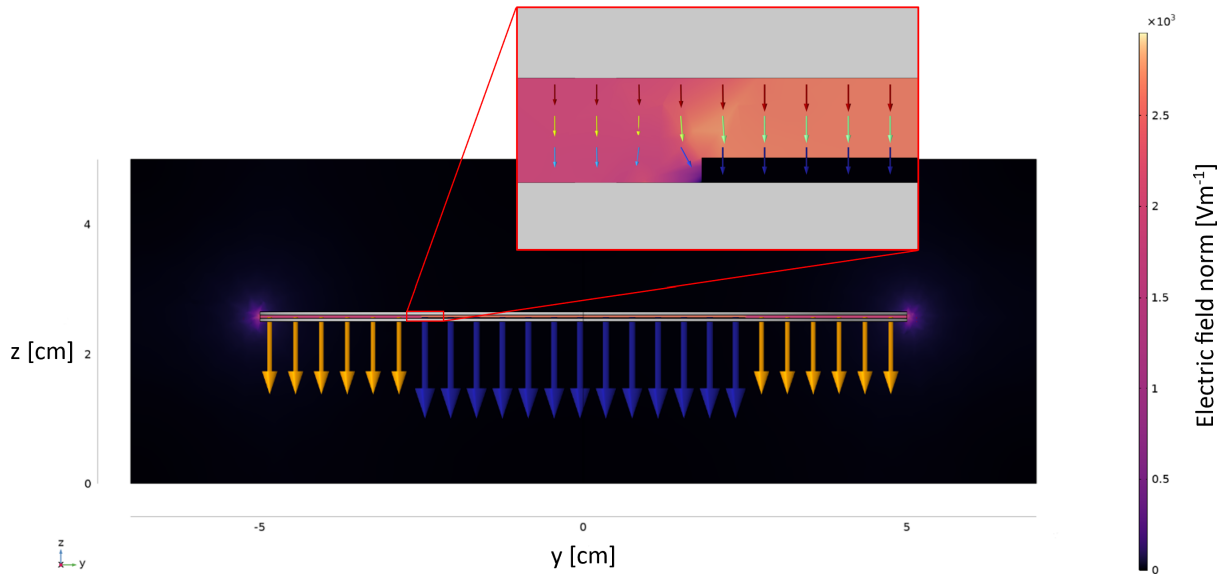


FIGURE 7.5: Electric field simulation of 50 mm diameter 240 N load case. With a zoomed section to show the electric field ‘fringe’ effects at the shoulder of the load cross-section. Volumetric arrows proportional to electric field strength.

### 7.3.3 Voltage and Energy Generation

To show the scale at which energy is generated an example scenario for the extra voltage generated is given. Given that the values from Figure 7.2 are,  $C_i = 10\text{pF}$ ,  $C_{ii} = 15\text{pF}$ , and  $V_i = 5\text{kV}$ . We get a charge  $Q = 75\text{nC}$ , and then at stage D,  $V_{ii} = \frac{Q}{C_i} = 7.5\text{kV}$ . This gives a voltage change,  $\Delta V = +2.5\text{kV}$ .

The parallel plate assumption for calculating capacitance of the DEA-EIT becomes invalid for the deformed DEA-EIT device. An approximation utilising the electric field FEM result on the deformed DEA-EIT FEM result is calculated using Maxwell capacitance matrix.

The change in capacitance was used to calculate the generated energy and voltage, values from the experiment are shown in Tables 7.1 and 7.2.

TABLE 7.1: Voltage and energy generation results calculated from FEM values for the 13 mm diameter load cases.

Load [N]	ESTRN	C [pF]	dC [pF]	dV <sub>DE</sub> [V]	dU [uJ]
0.00	0.00	588.86	0.00	0.00	0.00
2.50	0.08	589.69	0.83	7.04	31.14
5.00	0.15	590.73	1.87	15.83	70.20
10.00	0.30	593.40	4.54	38.25	170.68
20.00	0.60	605.53	16.67	137.65	630.86
30.00	0.91	688.18	99.32	721.61	3903.68

TABLE 7.2: Voltage and energy generation results calculated from FEM values for the 50 mm diameter load cases.

Load [N]	ESTRN	C [pF]	dC [pF]	dV <sub>DE</sub> [V]	dU [uJ]
0.00	0.00	588.86	0.00	0.00	0.00
10.00	0.02	591.90	3.04	25.68	0.20
20.00	0.04	595.00	6.14	51.60	0.79
30.00	0.06	598.33	9.47	79.14	1.87
60.00	0.12	609.24	20.38	167.26	8.52
120.00	0.24	635.86	47.00	369.58	43.43
240.00	0.48	727.10	138.24	950.63	328.54

To validate the capacitance results form Tables 7.1 and 7.2 the the capacitance was solved analytically using the parallel-plate capacitance approximation given in Equation 7.6. Matching the parameters of the FEA simulation the capacitance of the 100 mm DEA device with no load applied, the capacitance was approximated to be 584.13 pF.

A comparison of two similar trends for different loads applied to the DEG using FEM and an analytical method can be observed in Figure 7.6. The analytical solution is given in Appendix E.

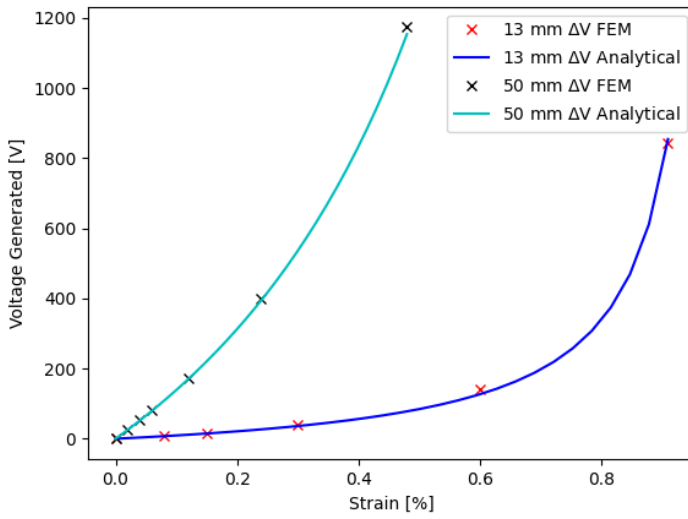


FIGURE 7.6: FEM vs analytical solution for voltage generation,  $\Delta V$ , for an initial voltage input of 5 kV, for the range of loads applied.

## 7.4 Discussion

The results from this work show promise towards understanding the energy generated from an EIT-DEA device when used in a particular fashion. The FEA simulations completed were validated analytically with a small discrepancy of 4.73 pF, i.e. 0.8% error, due to the electric field fringe effects the parallel plate capacitor assumption does not account for. The plot shown in Figure 7.6 shows the trends for a 13 mm and 50 mm load applicator, from this decreasing the dielectric thickness is seen to give a large increase in voltage and energy generated. At these high strains the likelihood of dielectric break through is significantly increased, especially so in a real world scenario when the load surface may contain sharp features, piercing or forming stress concentrations within the DE. The comparison of the FEM and analytical approximation in Figure 7.7 shows that the fringing electric field effect increases with increasing input strain deformation.

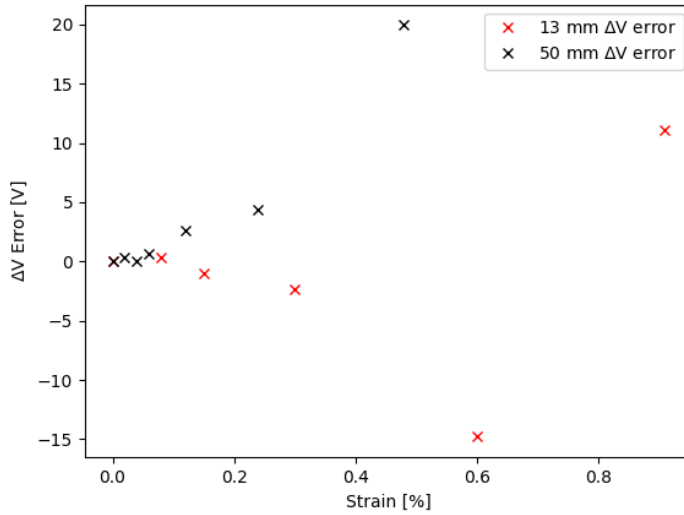


FIGURE 7.7: FEM vs analytical solution error for voltage generation,  $\Delta V$ , for an initial voltage input of 5 kV for the range of loads applied.

The energy generated by the sequence shown in Figure 7.2, can be harnessed if there is a sensing mechanism put in place to determine when the capacitance of the DEA will change and apply the voltage appropriately. Conversely, this energy generation can be undesirable for certain applications as it may cause damage to the attached circuitry.

Such energy generation case may be avoided in a system by detecting that a pressure event has occurred and preventing the excitation of the DEA or limiting the charge accumulation on each plate of the capacitor. Example applications could include a DEA-EIT device laid on a surface such as a road or footpath for surveying and energy generation from vehicular or foot traffic loads.

An example scenario of voltage and energy generation was given in Section 7.3.3. This voltage change transient could be connected to an EIT multiplexer through the capacitance of the DEA, as shown by Equation 6.6. The multiplexer pins used in this case are limited to between the power rails, i.e.  $\pm 22$  V [205]. In the case described above the minute change in capacitance of the DEA is calculated to generate  $93.75 \mu\text{J}$  of energy.

To determine the device's tolerance against transient voltage spikes, the EIT multiplexer limits would need to be characterised. Otherwise, in the case of an input pin overvoltage CMOS latch-up may occur [303] . Typical ESD standards [304] state that electronic devices must be tolerant to 200 pF capacitance charged to  $\pm 15$  kV, giving an energy dissipation of 22.5 mJ. This is several orders of magnitude larger than the energy generated in the simulation results

shown in Tables 7.1 and 7.2. However, for different configurations of DEA device this energy generation may become significant.

## 7.5 Conclusions

This work has investigated the prominence of energy generation of a 100 mm diameter DEA device with a 500  $\mu\text{m}$  dielectric elastomer. The sequence by which this energy generation occurs has been explained, and several scenarios have been tested for energy generation from localised 13 mm and 50 mm diameter loads with magnitudes ranging from 0 - 240 N. Depending on the load force, 0.2  $\mu\text{J}$  to 4 mJ of energy generation has been estimated. Although these are small energy values, often DEAs require large voltages to actuate so any amplification of these voltages needs to be handled on a case by case basis for each application and DEA device. Using methods to estimate the occurrence of a change in DEA capacitance is recommended in all applications to either avoid or harness this energy generation. Potential future applications of a device that utilises this energy generation ranges from vehicular traffic loads to foot traffic loads. Future work aims to validate the simulated findings and determine the energy losses in a real world application. Then in further future work the designed DEG system may be created and used to power a EIT-based pressure sensing circuit.



## Chapter 8

# Beyond Rigid - A Softer Future

A literature review comparing human skin and muscle tissue to current soft pressure mapping and soft electroactive actuator technologies was completed. From this review it was determined that CBSR material would be suitable for a range of soft pressure mapping and actuation devices because it is readily available, non-toxic, conductive, piezoresistive, mouldable, and highly deformable. Two specific technologies that emulate skin in terms of pressure mapping and muscle in terms of actuation were chosen and combined; EIT-based pressure mapping and dielectric elastomer actuators. Both sensor and actuator technologies use CBSR material as the electroactive polymer (EAP) component.

The first novel work in this thesis explored the CPEC material characterisation and selection of carbon black (CB) silicone rubber (SR) composites through several imaging techniques, including microscopy, scanning electron microscopy, and Raman spectroscopy. This imaging showed the carbon black micro-structure and how it was dispersed through a the micro-void filled elastomer composite. Then a macro-characterisation of the material was completed by determining several repeatable dynamic and transient characteristics by fitting several mathematical formulae to the repeated phenomena. This characterisation shows that the material has repeatable characteristics and elucidated how the material reacts to different time series tensile strain inputs, setting a foundation for development of sensors and actuators from the composite.

Using different configurations of the same CBSR material in Chapter 3, electrical impedance tomography (EIT) was used to map dynamic changes in resistance within a CBSR sheet of material undergoing a series of compressive loads. A set of performance metrics were developed as tools to determine the quality of a reconstruction given a known load input. The resistive

relaxation was quantified in the 2D EIT reconstruction and compared to a 1D equivalent resistive relaxation to show that 1D data and characterisation could be extrapolated to handle 2D problems. A model was then created which translates changes in conductivity to force for elements within the 2D image reconstruction.

To allow EIT-based pressure mapping to be used in a variety of portable/wearable, small scale applications a open-source circuit was developed. In parallel, a Cartesian force applicator was developed especially to capture compressive load data so that such pressure sensor could be calibrated and characterised for a range of different sensor domain materials.

Dielectric elastomer actuators are soft actuators that can emulate human muscle tissue function. To enhance the functionality of these actuator devices dielectric elastomer actuator technology was combined with the EIT-based sensor developed in this thesis to give a sense of touch to the actuator in the form of EIT-based pressure mapping. Such a DEA-EIT actuator-sensor device has not been disseminated, so a patent towards this technology has been filed provisionally. This work has investigated the complications with integrating the two technologies such as the inherent trade off between pressure mapping resolution and actuation performance with the current construction of the device.

During the validation and characterisation of the DEA-EIT device this work shows the formation of an unintentional dielectric elastomer generator (DEG) and the ability to map and localise compressive events triggering the generation of energy. The energy generated by such a device in practice is dependent on the topology of the device. Using FEM studies, energy generation within the DEA-EIT device was estimated for a range of loading cases and compared to a simplified analytical approach.

## 8.1 Future Work

To move the technology developed from Chapters 3 to 7 of this thesis into real-world applications and further enhance their performance, more research and development is required.

Although several methods of macro-modelling have been developed to represent a piezoresistive relationship in a conductive particle elastomer composite. There has been no evidence in literature of in-situ particle scale imaging of a CPEC specimen undergoing a known strain event. This in-situ imaging experiment could be done using imaging devices such as transmission electron microscopy (TEM) and small angle x-ray scattering (SAXS). This would show researchers

how the particles move within a strained material. If using SAXS for nanoparticle imaging, an electrical current could also be applied to the material to determine whether an applied electric field changes the motion of the particles significantly and explains other electromechanical phenomena measured in the material. In parallel with this particle modelling, additional macro-level non-linear modelling needs to be pursued to mitigate time dependent phenomena slowing down the response time of the sensor.

A core issue for the CBSR composite material is quantifying the degree of material homogeneity in terms of carbon black particle and void dispersion and how to determine the piezoresistivity to calibrate based on non-homogeneity within the CBSR material volume. Depending on the location of a compressive load the detected change in resistance would vary massively. Determining this dispersion could be done with the same imaging methods mentioned above, TEM and SAXS.

Development of soft EIT-based pressure sensors have been limited by the time response of the material and measurement system in this work and previous works. Future work will investigate adding capacitive functionality to EIT-based pressure mapping by using a dielectric elastomer (DE) to aid capacitively shunt current so that not just the resistance of the device changes but also the capacitance. The hypothesis is that the non-linear time dependent effects of resistive sensing will be mitigated using this capacitive shunting. The viscoelasticity within the deformed DE is less prominent than that seen in the CBSR material giving the improved response time. As described in previous works [17] there have been various attempts at created EIT-based pressure sensing devices. However, all of the state-of-the-art EIT-based pressure sensors rely on the change of resistance for pressure mapping. Zhang et. al [305] utilised capacitive shunting for EIT touch mapping on a variety of surfaces with conductive coatings. Their work used a human touch input to shunt electrical current through the person's contact point, essentially mapping localised changes in capacitance, but not applied surface pressure. Work from Reynolds-Smith [306, 307] showed the similarities and methods for Electric Field Tomography (EFT) as a method of localising touch and proximity of a grounded body.

Another ubiquitous problem for an EIT-based pressure sensor is miniaturising the EIT reconstruction processor. The smallest processors used in literature are SoCs or FPGA implementations, however these are much slower than PCs in their current state [308–311]. With the current developments miniaturisation of parallel computing ICs, there are more possibilities to create an EIT-based pressure mapping sensor PCB with a processor, and/or FPGA or ASIC that can do complete both EIT data acquisition and reconstruction tasks.

The DEA-EIT device showed potential to also act as a DEG with with the simultaneous pressure localisation function. Simulations showed a range of energy generation quantities with a range of applied loads to determine the energy generation potential of real-world loading scenarios. The next step is to modify the existing electrical hardware to run the DEG sequence and measure the losses within the system to validate the potential for running EIT with the DEG generated power. Future work is going towards creating a DEA daughter board to fit the ERT circuit developed in this work, for further development of the DEA-EIT based solution.

## 8.2 Concluding Statements

Current commercially viable soft pressure mapping and soft actuator options are extremely limited so this thesis has explored soft sensor and actuator technology while maintaining specifications derived from biological human skin and muscle throughout the research and design process. In biology, we see the fusion of sensors in the form of receptors and actuators in the muscle cells within biological tissue. This work has taken inspiration from this sensor-actuator fusion and combined a soft pressure mapping sensor with a dielectric elastomer actuator to form a soft tissue-like multi-functional device.

Soft robotics is an emerging sub-market of the growing robotics and automation market. Currently we see soft sensor and actuator companies emerging, but adoption of the technology is slow. In production lines often there is a combination of human and robotic handling, especially in agricultural industries. This can lead to a dangerous and inefficient environment for human handlers to work in. In future applications, soft robotic solutions will be investigated to replace the human handlers in the production line for instances where safety and efficiency is desired. Another key field of application is the biomedical industry. It has been estimated that globally approximately 13 million amputations happen per year [312], and 0.9 million people per year have a spinal injury [313]. Current prosthetic and assistive technology do not retain the characteristics of soft human skin and muscle tissue. Commercially viable soft sensor and actuator options are extremely limited, potentially indicating that the sensor and actuator technology requires further research to become more practical and reliable. Consequently, specific real-world applications were not pursued in this thesis; instead, the technology was characterised. The characterisation of device performance, and limitations help to affirm for future research that the technology is suitable for applications. Ultimately, the hope is that the biomimetic technology developed can be further researched and developed to improve human lives.

## Appendix A

# Strain-Stress-Resistance Experiments

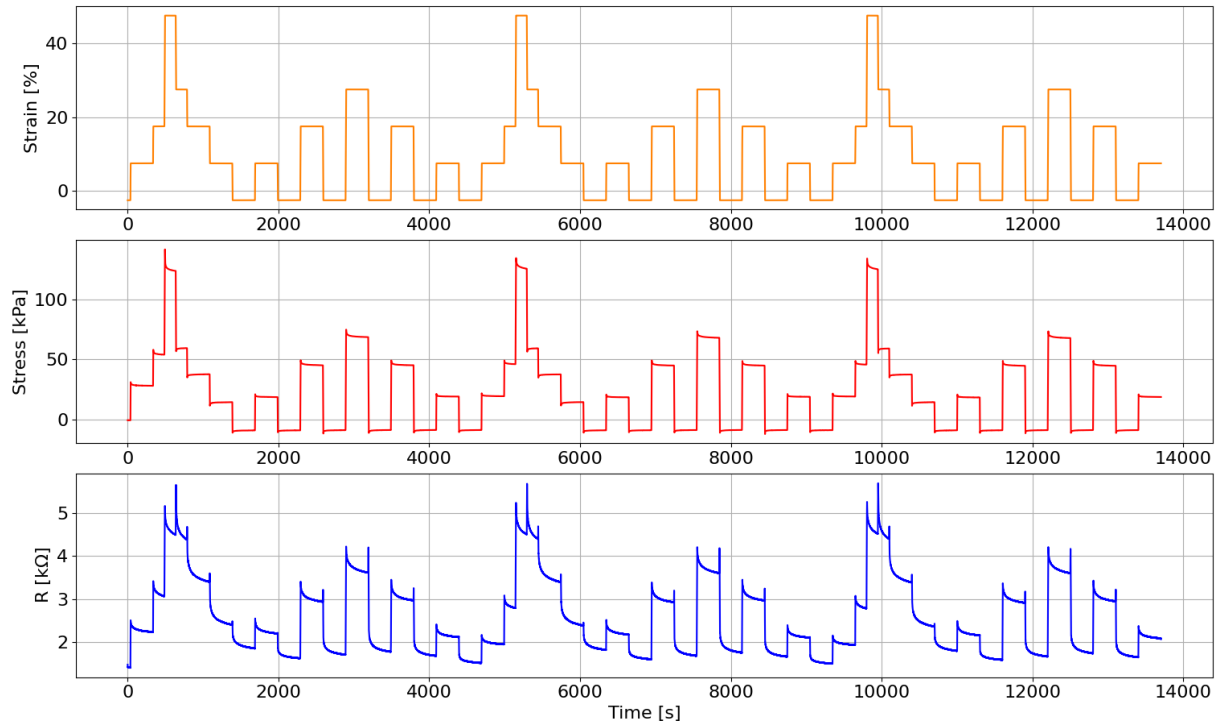


FIGURE A.1: Strain test sequence showing the shoulder phenomena correlation for varying magnitudes of strain for a 7.5 wt% CBSR specimen dogbone sample. This experiment had an unintentional offset of 1 mm, however this showed a drastic decrease shoulder phenomena when the falling edge is crossing the x-axis.

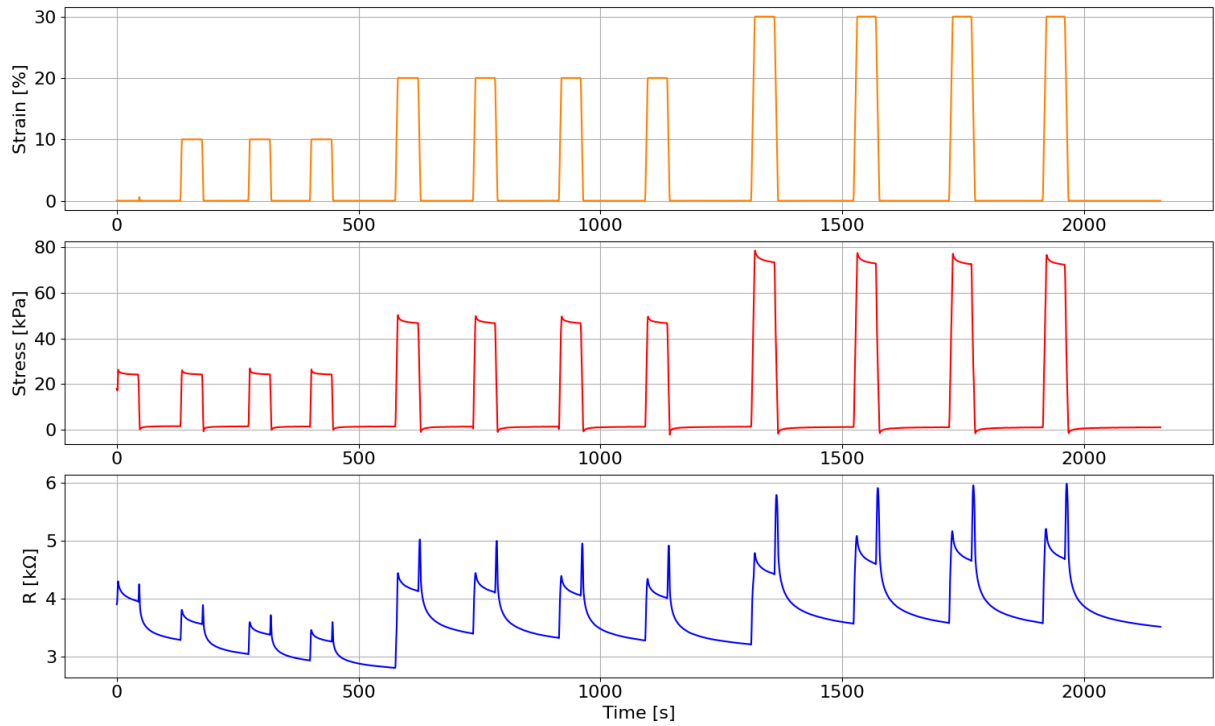


FIGURE A.2: Strain test sequence showing the shoulder phenomena correlation for varying magnitudes of strain for a 7.5 wt% CBSR specimen dogbone sample. This experiment used DC measurements, so the macro downward trend in resistance is more obvious than other experimental data given in this work with used a switched AC signal.

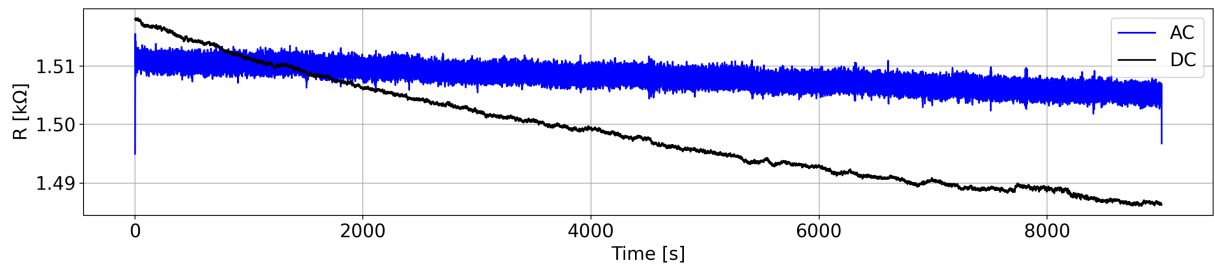


FIGURE A.3: AC vs DC downward trend in resistance for an unstrained 7.5 wt% CBSR composite dogbone specimen.

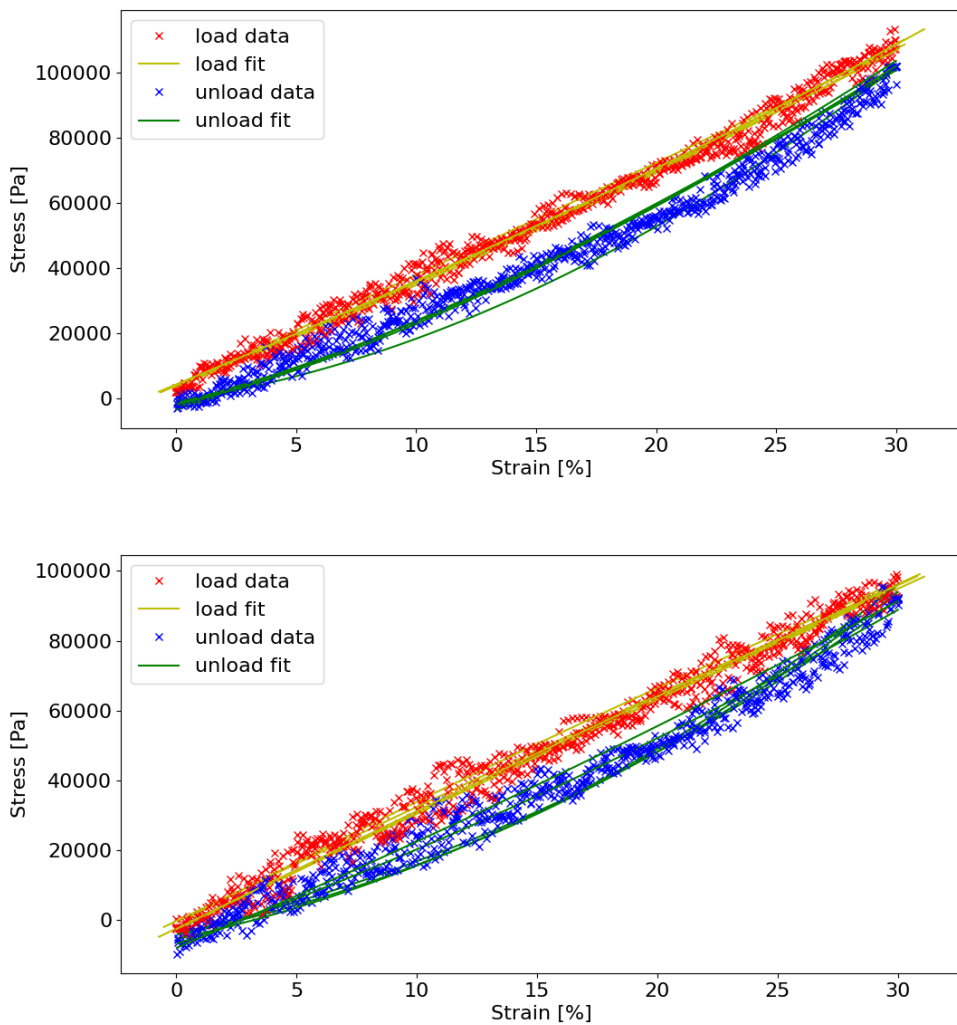


FIGURE A.4: The loading and unloading of 30% strain on a composite test specimens over five loading and unloading cycles with fitted second-order polynomial curves for determining hysteresis loop area. Top: 10 wt% CB. Bottom: 7.5 wt% CB.



## **Appendix B**

### **EIT-based Pressure Sensor Review**



TABLE B.1: Comparison of EIT-based soft pressure mapping sensor technologies. Dashes represent data not present in the related paper.

1st Author	DUT material(s)	Electrode type / number	Repeatability	Resistivity / Conductivity	Softness or max stretch range	Range of applied loads / strains	Transients compensated	Pre/post-processing algorithms for EIT image?	Spatial Performance metrics	Centre-of-mass error value range	Quant/qualitative force/ $\sigma$ analysis
Ellingham (this work)	Custom carbon-black silicone composite	Gold plated electrical pin / x16	data from 360 loads	1.58 k $\Omega$ /cm - 14.2 k $\Omega$ /cm	Tested over 0 - 30%. Elastic moduli 98.1 kPa and 132.5 kPa	0 - 55.8 kPa	No. But transients are quantified.	Positive and negative threshold	Centre-of-mass error ( $E_{CoM}$ ), Area overlap ( $A_{OL}$ ), & shape deform ( $SD$ ).	0.67 - 6.95 mm	Quant
Russo [185]	Polypyrrole and EeonTex NW170-PI fabric (Eeonyx, Pinole, USA)	- / x16	Means and variances given. Trial no. unknown	102 S/cm to 103 S/cm cast film per ASTM F84 & D257	Max stretch = 40%. Tensile strength >450 N.	-	-	Positive and negative threshold	Size Error, Position Error ( $E_{CoM}$ ) and Ringing (RNG)	1.4 - 6.7 %	Qual
Nagakubo [235]	PCR® piezoresistive silicone composite (JMT, Hidaka, Japan)	Crocodile clips / x16	x3 pulses of strain applied.	760 $\Omega$ /cm and 14.6 k $\Omega$ /cm	-	0 - 160 kPa	-	-	-	-	Quant
Hassan [197]	Copper sulphide nylon thread and Ag coated fabric	- / x16	-	-	-	0 - 150 kPa	-	-	-	-	Quant
Kato [198]	Pressure-sensitive conductive rubber	Copper tape / x16	-	-	-	-	-	-	-	-	Qual
Silvera-Tawil [262]	Piezoresistive fabrics (Eeonyx, Pinole, USA; Less EMF, Inc., Latham, USA)	Eyelets 7-mm diameter / x19	-	12.5 mS/sq and 660 mS/sq	-	-	-	50 and 75% thresholds	Resolution error (two touch test) and distance error ( $E_{CoM}$ )	~ 4 mm	Qual

TABLE B.2: Continuation of the comparison of EIT-based soft pressure mapping sensor technologies from Table B.1. Dashes represent data not present in the related paper.

1st Author	DUT material(s)	Electrode type / number	Repeatability	Resistivity / Conductivity	Softness or max stretch range	Range of applied loads / strains	Transients compensated	Pre/post-processing algorithms for EIT image?	Spatial Performance metrics	Centre-of-mass error value range	Quant/qualitative force/ $\sigma$ analysis
Yoon [236]	CBSR ELASTOSIL LR 3162 (Wacker Ltd., Munich, Germany)	'jewellery ribbon crimps' / x8 and x16	Mean and variance calculated. Trial no. unknown.	11 $\Omega\cdot\text{cm}$	54 A	5.5 - 15.8 kPa	Capacitive touch channel compensation	-	Distance error ( $E_{CoM}$ )	3.8 - 18.4 mm	Quant
Sun [65]	Custom PUT-CB pressure-sensitive film	Silver conductive paste squares 10x10mm / x8	5500 load cycles	-	-	-	-	-	-	-	Qual
Yao [84]	Medical-grade silver-plated nylon Dorlastan fabric (Less EMF, Inc., Latham, USA)	Copper tape / x16	-	< 1 $\Omega/\text{sq}$	Max stretch 100% / 65% in perpendicular directions	-	'Relatively static, image generated in 60 s'	-	-	-	Qual
Visentin [195]	Conductive textile, MedTex180 (Shieldex®, Kleiner, Germany)	Crocodile clips / x8	'low repeatability rate, high hysteresis, and noise sensitivity'	< 1 $\Omega/\text{sq}$	75- 155 % stretch	10.2 - 28.3 kPa	-	Centroid detection and threshold masking	-	-	Qual
Biasi [238]	Conductive ink, EptaTech (EptaNova, Luizago, Italy)	screen printed conductive ink / x16	6 positions x 5 trials	247.56 S/m (Estimated)	-	-	-	ANN used as well as EIT for solver. 40 % threshold.	-	-	Qual

## Appendix C

# EIT-based Pressure Sensor Performance Metrics

### C.1 Noise Removal

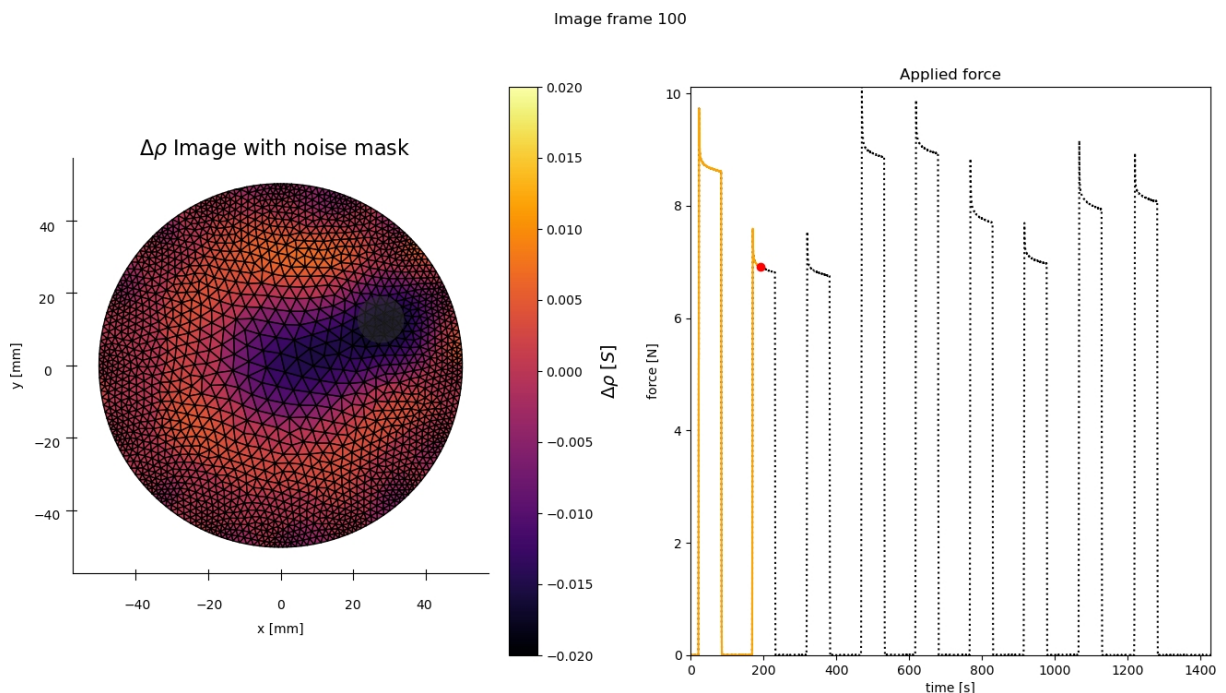


FIGURE C.1: An experimental snapshot. Left: Before executing the performance metrics calculations, the noise floor mask was applied to the 9% CBSR material. Right: Time series force data

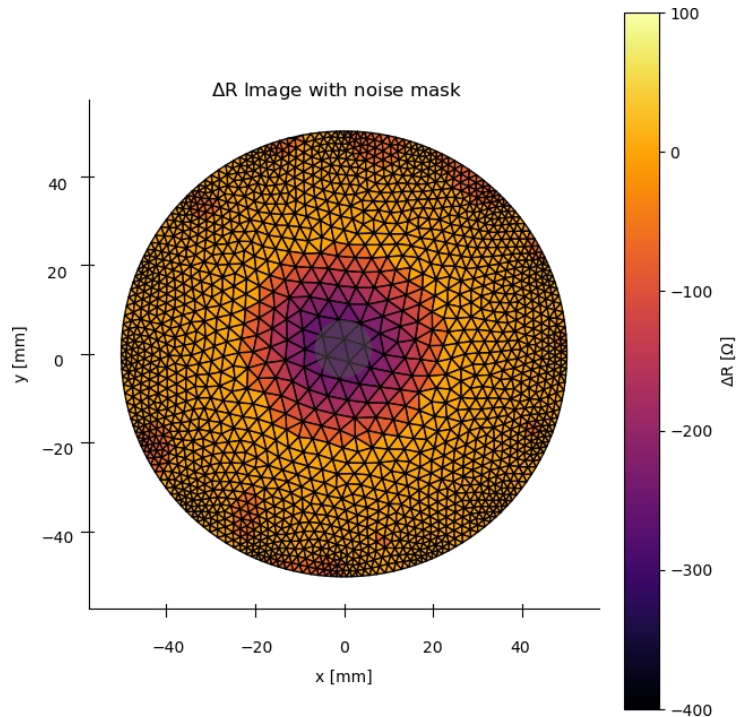


FIGURE C.2: Before executing the performance metrics calculations, the noise floor mask was applied to the 8% CBSR material shown in Figure 4.1

## C.2 More Threshold Percentage Masks

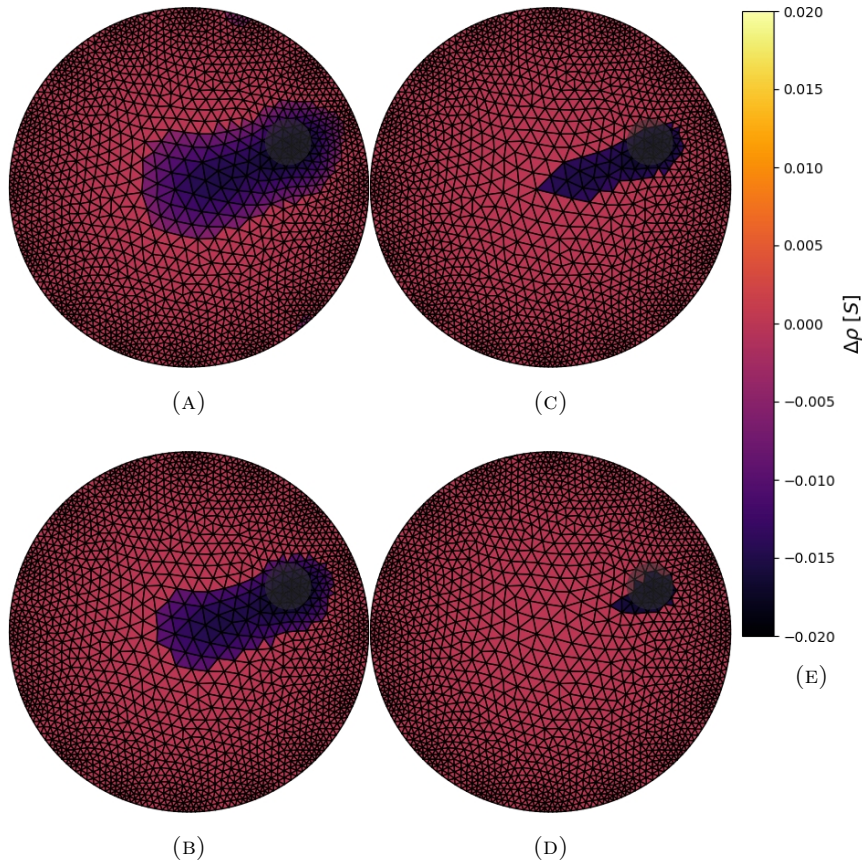


FIGURE C.3: A series of threshold percentage masks (a) 25%, (b) 50%, (c) 75, and (d) 85% for the same reconstruction given in Figure C.1. (e) is the resistance change scale bar.

### C.3 Quasi-static Conductance Strain Fitted Data

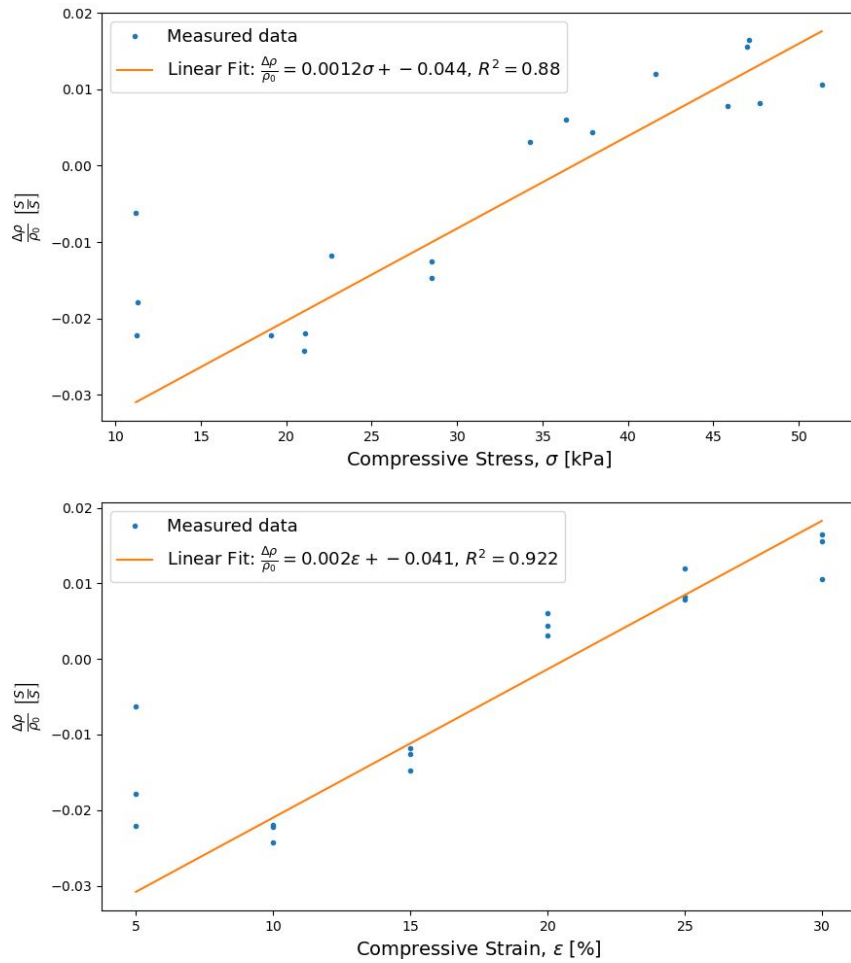


FIGURE C.4: Conductance change vs. stress (top) and strain (bottom) data and fitted curves for 9 wt% CBSR. The 5% strain values ignored as the std were larger than the conductance change values.

#### C.4 1D and 2D Strain Settling Times

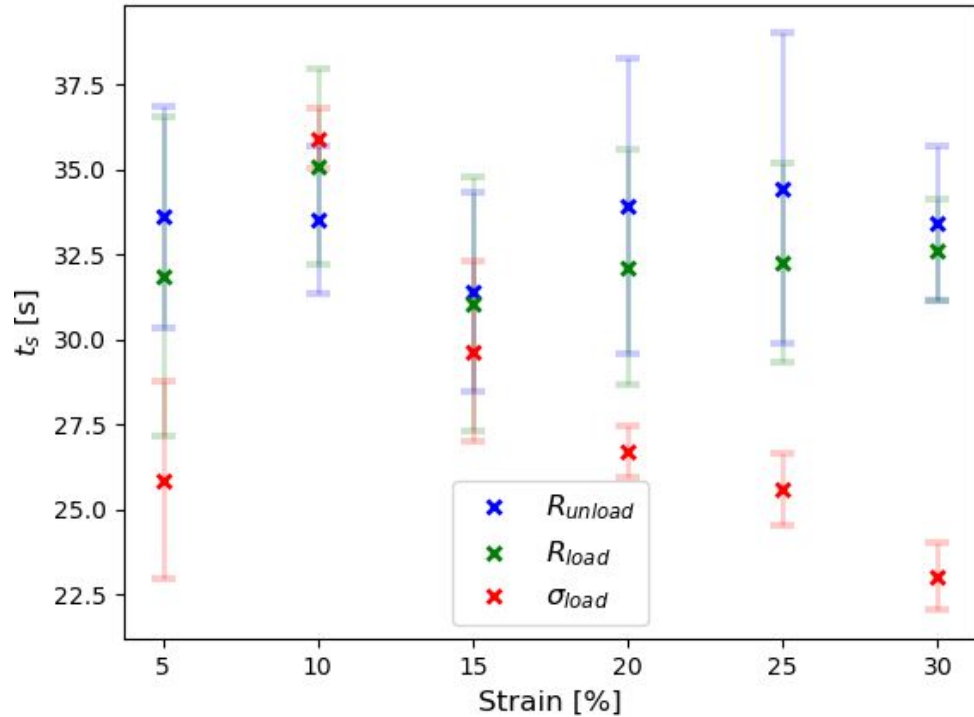


FIGURE C.5: Mean settling times for 5 - 30% compressive strain applied to CBSR 8 wt% with the error bars showing the standard deviation from 1D compressive test data.

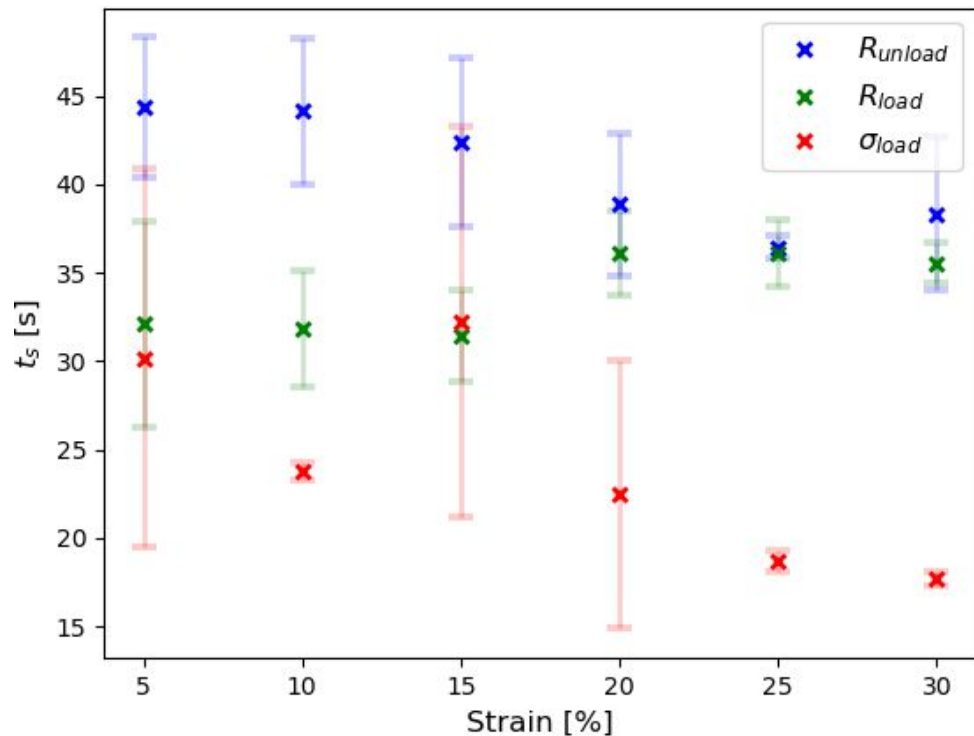


FIGURE C.6: Mean settling times for 5 - 30% compressive strain applied to CBSR 9 wt% with the error bars showing the standard deviation from 1D compressive test data.

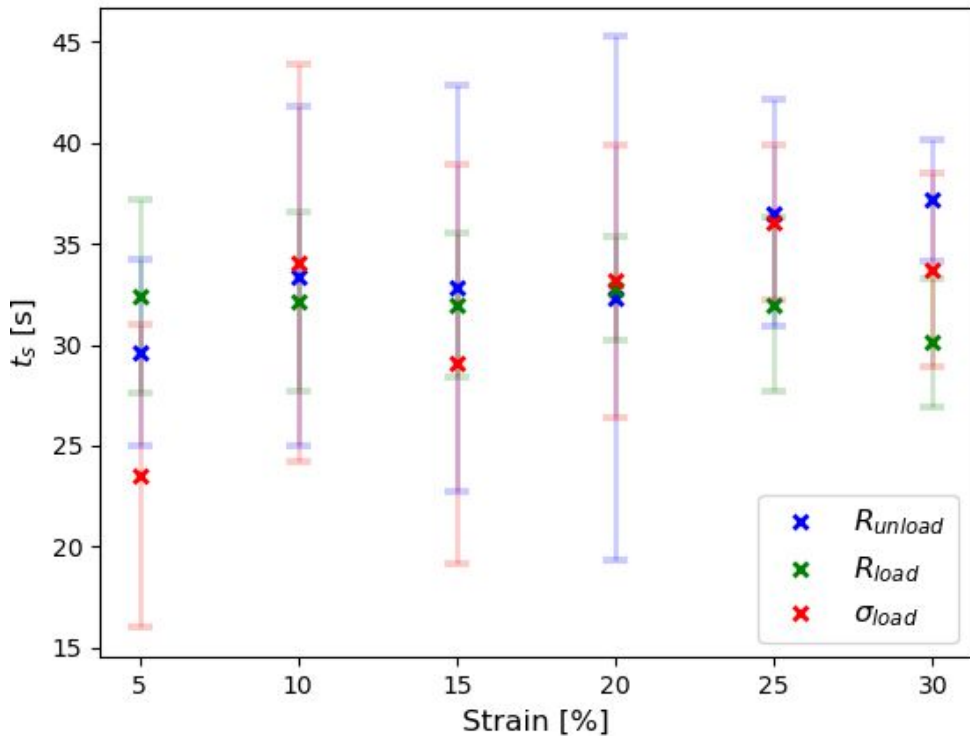


FIGURE C.7: Mean settling times for various strains applied to CBSR 8 wt% with the error bars showing the standard deviation of each settling time from the 2D EIT experimental data.

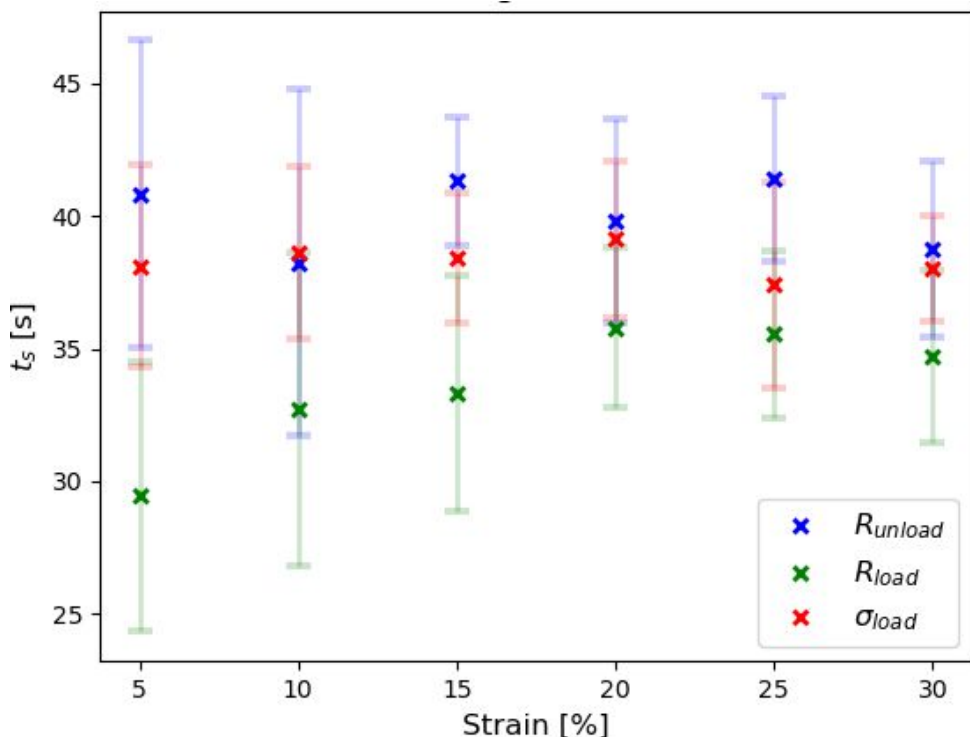


FIGURE C.8: Mean settling times for various strains applied to CBSR 9 wt% with the error bars showing the standard deviation of each settling time from the 2D EIT experimental data.

### C.5 Performance Metrics Example

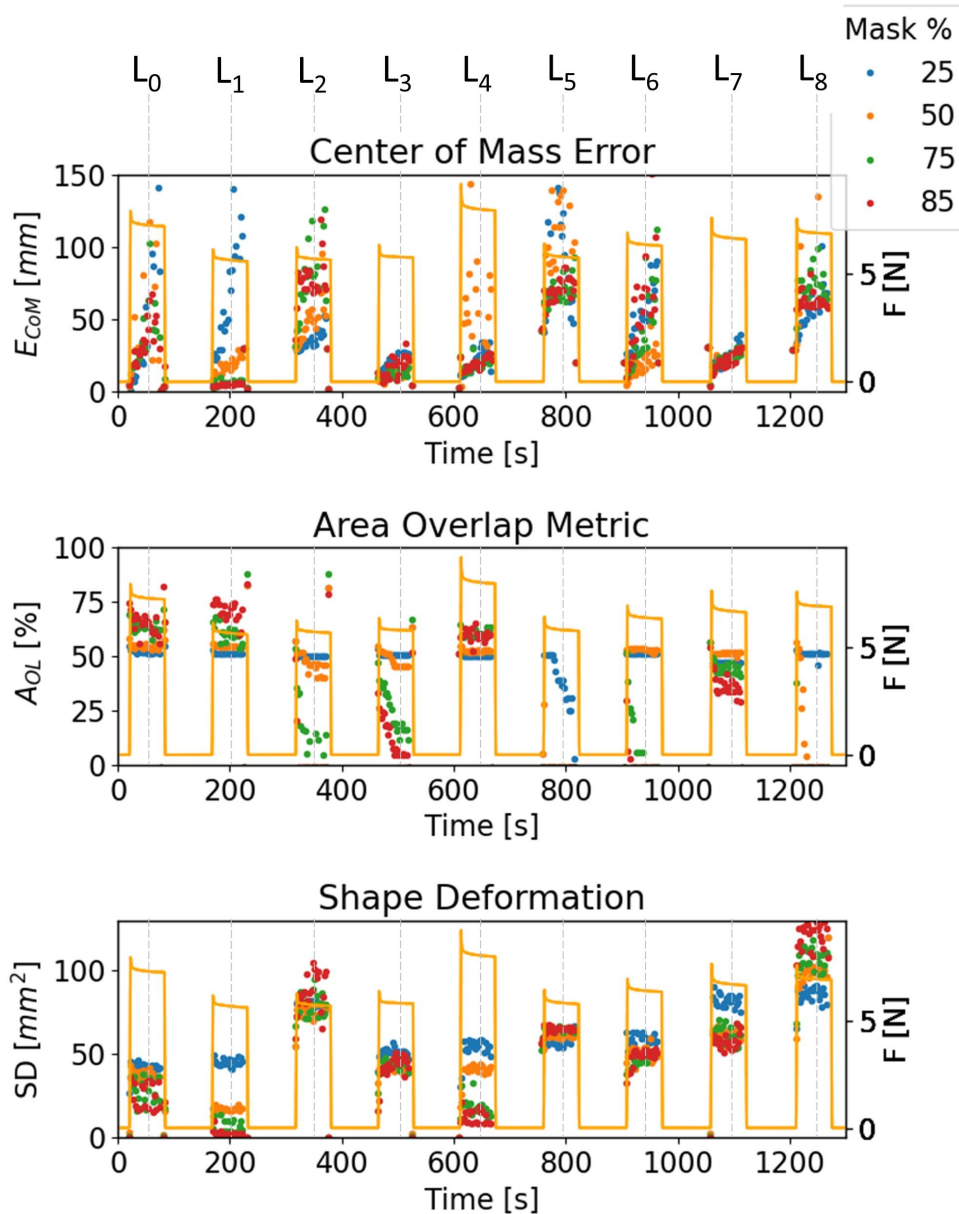


FIGURE C.9: Spatial performance metrics comparing threshold percentages of 25, 50, 75, and 85% for 9 wt% CBSR sample being loaded with 20% compressive strain in nine areas,  $L_{0-8}$ , shown in Fig 6.8.

## C.6 Randomised test $SD$ metrics data

TABLE C.1: CBSR 8 and 9 wt% mean and standard deviation for  $SD$  spatial performance metrics of ten random locations,  $L_{rand}$  and random strains  $\varepsilon$

$L_{rand}(r, \theta)$ [mm, °]	$\varepsilon [\%]$	8wt% [mm]	$SD$ [mm]	9wt% [mm]	$SD$ [mm]
(5.4, 10)	17.9	10.1 ± 0.8		9.8 ± 0.6	
(29.8, 337)	24.0	62.2 ± 1.3		52.8 ± 1.3	
(4.2, 317)	17.0	18.7 ± 5.9		21.7 ± 2.2	
(34.0, 70)	10.9	20.2 ± 4.7		13.7 ± 0.8	
.					
(35.8, 137)	8.1	124.7 ± 2.8		81.5 ± 13.8	
(9.6, 55)	13.8	24.8 ± 1.9		19.2 ± 1.8	
(2.8, 260)	7.0	15.6 ± 4.5		12.7 ± 1.0	
(11.2, 114)	10.0	4.5 ± 0.9		4.6 ± 0.6	
(24.6, 241)	28.5	2.6 ± 0.1		2.6 ± 0.1	
(16.6, 253)	23.6	0.3 ± 0.1		1.1 ± 0.1	

## Appendix D

# Portable EIT-based Pressure Sensor Build and Operation

This appendix is partially based on my HardwareX paper "A Portable Electrical Impedance Tomography Based Pressure Mapping Sensor and Validation System"<sup>1</sup> and gives a high-level description of the build process for both the ERT sensor module, the sensing domain, and the Cartesian force applicator (CFA). The build section are followed by an operation instructions and safety section.

## D.1 Build Methodology

The build was split into two main parts the ERT sensor module electronics and the CFA construction. An example of how a piezoresistive nanoparticle elastomer composite is made is also re-iterated from previous chapters.

### D.1.1 ERT Sensor

The manufacturing process of the PCB involves first sending the PCB Gerber files to a PCB manufacturer. This work used JLC PCB with their default parameters for a 4 layer PCB.

Next populate the PCBs with the SMD parts given in the BOM and place in a reflow oven. First complete the rear side then the top side to ensure components stick. Once all SMD parts

---

<sup>1</sup>currently under review as of 26 September 2024

have been firmly soldered, solder all of the THT components. Finally attach the jumpers for the desired power mode, explained in Section D.2.1.

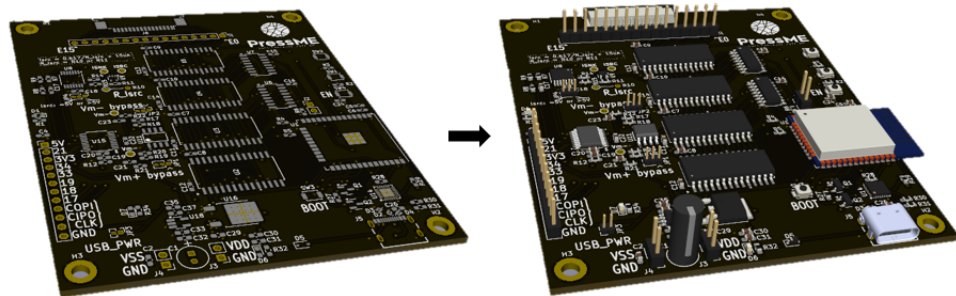


FIGURE D.1: ERT PCB [PCB1] before and after electrical component population.

To ensure simple protection against electrical shorts and low-level ingress protection (equivalent to IP20) 3D print an enclosure in PLA using the STL files given in the BOM, *ert\_housing\_top.stl* [PR1]<sup>2</sup> and *ert\_housing\_base.stl* [PR2]. There are 4 threaded inserts [HW2] to mount the PCB securely in the 3D printed enclosure using four M3 14 mm bolts [HW1].

Attach the 16 way ribbon connector [W1] to the ERT electrodes. In this example there is a ribbon to IDC connector interface board [J8], which then connects to a custom built electrode pin to domain interface [DUT1, DUT2, PR3, PR4]. This electrode interface will vary based on the required sensing domain.

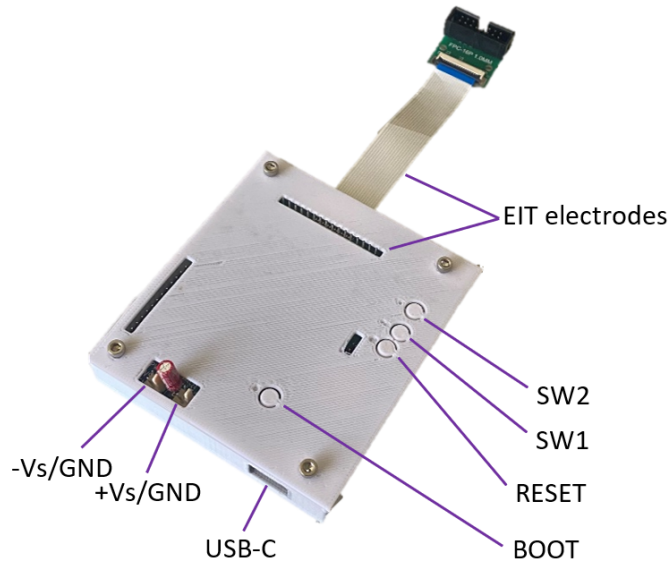


FIGURE D.2: ERT sensor PCBA mounted in enclosure and attached electrode harness showing buttons and the main electrical connections.

<sup>2</sup>Text within square brackets in this section refers to part reference designators (e.g. U1 for the ESP32 module) in the BOMs given in the supplementary material

The sensor device shown in Figure D.2 shows all of the connections and buttons necessary for the programming and operation of the sensor, as well as two optional buttons SW1 and SW2 for any other desired functions.

### D.1.2 Sensing Domain

As a reference the method for fabricating a specific sensing domain is given in this section. The sensing domain used was a carbon black (CB) nanoparticle silicone rubber composite.

With the material requirements of a low Shore hardness of 5A - 25A, similar to that of human skin and muscle tissue [194, 239], low viscoelasticity, high yield strength, low resistivity, high strain gauge factor, and non-toxic. Other sensor domain materials may be used for the sensor, such as soft conductive particle composites, conductive polymers, and hydrogels [74, 87, 212].

Researchers fabricating their own sensing domain for use with this system should follow three key requirements,

1. The size of the sensing domain must fit within a 220 x 180 x 160 mm volume ( $X \times Y \times Z$ ) on the CFA test bed.
2. The bulk modulus of the domain material must be chosen such that the required loads applied to the domain must not exceed 100 N.
3. The inter-electrode resistance,  $R_{int}$ , must be low enough to not saturate the current source,  $I_{src}$ , given a power supply voltage,  $V_s$ , as shown in Equation D.1,

$$R_{int} < \alpha \frac{V_s}{I_{src}} \quad (\text{D.1})$$

Where  $R_{int}$  is the resistance values between every configuration of the current drive electrodes during an EIT capture cycle and  $\alpha$  is the factor of safety for any electrode movement or incidental increase of  $R_{int}$  during experimentation.

The domain under test (DUT) used in this work was a composite comprised of XC 72R carbon black (CB) nanoparticles (Cabot, Alpharetta, USA) [DUT5] of 50 nm average diameter, dispersed in a two part Dragon Skin 10 NV silicone rubber (SR) matrix (SmoothOn, Macungie, USA) [DUT6]. The weight percentage (wt%) of CB to liquid silicone rubber which resulted in near optimal piezoresistive characteristics was found to be between 8 - 10%. To ensure homogeneous CB particle dispersion and mitigate air bubble formation an ARV-310 vacuum planetary

mixer (Thinky, Tokyo, Japan) was used to mix the CB particles through the liquid silicone matrix. Upon completion of mixing, the uncured composite was poured into the circular sheet domain mould. The curing of the composite was controlled by heating the newly-mixed material in the mould at 80°C for 90 min. The domain samples used in this work and previous work [17, 18] had a diameter of 100 mm as shown in Figure D.3.



FIGURE D.3: Left: An example of a CBSR sample with copper tape electrodes integrated with a dielectric elastomer actuator setup [19]. Right: Example of a CBSR sensing domain with gold pin electrodes penetrating material surface around the sensing region boundary.

### D.1.3 Cartesian force applicator

To test the spatial and force resolution of the ERT pressure mapping device, the CFA was designed using a Prusa MK3s 3D printer to provide a stable platform. First a functional Prusa MK3s 3D printer was acquired with its printing capabilities tested on several standard demo PLA prints to ensure the print head can move with the expected resolution in the X, Y, and Z directions. Standard benchmark tests and tuning for the printing platform can be found [here](#) and [here](#) [314, 315].



FIGURE D.4: MK3s print head. Left: Original print head assembly. Right: Dismantled print head assembly [20].

Next the print head of the MK3s was dismantled, as shown in Figure D.4, leaving a flat surface to attach first the PINDA adaptor [PR8] and the loadcell bracket [PR9], as shown in Figure

**D.5.** Use M3 bolts to attach the loadcell bracket and PINDA adaptor to the dismantled print head surface. See read the printer [assembly manual](#) for more detail on the part assembly[316]. Bolt the TAL220 10 kg loadcell [E3] onto the loadcell bracket using M5 bolts [HW4]. Bolt the force applicator head [PR5-7, HW5] onto the other end of the loadcell using M4 bolts [HW3]. A range of force applicator heads shapes and sizes have been created to test the resolution of the sensor.

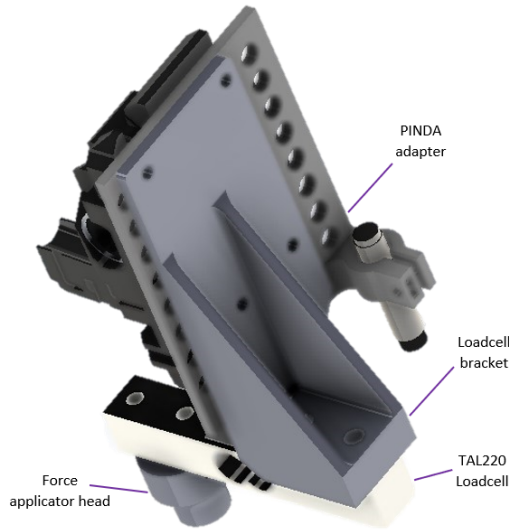


FIGURE D.5: Force applicator head assembly.

With the thermistor from the original printhead no longer required, a trimpot [RV1] is attached to the thermistor port on the printer's [control circuit PCBA](#)[317]. While the 3D printer is turned on, the trimpot is manually adjusted until room temperature is reached on the 3D printer display to avoid any future under/over temperature errors.

The print bed of the MK3s 3D printer is removed and replaced with a mount tray [LC1] for the sensing domain. The ERT tray bearing part [PR10] mounted and bolted [HW6] onto the frame of the MK3s as shown in Figure D.6. The ERT sensor tray [LC2] and the sensing domain mount tray are fixed together onto the print bed with two M3 bolts [HW6] clamping the trays to the edge of the print bed.

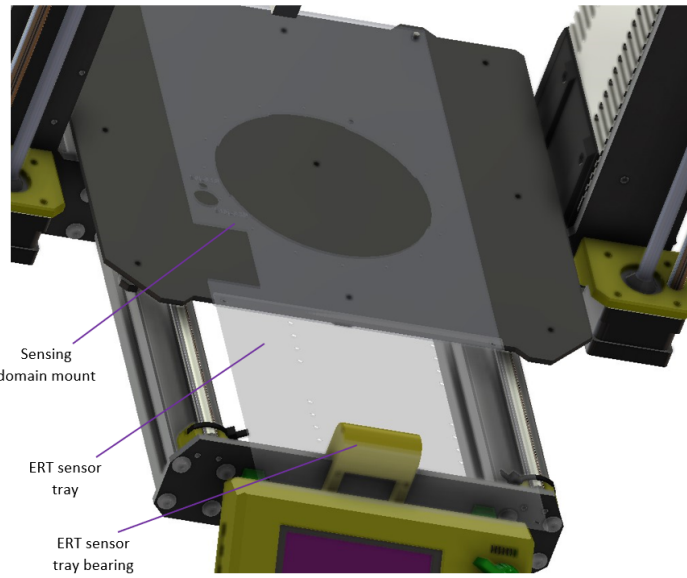


FIGURE D.6: MK3s with original print bed tray removed and the ERT sensor trays added.

The firmware version used in this work was MK3s 3.9.0. Later versions may be compatible. Other 3D printer platforms with a similar gcode command set and a similar core firmware such as the [Marlin firmware](#) may also be used as a CFA. However, minor configuration changes in this work's software and hardware may be required.

## D.2 Operation instructions

To validate and characterise the ERT pressure mapping sensor the CFA is used to apply a sequence of loads to the material. The below sequence of required operations to complete this experiment includes:

1. ERT sensor power modes
2. ERT sensor programming
3. ERT sensing domain preparation
4. Load application point and strain configuration
5. Touch based mesh bed levelling
6. Load experiment execution
7. Data capture

## 8. Data processing

This sequence of events is repeated for different sensing domains and different loading conditions.

### D.2.1 ERT sensor power modes

Before running any experiments, the ERT sensor power mode must be configured. The jumper configuration for the bipolar supply (blue) and +5 V USB single-ended supply (red) mode is shown in Figure D.8.

The bipolar supply first mode is recommended for driving the ERT signal through a wider range of sensing domains at a higher voltage. A bipolar supply of  $\pm 20$  V is connected to  $\pm V_s$  for the best performance of the circuit.

The second power mode uses a +5 V USB 3.X power supply to run the ERT circuit. The second mode is limited to lower resistance sensing domains that can be tested as it can only drive constant currents using +5 V. When using the +5 V supply mode the  $-V_s$  and GND pins on the power input must be shorted for the multiplexers to operate.

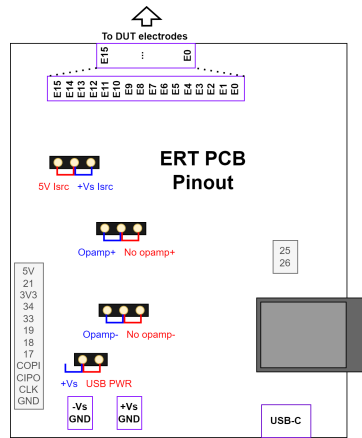


FIGURE D.7: ERT PCB pin-out and power mode options. Blue jumpers are for the bipolar supply mode (i.e.  $\pm V_s$  attached). Red jumpers are for the +5 V USB supply mode.

For each power mode there will be a distortion of the signal dependent on the power supply voltages and input signal as exemplified in Figure 5.9.

### D.2.2 ERT sensor programming

The ERT sensor contains an ESP-WROOM32 module [U1] which requires the `main_ert.c` program to be built and flashed. This can be achieved using the default project template from

the [ESP-IDF environment](#)[318]. The default ERT circuit firmware `main_ert` completes the well proven adjacent electrode drive pattern [263, 319? , 320]. Upon successful programming of the ERT circuit it will output a constant serial stream of the adjacent electrode pattern ERT data separating each frame of 256 measurements with an ‘A’. The ERT sensor circuit has the capability to send the real-time serial ERT data via a USB serial, Bluetooth, or WiFi connection to a EIT reconstruction capable computer.

### D.2.3 ERT sensing domain preparation

For sensing domain fabrication instructions refer to Section D.1.2. The ERT sensing domain needs to have sufficiently low adjacent inter-electrode resistance to function, so that the current source will not saturate due the power supply voltage. The ET electrodes can be attached to the domain in many ways as shown in Figure D.3, ensure these connections provide a reliable electrical contact to the sensing domain. Connect sensing domain electrodes to the ERT circuit FPC connector[W1] via an adaptor[J8]. The ERT sensing domain must be flat and centred on the sensing domain holder [PR3, PR4] as shown in Figure D.3 (middle).

### D.2.4 Load application point and strain configuration

Load application points and strains applied to the sensing domain can be configured by altering variables in `ertpcb_cfa_reader.py` code. A loading sequence consists of a series of load applications, in the form of a strain pulse train, applied to a set of X and Y coordinates on the sensing domain. The main parameters to change for running a loading sequence are given in Table D.1.

TABLE D.1: CFA experimental parameter variables.

<b>Variable:</b>	<b>Unit:</b>	<b>Description:</b>
Strain speed ( <code>v_z_push</code> )	mm/min	The rising/falling edge gradient for each pulse.
Strain limit ( <code>strain_limit</code> )	%	The maximum compressive strain allowed.
Load locations ( <code>push_points</code> )	[mm, mm]	An array of XY locations of each load pulse.
Reference offset ( <code>ref_loc_mm</code> )	[mm, mm]	The XY offset of the zero point of the sensing domain relative to the CFA home reference.

These can all be found as variables in the software file `ertpcb_cfa_reader.py` within the `main` function. Before running this program the serial COM ports may need to be changed in the `ertpcb_cfa_reader.py` program to match the comports of the CFA and ERT sensor hardware.

### D.2.5 Load experiment execution

Once all hard-coded parameters have been set the command parameters are set and the load experiment begins. To begin the load experiment use the following terminal command:

```
>> python ertpcb_cfa_reader.py <dir/filename> <Isrc_A> <Vmax> <sample_name> <date_fabricated>  
<load_time_s> <strain>
```

Where `<dir/filename>` includes the file directory and file name, `<Isrc_A>` is the constant current source value set in the ERT circuit in amps, `<Vmax>` is the maximum allowed voltage to be read by the ADC in volts (e.g. 20 V), `<sample_name>` is a descriptive sensing domain name, `<date_fabricated>` is the sample fabrication date ('NA' or leave blank if irrelevant), `<load_time_s>` is the strain pulse on and off time in seconds, and `<strain>` is the desired strain applied to the domain as a percentage. If a random test sequence is desired with randomised strain and locations this can be achieved by simply setting the `<strain>` value to -1.

### D.2.6 Touch-based mesh bed levelling

An undulating sensing domain surface can often be present during testing due to an intentionally curved sensor or manufacturing defects. To compensate for an uneven surface a touch-based mesh bed levelling process has been created to improve the quality of the stress/strain data gathered. The process involves the force applicator head travelling towards the sample until a change in force has been detected above 0.1 N. This mitigates the risk of any misalignment with the force applicator surface plane and the sensing domain surface plane and ensures more accurate strain data capture for low strain magnitudes. This touch-based mesh bed levelling is completed before the load sequence experiment begins. The sensing domain and holding trays should not be physically contacted in any form after beginning the `ertpcb_cfa_reader.py` program.

### D.2.7 Data capture

Once the `ertpcb_cfa_reader.py` program has completed capturing data, a time-series plot of the 16 inter-electrode resistances,  $R_{int}$ , will appear. A stable  $R_{int}$  is for stable EIT reconstructions of the sensing domain.

Any significant change in the inter-electrode resistance may cause a poor EIT reconstruction result. A significant change in the inter-electrode resistance could be a result of, applying force too close to the electrodes themselves, an inherently unstable electrode connection, or an external force applied near the electrode. If the  $R_{int}$  values are not stable it will be evident in the plot and there will be a warning message in the console.

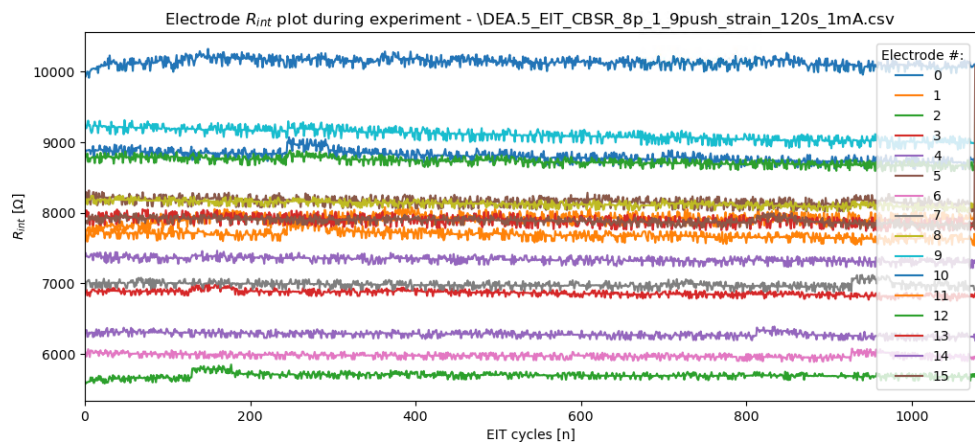


FIGURE D.8: An example plot of the  $R_{int}$  values generated on completion of an experiment for a stable experiment. Where the Electrode # ‘i’ represents the resistance between electrode ‘i’ and ‘i+1’.

Once the inter-electrode resistance plot is closed the program will continue to save all of the data in three separate files for the given `filename`,

1. `filename.csv` - Time series data for ERT voltages, compression forces, and force applicator XYZ locations. The UTC start date and time of the experiment is given in the top row.
2. `filename.pkl` - Logs the same data as the .csv file **and** all of the important experiment parameters into a serialised python ‘pickle’ file.
3. `filename.gcode` - The gcode file of the commands sent to the 3D printer platform for the experiment run.

### D.2.8 Data processing

Once all of the data has been collected in the above steps, the data can be processed. Data processing includes the following,

1. Pre-processing of the raw voltage, force, and position data. Filtering and data cleaning could be included in this step.
2. Image reconstruction using a chosen EIT algorithm with the pre-processing or raw data. EIT reconstruction could include algorithms such as regularised Newton's methods [191], neural network based methods [238, 321], and back projection methods [319].
3. Any post-processing of the EIT image reconstruction data and integration with the force applicator stress and/or strain data. Post-processing could include resistance to force inverse modelling, pressure mapping performance metric quantification, an application specific software interface.

In this work EIDORS [186] has been used to complete the EIT reconstructions of the domain and any post processing is then completed with a python program as shown in Section 5.3.

## D.3 Construction and Operational Safety

Various safety concerns must be stated for the construction and operation precautions of this system. This is not a comprehensive safety guide, but will give an overview of some potential safety concerns. Other precautions may be necessary depending on the development location and sensing domain materials used. The construction and operation of the system can each be separated into three parts, the ERT sensor circuit, the CFA, and the sensing domain.

### D.3.1 Construction

During the assembly of the ERT sensor circuit the regular health and safety procedures for assembling and soldering a PCB must be followed.

During testing of the CFA as a 3D printer there will be moving parts which could get caught on long hair or collide with a person too close. Steps must be taken to avoid any undesired collisions or any people touching the CFA during operation.

When fabricating the sensing domain often this involves micro/nano sized conductive particles dangerous for inhalation and sometimes dangerous to touch. The material safety datasheet must be consulted for any material used in the sensing domain. Any safety procedures with mixing machines and curing devices must be followed.

### D.3.2 Operation

The PCBA can operate on up to  $\pm 20$  VDC which is within the safe level the SELV as defined by IEC [322]. However, should the contacts of the power supply to the ERT circuit be electrically shorted, a burn or fire hazard may arise. The current on the sensing domain electrodes is limited to prevent a dangerous short circuit current.

During the operation of the CFA there will be moving parts which could collide tangle long hair or collide with the person operating. Steps must be taken to avoid any undesired collisions or any people touching the CFA during operation.

The sensing domain may not be bio-compatible so the material safety datasheet(s) for each domain must be followed for each real world sensor application.

## Appendix E

# Dielectric Elastomer Generator Validation

### E.1 $\Delta V$ Calculation

An estimate of the ideal voltage,  $\Delta V$ , generated from a circular compression load of radius,  $r_L$ , on a circular DE domain of radius,  $r_{DE}$ , with two conductive compliant electrodes covering the area  $A_{DE}$  of the DE.

Several assumptions are made to simplify the calculation to be solved analytically:

1. The capacitance of the unloaded system is made up of the base DE capacitance.
2. The capacitance of the loaded system is a summation of the base DE capacitance and loaded area capacitance.
3. The parallel plate capacitor assumptions are made for both DE and loaded area capacitances.
4. The relative permittivity of the DE remains constant with changing strain.

The dependent parameters voltage,  $\Delta V$ , and energy,  $\Delta U$ , generated by the DEG are a result of the change in the DE capacitance, the charge,  $Q$ , on the DE electrodes, and the physical parameters of the DE. The independent physical parameters of the DE system include:

- $A_{DE}$  - area of the dielectric elastomer capacitance

- $d_i$  - relaxed DE thickness
- $\epsilon_r$  - relative permittivity of free space
- $V_i$  - initial priming voltage input
- $Q$  - DE charge

The parameters independent parameters for driving energy generation include:

- $\varepsilon$  - compressive strain of the load applied
- $A_L$  - area of the applied load

Using Equations 7.1 - 7.5 as a basis for the DEG method, we form a formula for the voltage generated  $\Delta V$ , based on the priming voltage,  $V_i$  and the stage two voltage,  $V_{ii}$  as,

$$\Delta V = V_{ii} - V_i = \frac{Q}{C_i} - \frac{Q}{C_{ii}}. \quad (\text{E.1})$$

Which then can be rearranged to obtain a formula for  $\Delta V$  as a function of  $C$  and  $V_i$ ,

$$\Delta V = V_i \left( \frac{C_{ii}}{C_i} - 1 \right) \quad (\text{E.2})$$

For a load with a strain,  $\varepsilon$ , we get a compressed DE thickness  $d_{ii}$  such that,

$$d_{ii} = d_i(\varepsilon + 1). \quad (\text{E.3})$$

Substituting the parallel capacitance formulae for  $C_i$  and  $C_{ii}$  we get,

$$C_i = \frac{\epsilon(A_{DE})}{d_i} \quad (\text{E.4})$$

and

$$C_{ii} = \frac{\epsilon(A_{DE} - A_L)}{d_i} + \frac{\epsilon A_L}{d_{ii}} \quad (\text{E.5})$$

where  $\epsilon = \epsilon_0 \epsilon_r$ . By substituting Equations E.3 - E.5 into Equation E.2 we can obtain an analytical solution for the system.

For a more accurate analytical solution utilising surface integrals and Maxwell's equations could be used on a case by case basis for different loads. However this approach has not been used as each deriving each analytical solution is cumbersome and not extendable for a range of load shapes that may be experienced in real world scenarios.



# Bibliography

- [1] Meejin Kim and Sukwon Lee. Fusion Poser: 3D Human Pose Estimation Using Sparse IMUs and Head Trackers in Real Time. *Sensors*, 22:4846, June 2022. ISSN 1424-8220. doi: 10.3390/s22134846. URL <https://www.mdpi.com/1424-8220/22/13/4846/htm>.
- [2] Ryo Eguchi, Brendan Michael, Matthew Howard, and Masaki Takahashi. Shift-Adaptive Estimation of Joint Angle Using Instrumented Brace with Two Stretch Sensors Based on Gaussian Mixture Models. *IEEE Robotics and Automation Letters*, 5:5881–5888, October 2020. ISSN 23773766. doi: 10.1109/lra.2020.3010486.
- [3] Logan Thomas Chatfield. A hybrid assist-as-needed elbow exoskeleton for stroke rehabilitation. 2021. doi: 10.26021/11321. URL <https://hdl.handle.net/10092/102273>.
- [4] Ben O'Brien, Todd Gisby, and Iain A. Anderson. Stretch sensors for human body motion. volume 9056, pages 254–262. Spie, March 2014. ISBN 9780819499820. doi: 10.1117/12.2046143. URL <https://www.spiedigitallibrary.org/conference-proceedings-of-spie/9056/905618/Stretch-sensors-for-human-body-motion/10.1117/12.2046143.full>.
- [5] Xsensor. XSENSOR — Wheelchair Seating. URL <https://www.xsensor.com/solutions-and-platform/csm/wheelchair-seating>.
- [6] PressureProfile. Tactile Sensors for Robotic Applications — PPS, 2023. URL <https://pressureprofile.com/robotics>.
- [7] PowerOn. PowerON: Update of the “super sensitive” - Robotik-Insider.de. URL <https://mrk-blog.de/en/PowerON-Update-of-the-super-sensitive/>.
- [8] Tekscan. Thin-Film Pressure Sensors — Tekscan. URL <https://www.tekscan.com/thin-film-pressure-sensors>.

- [9] SensorProducts. Tactilus — Compression Force Sensing Resistor (fsr) — Force Sensing Resistors — Force Sensing Resistors — Tactilus — Surface Pressure Indicator — Mapping — Force Sensing And Profiling. URL <https://www.sensorprod.com/tactilus.php>.
- [10] Youcan Yan, Yajing Shen, Chaoyang Song, and Jia Pan. Tactile super-resolution model for soft magnetic skin. *IEEE Robotics and Automation Letters*, 7:2589–2596, 4 2022. ISSN 23773766. doi: 10.1109/LRA.2022.3141449. URL <https://ieeexplore.ieee.org/document/9676446>.
- [11] Marc Ramuz, Benjamin C.K. Tee, Jeffrey B.H. Tok, and Zhenan Bao. Transparent, Optical, Pressure-Sensitive Artificial Skin for Large-Area Stretchable Electronics. *Advanced Materials*, 24:3223–3227, June 2012. ISSN 1521-4095. doi: 10.1002/adma.201200523. URL <https://onlinelibrary.wiley.com/doi/full/10.1002/adma.201200523>.
- [12] Joseph Teran, Silvia Blemker, Victor Ng-Thow-Hing, and R. Fedkiw. Finite volume methods for the simulation of skeletal muscle. In *Proceedings of the 2003 ACM SIGGRAPH/Eurographics Symposium on Computer Animation*, Sca ’03, pages 68–74, Goslar, DEU, June 2003. Eurographics Association. ISBN 1581136595. doi: 10.5555/846276.846285.
- [13] Yanjie Wang and Takushi Sugino. *Ionic Polymer Actuators: Principle, Fabrication and Applications*, chapter 3. InTech, Rijeka, July 2018. ISBN 978-1-83881-583-7. doi: 10.5772/intechopen.75085. URL <http://dx.doi.org/10.5772/intechopen.75085>.
- [14] Yu-Jin Park, Seong Hwan Kim, Tae-Hoon Lee, Ae-Ri Cha, Gi-Woo Kim, and Seung-Bok Choi. Design analysis of a magnetorheological elastomer based bush mechanism. volume 10595, March 2018. doi: 10.1117/12.2318795. URL <https://doi.org/10.1117/12.2318795>.
- [15] Nicholas Kellaris, Vidyacharan Gopaluni Venkata, Garrett M. Smith, Shane K. Mitchell, and Christoph Keplinger. Peano-HASEL actuators: Muscle-mimetic, electrohydraulic transducers that linearly contract on activation. *Science Robotics*, 3(14):3276, January 2018. ISSN 24709476. doi: 10.1126/scirobotics.aar3276.
- [16] Y.C. Fung. *Biomechanics - Mechanical Properties of Living Tissues*. Springer Verlag, second edition, 1993. ISBN 0-387-97947-6. Pg 568.
- [17] Richie Ellingham, Chris Pretty, Lui Holder-Pearson, Kean Aw, and Tim Giffney. An electrical impedance tomography based artificial soft skin pressure sensor: Characterisation

- and force modelling. *Sensors and Actuators A: Physical*, 373:115427, 2024. ISSN 0924-4247. doi: 10.1016/j.sna.2024.115427. URL <https://www.sciencedirect.com/science/article/pii/S0924424724004217>.
- [18] Richie Ellingham and Tim Giffney. Carbon black silicone piezoresistive electrical impedance tomography stress sensor device. volume 12042, pages 207–214. Spie, April 2022. doi: 10.1117/12.2610694. URL <https://doi.org/10.1117/12.2610694>.
- [19] Richie Ellingham, Yeni Choi, and Tim Giffney. Deformation Mapping in Dielectric Elastomer Actuators using Electrical Impedance Tomography. March 2024. doi: 10.1117/12.3010073. URL <https://doi.org/10.1117/12.3010073>.
- [20] Jonathan Kayne. Prusa i3 MK3S SolidWorks Model. February 2019. URL <https://grabcad.com/library/prusa-i3-mk3-solidworks-1>.
- [21] Yann Roudaut, Aurélie Lonigro, Bertrand Coste, Jizhe Hao, Patrick Delmas, and Marcel Crest. Touch sense: functional organization and molecular determinants of mechanosensitive receptors. *Channels*, 6:234–245, July 2012. ISSN 1933-6950. doi: 10.4161/chan.22213. URL <https://europepmc.org/article/pmc/3508902>.
- [22] Francesco Stella and Josie Hughes. The science of soft robot design: A review of motivations, methods and enabling technologies. *Frontiers in Robotics and AI*, 9:1059026, January 2023. ISSN 22969144. doi: 10.3389/frobt.2022.1059026.
- [23] Yongchang Zhang, Pengchun Li, Jiale Quan, Longqiu Li, Guangyu Zhang, and Dekai Zhou. Progress, Challenges, and Prospects of Soft Robotics for Space Applications. *Advanced Intelligent Systems*, 5:2200071, March 2023. ISSN 2640-4567. doi: 10.1002/aisy.202200071. URL <https://onlinelibrary.wiley.com/doi/full/10.1002/aisy.202200071>.
- [24] Florian Hartmann, Melanie Baumgartner, Martin Kaltenbrunner, F Hartmann, M Baumgartner, and M Kaltenbrunner. Becoming Sustainable, The New Frontier in Soft Robotics. *Advanced Materials*, 33:2004413, May 2021. ISSN 1521-4095. doi: 10.1002/adma.202004413. URL <https://onlinelibrary.wiley.com/doi/full/10.1002/adma.202004413>.
- [25] Oncay Yasa, Yasunori Toshimitsu, Mike Y. Michelis, Lewis S. Jones, Miriam Filippi, Thomas Buchner, and Robert K. Katzschmann. An Overview of Soft Robotics. *Annual Review of Control, Robotics, and Autonomous Systems*, 6: 1–29, May 2023. ISSN 25735144. doi: 10.1146/annurev-control-062322-100607/

- cite/refworks. URL <https://www.annualreviews.org/content/journals/10.1146/annurev-control-062322-100607>.
- [26] Mariangela Manti, Vito Cacucciolo, and Matteo Cianchetti. Stiffening in soft robotics: A review of the state of the art. *IEEE Robotics and Automation Magazine*, 23:93–106, September 2016. ISSN 10709932. doi: 10.1109/mra.2016.2582718.
- [27] Chidanand Hegde, Jiangtao Su, Joel Ming Rui Tan, Ke He, Xiaodong Chen, and Shlomo Magdassi. Sensing in Soft Robotics. *ACS Nano*, 17:15277–15307, August 2023. ISSN 1936086x. doi: 10.1021/acsnano.3c04089. URL <https://pubs.acs.org/doi/full/10.1021/acsnano.3c04089>.
- [28] Cosimo Della-Santina, Christian Duriez, and Daniela Rus. Model-Based Control of Soft Robots: A Survey of the State of the Art and Open Challenges. *IEEE Control Systems*, 43:30–65, June 2023. ISSN 1941000x. doi: 10.1109/mcs.2023.3253419.
- [29] Costanza Armanini, Frederic Boyer, Anup Teejo Mathew, Christian Duriez, and Federico Renda. Soft Robots Modeling: A Structured Overview. *IEEE Transactions on Robotics*, June 2023. ISSN 19410468. doi: 10.1109/tro.2022.3231360.
- [30] S. Murugesan. An Overview of Electric Motors for Space Applications. *IEEE Transactions on Industrial Electronics and Control Instrumentation*, IECI-28:260–265, 1981. ISSN 00189421. doi: 10.1109/tieci.1981.351050.
- [31] T. Ashuri, A. Armani, R. Jalilzadeh Hamidi, T. Reasnор, S. Ahmadi, and K. Iqbal. Biomedical soft robots: current status and perspective. *Biomedical engineering letters*, 10: 369–385, August 2020. ISSN 2093-985x. doi: 10.1007/s13534-020-00157-6. URL <https://pubmed.ncbi.nlm.nih.gov/32864173/>.
- [32] F. Branz and A. Francesconi. Experimental evaluation of a Dielectric Elastomer robotic arm for space applications. *Acta Astronautica*, 133:324–333, April 2017. ISSN 0094-5765. doi: 10.1016/j.actaastro.2016.11.007.
- [33] Alessandro Bruschi, Davide Maria Donati, Peter Choong, Enrico Lucarelli, and Gordon Wallace. Dielectric Elastomer Actuators, Neuromuscular Interfaces, and Foreign Body Response in Artificial Neuromuscular Prostheses: A Review of the Literature for an In Vivo Application. *Advanced Healthcare Materials*, 10:2100041, July 2021. ISSN 2192-2659. doi: 10.1002/adhm.202100041. URL <https://onlinelibrary.wiley.com/doi/full/10.1002/adhm.202100041>.

- [34] Allied Market Research. Electric Motor Market Size, Share, Trends Forecast 2032, 2024. URL <https://www.alliedmarketresearch.com/electric-motor-market>.
- [35] Poornima Bharatha. Pressure Mapping in Healthcare Market, 2023. URL <https://www.linkedin.com/pulse/pressure-mapping-healthcare-market-booming-worldwide-cagr-bharatha-9a03c/>.
- [36] Todd A. Gisby, Benjamin M. Obrien, and Iain A. Anderson. Self sensing feedback for dielectric elastomer actuators. *Applied Physics Letters*, 102, May 2013. ISSN 00036951. doi: 10.1063/1.4805352/26744. URL [/aip/apl/article/102/19/193703/26744/Self-sensing-feedback-for-dielectric-elastomer](https://aip.org/article/102/19/193703/26744/Self-sensing-feedback-for-dielectric-elastomer).
- [37] Samuel Rosset, Benjamin M. O'Brien, Todd Gisby, Daniel Xu, Herbert R. Shea, and Iain A. Anderson. Self-sensing dielectric elastomer actuators in closed-loop operation. *Smart Materials and Structures*, 22:104018, September 2013. ISSN 0964-1726. doi: 10.1088/0964-1726/22/10/104018. URL <https://iopscience.iop.org/article/10.1088/0964-1726/22/10/104018>.
- [38] Xiqiang Liu, Li Wang, Guidong Chen, al, Joseph W Lowdon, Kasper Eersels, Bart van Grinsven, G Rizzello, D Naso, A York, and S Seelecke. Closed loop control of dielectric elastomer actuators based on self-sensing displacement feedback. *Smart Materials and Structures*, 25:035034, February 2016. ISSN 0964-1726. doi: 10.1088/0964-1726/25/3/035034. URL <https://iopscience.iop.org/article/10.1088/0964-1726/25/3/035034>.
- [39] Weiyang Huang, Guozheng Kang, and Pengyu Ma. Uniaxial Electro-Mechanically Coupled Cyclic Deformation of VHB 4905 Dielectric Elastomer: Experiment and Constitutive Model. *Journal of Materials Engineering and Performance*, pages 1–16, April 2023. ISSN 15441024. doi: 10.1007/s11665-023-08179-8.
- [40] Wan Hasbullah MohdIsa, Andres Hunt, and S. Hassan HosseinNia. Sensing and Self-Sensing Actuation Methods for Ionic Polymer–Metal Composite (IPMC): A Review. *Sensors* 2019, Vol. 19, Page 3967, 19:3967, September 2019. ISSN 1424-8220. doi: 10.3390/s19183967. URL <https://www.mdpi.com/1424-8220/19/18/3967/htm>.
- [41] Richard Ellingham and Tim Giffney. Stress and Resistance Relaxation for Carbon Nanoparticle Silicone Rubber Composite Large-Strain Sensors. *Volume 7: 17th IEEE/ASME International Conference on Mechatronic and Embedded Systems and Applications (MESA)*, November 2021. doi: 10.1115/detc2021-69206.

- URL <https://asmedigitalcollection.asme.org/IDETC-CIE/proceedings/IDETC-CIE2021/85437/V007T07A046/1128153>.
- [42] John A. McGrath and Jouni Uitto. Anatomy and Organization of Human Skin. *Rook's Textbook of Dermatology: Eighth Edition*, 1:1–53, May 2010. doi: 10.1002/9781444317633.ch3. URL <https://onlinelibrary.wiley.com/doi/full/10.1002/9781444317633.ch3>.
- [43] Guillaume Landry, Katia Parodi, Joachim E Wildberger, al, Mikaël Simard, Arthur Lalonde, Hugo Bouchard, Gurpreet Singh, and Arnab Chanda. Mechanical properties of whole-body soft human tissues: a review. *Biomedical Materials*, 16:062004, October 2021. ISSN 1748-605x. doi: 10.1088/1748-605x/ac2b7a. URL <https://iopscience.iop.org/article/10.1088/1748-605X/ac2b7a>.
- [44] Holger J. Klein, Richard M. Fakin, Pascal Ducommun, Thomas Giesen, Pietro Giovanoli, and Maurizio Calcagni. Evaluation of cutaneous spatial resolution and pressure threshold secondary to digital nerve repair. *Plastic and Reconstructive Surgery*, 137:1203–1212, 2016. ISSN 00321052. doi: 10.1097/prs.0000000000002023. URL [https://journals.lww.com/plasreconsurg/fulltext/2016/04000/evaluation\\_of\\_cutaneous\\_spatial\\_resolution\\_and.20.aspx](https://journals.lww.com/plasreconsurg/fulltext/2016/04000/evaluation_of_cutaneous_spatial_resolution_and.20.aspx).
- [45] Judith Krotoski, Sidney Weinstein, and Curt Weinstein. Testing Sensibility, Including Touch-Pressure, Two-point Discrimination, Point Localization, and Vibration. *Journal of Hand Therapy*, 6:114–123, April 1993. ISSN 0894-1130. doi: 10.1016/s0894-1130(12)80292-4.
- [46] Aisling Ní Annaidh, Karine Bruyère, Michel Destrade, Michael D. Gilchrist, and Mélanie Otténio. Characterization of the anisotropic mechanical properties of excised human skin. *Journal of the Mechanical Behavior of Biomedical Materials*, 5:139–148, January 2012. ISSN 1751-6161. doi: 10.1016/j.jmbbm.2011.08.016.
- [47] Krisakorn Khaothong, J C H Goh, and C T Lim. In Vivo Measurements of the Mechanical Properties of Human Skin and Muscle by Inverse Finite Element Method Combined with the Indentation Test. *IFMBE Proceedings*, 31 Ifmbe:1467–1470, 2010. ISSN 1433-9277. doi: 10.1007/978-3-642-14515-5\_374.
- [48] Y. Zheng and A. F.T. Mak. Effective elastic properties for lower limb soft tissues from manual indentation experiment. *IEEE Transactions on Rehabilitation Engineering*, 7: 257–267, September 1999. ISSN 10636528. doi: 10.1109/86.788463.

- [49] Brian Holt, Anubhav Tripathi, and Jeffrey Morgan. Viscoelastic Response of Human Skin to Low Magnitude Physiologically Relevant Shear. *Journal of biomechanics*, 41: 2689, August 2008. ISSN 00219290. doi: 10.1016/j.jbiomech.2008.06.008. URL <https://www.ncbi.nlm.nih.gov/pmc/articles/PMC2584606/>.
- [50] Cameron H. Parvini, Alexander X. Cartagena-Rivera, and Santiago D. Solares. Viscoelastic parameterization of human skin cells characterize material behavior at multiple timescales. *Communications Biology* 2022 5:1, 5:1–11, January 2022. ISSN 2399-3642. doi: 10.1038/s42003-021-02959-5. URL <https://www.nature.com/articles/s42003-021-02959-5>.
- [51] Mélanie Ottenio, Doris Tran, Aisling Ní Annaidh, Michael D. Gilchrist, and Karine Bruyère. Strain rate and anisotropy effects on the tensile failure characteristics of human skin. *Journal of the Mechanical Behavior of Biomedical Materials*, 41:241–250, January 2015. ISSN 1751-6161. doi: 10.1016/j.jmbbm.2014.10.006.
- [52] Sharad P. Paul. Biodynamic excisional skin tension lines for surgical excisions: untangling the science. *Annals of The Royal College of Surgeons of England*, 100:330, April 2018. ISSN 00358843. doi: 10.1308/rcsann.2018.0038. URL <https://www.ncbi.nlm.nih.gov/pmc/articles/PMC5958865/>.
- [53] Davide Deflorio, Massimiliano Di Luca, and Alan M. Wing. Skin and Mechanoreceptor Contribution to Tactile Input for Perception: A Review of Simulation Models. *Frontiers in Human Neuroscience*, 16:862344, June 2022. ISSN 16625161. doi: 10.3389/fnhum.2022.862344/bibtex.
- [54] Hirotake Yokota, Naofumi Otsuru, Rie Kikuchi, Rinako Suzuki, Sho Kojima, Kei Saito, Shota Miyaguchi, Yasuto Inukai, and Hideaki Onishi. Establishment of optimal two-point discrimination test method and consideration of reproducibility. *Neuroscience Letters*, 714:134525, January 2020. ISSN 0304-3940. doi: 10.1016/j.neulet.2019.134525.
- [55] Rochelle Ackerley, Ida Carlsson, Henric Wester, Håkan Olausson, and Helena Backlund Wasling. Touch perceptions across skin sites: differences between sensitivity, direction discrimination and pleasantness. *Frontiers in Behavioral Neuroscience*, 8, February 2014. ISSN 16625153. doi: 10.3389/fnbeh.2014.00054. URL <https://www.ncbi.nlm.nih.gov/pmc/articles/PMC3928539/>.
- [56] Nicholas D.J. Strzalkowski, Robyn L. Mildren, and Leah R. Bent. Neurophysiology of Tactile Perception: A Tribute to Steven Hsiao: Thresholds of cutaneous afferents related

- to perceptual threshold across the human foot sole. *Journal of Neurophysiology*, 114:2144, August 2015. ISSN 15221598. doi: 10.1152/jn.00524.2015. URL <https://www.ncbi.nlm.nih.gov/pmc/articles/PMC4595609/>.
- [57] Mohsin I. Tiwana, Stephen J. Redmond, and Nigel H. Lovell. A review of tactile sensing technologies with applications in biomedical engineering. *Sensors and Actuators A: Physical*, 179:17–31, June 2012. ISSN 0924-4247. doi: 10.1016/j.sna.2012.02.051.
- [58] Samta Sapra, Aniket Chakraborty, Suresh Nuthalapati, Anindya Nag, David W. Inglis, Subhas Chandra Mukhopadhyay, and Mehmet Ercan Altinsoy. Printed, wearable e-skin force sensor array. *Measurement*, 206:112348, January 2023. ISSN 0263-2241. doi: 10.1016/j.measurement.2022.112348.
- [59] Yuting Zhu, Kean Aw, and Tim Giffney. *Dielectric Elastomer-based Multi-location Capacitive Sensor*. The University of Auckland Mechanical Engineering Department, December 2021. URL <https://researchspace.auckland.ac.nz/handle/2292/60603>.
- [60] Guanhao Liang, Yancheng Wang, Deqing Mei, Kailun Xi, and Zichen Chen. Flexible Capacitive Tactile Sensor Array with Truncated Pyramids as Dielectric Layer for Three-Axis Force Measurement. *Journal of Microelectromechanical Systems*, 24:1510–1519, October 2015. ISSN 10577157. doi: 10.1109/jmems.2015.2418095.
- [61] Youcan Yan, Zhe Hu, Zhengbao Yang, Wenzhen Yuan, Chaoyang Song, Jia Pan, and Yajing Shen. Soft magnetic skin for super-resolution tactile sensing with force self-decoupling. *Science Robotics*, 6:8801, February 2021. ISSN 24709476. doi: 10.1126/scirobotics.abc8801. URL <https://www.science.org/doi/10.1126/scirobotics.abc8801>.
- [62] Gihun Lee, Hyunjin Kim, and Inkyu Park. A Mini Review of Recent Advances in Optical Pressure Sensor. *Journal of Sensor Science and Technology*, 32:22–30, 2023. ISSN pISSN 1225-5475/eISSN 2093-7563. doi: 10.46670/JSST.2023.32.1.22.
- [63] K. Park, H. Yuk, M. Yang, J. Cho, H. Lee, and J. Kim. A biomimetic elastomeric robot skin using electrical impedance and acoustic tomography for tactile sensing. *Science Robotics*, 7:7187, June 2022. ISSN 24709476. doi: 10.1126/scirobotics.abm7187. URL <https://www.science.org/doi/10.1126/scirobotics.abm7187>.
- [64] Dana Hughes and Nikolaus Correll. Texture recognition and localization in amorphous robotic skin. *Bioinspiration & Biomimetics*, 10:055002, September 2015. ISSN 1748-3190. doi: 10.1088/1748-3190/10/5/055002. URL <https://iopscience.iop.org/article/10.1088/1748-3190/10/5/055002>.

- [65] Lei Sun, Shuwen Jiang, Yao Xiao, and Wanli Zhang. Realization of flexible pressure sensor based on conductive polymer composite via using electrical impedance tomography. *Smart Materials and Structures*, 29:055004, March 2020. ISSN 0964-1726. doi: 10.1088/1361-665x/ab75a3. URL <https://iopscience.iop.org/article/10.1088/1361-665X/ab75a3>.
- [66] Yun Lu, Weina He, Tai Cao, Haitao Guo, Yongyi Zhang, Qingwen Li, Ziqiang Shao, Yulin Cui, and Xuetong Zhang. Elastic, Conductive, Polymeric Hydrogels and Sponges. *Scientific Reports* 2014 4:1, 4:1–8, July 2014. ISSN 2045-2322. doi: 10.1038/srep05792. URL <https://www.nature.com/articles/srep05792>.
- [67] Michael E. Spahr, Raffaele Gilardi, and Daniele Bonacchi. *Carbon Black for Electrically Conductive Polymer Applications*, pages 375–400. Springer, Cham, 2017. doi: 10.1007/978-3-319-28117-9\_32.
- [68] Patricia Hazelton, Mengguang Ye, and Xianfeng Chen. *Introduction to Conducting Polymers*. 2023. doi: 10.1021/bk-2023-1438.ch001. URL <https://pubs.acs.org/sharingguidelines>.
- [69] Adravit Mukherjee, Afshin Dianatdar, Magdalena Z. Gladysz, Hamoon Hemmatpour, Mart Hendriksen, Petra Rudolf, Małgorzata K. Włodarczyk-Biegun, Marleen Kamperman, Ajay Giri Prakash Kottapalli, and Ranjita K. Bose. Electrically Conductive and Highly Stretchable Piezoresistive Polymer Nanocomposites via Oxidative Chemical Vapor Deposition. *ACS Applied Materials and Interfaces*, 15:31899–31916, July 2023. ISSN 19448252. doi: 10.1021/acsami.3c06015. URL <https://pubs.acs.org/doi/full/10.1021/acsami.3c06015>.
- [70] Yong Lae Park, Carmel Majidi, Rebecca Kramer, Phillip Brard, and Robert J. Wood. Hyperelastic pressure sensing with a liquid-embedded elastomer. *Journal of Micromechanics and Microengineering*, 20:125029, November 2010. ISSN 0960-1317. doi: 10.1088/0960-1317/20/12/125029. URL <https://iopscience.iop.org/article/10.1088/0960-1317/20/12/125029>.
- [71] Taekeon Jung and Sung Yang. Highly Stable Liquid Metal-Based Pressure Sensor Integrated with a Microfluidic Channel. *Sensors* 2015, Vol. 15, Pages 11823-11835, 15: 11823–11835, May 2015. ISSN 1424-8220. doi: 10.3390/s150511823. URL <https://www.mdpi.com/1424-8220/15/5/11823/htm>.

- [72] Daehan Kim, Sung Hwan Kim, and Joong Yull Park. Floating-on-water fabrication method for thin polydimethylsiloxane membranes. *Polymers*, 11:1264, August 2019. ISSN 20734360. doi: 10.3390/polym11081264. URL <https://www.ncbi.nlm.nih.gov/pmc/articles/PMC6722912/>.
- [73] Hyunwoo Yuk, Teng Zhang, German Alberto Parada, Xinyue Liu, and Xuanhe Zhao. Skin-inspired hydrogel-elastomer hybrids with robust interfaces and functional microstructures. *Nature communications*, 7:12028, June 2016. ISSN 2041-1723. doi: 10.1038/ncomms12028.
- [74] Haofeng Chen, Xuanxuan Yang, Jialu Geng, Gang Ma, and Xiaojie Wang. A Skin-Like Hydrogel for Distributed Force Sensing Using an Electrical Impedance Tomography-Based Pseudo-Array Method. *ACS Applied Electronic Materials*, March 2023. ISSN 2637-6113. doi: 10.1021/acsaelm.2c01394. URL <https://pubs.acs.org/doi/abs/10.1021/acsaelm.2c01394>.
- [75] Shuoyan Xu, Zigan Xu, Ding Li, Tianrui Cui, Xin Li, Yi Yang, Houfang Liu, and Tianling Ren. Recent Advances in Flexible Piezoresistive Arrays: Materials, Design, and Applications. *Polymers* 2023, Vol. 15, Page 2699, 15:2699, June 2023. ISSN 2073-4360. doi: 10.3390/polym15122699. URL <https://www.mdpi.com/2073-4360/15/12/2699/htm>.
- [76] Kyoseung Sim, Zhouyu Rao, Zhanan Zou, Faheem Ershad, Jianming Lei, Anish Thukral, Jie Chen, Qing An Huang, Jianliang Xiao, and Cunjiang Yu. Metal oxide semiconductor nanomembrane-based soft unnoticeable multifunctional electronics for wearable human-machine interfaces. *Science advances*, 5, August 2019. ISSN 2375-2548. doi: 10.1126/sciadv.aav9653. URL <https://pubmed.ncbi.nlm.nih.gov/31414044/>.
- [77] Baolin Guo and Peter X. Ma. Conducting Polymers for Tissue Engineering. *Biomacromolecules*, 19:1764, June 2018. ISSN 15264602. doi: 10.1021/acs.biomac.8b00276. URL <https://www.ncbi.nlm.nih.gov/pmc/articles/PMC6211800/>.
- [78] Mitradip Bhattacharjee, Mahesh Soni, Pablo Escobedo, and Ravinder Dahiya. PEDOT:PSS Microchannel-Based Highly Sensitive Stretchable Strain Sensor. *Advanced Electronic Materials*, 6:2000445, August 2020. ISSN 2199-160x. doi: 10.1002/aelm.202000445. URL <https://onlinelibrary.wiley.com/doi/full/10.1002/aelm.202000445>.
- [79] Zequn Shen, Zhilin Zhang, Ningbin Zhang, Jinhao Li, Peiwei Zhou, Faqi Hu, Yu Rong, Baoyang Lu, Guoying Gu, Z Shen, N Zhang, J Li, P Zhou, Y Rong, G Gu, Z Zhang,

- F Hu, and B Lu. High-Stretchability, Ultralow-Hysteresis ConductingPolymer Hydrogel Strain Sensors for Soft Machines. *Advanced Materials*, 34:2203650, August 2022. ISSN 1521-4095. doi: 10.1002/adma.202203650. URL <https://onlinelibrary.wiley.com/doi/full/10.1002/adma.202203650>.
- [80] Lin Li, Jiahong Zheng, Jing Chen, Zebang Luo, Yi Su, Wei Tang, Xing Gao, Yingtian Li, Chongjing Cao, Qiuhua Liu, Xiaoyang Kang, Lei Wang, and Hui Li. Flexible Pressure Sensors for Biomedical Applications: From Ex Vivo to In Vivo. *Advanced Materals Interfaces*, 7:2000743, September 2020. ISSN 2196-7350. doi: 10.1002/admi.202000743. URL <https://onlinelibrary.wiley.com/doi/full/10.1002/admi.202000743>.
- [81] Z Li, L Zhao, G Luo, Z Jiang, S Zhang, R Haghniaz, K Lee, W Sun, H Kim, J Lee, S Ahadian, M R Dokmeci, A Khademhosseini, H Ling, X Wang, H Liu, Zhikang Li, Shiming Zhang, Yihang Chen, Haonan Ling, Libo Zhao, Guoxi Luo, Xiaochen Wang, Martin C Hartel, Hao Liu, Yumeng Xue, Reihaneh Haghniaz, KangJu Lee, Wujin Sun, HanJun Kim, Junmin Lee, Yichao Zhao, Yepin Zhao, Sam Emaminejad, Samad Ahadian, Nureddin Ashammakhi, Mehmet R Dokmeci, Zhuangde Jiang, Ali Khademhosseini, Y Chen, M C Hartel, Y Xue, N Ashammakhi, and Y Zhao. Gelatin Methacryloyl-Based Tactile Sensors for Medical Wearables. *Advanced Functional Materials*, 30: 2003601, December 2020. ISSN 1616-3028. doi: 10.1002/adfm.202003601. URL <https://onlinelibrary.wiley.com/doi/full/10.1002/adfm.202003601>.
- [82] Sen Chen, Hong Zhang Wang, Rui Qi Zhao, Wei Rao, and Jing Liu. Liquid Metal Composites. *Matter*, 2:1446–1480, June 2020. ISSN 25902385. doi: 10.1016/j.matt.2020.03.016. URL <http://www.cell.com/article/S2590238520301296/fulltext>.
- [83] You Jeong Jeong, Young Eun Kim, Kap Jin Kim, Eung Je Woo, and Tong In Oh. Multi-layered Fabric Pressure Sensor for Real-Time Piezo-Impedance Imaging of Pressure Distribution. *IEEE Transactions on Instrumentation and Measurement*, 69:565–572, February 2020. ISSN 15579662. doi: 10.1109/tim.2019.2903701.
- [84] A. Yao and M. Soleimani. A pressure mapping imaging device based on electrical impedance tomography of conductive fabrics. *Sensor Review*, 32:310–317, 2012. ISSN 02602288. doi: 10.1108/02602281211257542.
- [85] Iqra Abdul Rashid, Iqra Saif, Muhammad Usama, Muhammad Umer, Amjed Javid, Zulfiqar Ahmad Rehan, and Usman Zubair. Highly resilient and responsive fabric strain

- sensors: Their effective integration into textiles and wireless communication for wearable applications. *Sensors and Actuators A: Physical*, 346:113836, October 2022. ISSN 0924-4247. doi: 10.1016/j.sna.2022.113836.
- [86] K G Princy, Rani Joseph, and C Sudha Kartha. Studies on Conductive Silicone Rubber Compounds. *Applied Polymers*, 69, August 1998. doi: 10.1002/(sici)1097-4628(19980801)69:5.
- [87] Lingyan Duan, Sirui Fu, Hua Deng, Qin Zhang, Ke Wang, Feng Chen, and Qiang Fu. The resistivity-strain behavior of conductive polymer composites: stability and sensitivity. *Journal of Materials Chemistry A*, 2:17085–17098, September 2014. ISSN 2050-7496. doi: 10.1039/c4ta03645j. URL <https://pubs.rsc.org/en/content/articlehtml/2014/ta/c4ta03645j>.
- [88] Andriy Buketov, Serhii Smetankin, Eduard Lysenkov, Kyrylo Yurenin, Oleksandr Akimov, Serhii Yakushchenko, and Iryna Lysenkova. Electrophysical Properties of Epoxy Composite Materials Filled with Carbon Black Nanopowder. *Advances in Materials Science and Engineering*, 2020, 2020. ISSN 16878442. doi: 10.1155/2020/6361485.
- [89] Hideki Shirakawa, Edwin J. Louis, Alan G. MacDiarmid, Chwan K. Chiang, and Alan J. Heeger. Synthesis of electrically conducting organic polymers: halogen derivatives of polyacetylene,  $(CH)_x$ . *Journal of the Chemical Society, Chemical Communications*, pages 578–580, 1 1977. ISSN 0022-4936. doi: 10.1039/C39770000578. URL <https://pubs.rsc.org/en/content/articlehtml/1977/c3/c39770000578>.
- [90] Golezar Gilanizadehdizaj, Kean C. Aw, Jonathan Stringer, and Debes Bhattacharyya. Facile fabrication of flexible piezo-resistive pressure sensor array using reduced graphene oxide foam and silicone elastomer. *Sensors and Actuators A: Physical*, 340:113549, June 2022. ISSN 0924-4247. doi: 10.1016/j.sna.2022.113549.
- [91] Ya Fei Fu, Feng Lian Yi, Jin Rui Liu, Yuan Qing Li, Ze Yu Wang, Gang Yang, Pei Huang, Ning Hu, and Shao Yun Fu. Super soft but strong E-Skin based on carbon fiber/carbon black/silicone composite: Truly mimicking tactile sensing and mechanical behavior of human skin. *Composites Science and Technology*, 186:107910, January 2020. ISSN 0266-3538. doi: 10.1016/j.compscitech.2019.107910.

- [92] Kun Yang, Xinkai Xia, Fan Zhang, Huanzhou Ma, Shengbo Sang, Qiang Zhang, and Jianlong Ji. Implementation of a Sponge-Based Flexible Electronic Skin for Safe Human–Robot Interaction. *Micromachines*, 13:1344, August 2022. ISSN 2072666x. doi: 10.3390/mi13081344/s1. URL <https://www.mdpi.com/2072-666X/13/8/1344/htm>.
- [93] Jonathan Rossiter and Toshiharu Mukai. A novel tactile sensor using a matrix of LEDs operating in both photoemitter and photodetector modes. *Proceedings of IEEE Sensors*, 2005:994–997, 2005. doi: 10.1109/icsens.2005.1597869.
- [94] Sho Shimadera, Kei Kitagawa, Koyo Sagehashi, Yoji Miyajima, Tomoaki Niiyama, and Satoshi Sunada. Speckle-based high-resolution multimodal soft sensing. *Scientific Reports* 2022 12:1, 12:1–11, July 2022. ISSN 2045-2322. doi: 10.1038/s41598-022-17026-0. URL <https://www.nature.com/articles/s41598-022-17026-0>.
- [95] R. D. Keynes, David J. Aidley, and Christopher L.-H Huang. *Nerve and Muscle*. Cambridge University Press, 4 edition, 2011. ISBN 9780511853067.
- [96] Gregory N. Filatov, Martin J. Pinter, and Mark M. Rich. Resting potential-dependent regulation of the voltage sensitivity of sodium channel gating in rat skeletal muscle in vivo. *The Journal of General Physiology*, 126:161, 8 2005. ISSN 00221295. doi: 10.1085/JGP.200509337. URL <https://pmc.ncbi.nlm.nih.gov/articles/PMC2266572/>.
- [97] Knut Schmidt Nielsen. *Animal Physiology: Adaptation and Environment*. Cambridge University Press, 5 edition, 2002. ISBN 521 57098. URL [https://books.google.co.nz/books?id=hcw2AAAAQBAJ&printsec=frontcover&redir\\_esc=y#v=onepage&q&f=false](https://books.google.co.nz/books?id=hcw2AAAAQBAJ&printsec=frontcover&redir_esc=y#v=onepage&q&f=false).
- [98] Milos R. Popovic and T. Adam Thrasher. Neuroprostheses. *Encyclopedia of Biomaterials and Biomedical Engineering*, 2004. doi: 10.1081/e-ebbe120013941. URL <http://toronto-fes.ca/publications/2004Popovic.pdf>.
- [99] R Mcn. Alexander and H C Bennet-Clark. Storage of elastic strain energy in muscle and other tissues. *Nature*, 265(5590):114–117, 1977. doi: 10.1038/265114a0. URL <https://www.nature.com/articles/265114a0>.
- [100] Robert Full and Kenneth Meijer. *Metrics of Natural Muscle Function*, chapter Metrics of Natural Muscle Function, pages 73–89. Spie, March 2004. doi: 10.1117/3.547465.ch3. URL <http://ebooks.spiedigitallibrary.org/content.aspx?doi=10.1117/3.547465.ch3>.

- [101] Mihai Duduta, Ehsan Hajiesmaili, Huichan Zhao, Robert J. Wood, and David R. Clarke. Realizing the potential of dielectric elastomer artificial muscles. *Proceedings of the National Academy of Sciences of the United States of America*, 116(30679271):2476–2481, February 2019. ISSN 0027-8424. doi: 10.1073/pnas.1815053116. URL <https://www.pnas.org/content/116/7/2476>.
- [102] Nicholas P Smith, Christopher J Barclay, and Denis S Loiselle. The efficiency of muscle contraction. *Progress in Biophysics and Molecular Biology*, 88(1):1–58, 2005. ISSN 0079-6107. URL <http://www.sciencedirect.com/science/article/pii/S0079610703001081>.
- [103] Archibald Vivian Hill. The heat of shortening and the dynamic constants of muscle. *Proceedings of the Royal Society of London. Series B - Biological Sciences*, 126(843):136–195, 1938. doi: 10.1098/rspb.1938.0050. URL <https://royalsocietypublishing.org/doi/pdf/10.1098/rspb.1938.0050>.
- [104] Dale Purves, George J Augustine, David Fitzpatrick, Lawrence C Katz, Anthony-Samuel LaMantia, James O McNamara, and S Mark Williams. *The Regulation of Muscle Force*. Sinauer Associates, 2 edition, 2001. ISBN 0878937420. URL <https://www.ncbi.nlm.nih.gov/books/NBK11021/>.
- [105] Guangqiang Ma, Xiaojun Wu, Lijin Chen, Xin Tong, and Weiwei Zhao. Characterization and Optimization of Elastomeric Electrodes for Dielectric Elastomer Artificial Muscles. *Materials* 2020, Vol. 13, Page 5542, 13(1908508):5542, December 2020. ISSN 1996-1944. doi: 10.3390/ma13235542. URL <https://www.mdpi.com/1996-1944/13/23/5542/htm>.
- [106] Raphael Neuhaus, Nima Zahiri, Jan Petrs, Yasaman Tahouni, Jörg Siegert, Ivica Kolaric, Hanaa Dahy, and Thomas Bauernhansl. Integrating Ionic Electroactive Polymer Actuators and Sensors Into Adaptive Building Skins – Potentials and Limitations. *Frontiers in Built Environment*, 6:546334, July 2020. ISSN 22973362. doi: 10.3389/fbuil.2020.00095.
- [107] Daniel Segalman, Walter Witkowski, D Adolf, and Mohsen Shahinpoor. Theory and application of electrically controlled polymeric gels. *Smart Materials and Structures*, 1:95, January 1999. doi: 10.1088/0964-1726/1/1/015.
- [108] Mohsen Shahinpoor. *Ionic Polymer Metal Composites (IPMCs). Fundamentals of Smart Materials*. The Royal Society of Chemistry, 2016. ISBN 978-1-78262-720-3. doi: 10.1039/9781839168819.

- [109] S Ma, Y Zhang, Y Liang, L Ren, W Tian, and L Ren. High-Performance Ionic-Polymer-Metal Composite: Toward Large-Deformation Fast-Response Artificial Muscles. *Advanced Functional Materials*, 30, 2020. doi: 10.1002/adfm.201908508. Export Date: 14 May 2020.
- [110] Masahiro Homma and Yoshio Nakano. Development of Electro-driven Polymer Gel/Platinum Composite Membranes. *Kagaku Kogaku Ronbunshu*, 25(6):1010–1014, 1999. ISSN 13499203. doi: 10.1252/kakoronbunshu.25.1010.
- [111] Raymond Liu. In Situ Electrode Formation on a Nafion Membrane by Chemical Platinization. *Journal of The Electrochemical Society*, 139(1):15, 1992. ISSN 0013-4651. URL <http://dx.doi.org/10.1149/1.2069162>.
- [112] James D Carrico, Nicklaus W Traeden, Matteo Aureli, and Kam K Leang. Fused filament 3D printing of ionic polymer-metal composites (IPMCs). *Smart Materials and Structures*, 24(12):125021, November 2015. doi: 10.1088/0964-1726/24/12/125021. URL <https://doi.org/10.1088%2F0964-1726%2F24%2F12%2F125021>.
- [113] Mohsen Shahinpoor and Kwang J. Kim. Ionic polymer-metal composites: III. Modeling and simulation as biomimetic sensors, actuators, transducers, and artificial muscles. *Smart Materials and Structures*, 13(6):1362–1388, December 2004. ISSN 09641726. doi: 10.1088/0964-1726/13/6/009.
- [114] Barbar Akle and Donald J. Leo. Electromechanical transduction in multilayer ionic transducers. *Smart Materials and Structures*, 13(5):1081–1089, October 2004. ISSN 09641726. doi: 10.1088/0964-1726/13/5/014.
- [115] Yan Xu, Gang Zhao, Changshun Ma, and Zhuangzhi Sun. Research on preparation and stacking performance of IPMC. *Journal of Biomimetics, Biomaterials and Biomedical Engineering*, 21(1):45–53, 2014. ISSN 22969845. doi: 10.4028/www.scientific.net/JBBBE. 21.45.
- [116] Shuxiang Guo, T Fukuda, K Kosuge, F Arai, K Oguro, and M Negoro. Micro catheter system with active guide wire-structure, experimental results and characteristic evaluation of active guide wire catheter using ICPF actuator. In *1994 5th International Symposium on Micro Machine and Human Science Proceedings*, page 191, 1994. doi: 10.1109/ISMMHS. 1994.512923.
- [117] Akio Kodaira, Kinji Asaka, Tetsuya Horiuchi, Gen Endo, Hiroyuki Nabae, and Koichi Suzumori. IPMC monolithic thin film robots fabricated using a multi-layer casting process.

- IEEE Robotics and Automation Letters, 4(2):1335–1342, April 2019. ISSN 23773766. doi: 10.1109/lra.2019.2895398.
- [118] Yi Chu Chang and Won Jong Kim. Aquatic ionic-polymer-metal-composite insectile robot with multi-DOF legs. IEEE/ASME Transactions on Mechatronics, 18(2):547–555, April 2013. ISSN 10834435. doi: 10.1109/tmech.2012.2210904.
- [119] Joel J. Hubbard, Maxwell Fleming, Viljar Palmre, David Pugal, Kwang J. Kim, and Kam K. Leang. Monolithic IPMC fins for propulsion and maneuvering in bioinspired underwater robotics. IEEE Journal of Oceanic Engineering, 39(3):540–551, July 2014. ISSN 03649059. doi: 10.1109/joe.2013.2259318.
- [120] Jasim Khawwaf, Jinchuan Zheng, Hai Wang, and Zhihong Man. Practical model-free robust control design for an underwater IPMC actuator. In 2019 Chinese Control Conference (CCC), volume 2019-July, pages 3214–3219. IEEE Computer Society, July 2019. ISBN 9789881563972. doi: 10.23919/ChiCC.2019.8866467.
- [121] Mark R Jolly, J David Carlson, Beth C Munoz, and Todd A Bullions. The Magnetoviscoelastic Response of Elastomer Composites Consisting of Ferrous Particles Embedded in a Polymer Matrix. Journal of Intelligent Material Systems and Structures, 7(6):613–622, November 1996. ISSN 1045-389x. doi: 10.1177/1045389x9600700601.
- [122] Holger Bose, Raman Rabindranath, and Johannes Ehrlich. Soft magnetorheological elastomers as new actuators for valves. Journal of Intelligent Material Systems and Structures, 23(9):989–994, January 2012. ISSN 1045-389x. doi: 10.1177/1045389x11433498. URL <https://doi.org/10.1177/1045389X11433498>. doi: 10.1177/1045389X11433498.
- [123] Nurul Liyana Burhannuddin, Nur Azmah Nordin, Saiful Amri Mazlan, Siti Aishah Abdul Aziz, Seung Bok Choi, Noriyuki Kuwano, Nurhazimah Nazmi, and Norhasnidawani Johari. Effects of corrosion rate of the magnetic particles on the field-dependent material characteristics of silicone based magnetorheological elastomers. Smart Materials and Structures, 29, August 2020. ISSN 1361665x. doi: 10.1088/1361-665x/ab972c.
- [124] Qi Ge, Zhiqin Li, Zhaolong Wang, Kavin Kowsari, Wang Zhang, Xiangnan He, Jianlin Zhou, and Nicholas X. Fang. Projection micro stereolithography based 3D printing and its applications. International Journal of Extreme Manufacturing, 2:022004, June 2020. ISSN 2631-7990. doi: 10.1088/2631-7990/ab8d9a. URL <https://iopscience.iop.org/article/10.1088/2631-7990/ab8d9a>.

- [125] Mohammadreza Lalegani Dezaki and Mahdi Bodaghi. Magnetorheological elastomer-based 4D printed electroactive composite actuators. *Sensors and Actuators A: Physical*, 349:114063, January 2023. ISSN 0924-4247. doi: 10.1016/j.sna.2022.114063.
- [126] Hannes Krueger, Mohammad Vaezi, and Shoufeng Yang. 3D printing of magnetorheological elastomers(MREs)smart materials. volume 0, pages 213–218. Pro-AM, May 2014. ISBN 9789810904463. doi: 10.3850/978-981-09-0446-3\_088.
- [127] Ioan Bica. Magnetoresistor sensor with magnetorheological elastomers. *Journal of Industrial and Engineering Chemistry*, 17:83–89, 1 2011. ISSN 1226-086X. doi: 10.1016/J.JIEC.2010.12.001.
- [128] Leone Costi, Antonia Georgopoulou, Somashree Mondal, Fumiya Iida, and Frank Clemens. 3d printable self-sensing magnetorheological elastomer. *Macromolecular Materials and Engineering*, 309:2300294, 2 2024. ISSN 1439-2054. doi: 10.1002/MAME.202300294. URL <https://onlinelibrary.wiley.com/doi/full/10.1002/mame.202300294>.
- [129] Yakub F. Ismail M. A. Unuh H, Muhamad P and Z. Tanasta. Experimental Validation to a Prototype Magnetorheological (MR) Semi-Active Damper for C-Class Vehicle. *Ijame*, 16(3):7034–7047, 2019.
- [130] Bing Chen, Xuan Zhao, Hao Ma, Ling Qin, and Wei-Hsin Liao. Design and characterization of a magneto-rheological series elastic actuator for a lower extremity exoskeleton. *Smart Materials and Structures*, 26(10):105008, 2017. ISSN 1361-665x. URL <http://dx.doi.org/10.1088/1361-665X/aa8343>.
- [131] Gregory J. Hiemenz, Young Tai Choi, and Norman M. Wereley. Semi-active control of vertical stroking helicopter crew seat for enhanced crashworthiness. *Journal of Aircraft*, 44(3):1031–1034, May 2007. ISSN 15333868. doi: 10.2514/1.26492. URL <https://arc.aiaa.org/doi/abs/10.2514/1.26492>.
- [132] E. Acome, S. K. Mitchell, T. G. Morrissey, M. B. Emmett, C. Benjamin, M. King, M. Radakovitz, and C. Keplinger. Hydraulically amplified self-healing electrostatic actuators with muscle-like performance. *Science*, 359(6371):61–65, January 2018. ISSN 10959203. doi: 10.1126/science.aa06139. URL <http://science.sciencemag.org/>.
- [133] Christoph Keplinger, Tiefeng Li, Richard Baumgartner, Zhigang Suo, and Siegfried Bauer. Harnessing snap-through instability in soft dielectrics to achieve giant voltage-triggered deformation. *Soft Matter*, 8(2):285–288, January 2012. ISSN 1744683x. doi: 10.1039/c1sm06736b. URL [www.rsc.org/advances](http://www.rsc.org/advances).

- [134] Charles Manion, Dinesh Patel, Mark Fuge, and Sarah Bergbrieter. Modeling and Evaluation of Additive Manufactured HASEL Actuators. 2018. URL [https://www.researchgate.net/publication/343949671\\_Modeling\\_and\\_Evaluation\\_of\\_Additive\\_Manufactured\\_HASEL\\_Actuators](https://www.researchgate.net/publication/343949671_Modeling_and_Evaluation_of_Additive_Manufactured_HASEL_Actuators).
- [135] Shane K Mitchell, Xingrui Wang, Eric Acome, Trent Martin, Khoi Ly, Nicholas Kellaris, Vidyacharan Gopaluni Venkata, and Christoph Keplinger. An Easy-to-Implement Toolkit to Create Versatile and High-Performance HASEL Actuators for Untethered Soft Robots. *Advanced Science*, 6(14):1900178, July 2019. ISSN 2198-3844. doi: 10.1002/advs.201900178. URL <https://doi.org/10.1002/advs.201900178>.
- [136] Yang Liu, Meng Gao, Shengfu Mei, Yanting Han, and Jing Liu. Ultra-compliant liquid metal electrodes with in-plane self-healing capability for dielectric elastomer actuators. *Applied Physics Letters*, 103:64101, August 2013. ISSN 0003-6951. URL <https://ui.adsabs.harvard.edu/abs/2013ApPhL.103f4101L>.
- [137] John A Rogers. A Clear Advance in Soft Actuators. *Science*, 341:968–969, August 2013. ISSN 0036-8075. URL <https://ui.adsabs.harvard.edu/abs/2013Sci...341..968R>.
- [138] A Bele, C Tugui, M Asandulesa, D Ionita, L Vasiliu, G Stiubianu, M Iacob, C Racles, and M Cazacu. Conductive stretchable composites properly engineered to develop highly compliant electrodes for dielectric elastomer actuators. *Smart Materials and Structures*, 27(105005), 2018. doi: 10.1088/1361-665X/aad977. URL <https://iopscience.iop.org/article/10.1088/1361-665X/aad977>.
- [139] Jose Enrico Q Quinsaat, Mihaela Alexandru, Frank A Nuesch, Heinrich Hofmann, Andreas Borgschulte, and Dorina M Opris. Highly stretchable dielectric elastomer composites containing high volume fractions of silver nanoparticles. *Journal of Materials Chemistry A*, 3(28):14675–14685, 2015. ISSN 2050-7488. doi: 10.1039/C5TA03122B. URL <http://dx.doi.org/10.1039/C5TA03122B>.
- [140] S. Hau, G. Rizzello, and S. Seelecke. A novel dielectric elastomer membrane actuator concept for high-force applications. *Extreme Mechanics Letters*, 23:24–28, 2018. ISSN 2352-4316. URL <http://www.sciencedirect.com/science/article/pii/S2352431618301019>.
- [141] G. Kovacs, L. During, S. Michel, and G. Terrasi. Stacked dielectric elastomer actuator for tensile force transmission. *Sensors and Actuators A: Physical*, 155(2):299–307,

2009. ISSN 0924-4247. URL <http://www.sciencedirect.com/science/article/pii/S0924424709004002>.
- [142] F. Carpi and D. De Rossi. Small-strain modeling of helical dielectric elastomer actuators. *IEEE/ASME Transactions on Mechatronics*, 17(5706367):318–325, 2012.
- [143] S. Pfeil, K. Katzer, A. Kanan, J. Mersch, M. Zimmermann, M. Kaliske, and G. Gerlach. A biomimetic fish fin-like robot based on textile reinforced silicone. *Micromachines*, 11(298):1–16, 2020. ISSN 2072-666X. doi: 10.3390/mi11030298. URL <https://www.mdpi.com/2072-666X/11/3/298>.
- [144] M. Ghilardi, H. Boys, P. Torok, J. J. C. Busfield, and F. Carpi. Smart Lenses with Electrically Tuneable Astigmatism. *Scientific Reports*, 9(16127), 2019. doi: 10.1038/s41598-019-52168-8. URL <https://www.nature.com/articles/s41598-019-52168-8>.
- [145] H. Amin and S. F. M. Assal. Design Methodology of a Spring Roll Dielectric Elastomer-Based Actuator for a Hand Rehabilitation System. pages 997–1002, 2018. doi: 10.1109/ICMA.2018.8484462.
- [146] Jang Ho Park, Daewon Kim, Eduardo Divo, and Abdullah El Atrache. Optimization of helical dielectric elastomer actuator with additive manufacturing. volume 10594, page 32. Spie, March 2018. ISBN 9781510616844. doi: 10.1117/12.2296720. URL <https://www.spiedigitallibrary.org/conference-proceedings-of-spie/10594/2296720/Optimization-of-helical-dielectric-elastomer-actuator-with-additive-manufacturing/10.1117/12.2296720.full>.
- [147] David McCoul, Samuel Rosset, Samuel Schlatter, and Herbert Shea. Inkjet 3D printing of UV and thermal cure silicone elastomers for dielectric elastomer actuators. *Smart Materials and Structures*, 26(12):125022, 2017. ISSN 1361665x. doi: 10.1088/1361-665X/aa9695. URL <http://dx.doi.org/10.1088/1361-665X/aa9695>.
- [148] K. Jung, K. J. Kim, and H. R. Choi. A self-sensing dielectric elastomer actuator. *Sensors and Actuators, A: Physical*, 143(2):343–351, 2008.
- [149] N. C. Goulbourne, E. M. Mockensturm, and M. I. Frecker. Electro-elastomers: Large deformation analysis of silicone membranes. *International Journal of Solids and Structures*, 44(9):2609–2626, 2007. ISSN 0020-7683. URL <http://www.sciencedirect.com/science/article/pii/S002076830600312X>.

- [150] D. D.L. Chung. A critical review of piezoresistivity and its application in electrical-resistance-based strain sensing. *Journal of Materials Science* 2020 55:32, 55:15367–15396, August 2020. ISSN 1573-4803. doi: 10.1007/s10853-020-05099-z.
- [151] Manuela Hindermann Bischoff and Françoise Ehrburger-Dolle. Electrical conductivity of carbon black–polyethylene composites: Experimental evidence of the change of cluster connectivity in the PTC effect. *Carbon*, 39:375–382, March 2001. ISSN 0008-6223. doi: 10.1016/s0008-6223(00)00130-5.
- [152] Hwa Kim, Kwangsik Park, and Moo Yeol Lee. Biocompatible Dispersion Methods for Carbon Black. *Toxicological Research*, 28:209, December 2012. ISSN 19768257. doi: 10.5487/tr.2012.28.4.209. URL <https://www.ncbi.nlm.nih.gov/pmc/articles/PMC3834425/>.
- [153] Di Wu, Mengni Wei, Rong Li, Tao Xiao, Shen Gong, Zhu Xiao, Zhenghong Zhu, and Zhou Li. A percolation network model to predict the electrical property of flexible CNT/PDMS composite films fabricated by spin coating technique. *Composites Part B: Engineering*, 174:107034, 2019. ISSN 13598368. doi: 10.1016/j.compositesb.2019.107034.
- [154] L. Flandin, J. Y. Cavaille, Y. Brechet, and R. Dendievel. Characterization of the damage in nanocomposite materials by a.c. electrical properties: experiment and simulation. *Journal of Materials Science*, 34:1753–1759, April 1999. ISSN 1573-4803. doi: 10.1023/a:1004546806226.
- [155] Sven Pegel, Petra Pötschke, Gudrun Petzold, Ingo Alig, Sergej M. Dudkin, and Dirk Lellinger. Dispersion, agglomeration, and network formation of multiwalled carbon nanotubes in polycarbonate melts. *Polymer*, 49:974–984, February 2008. ISSN 0032-3861. doi: 10.1016/j.polymer.2007.12.024.
- [156] Pan Song and Yong Zhang. Vertically aligned carbon nanotubes/graphene/cellulose nanofiber networks for enhancing electrical conductivity and piezoresistivity of silicone rubber composites. *Composites Science and Technology*, 222:109366, May 2022. ISSN 0266-3538. doi: 10.1016/j.compscitech.2022.109366.
- [157] Melika Eklund and Nellie Kjäll. *Silicone-based Carbon Black Composite for Epidermal Electrodes*. Uppsala Universitet Department of Engineering Science, Division of Microsystems Technology, December 2019. URL <http://uu.diva-portal.org/smash/get/diva2:1384429/FULLTEXT02.pdf>.
- [158] Yuanzhen Wang, Chensheng Xu, Timotheus Jahnke, Wolfgang Verestek, Siegfried Schmauder, and Joachim P. Spatz. Microstructural Modeling and Simulation of a

- Carbon Black-Based Conductive Polymer - A Template for the Virtual Design of a Composite Material. *ACS Omega*, 7:28820–28830, August 2022. ISSN 24701343. doi: 10.1021/acsomega.2c01755/asset/images/large/ao2c01755\_0009.jpeg. URL <https://pubs.acs.org/doi/full/10.1021/acsomega.2c01755>.
- [159] R. Neffati and J. M.C. Brokken-Zijp. Electric conductivity in silicone-carbon black nanocomposites: percolation and variable range hopping on a fractal. *Materials Research Express*, 6:125058, November 2019. ISSN 2053-1591. doi: 10.1088/2053-1591/ab58fd. URL <https://iopscience.iop.org/article/10.1088/2053-1591/ab58fd>.
- [160] D. Bloor, A. Graham, E. J. Williams, P. J. Laughlin, and D. Lussey. Metal-polymer composite with nanostructured filler particles and amplified physical properties. *Applied Physics Letters*, 88:102103, March 2006. ISSN 00036951. doi: 10.1063/1.2183359/902621. URL [/aip/apl/article/88/10/102103/902621/Metal-polymer-composite-with-nanostructured-filler](https://aip.org/apl/article/88/10/102103/902621/Metal-polymer-composite-with-nanostructured-filler).
- [161] Rui Zhang, Mark Baxendale, and Ton Peijs. Universal resistivity-strain dependence of carbon nanotube/polymer composites. *Physical Review B - Condensed Matter and Materials Physics*, 76:195433, November 2007. ISSN 10980121. doi: 10.1103/physrevb.76.195433/figures/6/medium. URL <https://journals.aps.org/prb/abstract/10.1103/PhysRevB.76.195433>.
- [162] Leonel P. Madrid, Carlos A. Palacio, Arnaldo Matute, and Carlos A. Parra Vargas. Underlying Physics of Conductive Polymer Composites and Force Sensing Resistors (FSRs) under Static Loading Conditions. *Sensors (Basel, Switzerland)*, 17, September 2017. ISSN 14248220. doi: 10.3390/s17092108. URL <https://www.ncbi.nlm.nih.gov/pmc/articles/PMC5621037/>.
- [163] Ning Hu, Yoshifumi Karube, Cheng Yan, Zen Masuda, and Hisao Fukunaga. Tunneling effect in a polymer/carbon nanotube nanocomposite strain sensor. *Acta Materialia*, 56: 2929–2936, August 2008. ISSN 1359-6454. doi: 10.1016/j.actamat.2008.02.030.
- [164] C. Grimaldi and I. Balberg. Tunneling and nonuniversality in continuum percolation systems. *Physical Review Letters*, 96:066602, February 2006. ISSN 10797114. doi: 10.1103/physrevlett.96.066602/figures/2/medium. URL <https://journals.aps.org/prl/abstract/10.1103/PhysRevLett.96.066602>.

- [165] Aykut Ilgaz. Impedance Analysis of Single Walled Carbon Nanotube/Vinylester Polymer Composites. *Kuwait Journal of Science*, July 2021. ISSN 2307-4116. doi: 10.48129/kjs.19891. URL <https://journalskuwait.org/kjs/index.php/KJS/article/view/19891>.
- [166] Abhinav Priyadarshi, Mohammad Khavari, Tungky Subroto, Paul Prentice, Koulis Pericleous, Dmitry Eskin, John Durodola, and Iakovos Tzanakis. Mechanisms of ultrasonic de-agglomeration of oxides through in-situ high-speed observations and acoustic measurements. *Ultrasonics Sonochemistry*, 79:1350–4177, November 2021. ISSN 18732828. doi: 10.1016/j.ultsonch.2021.105792. URL <https://www.ncbi.nlm.nih.gov/pmc/articles/PMC8524947/>.
- [167] Olga Kudryashova, Alexander Vorozhtsov, and Pavel Danilov. Deagglomeration and Coagulation of Particles in Liquid Metal Under Ultrasonic Treatment. 44:543–549, 2019. doi: 10.24425/aoa.2019.129269.
- [168] Samuel Rosset, Oluwaseun A. Ararom, Samuel Schlatter, and Herbert R. Shea. Fabrication process of silicone-based dielectric elastomer actuators. *Journal of Visualized Experiments*, page 53423, February 2016. ISSN 1940087x. doi: 10.3791/53423. URL [www.jove.com?url=https://www.jove.com/video/53423](http://www.jove.com?url=https://www.jove.com/video/53423).
- [169] Chaima Fekiri, Ho Chan Kim, and In Hwan Lee. 3d-printable carbon nanotubes-based composite for flexible piezoresistive sensors. *Materials*, 13:1–12, December 2020. doi: 10.3390/ma13235482.
- [170] A. K. Bastola, M. Paudel, and L. Li. Development of hybrid magnetorheological elastomers by 3D printing. *Polymer*, 149:213–228, August 2018. ISSN 00323861. doi: 10.1016/j.polymer.2018.06.076.
- [171] Ming Li, Sujie Chen, Boyu Fan, Bangyuan Wu, and Xiaojun Guo. Printed Flexible Strain Sensor Array for Bendable Interactive Surface. *Advanced Functional Materials*, 30:2003214, August 2020. ISSN 16163028. doi: 10.1002/adfm.202003214. URL <https://onlinelibrary-wiley-com/doi/full/10.1002/adfm.202003214>.
- [172] Jianan Yi, Frank Babick, Carsten Strobel, Samuel Rosset, Luca Ciarella, Dmitry Borin, Katherine Wilson, Iain Anderson, Andreas Richter, and E. F. Markus Henke. Characterizations and Inkjet Printing of Carbon Black Electrodes for Dielectric Elastomer Actuators. *ACS Applied Materials and Interfaces*, 15:41992–42003, September 2023. ISSN 19448252. doi: 10.1021/acsami.3c05444. URL <https://pubs.acs.org/doi/full/10.1021/acsami.3c05444>.

- [173] Jeong Hun Kim, Ji Young Hwang, Ha Ryeon Hwang, Han Seop Kim, Joong Hoon Lee, Jae Won Seo, Ueon Sang Shin, and Sang Hoon Lee. Simple and cost-effective method of highly conductive and elastic carbon nanotube/polydimethylsiloxane composite for wearable electronics. *Scientific Reports*, 8:54853, December 2018. ISSN 20452322. doi: 10.1038/s41598-017-18209-w. URL [www.nature.com/scientificreports.](http://www.nature.com/scientificreports/)
- [174] Bettina Fasolt, Micah Hodgins, Gianluca Rizzello, and Stefan Seelecke. Effect of screen printing parameters on sensor and actuator performance of dielectric elastomer (DE) membranes. *Sensors and Actuators A: Physical*, 265:10–19, October 2017. ISSN 0924-4247. doi: 10.1016/j.sna.2017.08.028.
- [175] Gargallo Ligia and Radic Deodato. *Viscoelastic Behaviour of Polymers*, pages 43–162. Springer Netherlands, 2009. ISBN 978-1-4020-9372-2. doi: 10.1007/978-1-4020-9372-2\_2. URL [https://doi.org/10.1007/978-1-4020-9372-2\\_2](https://doi.org/10.1007/978-1-4020-9372-2_2).
- [176] A. R. Payne, R. E. Whittaker, and J. F. Smith. Effect of vulcanization on the low-strain dynamic properties of filled rubbers. *Journal of Applied Polymer Science*, 16: 1191–1212, May 1972. ISSN 1097-4628. doi: 10.1002/app.1972.070160513. URL <https://onlinelibrary.wiley.com/doi/full/10.1002/app.1972.070160513>.
- [177] D. Jalocha. Payne effect: A Constitutive model based on a dynamic strain amplitude dependent spectrum of relaxation time. *Mechanics of Materials*, 148:103526, September 2020. ISSN 0167-6636. doi: 10.1016/j.mechmat.2020.103526.
- [178] Martin AvilaTorrado, Andrei Constantinescu, Michael Johlitz, and Alexander Lion. Viscoelastic behavior of filled silicone elastomers and influence of aging in inert and hermetic environment. *Continuum Mechanics and Thermodynamics*, 36:333–350, June 2022. ISSN 14320959. doi: 10.1007/s00161-022-01112-9.
- [179] L. Mullins. Softening of Rubber by Deformation. *Rubber Chemistry and Technology*, 42: 339–362, March 1969. ISSN 0035-9475. doi: 10.5254/1.3539210. URL <https://dx.doi.org/10.5254/1.3539210>.
- [180] Behzad Babaei, Ali Davarian, Kenneth M. Pryse, Elliot L. Elson, and Guy M. Genin. Efficient and optimized identification of generalized Maxwell viscoelastic relaxation spectra. *Journal of the mechanical behavior of biomedical materials*, 55:32, March 2015. ISSN 18780180. doi: 10.1016/j.jmbbm.2015.10.008. URL <https://www.ncbi.nlm.nih.gov/pmc/articles/PMC5668653/>.

- [181] Chen Tzikang. Determining a Prony Series for a Viscoelastic Material From Time Varying Strain Data. *NASA Langley Research Center - Technical Memorandum*, 2000.
- [182] A. Bonfanti, J. L. Kaplan, G. Charras, and A. Kabla. Fractional viscoelastic models for power-law materials. *Soft Matter*, 16:6002–6020, July 2020. ISSN 17446848. doi: 10.1039/d0sm00354a. URL <https://pubs.rsc.org/en/content/articlehtml/2020/sm/d0sm00354a>.
- [183] Zoran B. Vosika, Goran M. Lazovic, Gradimir N. Misevic, and Jovana B. Simic-Krstic. Fractional calculus model of electrical impedance applied to human skin. *PloS one*, 8, April 2013. ISSN 1932-6203. doi: 10.1371/journal.pone.0059483. URL <https://pubmed.ncbi.nlm.nih.gov/23577065/>.
- [184] Byoung-Yong Chang. The Effective Capacitance of a Constant Phase Element with Resistors in Series. *J. Electrochem. Sci. Technol*, 2022:479–485, 2022. doi: 10.33961/jecst.2022.00451. URL <https://doi.org/10.33961/jecst.2022.00451>.
- [185] Stefania Russo, Samia Nefti-Meziani, Nicola Carbonaro, and Alessandro Tognetti. A Quantitative Evaluation of Drive Pattern Selection for Optimizing EIT-Based Stretchable Sensors. *Sensors*, 17, 2017. doi: 10.3390/s17091999.
- [186] David Sherry, Archie McCulloch, Qing Liang, al, Jian Wu, Pranav Garg, Suxing Pan, Andy Adler, and William R B Lionheart. Uses and abuses of EIDORS: an extensible software base for EIT. *Physiological Measurement*, 27:S25, April 2006. ISSN 0967-3334. doi: 10.1088/0967-3334/27/5/s03. URL <https://iopscience-iop-org/article/10.1088/0967-3334/27/5/S03>.
- [187] B H Brown and A D Seagar. The Sheffield data collection system. *Clinical Physics and Physiological Measurement*, 8:91–97, November 1987. ISSN 0143-0815. doi: 10.1088/0143-0815/8/4a/012.
- [188] Andy Adler and David Holder. *Electrical Impedance Tomography*. CRC Press, 2 edition, November 2021. ISBN 9780429399886. doi: 10.1201/9780429399886.
- [189] Margaret Cheney, David Isaacson, and Jonathan C. Newell. Electrical impedance tomography. *SIAM Review*, 41:85–101, 1999. ISSN 00361445. doi: 10.1137/s0036144598333613. URL <http://www.siam.org/journals/sirev/41-1/33361.html>.

- [190] Richard Bayford. Basic Electrical Impedance Tomography, pages 29–44. Springer, Cham, March 2018. doi: 10.1007/978-3-319-74388-2\_3. URL [https://link.springer.com/chapter/10.1007/978-3-319-74388-2\\_3](https://link.springer.com/chapter/10.1007/978-3-319-74388-2_3).
- [191] William R. B. Lionheart. EIT Reconstruction Algorithms: Pitfalls, Challenges and Recent Developments. *Physiological Measurement*, 25:125–142, October 2003. doi: 10.1088/0967-3334/25/1/021. URL <http://arxiv.org/abs/physics/0310151>.
- [192] Thiago de Castro Martins, André Kubagawa Sato, Fernando Silva de Moura, Erick Dario León Bueno de Camargo, Olavo Luppi Silva, Tales Batista Rattis Santos, Zhanqi Zhao, Knut Möller, Marcelo Brito Passos Amato, Jennifer L. Mueller, Raul Gonzalez Lima, and Marcos de Sales Guerra Tsuzuki. A review of electrical impedance tomography in lung applications: Theory and algorithms for absolute images. *Annual Reviews in Control*, 48: 442–471, January 2019. ISSN 1367-5788. doi: 10.1016/j.arcontrol.2019.05.002.
- [193] Andy Adler, John H. Arnold, Richard Bayford, Andrea Borsic, Brian Brown, Paul Dixon, Theo J.C. Faes, Inéz Frerichs, Hervé Gagnon, Yvo Gärber, Bartłomiej Grychtol, Günter Hahn, William R.B. Lionheart, Anjum Malik, Robert P. Patterson, Janet Stocks, Andrew Tizzard, Norbert Weiler, and Gerhard K. Wolf. GREIT: a unified approach to 2D linear EIT reconstruction of lung images. *Physiological measurement*, 30, 2009. ISSN 0967-3334. doi: 10.1088/0967-3334/30/6/s03. URL <https://pubmed.ncbi.nlm.nih.gov/19491438/>.
- [194] David Silvera-Tawil, David Rye, Manuchehr Soleimani, and Mari Velonaki. Electrical impedance tomography for artificial sensitive robotic skin: A review. *IEEE Sensors Journal*, 15:2001–2016, April 2015. doi: 10.1109/jsen.2014.2375346.
- [195] Francesco Visentin, Paolo Fiorini, and Kenji Suzuki. A Deformable Smart Skin for Continuous Sensing Based on Electrical Impedance Tomography. *Sensors 2016, Vol. 16, Page 1928*, 16:1928, November 2016. ISSN 1424-8220. doi: 10.3390/s16111928. URL <https://www.mdpi.com/1424-8220/16/11/1928/htm>.
- [196] Tyler N. Tallman and Danny J. Smyl. Structural health and condition monitoring via electrical impedance tomography in self-sensing materials: a review. *Smart Materials and Structures*, 29:123001, October 2020. ISSN 0964-1726. doi: 10.1088/1361-665X/abb352. URL <https://iopscience.iop.org/article/10.1088/1361-665X/abb352>.
- [197] Alirezaei Hassan, Akihiko Nagakubo, and Yasuo Kuniyoshi. A tactile distribution sensor which enables stable measurement under high and dynamic stretch. *3DUI -*

- IEEE Symposium on 3D User Interfaces 2009 - Proceedings, pages 87–93, 2009. doi: 10.1109/3dui.2009.4811210.
- [198] Yo Kato, Toshiharu Mukai, Tomonori Hayakawa, and Tetsuyoshi Shibata. Tactile sensor without wire and sensing element in the tactile region based on EIT method. Proceedings of IEEE Sensors, pages 792–795, 2007. doi: 10.1109/icsens.2007.4388519.
- [199] M Lacasse, V Duchaine, and C Gosselin. Characterization of the electrical resistance of carbon-black-filled silicone: Application to a flexible and stretchable robot skin. pages 4842–4848, May 2010. doi: 10.1109/robot.2010.5509283.
- [200] E. F.M. Henke, Katherine E. Wilson, and I. A. Anderson. Modeling of dielectric elastomer oscillators for soft biomimetic applications. Bioinspiration and Biomimetics, 13:046009, June 2018. ISSN 17483190. doi: 10.1088/1748-3190/aac911. URL <https://doi.org/10.1088/1748-3190/aac911>.
- [201] Yanju Liu, Liwu Liu, Zhen Zhang, and Jinsong Leng. Dielectric elastomer film actuators: Characterization, experiment and analysis. Smart Materials and Structures, 18:095024, July 2009. ISSN 09641726. doi: 10.1088/0964-1726/18/9/095024. URL <https://iopscience-iop-org/article/10.1088/0964-1726/18/9/095024>.
- [202] Federico Carpi, Stanisa Raspopovic, Gabriele Frediani, and Danilo De Rossi. Real-time control of dielectric elastomer actuators via bioelectric and biomechanical signals. Polymer International, 59:422–429, March 2010. ISSN 09598103. doi: 10.1002/pi.2757. URL <http://doi.wiley.com/10.1002/pi.2757>.
- [203] Yasuhiro Mouri, Yuta Murai, Yoshiko Yabuki, Takumi Kato, Hideki Ohmae, Yoshihiro Tomita, Shunta Togo, Yinlai Jiang, and Hiroshi Yokoi. Development of new flexible dry electrode for myoelectric sensor using conductive silicone. pages 478–482. Institute of Electrical and Electronics Engineers Inc., January 2019. ISBN 9781538673553. doi: 10.1109/cbs.2018.8612280. URL <https://ieeexplore-ieee-org/document/8612280>.
- [204] S. L. Wang, P. Wang, and T. H. Ding. Development of wireless compressive/relaxation-stress measurement system integrated with pressure-sensitive carbon black-filled silicone rubber-based sensors. Sensors and Actuators, A: Physical, 157:36–41, January 2010. ISSN 09244247. doi: 10.1016/j.sna.2009.11.037.
- [205] VishayPG. Strain Gage Selection: Criteria, Procedures, Recommendations - Tech Note, May 2018. URL [https://intertechnology.com/Vishay/pdfs/TechNotes\\_TechTips/TN-505.pdf](https://intertechnology.com/Vishay/pdfs/TechNotes_TechTips/TN-505.pdf).

- [206] Dinesh Maddipatla, Binu B. Narakathu, Mohammed M. Ali, Amer A. Chlaihawi, and Massood Z. Atashbar. Development of a novel carbon nanotube based printed and flexible pressure sensor. Institute of Electrical and Electronics Engineers Inc., April 2017. ISBN 9781509032020. doi: 10.1109/sas.2017.7894034.
- [207] Luheng Wang and Yanyan Han. Compressive relaxation of the stress and resistance for carbon nanotube filled silicone rubber composite. *Composites Part A: Applied Science and Manufacturing*, 47:63–71, April 2013. ISSN 1359835x. doi: 10.1016/j.compositesa.2012.11.018.
- [208] C Racles, M Asandulesa, V Tiron, C Tugui, N Vornicu, Ciubotaru B, M Mičušík, M Omastova, A Vasiliu, and C Ciomaga. Elastic composites with PDMS matrix and polysulfone-supported silver nanoparticles as filler. *Polymer*, 217, March 2021. ISSN 0032-3861. doi: <https://doi.org/10.1016/j.polymer.2021.123480>. URL <https://www.sciencedirect.com/science/article/pii/S0032386121001038>.
- [209] Shoji Fukushima, Tatsuya Kasai, Yumi Umeda, Makoto Ohnishi, Toshiaki Sasaki, and Michiharu Matsumoto. Carcinogenicity of multi-walled carbon nanotubes: Challenging issue on hazard assessment. *Journal of Occupational Health*, 60:10–30, 2018. ISSN 13489585. doi: 10.1539/joh.17-0102-RA. URL <https://www.ncbi.nlm.nih.gov/pmc/articles/PMC5799097/>.
- [210] Zannatul Ferdous and Abderrahim Nemmar. Health impact of silver nanoparticles: A review of the biodistribution and toxicity following various routes of exposure. *International Journal of Molecular Sciences*, 21, April 2020. ISSN 14220067. doi: 10.3390/ijms21072375. URL <https://www.ncbi.nlm.nih.gov/pmc/articles/PMC7177798/>.
- [211] L. J. Rausch, E. C. Bisinger, and A. Sharma. Carbon black should not be classified as a human carcinogen based on rodent bioassay data. *Regulatory Toxicology and Pharmacology*, 40:28–41, August 2004. ISSN 02732300. doi: 10.1016/j.yrtph.2004.04.004.
- [212] Tim Giffney, Estelle Bejanin, Agee S. Kurian, Jadranka Travas-Sejdic, and Kean Aw. Highly stretchable printed strain sensors using multi-walled carbon nanotube/silicone rubber composites. *Sensors and Actuators, A: Physical*, 259:44–49, June 2017. ISSN 09244247. doi: 10.1016/j.sna.2017.03.005.
- [213] Harish Devaraj, Tim Giffney, Adeline Petit, Mahtab Assadian, and Kean Aw. The development of highly flexible stretch sensors for a Robotic Hand. *Robotics*, 7, September 2018. ISSN 22186581. doi: 10.3390/robotics7030054.

- [214] J Kost, A Foux, and M Narkis. Quantitative model relating electrical resistance, strain, and time for carbon black loaded silicone rubber. *Polymer Engineering and Science*, 34: 1628, November 1994. ISSN 00323888. doi: 10.1002/pen.760342108.
- [215] Peng Wang, Feng Xu, Ding Tianhuai, and Qin Yuanzhen. Time dependence of electrical resistivity under uniaxial pressures for carbon black/polymer composites. *Journal of Materials Science*, 39:4937–4939, 2004. URL <http://search.proquest.com/docview/2259673740?accountid=14499>.
- [216] Johannes Mersch, Hans Winger, Andreas Nocke, Chokri Cherif, and Gerald Gerlach. Experimental Investigation and Modeling of the Dynamic Resistance Response of Carbon Particle-Filled Polymers. *Macromolecular Materials and Engineering*, 305, October 2020. ISSN 14392054. doi: 10.1002/mame.202000361.
- [217] Laaraibi Abdo-Rahmane Anas, Guruvan Jodin, Damien Hoareau, Nicolas Bideau, and Florence Razan. Flexible Dynamic Pressure Sensor for Insole Based on Inverse Viscoelastic Model. *IEEE Sensors Journal*, 7:7634–7643, April 2023. doi: 10.1109/JSEN.2023.3245822.
- [218] SmoothOn. Dragon Skin™ 10 NV Product Information — Smooth-On, Inc., February 2021. URL <https://www.smooth-on.com/products/dragon-skin-10-nv/>.
- [219] ASTM. D412-16 Standard Test Methods for Vulcanized Rubber and Thermoplastic Elastomers—Tension, 2020. URL [https://compass.astm.org/EDIT/html\\_annot.cgi?D412+16](https://compass.astm.org/EDIT/html_annot.cgi?D412+16).
- [220] I. D. Johnston, D. K. McCluskey, C. K.L. Tan, and M. C. Tracey. Mechanical characterization of bulk Sylgard 184 for microfluidics and microengineering. *Journal of Micromechanics and Microengineering*, 24:035017, February 2014. ISSN 0960-1317. doi: 10.1088/0960-1317/24/3/035017. URL <https://iopscience.iop.org/article/10.1088/0960-1317/24/3/035017>.
- [221] Yuhong Wu, Frederick J. McGarry, Bisheng Zhu, John R. Keryk, and Dimitris E. Katsoulis. Temperature effect on mechanical properties of toughened silicone resins. *Polymer Engineering & Science*, 45:1522–1531, November 2005. ISSN 1548-2634. doi: 10.1002/pen.20423. URL <https://onlinelibrary.wiley.com/doi/full/10.1002/pen.20423>.
- [222] Jie Luo. Machining of Elastomers. 2005. URL <https://wumrc.engin.umich.edu/wp-content/uploads/sites/51/2013/08/LuoJie-MachiningofElastomers.pdf>.

- [223] Miroslawa Pawlyta, Jean Noël Rouzaud, and Stanislaw Duber. Raman microspectroscopy characterization of carbon blacks: Spectral analysis and structural information. *Carbon*, 84:479–490, April 2015. ISSN 0008-6223. doi: 10.1016/j.carbon.2014.12.030.
- [224] RamanLife. PDMS Raman spectrum. *Raman Spectra Database*, 2024. URL <https://ramanlife.com/library/pdms-raman/>.
- [225] Hui Xu, Li Xiu Gong, Xu Wang, Li Zhao, Yong Bing Pei, Gang Wang, Ya Jun Liu, Lian Bin Wu, Jian Xiong Jiang, and Long Cheng Tang. Influence of processing conditions on dispersion, electrical and mechanical properties of graphene-filled-silicone rubber composites. *Composites Part A: Applied Science and Manufacturing*, 91:53–64, December 2016. ISSN 1359835x. doi: 10.1016/j.compositesa.2016.09.011.
- [226] Michael Wissler and Edoardo Mazza. Electromechanical coupling in dielectric elastomer actuators. *Sensors and Actuators A: Physical*, 138:384–393, August 2007. ISSN 0924-4247. doi: 10.1016/j.sna.2007.05.029.
- [227] Guggi Kofod, Peter Sommer-Larsen, Roy Kornbluh, and Ron Pelrine. Actuation Response of Polyacrylate Dielectric Elastomers. *Journal of Intelligent Material Systems and Structures*, 14:787–793, December 2003. ISSN 1045389x. doi: 10.1177/104538903039260. URL <https://journals.sagepub.com/doi/10.1177/104538903039260>.
- [228] Laura Wegener Parfrey, Daniel J.G. Lahr, Andrew H. Knoll, and Laura A. Katz. Estimating the timing of early eukaryotic diversification with multigene molecular clocks. *Proceedings of the National Academy of Sciences of the United States of America*, 108:13624–13629, August 2011. ISSN 00278424. doi: 10.1073/pnas.1110633108. URL <https://www.ncbi.nlm.nih.gov/pmc/articles/PMC3158185/>.
- [229] Kamkim Andre and Irina Kiseleva. *Mechanosensitivity of the Nervous System*. Springer Dordrecht, 1 edition, September 2008. ISBN 978-1-4020-8716-5. doi: 10.1007/978-1-4020-8716-5.
- [230] Charles Molnar and Jane Gair. *Somatosensation*. OpenTextBC, 1 edition, 2015. ISBN 978-1-989623-99-2. URL <https://opentextbc.ca/biology/chapter/17-2-somatosensation/>.
- [231] B. F. Gonçalves, J. Oliveira, P. Costa, V. Correia, P. Martins, G. Botelho, and S. Lanceros-Mendez. Development of water-based printable piezoresistive sensors for large strain applications. *Composites Part B: Engineering*, 112:344–352, March 2017. ISSN 1359-8368. doi: 10.1016/j.compositesb.2016.12.047.

- [232] Philipp Loew, Marius Brill, Gianluca Rizzello, and Stefan Seelecke. Development of a nonintrusive pressure sensor for polymer tubes based on dielectric elastomer membranes. *Sensors and Actuators A: Physical*, 292:1–10, June 2019. ISSN 0924-4247. doi: 10.1016/j.sna.2019.03.006.
- [233] Jaehyuk Lee, Jaehyung Kim, Yujin Shin, and Inhwa Jung. Ultra-robust wide-range pressure sensor with fast response based on polyurethane foam doubly coated with conformal silicone rubber and CNT/TPU nanocomposites islands. *Composites Part B: Engineering*, 177:107364, November 2019. ISSN 1359-8368. doi: 10.1016/j.compositesb.2019.107364.
- [234] R.A. Knight and R.T. Lipczynski. The Use Of Eit Techniques To Measure Interface Pressure. pages 2307–2308. Institute of Electrical and Electronics Engineers (IEEE), August 1990. doi: 10.1109/iembs.1990.692299. URL <https://doi-org/10.1109/IEMBS.1990.692299>.
- [235] Akihiko Nagakubo, Hassan Alirezaei, and Yasuo Kuniyoshi. A deformable and deformation sensitive tactile distribution sensor. *2007 IEEE International Conference on Robotics and Biomimetics, ROBIO*, pages 1301–1308, 2007. doi: 10.1109/robio.2007.4522352.
- [236] Sang Ho Yoon, Ke Huo, Yunbo Zhang, Guiming Chen, Luis Paredes, Subramanian Chidambaram, and Karthik Ramani. iSoft: A Customizable Soft Sensor with Real-time Continuous Contact and Stretching Sensing. *Proceedings of the 30th Annual ACM Symposium on User Interface Software and Technology*, pages 665–678, October 2017. doi: 10.1145/3126594. URL <https://doi.org/10.1145/3126594.3126654>.
- [237] Akira Kato. EIT tactile sensor. April 2007.
- [238] Niccolo Biasi, Andrea Gargano, Lucia Arcarisi, Nicola Carbonaro, and Alessandro Tognetti. Physics-based Simulation and Machine Learning for the Practical Implementation of EIT-based Tactile Sensors. *IEEE Sensors Journal*, 2022. ISSN 15581748. doi: 10.1109/jsen.2022.3144038.
- [239] Panagiotis E. Chatzistergos, David Allan, Nachiappan Chockalingam, and Roozbeh Naemi. Shore hardness is a more representative measurement of bulk tissue biomechanics than of skin biomechanics. *Medical Engineering & Physics*, 105:103816, July 2022. ISSN 1350-4533. doi: 10.1016/j.medengphy.2022.103816.
- [240] Barry McDermott, Brian McGinley, Katarzyna Krukiewicz, Brendan Divilly, Marggie Jones, Manus Biggs, Martin O'Halloran, and Emily Porter. Stable tissue-mimicking materials and an anatomically realistic, adjustable head phantom for electrical impedance

- tomography. *Biomedical Physics & Engineering Express*, 4:015003, November 2017. ISSN 2057-1976. doi: 10.1088/2057-1976/aa922d. URL <https://iopscience.iop.org/article/10.1088/2057-1976/aa922d>.
- [241] Matthew E. D'Asaro, Michael S. Otten, Stephanie Chen, and Jeffrey H. Lang. Multidimensional characterization of piezoresistive carbon black silicone rubber composites. *Journal of Applied Polymer Science*, 134, May 2017. ISSN 10974628. doi: 10.1002/app.44773. URL <http://doi.wiley.com/10.1002/app.44773>.
- [242] Shuying Shang, Yujuan Yue, and Xiaoer Wang. Piezoresistive strain sensing of carbon black /silicone composites above percolation threshold. *Review of Scientific Instruments*, 87:123910, December 2016. ISSN 10897623. doi: 10.1063/1.4973274/916719. URL [/aip/rsi/article/87/12/123910/916719/Piezoresistive-strain-sensing-of-carbon-black](https://aip/rsi/article/87/12/123910/916719/Piezoresistive-strain-sensing-of-carbon-black).
- [243] Shuai Dong and Xiaojie Wang. Alignment of carbon iron into polydimethylsiloxane to create conductive composite with low percolation threshold and high piezoresistivity: experiment and simulation. *Smart Materials and Structures*, 26:045027, March 2017. ISSN 0964-1726. doi: 10.1088/1361-665x/aa62d2. URL <https://iopscience-iop-org/article/10.1088/1361-665X/aa62d2>.
- [244] Heng Yang, Lin Hui Gong, Zhong Zheng, and Xue Feng Yao. Highly stretchable and sensitive conductive rubber composites with tunable piezoresistivity for motion detection and flexible electrodes. *Carbon*, 158:893–903, 2020. ISSN 0008-6223. doi: 10.1016/j.carbon.2019.11.079. URL <http://www.sciencedirect.com/science/article/pii/S0008622319312126>.
- [245] Yu Cheng Ju, Donyau Chiang, Ming Yen Tsai, Hao Ouyang, and Sanboh Lee. Stress Relaxation Behavior of Poly(Methyl Methacrylate)/Graphene Composites: Ultraviolet Irradiation. *Polymers*, 14, October 2022. ISSN 20734360. doi: 10.3390/polym14194192/s1.
- [246] Junhui Zhao, Kun Dai, Chenggang Liu, Guoqiang Zheng, Bo Wang, Chuntai Liu, Jingbo Chen, and Changyu Shen. A comparison between strain sensing behaviors of carbon black-/polypropylene and carbon nanotubes/polypropylene electrically conductive composites. *Composites Part A: Applied Science and Manufacturing*, 48:129–136, May 2013. ISSN 1359-835x. doi: 10.1016/j.compositesa.2013.01.004.
- [247] Shailesh Vidhate, Jaycee Chung, Vijay Vaidyanathan, and Nandika Anne D'Souza. Resistive-conductive transitions in the time-dependent piezoresponse of PVDF-MWCNT

- nanocomposites. *Polymer Journal* 2010 42:7, 42:567–574, May 2010. ISSN 1349-0540. doi: 10.1038/pj.2010.44. URL <https://www.nature.com/articles/pj201044>.
- [248] D. H. Griffiths and R. D. Barker. Two-dimensional resistivity imaging and modelling in areas of complex geology. *Journal of Applied Geophysics*, 29:211–226, April 1993. ISSN 09269851. doi: 10.1016/0926-9851(93)90005-j.
- [249] Liangqi Yuan, Student Member, Yuan Wei, Jia Li, and Senior Member. Smart Pressure e-Mat for Human Sleeping Posture and Dynamic Activity Recognition. *arxiv*, May 2023. URL <https://arxiv.org/abs/2305.11367v1>.
- [250] Richie Ellingham, Lui Holder-Pearson, Chris Pretty, and Tim Giffney. A portable electrical impedance tomography based pressure mapping sensor and validation system. *HardwareX*, 21, 2025. [Under Review].
- [251] Sunjoo Hong, Kwonjoon Lee, Unsoo Ha, Hyunki Kim, Yongsu Lee, Youchang Kim, and Hoi Jun Yoo. A 4.9 mOhm-sensitivity mobile electrical impedance tomography IC for early breast-cancer detection system. *IEEE Journal of Solid-State Circuits*, 50:245–257, January 2015. ISSN 00189200. doi: 10.1109/jssc.2014.2355835.
- [252] Jaehyuk Lee, Surin Gweon, Kwonjoon Lee, Soyeon Um, Kyoung Rog Lee, Kwantae Kim, Jihee Lee, and Hoi Jun Yoo. A 9.6 mW per Ch 10 MHz Wide-bandwidth Electrical Impedance Tomography IC with Accurate Phase Compensation for Breast Cancer Detection. *Proceedings of the Custom Integrated Circuits Conference*, 2020-March, March 2020. ISSN 08865930. doi: 10.1109/cicc48029.2020.9075950. URL <https://doaj.org/article/2c43b707327d45f8b141ee0b6dbe3433>.
- [253] Yang Li, Nan Wang, Li Feng Fan, Peng Fei Zhao, Jin Hai Li, Lan Huang, and Zhong Yi Wang. Robust electrical impedance tomography for biological application: A mini review. *Heliyon*, 9:e15195, April 2023. ISSN 2405-8440. doi: 10.1016/j.heliyon.2023.e15195.
- [254] Manuchehr Soleimani. Electrical impedance tomography system: An open access circuit design. *BioMedical Engineering Online*, 5:1–8, May 2006. ISSN 1475925x. doi: 10.1186/1475-925x-5-28.
- [255] Ji Hoon Suh, Haidam Choi, Yoontae Jung, Sein Oh, Hyungjoo Cho, Nahmil Koo, Seong Joong Kim, Chisung Bae, Sohmyung Ha, and Minkyu Je. A Synchronous-Sampling Impedance-Readout IC with Baseline-Cancellation-Based Two-Step Conversion for Fast Neural Electrical Impedance Tomography. *2022 IEEE Asian Solid-State Circuits Conference, A-SSCC 2022 - Proceedings*, 2022. doi: 10.1109/a-sscc56115.2022.9980820.

- [256] Varun Kumar Tiwari, Mahmoud Meribout, Lyes Khezzar, Khalid Alhammadi, and Mohamed Tarek. Electrical Tomography Hardware Systems for Real-time Applications: A Review. *IEEE Access*, 2022. ISSN 21693536. doi: 10.1109/access.2022.3203584.
- [257] Jiawei Xu and Zhiliang Hong. Low Power Bio-Impedance Sensor Interfaces: Review and Electronics Design Methodology. *IEEE Reviews in Biomedical Engineering*, 15:23–35, 2022. ISSN 19411189. doi: 10.1109/rbme.2020.3041053.
- [258] Yang Zhang and Chris Harrison. Tomo. volume 119, pages 167–173. Association for Computing Machinery (ACM), November 2015. ISBN 9781450337793. doi: 10.1145/2807442.2807480. URL <https://dl.acm.org/doi/10.1145/2807442.2807480>.
- [259] Yang Zhang, Junhan Zhou, Gierad Laput, and Chris Harrison. Skintrack: Using the body as an electrical waveguide for continuous finger tracking on the skin. *Conference on Human Factors in Computing Systems - Proceedings*, pages 1491–1503, May 2016. doi: 10.1145/2858036.2858082. URL <https://dl.acm.org/doi/10.1145/2858036.2858082>.
- [260] Yang Zhang, Gierad Laput, and Chris Harrison. Electrick: Low-cost touch sensing using electric field tomography. volume 2017-May, pages 1–14. Association for Computing Machinery, May 2017. ISBN 9781450346559. doi: 10.1145/3025453.3025842. URL <https://dl.acm.org/doi/10.1145/3025453.3025842>.
- [261] Fabrice Salvaire. PySpice. URL <https://pyspice.fabrice-salvaire.fr>.
- [262] David Silvera Tawil, David Rye, and Mari Velonaki. Improved image reconstruction for an EIT-based sensitive skin with multiple internal electrodes. *IEEE Transactions on Robotics*, 27:425–435, June 2011. ISSN 15523098. doi: 10.1109/tro.2011.2125310.
- [263] Hua Xu, Shixong Zhang, Steven M. Anlage, Liangbing Hu, and George Grüner. Frequency- and electric-field-dependent conductivity of single-walled carbon nanotube networks of varying density. *Physical Review B - Condensed Matter and Materials Physics*, 77:075418, February 2008. ISSN 10980121. doi: 10.1103/physrevb.77.075418/figures/6/medium. URL <https://journals.aps.org/prb/abstract/10.1103/PhysRevB.77.075418>.
- [264] Vishay. DG406/407 - 16-Ch/Dual 8-Ch High-Performance CMOS Analog Multiplexers, 2024. URL <https://www.vishay.com/docs/70061/dg406.pdf>.

- [265] Luis SosaVivas, Jhon Gonzalez-Delgado, and Gabriel Torrente-Prato. Experimental and numerical study of orthotropic behavior of 3D printed polylactic acid by material extrusion. *Progress in Additive Manufacturing*, 8:947–959, October 2023. ISSN 23639520. doi: 10.1007/s40964-022-00369-5.
- [266] Guido Dhondt and Klaus Wittig. CalculiX, 2023. URL <https://www.calculix.de/>.
- [267] HTCSensor. TAL220 datasheet, 2024. URL <https://cdn.sparkfun.com/datasheets/Sensors/ForceFlex/TAL220M4M5Update.pdf>.
- [268] Dilhan M. Kalyon, Elvan Birinci, Rahmi Yazici, Bahadir Karuv, and Shawn Walsh. Electrical properties of composites as affected by the degree of mixedness of the conductive filler in the polymer matrix. *Polymer Engineering & Science*, 42:1609–1617, July 2002. ISSN 1548-2634. doi: 10.1002/pen.11056. URL <https://onlinelibrary.wiley.com/doi/full/10.1002/pen.11056>.
- [269] T. L. Rodgers and A. Kowalski. An electrical resistance tomography method for determining mixing in batch addition with a level change. *Chemical Engineering Research and Design*, 88:204–212, February 2010. ISSN 0263-8762. doi: 10.1016/j.cherd.2009.08.003.
- [270] F. Lux. Models proposed to explain the electrical conductivity of mixtures made of conductive and insulating materials. *Journal of Materials Science*, 28:285–301, January 1993. ISSN 00222461. doi: 10.1007/bf00357799.
- [271] Thinky Co. CNT Dispersion Application. Tokyo University of Science, Department of Applied Chemistry, 2010. URL [https://www.c3-analysentechnik.de/downloads/applikationsberichte/thinky/CNT\\_dispersion\\_application\\_eng\\_for\\_email.pdf](https://www.c3-analysentechnik.de/downloads/applikationsberichte/thinky/CNT_dispersion_application_eng_for_email.pdf).
- [272] Tianhuai Ding, Luheng Wang, and Peng Wang. Changes in electrical resistance of carbon-black-filled silicone rubber composite during compression. *Journal of Polymer Science Part B: Polymer Physics*, 45:2700–2706, October 2007. ISSN 08876266. doi: 10.1002/polb.21272. URL <http://doi.wiley.com/10.1002/polb.21272>.
- [273] Ehsan Hajiesmaili and David R. Clarke. Dielectric elastomer actuators. *Journal of Applied Physics*, 129:151102, April 2021. ISSN 0021-8979. doi: 10.1063/5.0043959. URL <https://aip-scitation-org/doi/abs/10.1063/5.0043959>.
- [274] Yaguang Guo, Liwu Liu, Yanju Liu, and Jinsong Leng. Review of Dielectric Elastomer Actuators and Their Applications in Soft Robots. *Advanced Intelligent Systems*, 3:

- 2000282, October 2021. ISSN 2640-4567. doi: 10.1002/aisy.202000282. URL <https://onlinelibrary.wiley.com/doi/full/10.1002/aisy.202000282>.
- [275] Franklin Iheanacho and Anantha Ramana Vellipuram. Physiology, Mechanoreceptors. *StatPearls*, September 2023. URL <https://www.ncbi.nlm.nih.gov/books/NBK541068/>. PMID: 31082112.
- [276] William H McKnight and Wayne C. McGinnis. Energy-harvesting device using electrostrictive polymers, January 2002. URL <http://www.patentbuddy.com/Patent/6433465>.
- [277] Federico Carpi, Danilo De Rossi, Roy Kornbluh, Ronald Pehrle, and Peter Sommer-Larsen. Dielectric elastomers as electromechanical transducers: Fundamentals, Materials, Devices, Models and Applications of an Emerging Electroactive Polymer Technology. *Dielectric Elastomers as Electromechanical Transducers*, page 329, July 2008. doi: 10.1016/b978-0-08-047488-5.x0001-9. URL <http://www.sciencedirect.com:5070/book/9780080474885/dielectric-elastomers-as-electromechanical-transducers>.
- [278] Soo Jin Adrian Koh, Xuanhe Zhao, and Zhigang Suo. Maximal energy that can be converted by a dielectric elastomer generator. *Applied Physics Letters*, 94, 2009. URL <http://imechanica.org/files/MaximalEnergyAPL.pdf>.
- [279] Hyouk Ryeol Choi, Kwangmok Jung, Nguyen Huu Chuc, Minyoung Jung, Igmo Koo, Jachoon Koo, Joonho Lee, Jonghoon Lee, Jaedo Nam, Misuk Cho, Youngkwan Lee, Hyouk Ryeol Choi, Kwangmok Jung, Nguyen Huu Chuc, Minyoung Jung, Igmo Koo, Jachoon Koo, Joonho Lee, Jonghoon Lee, Jaedo Nam, Misuk Cho, and Youngkwan Lee. Effects of prestrain on behavior of dielectric elastomer actuator. *Proceedings of the SPIE*, 5759:283–291, May 2005. ISSN 0277-786x. doi: 10.1117/12.599363. URL <https://ui.adsabs.harvard.edu/abs/2005SPIE.5759..283C/abstract>.
- [280] Yunwei Mao and Lallit Anand. Fracture of elastomeric materials by crosslink failure. *Journal of Applied Mechanics, Transactions ASME*, 85, August 2018. ISSN 15289036. doi: 10.1115/1.4040100.
- [281] Huichan Zhao, Aftab M. Hussain, Mihai Duduta, Daniel M. Vogt, Robert J. Wood, and David R. Clarke. Compact Dielectric Elastomer Linear Actuators. *Advanced Functional Materials*, 28, October 2018. ISSN 1616301x. doi: 10.1002/adfm.201804328. URL <http://doi.wiley.com/10.1002/adfm.201804328>.

- [282] P ; Thummala, L ; Huang, Z ; Zhang, and M A E Andersen. Analysis of Dielectric Electro Active Polymer Actuator and its High Voltage Driving Circuits. *Proceedings of the International Power Modulator Symposium and High Voltage Workshop*, 2012. doi: 10.1109/ipmhvc.2012.6518779. URL <https://doi.org/10.1109/IPMHVC.2012.6518779>.
- [283] Chongjing Cao and Andrew T. Conn. Performance Optimization of a Conical Dielectric Elastomer Actuator. *Actuators*, 7:32, June 2018. ISSN 2076-0825. doi: 10.3390/act7020032. URL <http://www.mdpi.com/2076-0825/7/2/32>.
- [284] Krunal Koshiya, Sebastian Gratz-Kelly, Paul Motzki, and Gianluca Rizzello. An embedded self-sensing motion control system for a strip-shaped dielectric elastomer actuators. volume 12482, pages 147–155. Spie, April 2023. ISBN 9781510660717. doi: 10.1117/12.2657131.
- [285] Canh Toan Nguyen, Hoa Phung, Tien Dat Nguyen, Hosang Jung, and Hyouk Ryeol Choi. Multiple-degrees-of-freedom dielectric elastomer actuators for soft printable hexapod robot. *Sensors and Actuators A: Physical*, 267:505–516, November 2017. ISSN 0924-4247. doi: 10.1016/j.sna.2017.10.010.
- [286] Yang Zhang, Yong Huang, Wenjie Sun, Hang Jin, Jinhui Zhang, Lida Xu, Shuai Dong, Zhenjin Xu, Bin Zhu, Jinrong Li, and Dezhi Wu. A multi-electrode electroelastomer cylindrical actuator for multimodal locomotion and its modeling. *International Journal of Mechanical Sciences*, 266:108964, March 2024. ISSN 0020-7403. doi: 10.1016/j.ijmecsci.2024.108964.
- [287] Jiang Zou, Shakiru Olajide Kassim, Jieji Ren, Vahid Vaziri, Sumeet S. Aphale, and Guoying Gu. A Generalized Motion Control Framework of Dielectric Elastomer Actuators: Dynamic Modeling, Sliding-Mode control and Experimental Evaluation. *IEEE Transactions on Robotics*, 2023. ISSN 19410468. doi: 10.1109/tro.2023.3338973.
- [288] Qibing Pei, Marcus Rosenthal, Scott Stanford, Harsha Prahlad, and Ron Pelrine. Multiple-degrees-of-freedom electroelastomer roll actuators. *Smart Materials and Structures*, 13: N86, September 2004. ISSN 0964-1726. doi: 10.1088/0964-1726/13/5/n03. URL <https://iopscience.iop.org/article/10.1088/0964-1726/13/5/N03>.
- [289] Federico Carpi, Iain Anderson, Siegfried Bauer, Gabriele Frediani, Giuseppe Gallone, Massimiliano Gei, Christian Graaf, Claire Jean-Mistral, William Kaal, Guggi Kofod, Matthias Kollosche, Roy Kornbluh, Benny Lassen, Marc Matysek, Silvain Michel, Stephan Nowak,

- Benjamin O'Brien, Qibing Pei, Ron Pelrine, Björn Rechenbach, Samuel Rosset, and Herbert Shea. Standards for dielectric elastomer transducers. *Smart Materials and Structures*, 24:105025, September 2015. ISSN 0964-1726. doi: 10.1088/0964-1726/24/10/105025. URL <https://iopscience.iop.org/article/10.1088/0964-1726/24/10/105025>.
- [290] Jianjian Huang, Fang Wang, Li Ma, Zhiqiang Zhang, Erchao Meng, Chao Zeng, Hao Zhang, and Dongjie Guo. Vinylsilane-rich silicone filled by polydimethylsiloxane encapsulated carbon black particles for dielectric elastomer actuator with enhanced out-of-plane actuations. *Chemical Engineering Journal*, 428:131354, January 2022. ISSN 1385-8947. doi: 10.1016/j.cej.2021.131354.
- [291] Hiroki Shigemune, Shigeki Sugano, Jun Nishitani, Masayuki Yamauchi, Naoki Hosoya, Shuji Hashimoto, and Shingo Maeda. Dielectric Elastomer Actuators with Carbon Nanotube Electrodes Painted with a Soft Brush. *Actuators*, 7:51, August 2018. ISSN 2076-0825. doi: 10.3390/act7030051. URL <https://www.mdpi.com/2076-0825/7/3/51/htm>.
- [292] Leipeng Liu, Yanfei Huang, Yihe Zhang, Elshad Allahyarov, Zhongbo Zhang, Fengzhu Lv, and Lei Zhu. Understanding reversible Maxwellian electroactuation in a 3M VHB dielectric elastomer with prestrain. *Polymer*, 144:150–158, May 2018. ISSN 0032-3861. doi: 10.1016/j.polymer.2018.04.048.
- [293] Alexander Helal, Marc Doumit, and Robert Shaheen. Biaxial experimental and analytical characterization of a dielectric elastomer. *Applied Physics A: Materials Science and Processing*, 124:1–11, January 2018. ISSN 14320630. doi: 10.1007/s00339-017-1422-3.
- [294] Deng Pan and Adrian Koh Soo Jin. Uniaxial Prestretch Dependence of Dielectric Permittivity in Polyacrylate Elastomers, July 2015. URL <http://dengpan.ca/reports/vhb.pdf>.
- [295] Federico Carpi, Piero Chiarelli, Alberto Mazzoldi, and Danilo De Rossi. Electromechanical characterisation of dielectric elastomer planar actuators: comparative evaluation of different electrode materials and different counterloads. *Sensors and Actuators A: Physical*, 107:85–95, October 2003. ISSN 0924-4247. doi: 10.1016/s0924-4247(03)00257-7.
- [296] Florian M. Weiss, Frederikke B. Madsen, Tino Töpper, Bekim Osmani, Vanessa Leung, and Bert Müller. Molecular beam deposition of high-permittivity polydimethylsiloxane for nanometer-thin elastomer films in dielectric actuators. *Materials and Design*, 105: 106–113, 2016. ISSN 18734197. doi: 10.1016/j.matdes.2016.05.049.

- [297] Musthafa O. Mavukkandy, Samantha A. McBride, David M. Warsinger, Nadir Dizge, Shadi W. Hasan, and Hassan A. Arafat. Thin film deposition techniques for polymeric membranes– A review. *Journal of Membrane Science*, 610:118258, September 2020. ISSN 18733123. doi: 10.1016/j.memsci.2020.118258.
- [298] Julie Diani, Bruno Fayolle, and Pierre Gilormini. A review on the Mullins effect. *European Polymer Journal*, 45:601–612, March 2009. ISSN 0014-3057. doi: 10.1016/j.eurpolymj.2008.11.017.
- [299] Junshi Zhang, Lei Liu, and Hualing Chen. Electromechanical properties of soft dissipative dielectric elastomer actuators influenced by electrode thickness and conductivity. *Journal of Applied Physics*, 127:184902, May 2020. ISSN 10897550. doi: 10.1063/5.0001580/280844. URL [/aip/jap/article/127/18/184902/280844/Electromechanical-properties-of-soft-dissipative](https://aip/jap/article/127/18/184902/280844/Electromechanical-properties-of-soft-dissipative).
- [300] Neil Savage. Squishy Power Generators. *IEEE Spectrum*, December 2012. URL <https://spectrum.ieee.org/squishy-power-generators>.
- [301] COMSOL. COMSOL Multiphysics, 2022. URL <https://www.comsol.com>.
- [302] Ivica Smolic and Bruno Klajn. Capacitance Matrix Revisited. *Progress in Electromagnetics Research B*, 92:1–18, March 2021. URL <https://www.jpier.org/api/download.php?id=21011501>.
- [303] Catherine Redmond. Winning the Battle Against Latch-up in CMOS Analog Switches. *ADI Analog Dialogue*, October 2001. URL <https://analog.com/media/en/analog-dialogue/volume-35/number-1/articles/winning-the-battle-against-latchup.pdf>.
- [304] IEC. IEC 61000-4-2 - Testing and Measurement Techniques – Electrostatic Discharge Immunity Test, September 2008. URL <https://webstore.iec.ch/en/publication/4189>.
- [305] John H. Zhang, Andre Obenaus, David S. Liebeskind, Jiping Tang, Richard Hartman, and William J. Pearce. Recanalization, reperfusion, and recirculation in stroke. *Journal of Cerebral Blood Flow and Metabolism*, 37:3818–3823, 2017. ISSN 15597016. doi: 10.1177/0271678x17732695.
- [306] Joshua Reynolds Smith. Toward Electric Field Tomography. Massachusetts Institute of Technology, August 1995. URL <https://cba.mit.edu/docs/theses/95.08.smith.pdf>.

- [307] Joshua Reynolds Smith. Electric Field Imaging. Massachusetts Institute of Technology, February 1999. URL <https://cba.mit.edu/docs/theses/99.02.smithphd.pdf>.
- [308] Francisco Zamora-Arellano, Oscar Roberto López-Bonilla, Enrique Efrén García-Guerrero, Jesús Everardo Olguín-Tiznado, Everardo Inzunza-González, Didier López-Mancilla, and Esteban Tlelo-Cuautle. Development of a Portable, Reliable and Low-Cost Electrical Impedance Tomography System Using an Embedded System. Electronics 2021, Vol. 10, Page 15, 10:15, December 2020. ISSN 2079-9292. doi: 10.3390/electronics10010015. URL <https://www.mdpi.com/2079-9292/10/1/15/htm>.
- [309] Minseo Kim, Hyunki Kim, Jaeeun Jang, Jihee Lee, Jaehyuk Lee, Jiwon Lee, Kyungrog Lee, Kwantae Kim, Yongsu Lee, and Hoi Jun Yoo. A 1.4mO-sensitivity 94dB-dynamic-range electrical impedance tomography SoC and 48-channel Hub SoC for 3D lung ventilation monitoring system. Digest of Technical Papers - IEEE International Solid-State Circuits Conference, 60:354–355, March 2017. ISSN 01936530. doi: 10.1109/isscc.2017.7870407.
- [310] Mohammad Takhti and Kofi Odame. A power adaptive, 1.22-pw/Hz, 10-mHz read-out front-end for bio-impedance measurement. IEEE Transactions on Biomedical Circuits and Systems, 13:725–734, August 2019. ISSN 19409990. doi: 10.1109/tbcas.2019.2918262.
- [311] Boxiao Liu, Guoxing Wang, Yongfu Li, Hui Li, Yue Gao, Lei Zeng, Yixin Ma, Yong Lian, and Chun Huat Heng. 22.6 A 13-Channel 1.53-mW 11.28-mm<sup>2</sup> Electrical Impedance Tomography SoC Based on Frequency Division Multiplexing with 10× Throughput Reduction. Digest of Technical Papers - IEEE International Solid-State Circuits Conference, 2019-February:370–372, March 2019. ISSN 01936530. doi: 10.1109/isscc.2019.8662352.
- [312] Bei Yuan, Dong Hu, Suxi Gu, Songhua Xiao, and Fei Song. The global burden of traumatic amputation in 204 countries and territories. Frontiers in Public Health, 11:1258853, 2023. ISSN 22962565. doi: 10.3389/fpubh.2023.1258853. URL <https://www.ncbi.nlm.nih.gov/pmc/articles/PMC10622756/>.
- [313] Weizhong Ding, Shian Hu, Pengju Wang, Honglei Kang, Renpeng Peng, Yimin Dong, and Feng Li. Spinal Cord Injury: The Global Incidence, Prevalence, and Disability From the Global Burden of Disease Study 2019. Spine, 47:1532, November 2022. ISSN 15281159. doi: 10.1097/brs.0000000000004417. URL <https://www.ncbi.nlm.nih.gov/pmc/articles/PMC9554757/>.
- [314] Ondrej Stritesky. Does your newly assembled Original Prusa i3 MK3 print the best it can, January 2019. URL <https://blog.prusa3d.com/>

[does-your-freshly-assembled-original-prusa-i3-mk3-print-as-the-best-it-can\\_29445/](#).

- [315] Prusa. Print Quality and Troubleshooting, 2024. URL [https://help.prusa3d.com/category/print-quality-troubleshooting\\_225](https://help.prusa3d.com/category/print-quality-troubleshooting_225).
- [316] Prusa. Original Prusa i3 MK3S+ kit assembly - 5. E-axis assembly, 2023. URL [https://help.prusa3d.com/guide/5-e-axis-assembly\\_169235](https://help.prusa3d.com/guide/5-e-axis-assembly_169235).
- [317] Prusa. Original Prusa i3 MK3S+ kit assembly - 8. Electronics Assembly, 2023. URL [OriginalPrusa i3MK3S+kitassembly](#).
- [318] Espressif. Get Started - ESP32 - — ESP-IDF Programming Guide v5.2.2, 2024. URL <https://docs.espressif.com/projects/esp-idf/en/stable/esp32/get-started/index.html>.
- [319] N. J. Avis and D. C. Barber. Adjacent or polar drive?: Image reconstruction implications in electrical impedance tomography systems employing filtered back projection. *Proceedings of the Annual International Conference of the IEEE Engineering in Medicine and Biology Society, EMBS*, 5:1689–1690, 1992. ISSN 1557170x. doi: 10.1109/иемbs.1992.5761991.
- [320] Chunhui Dang, Cédric Bellis, Mathieu Darnajou, Guillaume Ricciardi, Saba Mylvaganam, and Salah Bourennane. Practical comparisons of EIT excitation protocols with applications in high-contrast imaging. *Measurement Science and Technology*, 32, 2021. doi: 10.1088/1361-6501/abe742. URL <https://hal.science/hal-03370772>.
- [321] Zainab Husain, Nadya Abdel Madjid, and Panos Liatsis. Tactile sensing using machine learning-driven electrical impedance tomography. *IEEE Sensors Journal*, 21:11628–11642, May 2021. ISSN 15581748. doi: 10.1109/jsen.2021.3054870.
- [322] IEC. Part 4-41: Protection for safety – Protection against electric shock. IEC, 5 edition, December 2005.